$$m'BaO + BaTiO_3 \rightleftharpoons Ba_{1+m'}TiO_{3+m'}$$
$$\equiv (1+m')Ba_{Ba}^{\times} + Ti_{Ti}^{\times} + m'V_{Ti}'''' + (3+m')O_O^{\times} + 2m'V_O^{\bullet\bullet}$$

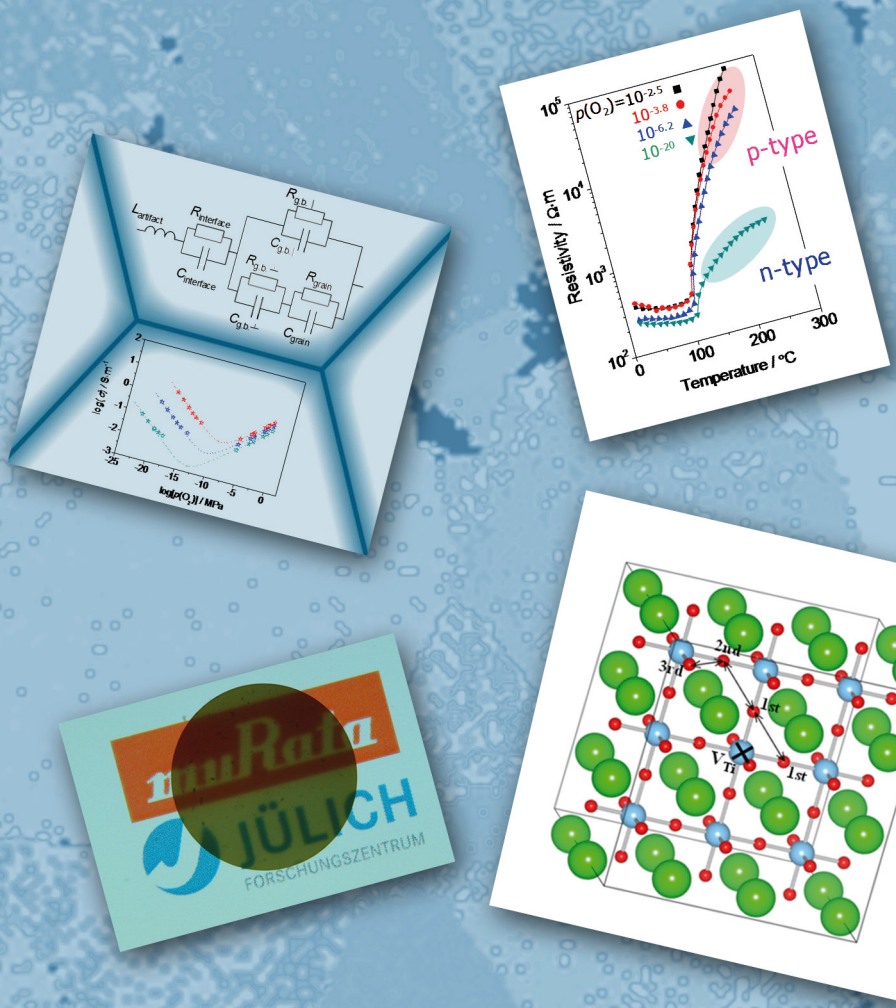

Crystal- and Defect-Chemistry of Fine Grained Thermistor Ceramics on $BaTiO_3$ Basis with BaO-Excess

Hayato Katsu

JÜLICH
FORSCHUNGSZENTRUM

Mitglied der Helmholtz-Gemeinschaft

Schriften des Forschungszentrums Jülich
Reihe Information / Information Band / Volume 18

Forschungszentrum Jülich GmbH
Peter Grünberg Institut (PGI)
Elektronische Materialien (PGI-7)

Crystal- and Defect-Chemistry of Fine Grained Thermistor Ceramics on $BaTiO_3$ Basis with BaO-Excess

Hayato Katsu

Schriften des Forschungszentrums Jülich
Reihe Information / Information Band / Volume 18

ISSN 1866-1777 ISBN 978-3-89336-741-2

Bibliographic information published by the Deutsche Nationalbibliothek.
The Deutsche Nationalbibliothek lists this publication in the Deutsche Nationalbibliografie; detailed bibliographic data are available in the Internet at http://dnb.d-nb.de.

Publisher and Distributor:	Forschungszentrum Jülich GmbH Zentralbibliothek 52425 Jülich Phone +49 (0) 24 61 61-53 68 · Fax +49 (0) 24 61 61-61 03 e-mail: zb-publikation@fz-juelich.de Internet: http://www.fz-juelich.de/zb
Cover Design:	Grafische Medien, Forschungszentrum Jülich GmbH
Printer:	Grafische Medien, Forschungszentrum Jülich GmbH
Copyright:	Forschungszentrum Jülich 2011

Schriften des Forschungszentrums Jülich
Reihe Information / Information Band / Volume 18

D 82 (Diss., RWTH Aachen University, 2011)

ISSN 1866-1777
ISBN 978-3-89336-741-2

The complete volume is freely available on the Internet on the Jülicher Open Access Server (JUWEL) at http://www.fz-juelich.de/zb/juwel

Preface

The present study was carried out during the period between September 2008 and January 2011 in the Department for Electronic Materials at the former Institute for Solid State Research of the Research Center Jülich – the present Peter Grünberg Institute – in my function as a visiting research scientist, delegated by the Materials Development Group of Murata Manufacturing Corporation Limited, Japan.

I would like to address my sincere gratitude to Professor Dr. Georg Roth, the director of the institute for crystallography of University of Aachen RWTH and the supervisor of this work, for supporting the realization of my wish to submit and defend this thesis. I am deeply grateful to Professor Dr. Rainer Waser for accepting me as a guest in Electronic Materials Research Laboratory in Jülich, for giving me the unique opportunity to conduct research on defect chemistry and for encouraging me to prepare this thesis. He significantly contributed to the completion of my Ph.D. work and its defense.

My company, Murata Manufacturing Corporation Limited, is acknowledged for the opportunity to stay here in Germany for more than two years as a research fellow. Representatively I would like to thank Dr. Hiroshi Takagi, the vice president of Murata Co. Ltd., for his continuous interest in my research and its promotion.

Dr. Christian Pithan directly supervised my work. I am very thankful for his personal dedication, without which this work could not have been put into reality. He encouraged me to take a doctor degree. In the same manner I would like to thank Dr. Detlev Hennings for many constructive scientific discussions and advices. Many ideas and suggestions from him significantly contributed to the development of my thesis.

Many persons helped me in completing experiments, not only in Jülich. Their support is gratefully acknowledged:

Dr. Jürgen Dornseiffer and Dipl.-Ing. Joachim Borchardt and their coworkers, Institute of Energy and Climate Research in Jülich, represented a precious assistance in the synthesis of nanocrystalline powders and their respective further processing and characterization.

Professor James Shen and his colleagues, from the Arrhenius Laboratory of Stockholm University, were so kind to carry out spark plasma sintering experiments.

Dipl.-Ing. Jochen Friedrich from my host group excellently solved many engineering related problems during the setup of my measuring equipment. He also helped me with thermogravimetric experiments. Similar holds for Mr. Marcel Gerst, who designed and set up the measuring software of my high temperature measurement system for DC conductivity.

Dr. Leszek Niewolack and Dr. Willem J. Quadakkers, Institute of Energy and Climate Research in Jülich, invested a lot of time and efforts in supporting me with the experimental determination of oxygen isotope diffusion profiles. Their commitment is heart fully acknowledged.

Mr. Volker Gutzeit, chief metallographer of the Institute of Energy and Climate Research in Jülich gave me many advices and supported me in the preparation of microsections. Dr. Egbert Wessel of the same institute significantly contributed to the microstructural and analytical characterization of my samples by scanning electron microscopy and EBSD. So did, Dr. Jin Lei, Ernst Ruska Centre in Jülich, for studies by transmission electron microscopy and spectroscopy. Mrs. Gabi Knauf, Institute of Energy and Climate Research in Jülich, assisted me in quantitative metallographical analysis.

I would like to thank Dipl.-Ing. Alain Doumit, Dr. Thomas Beckers and Dipl.-Ing. Josef Klomfaß, Institute of Energy and Climate Research in Jülich, for their extremely cooperative contribution in measuring the optical properties of my specimens.

My dear colleagues Dr. Shin´ichi Higai, Mr. Atsushi Honda and Mr. Yasuaki Okada, from Murata, provided very valuable contributions with their theoretical DFT calculations on oxygen diffusivity. Thanks a lot for their help.

Finally I'd like to thank my beloved family, Keiko, Yutaro Katsu and my coming baby. Without their support and understanding, this work and the life in Jülich could not have been such a wonderful time. I want to dedicate this thesis to my father and late mother, Kuniyoshi and Keiko Katsu.

Kurzfassung (German abstract)

Massive Thermistorkeramiken auf $BaTiO_3$-Basis mit positivem Temperaturkoeffizienten (PTC) des spezifischen elektrischen Widerstandes werden seit langer Zeit in Bauteilen zum Überlastschutz gegen Stromspitzen, als selbstregelnde Heizelemente oder als Temperaturfühler eingesetzt. Der Ursprung ihres hohen strombegrenzenden elektrischen Widerstandes, der lediglich beim Heizen oberhalb der Curie-Temperatur T_C der ferroelektrischen Phase $BaTiO_3$ in Erscheinung tritt, beruht auf gegengerichteten resistiven Schottky Barrieren und einer hiermit verbundenen Raumladungszone an den Korngrenzen. Diese isolierende Kornrandschicht ergibt sich durch die physikalische oder chemische Absorption von Sauerstoff in Verbindung mit segregierten Akzeptor-artigen Metallleerstellen, die an diesen Grenzflächen während des Herstellungsprozesses gebildet werden. Im Allgemeinen sind die Materialzusammensetzungen nicht stöchiometrisch, sondern angereichert an TiO_2 und müssen unter oxidierenden Bedingungen gesintert werden, da der Oxidationsprozess entscheidend für die Ausbildung der defektchemischen Vorgänge ist, die die Bildung der isolierenden Korngrenzenschicht bedingen.

Erst in jüngster Zeit wurden für die Herstellung von Vielschichttermistoren keramische $BaTiO_3$-basierte Formulierungen mit BaO-Überschuß entwickelt und vermarktet, die sich unter reduktiver Atmosphäre sintern lassen, ohne dass hierbei die internen metallischen Ni-Elektroden oxidiert werden. Nach sanfter Reoxidation im Anschluß an das Brennen weisen diese Materialien ebenfalls einen sehr hohen positiven Temperaturkoeffizienten des spezifischen elektrischen Widerstandes auf. Die kristall- und defektchemischen Mechanismen, die während dieses Prozesses ablaufen, sind allerdings bisher weitgehend nicht verstanden.

Aus diesem Grund wurden in der vorliegenden Arbeit die defektchemischen Hintergründe BaO-reicher, La-dotierter $BaTiO_3$-Thermistorkeramiken detailiert und in Hinblick auf ihre Zusammensetzung, auf die Herstellungsparameter und das Gefüge systematisch untersucht.

Im ersten Teil, wurden impedanzspektroskopische Messungen durchgeführt und jeweils hinsichtlich geigneter Ersatzschaltbilder, die den PTCR-Effekt in diesen Materialien auf adäquate Weise beschreiben, analysiert. Im Gegensatz zu den üblichen TiO_2-reichen Zusammensetzungen, tragen hier nicht nur die Korngrenzen zum PTCR-Effekt bei, sondern es bestimmen oder dominieren teilweise sogar auch Oberflächeneffekte maßgeblich die Temperaturcharakterisitk des spezifischen elektrischen Widerstandes. Temperversuche zeigen, dass resistiven Oberflächenschichten auf den Keramiken nur unter oxidierenden Bedingungen entstehen. Um den Ursprung dieses Phänomens näher zu verstehen, wurden Diffusionsprofile, die durch in-situ Oxidation mit dem Isotop ^{18}O als Sauerstoffquelle eingestellt wurden, mittels SNMS untersucht. Die Ergebnisse weisen darauf hin, dass Volumendiffusion nur an der unmittelbaren Oberfläche der keramischen Proben eine maßgebliche Rolle spielt. Das Eindringen des Sauerstoffes in das Innere des Materials erfolgt überwiegend durch Korngrenzendiffusion. Im Fall einer stöchiometrischen

Zusammensetzung ohne BaO-Überschuss, konnte im relevanten Temperaturbereich keine Korngrenzendiffusion beobachtet werden. Auf der Grundlage dieser Ergebnisse wurde eine defektchemische Beschreibung für den Mechanismus der Ausbildung resistiver Korngrenzenbarrieren vorgeschlagen.

Um dieses defektchemische Modell zu bestätigen, wurde im zweiten Teil dieser Arbeit die Abhängigkeit der Gleichstromleitfähigkeit vom Sauerstoffpartialdruck $p(O_2)$ untersucht. Die Ergebnisse wurden in einer Serie modifizierter Kröger-Vink Diagramme zusammengefasst und diskutiert, die zufriedenstellend die Punkt-Defektchemie der hier betrachteten PTCR-Keramiken beschreiben. Eine positive Steigung im Verlauf der elektrischen Leitfähigkeit über dem Sauerstoffpartialdruck $p(O_2)$ weist darauf hin, dass zumindest teilweise p-halbleitende Bereiche in den vorliegenden La-dotierten $BaTiO_3$-Keramiken existieren. Hieraus konnte geschlossen werden, dass der Einbau von BaO in das Perovskitgitter von Bariumtitanat sowohl Ti- als auch O-Leerstellen erzeugt. Höchstwahrscheinlich bilden hierbei Titanleerstellen die Akzeptor-artigen Zustände an den Korngrenzen. Es wird davon ausgegangen, dass sie die Ursache der isolierenden Barrierenschichten an den Korngrenzen sind, die zu der ausgeprägten PTCR-Charakteristik bei La-dotiertem $BaTiO_3$ mit BaO-Überschuß führen.

Der dritte Teil dieser Dissertation befasst sich mit Skalierungseffekten in extrem feinkörnigen PTCR-Keramiken mit einer durchschnittlichen Korngröße von etwa 300 nm. Diese ultrafeinkörnigen Keramiken wurden aus Pulvern, die über Mikroemulsionen synthetisiert wurden, durch eine anschließende Verdichtung mittels „spark plasma sintering“ konsolidiert. Bisherige experimentelle Studien aus dem wissenschaftlichen Schriftum schließen das Auftreten des PTCR-Effektes bei solch geringen Korngrößen aus. Es zeigte sich, dass für die Realisierung feinkörniger PTCR-Materialien ein BaO-Überschuss nicht geeignet ist. Offenbar liegt in diesem Größenbereich im Vergleich zu den vorher betrachteten Keramiken ein anderer Mechanismus zu Grunde, der für die Ausbildung eines großen positiven Temperaturkoeffizienten des Widerstandes verantwortlich ist. Hinsichtlich der Entwicklung künftiger miniaturisierter Vielschicht – PTC-Thermistorkomponenten, hat die Verwirklichung dieser extrem feinkörnigen Materialien große praktische Bedeutung.

Schließlich stellt der letzte Teil der vorliegenden Arbeit optisch transluzente La-dotierte Keramiken auf $BaTiO_3$-Basis vor, die über die konventionelle „mixed oxide“-Route und Sinterung in reinem Sauerstoff hergestellt wurden. Auch wenn diese Materialien keinen PTCR-Effekt aufweisen, sind sie dennoch interessant, da ihre optischen Eigenschaften deutlich denen von Dünnschichtsystemen oder Sol-Gel Keramiken, wie sie im Schriftum dokumentiert sind überlegen sind. Der optische Brechungsindex dieser tranzluzenten Keramiken hängt stark vom elektrischen Polungsgrad ab.

Abstract

Bulk thermistor ceramics on $BaTiO_3$-basis with positive temperature coefficient (PTC) are used for surge protection devices, self-regulating heaters or temperature sensing elements for a long time. The origin of their high current limiting electric insulation resistance that only appears upon heating above the Curie temperature T_C of the ferroelectric compound $BaTiO_3$ relies on a resistive back-to-back Schottky barrier layer, a space charge zone formed at the grain boundaries. This insulating layer is due to the physical or chemical absorption of oxygen combined with segregated acceptor-type metal vacancies created at the interface during processing. Generally the material compositions under mass production are off-stoichiometric, enriched in TiO_2 and must be sintered under oxidizing conditions, since the oxidation process is crucial for the defect chemical reactions involved in the formation of the insulating grain boundary layer.

Only in very recent years $BaTiO_3$-based ceramic formulations with BaO-excess for multilayer PTC thermistors, that can be fired even under reducing atmosphere, preventing the oxidation of internal metallic Ni electrodes, have been developed and commercialized. Upon careful reoxidation after firing these materials also show a very high positive temperature coefficient of resistance. The mechanisms in terms of defect chemistry involved in this process have not been understood clearly yet.

Therefore in the present study the defect chemical background of BaO-rich La-doped $BaTiO_3$ thermistor ceramics regarding to their chemical composition, processing conditions and microstructure has been systematically investigated in detail.

In the first part, experiments using impedance spectroscopy were conducted for electrical analysis using suitable equivalent circuits that adequately describe the PTCR effect in these materials. Unlike the case of conventional TiO_2-rich compositions not only a single resistive and capacitive (*RC*) components representing the grain boundary layers is responsible for the PTCR effect. Also surface effects represented by additional *RC* components significantly determine or even dominate the temperature characteristics of resistivity. Annealing experiments revealed that this resistive surface layer only appears when the ceramics are annealed in oxidizing atmosphere. In order to understand the origin of this phenomenon diffusion profiles obtained from in-situ oxidation treatments using ^{18}O isotope as oxygen source were analyzed by SNMS. The results indicate that bulk diffusion only plays a significant role at the very surface of the ceramic samples. Penetration of oxygen towards the interior mainly occurs via grain boundary diffusion. In the case of stoichiometric samples, without BaO-excess no grain boundary diffusion in the relevant temperature range was observed. On the basis of these findings a possible defect chemical explanation for the mechanism of grain boundary resistivity has been proposed.

In order to confirm this defect chemical model investigations on the DC conductivity in dependence of the oxygen partial pressure $p(O_2)$ were performed in the second part of this

work. The results are discussed and summarized in a series of modified Kröger-Vink diagrams that satisfactorily describe the point defect chemistry of the PTCR ceramics under consideration here. A positive slope of electrical conductivity versus $p(O_2)$ indicates that p-type semiconduction takes place at least partially in the present La-doped $BaTiO_3$ ceramics. It could be concluded that BaO incorporation into the perovskite lattice of barium titanate introduces both, Ti and O vacancies. Negatively charged titanium vacancies are believed to be the acceptor states bringing about the origin of the insulating barrier layer and resulting in the distinct PTCR characteristics of BaO-excess $BaTiO_3$ doped with La.

The third topic of this thesis addresses scaling effect of extremely fine grained PTCR ceramics with an average grain size as small as 300 nm. These ultrafine grained ceramics were realized through microemulsion mediated powder synthesis with subsequent consolidation by spark plasma sintering. Previous experimental studies from the scientific literature predict that in this range of grain size no PTCR effect should be observed due to overlapping of the insulating back-to-back Schottky barriers. It turned out that the introduction of BaO is not suitable to generate PTCR-type behavior in these fine grained materials. Apparently a different mechanism compared to the previously considered ceramics is responsible in this size range for the large positive temperature coefficient of resistivity. Anyhow, the realization of ultrafine grained PTCR ceramics has an important practical impact on the development of further miniaturized multilayer PTC thermistor components.

Finally in the last section of the present work optically translucent La-doped ceramics on $BaTiO_3$-basis, that have been prepared by conventional solid state reaction and sintering in pure oxygen are introduced. Although these materials did not reveal any PTCR effect they are still interesting, because their optical transmission is far superior even compared to values obtained for thin films or other sol-gel derived ceramics. The refractive index of these translucent ceramics is strongly affected by the degree of electric poling.

Table of contents

Index of figures

Index of acronyms and symbols

Acronyms

BET:	Brunnauer, Emmett and Teller
CPE:	Constant phase element
DFT:	Density functional theory
EBSD	Electron backscattered diffraction
EDX:	Energy dispersive X-ray spectroscopy
EELS:	Electron energy loss spectroscopy
e.m.f.:	Electromotive force
FE-SEM:	Field emission scanning electron microscope/microscopy
HR-TEM:	High resolution transmission electron microscope/microscopy
ML-PTCR:	Multilayer-PTCR
NTC:	Negative temperature coefficient
PSZ:	Partially stabilized zirconia
PTC:	Positive temperature coefficient
PTCR:	Positive temperature coefficient resistor or resistance
PVAc:	Polyvinyl acetate
SEM:	Scanning electron microscope/microscopy
SNMS:	Secondary neutralized particle mass spectroscopy
SPS:	Spark plasma sintering
TEM:	Transmission electron microscope/microscopy
UV/VIS:	Ultraviolet / visible light
XRD:	X-ray diffraction

Symbols

[i]:	Concentration of the chemical species i
a, c:	Lattice parameter
α:	Non-linearity coefficient
$\alpha_{T_2\text{-}T_1}$:	Generalized PTCR coefficient in the temperature range between T_1 and T_2
A:	Area
b:	Width of the depletion layer
β:	Empirical parameter in the single oscillator model
$c(x,t)$:	Concentration profile depending on the diffusion depth x and time t
$\tilde{c}(x,t)$:	Normalized concentration profile depending on the diffusion depth x and time t

c_g: Concentration of the isotope ^{18}O in the Ar/^{18}O gas mixture used for isotope exchange

c_0: Concentration of the isotope ^{18}O in ambient air

C^*: Representative real capacitance value of a CPE

C: Capacitance

C_0: Curie constant

C_{grain}: Capacitance contribution of the grains

$C_{g.b.\parallel}$: Capacitance contribution of grain boundaries running parallel to the path of electric conduction

$C_{g.b.\perp}$: Capacitance contribution of grain boundaries running perpendicular to the path of electric conduction

$C_{interface}$: Capacitance contribution of the interface ceramic-electrode

χ_S: Electron affinity of the semiconductor S

d: Sample thickness or distance

d_{BET}: Average particle diameter determined from the BET specific surface area

δ: Oxygen deficiency

$\delta_{g.b.}$: Grain boundary layer thickness or depletion layer width

D: (i) Average grain size or
(ii) Diffusion coefficient

$D_{g.b}$: Diffusion coefficient for grain boundary diffusion

$D_{vol.}$: Diffusion coefficient for volume diffusion

ΔH_{ox}: Enthalpy of oxidation

ΔH_{red}: Enthalpy of reduction

ΔG_{H_2O}: Standard Gibbs free energy for the water gas equilibrium

ΔP_n: Net portion of the spontaneous ferroelectric polarization normal to the grain boundary

Δt: Change in thickness

Δx, Δy: Amount of thermally decomposed water gas

e: Elementary electronic charge

ε_0: Permittivity of free space

ε_r: Relative dielectric constant

ε_{grain}: Relative dielectric constant of the grains

$\varepsilon_{g.b.}$: Relative dielectric constant of the grain boundaries

$\varepsilon_{g.b.\perp}$: Relative dielectric constant of the grain boundaries running parallel to the path of electric conduction

E: Electric field strength

E_0: Average oscillator strength

E_d: Dispersion energy

$E_{e.m.f.}$: Electromotive force

E_g: Width of the electronic energy band gap

E_C: Energy level of the conduction band

E_F: Fermi level

E_S: Energy difference between the acceptor level and conduction band

E_V: Energy level of the valence band

E_{redox}: Activation of the redox reaction

f: Frequency

F: Faraday constant

φ: Angle relative to the Brewster angle

G: Gibbs free energy

h: Concentration of electron holes

$\hbar$: Reduced Planck constant

η: PTCR parameter

I, I_0: Light intensity

I_p: Reflected intensity of p-polarized light

I_s: Reflected intensity of s-polarized light

$I(^{16}O)$: Plasma-SNMS intensity of the isotope ^{16}O

$I(^{18}O)$: Plasma-SNMS intensity of the isotope ^{16}O

j: Imaginary unit

J: Current

k_B: Boltzmann constant

k_r: Imaginary part of the refractive index

κ: Ratio of the Ba vacancy concentration to the one for Ti vacancies

K_{H_2O}: Equilibrium constant for the water gas reaction

$K^0_{H_2O}$: Preexponential factor of the equilibrium constant K_{H_2O}

$K_{recomb.}$: Equilibrium constant for the recombination reaction

$K^0_{recomb.}$: Preexponential factor of the equilibrium constant $K_{recomb.}$

K_{redox}: Equilibrium constant for the redox reaction

K^0_{red}: Preexponential factor of the equilibrium constant for the reduction reaction

K^0_{redox}: Preexponential factor of the equilibrium constant K_{redox}

K^0_{ox}: Preexponential factor of the equilibrium constant for the oxidation reaction

$K_{Schottky}$: Equilibrium constant for the Schottky reaction

$L_{artifacts}$: Inductance contribution stemming from the measuring equipment and connections to the sample

λ: Optical wavelength

m: (Ba+La)/Ti ratio

M:	Electric modulus
μ_e or μ_n:	Electron mobility
μ_h:	Electron hole mobility
$\mu_{V_{\ddot{O}}}$:	Mobility of oxygen vacancies
n:	Electron concentration
n_r:	Real part of the optical refractive index
n_{CPE}:	Parameter in CPE taking into account the deviation from a perfect capacitor
N_c:	(i) Number of nearest neighboring cations or (ii) Electron concentration in the conduction band
N_e:	Effective number of valence electrons per anion
N_s:	Density of acceptor states at the grain boundary interface
N_s^0:	Total number of available acceptor states
N_v:	Electron concentration in the valence band
N_D:	Donor concentration
ω:	Angular frequency
ω_{max}:	Relaxation angular frequency in impedance spectroscopy
$p(H_2)$:	Hydrogen partial pressure
$p(H_2O)$:	Partial pressure of water gas
$p(O_2)$:	Oxygen partial pressure
$p_{O_2}^{Ni/NiO}$:	Oxygen partial pressure at the equilibrium Ni/NiO
$p(O_2)_{min}$:	Oxygen partial pressure for the intrinsic minimum of conductivity
P:	Polarization
P_s:	Spontaneous polarization
ϕ:	Diameter
Φ_n:	Schottky barrier height
Q^0:	Idealized capacitance in a CPE
r_i:	Ionic radius of the ion i
R:	Gas constant
R:	Resistance
$R_{interface}$:	Resistance contribution of the interface ceramic-electrode
R_{grain}:	Resistance contribution of the grains
$R_{g.b.\parallel}$:	Resistance contribution of grain boundaries running parallel to the path of electric conduction
$R_{g.b.\perp}$:	Resistance contribution of grain boundaries running perpendicular to the path of electric conduction
ρ:	(i) Resistivity or (ii) Density
ρ_{grain}:	Resistivity of the grains

$\rho_{g.b.\perp}$: Resistivity of the grain boundaries running perpendicular to the path of electric conduction

ρ_{max}: Maximum resistivity

ρ_{min}: Minimum resistivity, cold resistivity

$\rho(T)$: Resistivity measured at the temperature T

S: Seebeck coefficient

σ: Conductivity

σ_h: Conductivity arising from electron holes

σ_n: Conductivity arising form electrons

$\sigma_{electronic}$: Electronic contribution to total conductivity

σ_{ionic}: Ionic contribution to total conductivity

σ_{total}: Total conductivity

t: (i) Goldschmidt tolerance factor or
(ii) Optical transmittance or
(iii) Time

T: Temperature

T_C: Curie temperature

T_{max}: Temperature of the resistivity maximum

T_{min}: Temperature of the resistivity minimum (cold resistance)

τ: Relaxation time

θ_C: Critical temperature in the Curie-Weiss law

V: Potential

V_{bi}: Built-in potential

W_M: Work function of the metal M

W_S: Work function of the semiconductor S

x: Diffusion distance

z: Valence number

Z' : Real part of impedance

Z'' : Imaginary part of impedance

Z_a: Formal anion valency

Z_{grain}: Impedance contribution of the grains

Z'_{grain} : Real part of Z_{grain}

Z''_{grain} : Imaginary part of Z_{grain}

$Z_{g.b.}$: Impedance contribution of the grains

$Z_{g.b.\perp}$: Impedance contribution of the grain boundaries running perpendicular to the path of electric conduction

$Z'_{g.b.\perp}$: Real part of $Z_{g.b.\perp}$

$Z''_{g.b.\perp}$: Imaginary part of $Z_{g.b.\perp}$

$Z_{g.b.\parallel}$: Impedance contribution of the grain boundaries running parallel to the path of electric conduction

Z_{total}: Total impedance

Z'_{total}: Real part of the total impedance

Z''_{total}: Imaginary part of the total impedance

Chapter 1

General introduction and technological relevance

Passive electronic components based on the perovskite-type ferroelectric compound barium titanate $BaTiO_3$ have been used since a long time in different industrial applications as basic material for a large variety of functional electronic devices. [1] During the past few decades several novel developments in electronic circuitry design and improved materials have resulted in an enormous progress and growth of miniaturized electric appliances, such as cellular phones or mobile personal computers – just to mention a few examples. Depending on the materials composition and on processing the electrical conductivity of $BaTiO_3$-based passive components can be generally modified in a very wide range over 10 or more orders of magnitude, extending from insulating to semiconducting behavior.[2] In particular the partial pressure of oxygen represents, besides temperature and material composition, a principle parameter determining the defect chemistry and hence the electrical conductivity behavior of $BaTiO_3$. On the account of their high dielectric permittivity, insulating $BaTiO_3$-based ceramics are commonly used as basic material for ceramic capacitors.[3,4] Semiconducting $BaTiO_3$, on the other hand, is employed for nonlinear resistors with a positive temperature coefficient (PTC).[5] At the transition temperature, where the ferroelectric modification of $BaTiO_3$ transforms into the paraelectric polymorph, the electrical resistivity of such PTCR (positive temperature coefficient resistors) drastically increases upon heating.

1.1 PTC thermistors based on barium titanate

PTC resistors are applied for numerous technical purposes, one major use, however, are resettable thermal fuses for current surge protection of sensitive parts in electrical engineering.[6] Electric or electronic circuits typically are subject to eventually occurring detrimental current perturbations that may result in malfunction, failure or – in the worst case – even in an irreversible damage of some of their components. Such unavoidable momentary overloads usually may arise from temporary

instabilities of the external power line or internal inductive or capacitive interactions related to switching processes of other devices or modules of the same circuit. The latter disturbances are inevitable; switching on or off a circuit containing capacitances or inductances always results in transients, because the currents and voltages do not reach their final values instantaneously. PTC resistors, also often referred to as PTC thermistors (Portemonteau expression, representing the abbreviated fusion of the words “thermal” and “resistor”), here act as guarding elements, absorbing transient rises of a flowing current, when connected in series to the unit that has to be protected, as illustrated in figure 1-1 (a). Various structural design configurations with different dimensions for these components, ranging from disc-type, over chip-type to multilayer-type are also shown in figure 1-1 (b) and (c).

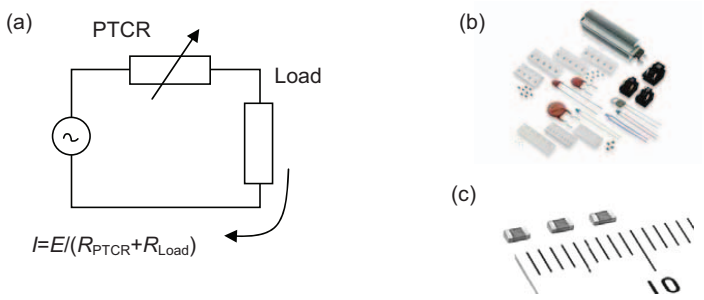

Fig. 1-1: (a) Implementation of a PTCR into an electric circuit and (b) various structural shapes. (c) Multilayer-PTCR (ML-PTCR).

Other important applications of $BaTiO_3$-based PTCR are self regulating resistive heaters and temperature sensing elements.[6-9] Above a certain critical value of the electric current the resistance rapidly and sharply increases through the effect of self heating, limiting any eventual further rise. PTCR heaters cannot overheat to create a fire hazard since the maximum temperature that the device can reach is intrinsically limited and determined by the material. In the past few years tens of millions of PTCRs were produced monthly world wide.

Alternatively to $BaTiO_3$-based PTCR also organic materials mixed with conductive fibers are commercially available.[10] Being more conductive compared to ceramic semiconducting $BaTiO_3$ at the cold state, however, a main drawback of these materials is their rather poor mechanical and geometrical stability after use due to large thermal expansion and shrinkage by the organic compound.

The present thesis focuses on materials for novel ceramic multilayer PTCR with reduced total resistance at low temperature compared to bulk ceramics, the ultralow values of organic PTCR, however, not being reached. This reduced total resistance directly results from an internal multilayered structure, as shown in figure 1-2.

Conventional commercial $BaTiO_3$-based ceramic formulations for chip-type PTC thermistors are generally off-stoichiometric in composition and contain a certain excess in TiO_2. These materials are relatively coarse in microstructure having typically an average grain size between a few µm and several tens µm and must be processed in oxidizing atmosphere in order to establish the PTCR effect. A high-temperature treatment in a reducing atmosphere would simply result in entirely semiconducting ceramics without any resistive jump upon heating during operation. A several years ago Murata Manufacturing Co. in Japan developed a new type of rare-earth doped $BaTiO_3$-based thermistor material enriched in BaO that attains excellent PTCR characteristics even when fired at elevated temperature under reducing conditions. The desired PTC effect, however, only appears if a subsequent gentle reoxidation treatment after firing is applied.[11-14] This material can be applied in contrast to conventional PTCR compositions to realize multilayer PTC thermistors (ML-PTCR) with internal transition metal electrodes consisting of Ni- or Ti-based metallic alloys. Preferably, Ni-based electrodes are used in view of ensuring an ohmic contact to the n-type semiconducting ceramics. Figure 1-2 shows a schematic illustration representing the geometrical arrangement of ceramic and internal electrode layers inside of a ML-PTCR.

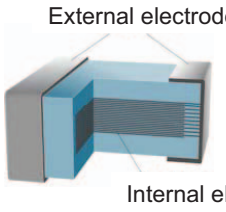

Fig. 1-2:
Internal structural image of a ML-PTCR.

Physically the laminated metallic and ceramic layers are configurated in a consecutive but alternating order in series, internal electrodes reciprocally terminating at the two lateral contacts of the device. Usually the layer thickness of the semiconducting ceramics measures a few tens of µm and each layer is built up by several tens of grains. A single typical ML-PTCR presently contains up to around 20

internal electrodes. Since the individual successive ceramic layers are all electrically connected in parallel, the total resistance of the device can be significantly reduced compared to a chip-type geometry with comparable dimensions. Therefore ML-PTCRs are especially attractive to technical applications, where a low resistance is required below the transition temperature.

1.2 Objectives and scientific approach of the present study

The physical background and microstructural mechanisms of the resistivity anomaly for conventional, coarse grained PTC ceramics based on $BaTiO_3$ with TiO_2-excess which are typically fired in oxidizing atmosphere is quite well understood in terms of semiconductor physics and defect chemistry. It is generally well accepted for a long time, that acceptor-type electronic states in the grain boundaries create an insulating back-to-back Schottky-type barrier above the Curie temperature. The formation of these acceptor states is associated with oxidation or oxygen adsorption along the grain boundaries. More specifically the local generation of negatively charged metal vacancies at grain boundaries is believed to be the essential origin of their insulating effect. The theoretical background for the classical PTCR models is presented in detail in chapter 3 of this thesis.

Concerning the defect chemical and microstructural mechanisms that are responsible for the outstanding PTCR properties of BaO-excess compositions sintered under reducing atmosphere only very little is reported in the scientific literature. For this reason the present work focuses on a systematic fundamental investigation of the influence of materials composition and processing parameter on the resulting PTCR characteristics. The objective of this work was to find out which elementary physico-chemical processes are involved in the formation of insulating grain boundary layers in these novel PTCR compositions. To achieve this purpose the defect chemistry of donor-doped non-stoichiometric $BaTiO_3$ ceramics with BaO-excess had to be elucidated in particular. For the sake of simplicity La was selected as donor, since it only substitutes the barium ion sites. Commercial compositions often contain amphoteric donor ions that may replace either the sites of the Ba or the Ti ion. This, however, leads to a further degree of complexity. Therefore the model system $(Ba_{m-x},La_x)TiO_3$ with $m > 1$ was selected.

In particular the following questions are addressed in this work:

(i) Are the well established theories regarding the PTC effect applicable to the newly developed $BaTiO_3$-based compositions with BaO-excess or with ultrafine grained microstructure below the μm-level?

(ii) What is the defect chemical nature of the insulating grain boundary layers in reoxidized donor-doped $BaTiO_3$ ceramics with BaO-excess and which role does the addition of excessive BaO play?

(iii) What kinds of defect chemical species are involved to realize the PTCR effect?

(iv) How does the PTCR effect develop during the reoxidation treatment?

(v) Are there any scaling effects determining the PTCR effect in this system?

(vi) If yes, what is the influence of the grain size on the resistivity increase and on the mechanism responsible for it?

The novel scientific focus of the present thesis thus relies on the elaboration of the physico-chemical mechanisms governed by point-like lattice disorder that explain the electrical properties of donor-doped, fine grained BaO-rich PTCR ceramics on $BaTiO_3$-basis, which were sintered under reducing conditions and thereafter reoxidized. The major experimental techniques employed to reach this objective are AC impedance spectroscopy, the study of the DC conductivity under different oxygen partial pressures $p(O_2)$ and at various temperatures T, analytical and microstructural characterization and experiments using ^{18}O isotope tracer diffusion profiles.

The results of these respective studies are presented in chapters 5 to 7 of this work. Chapter 8 describes how on the basis of the experience gained during these investigations optically translucent $BaTiO_3$ ceramics can be manufactured by defect chemical design. This last chapter therefore is not directly related to the PTCR itself but still presents surprising material properties that are possibly interesting for electro-optical applications.

Chapter 2

Phenomenlogy of $BaTiO_3$ based PTC thermistors

2.1 Temperature characteristics of resistivity

Semiconducting $BaTiO_3$-based PTC thermistors show a strongly non-linear temperature dependence of resistivity as shown for a representatively selected commercial PTC thermistor material presented in figure 2-1. In contrast to a typical intrinsic semiconductor with negative temperature coefficient (e.g. the element germanium), where resistivity gradually decreases with raising temperature, and to a typical metallic conductor with posistive temperature coefficient (such as for instance copper), where resistivity progressively increases with temperature, PTCR ceramics on $BaTiO_3$ basis reveal a discontinuous step at the transition temperature T_C (Curie temperature) from the ferro- to the paraelectric state (more detailed description in section 3.1).

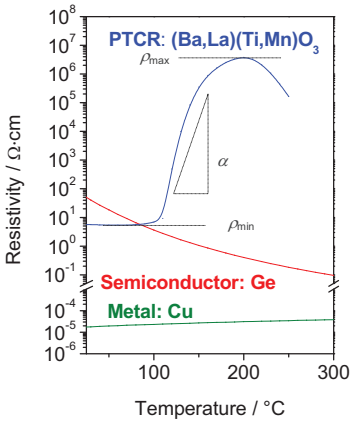

Fig. 2-1:
Temperature dependence of electrical resistivity of a La-donor and Mn-acceptor co-doped $BaTiO_3$-PTCR (Sample A) in comparison to a typical semiconductor such as Ge and to a metallic conductor such as Cu. The temperatures which give maximum and minimum resistivities are referred to T_{min} and T_{max}, respectively.

Typically three regimes in the temperature characterisitics can be distinguished:

(i) Below the Curie temperature T_C, the material is in its ferroelectric state and reveals normal n-type semiconduction that arises from electrons created through appropriate donor doping. The minimum resistivity ρ_{min} in this

regime, also referred to as cold resistivity, is strongly affected by the microstructure: fine grained ceramics being more insulating than coarse grained materials of comparable composition. In order to ensure an economic power consumption during steady state operation, i.e. in periods where current surges do not occur, the value of ρ_{min} is generally desired to be as small as possible.

(ii) Upon heating to temperatures above T_C a drastic increase in resistivity occurs and the material becomes highly insulating within a relatively narrow temperature window until the maximum resistivity ρ_{max} is reached. The value of ρ_{max} is desired to be as large as possible. As a figure of merit often the non-linearity coefficient α is used to characterize PTCR elements:

$$\alpha = \ln 10 \cdot \frac{\log\left(\rho_{max} / \rho_{min}\right)}{T_{max} - T_{min}} \qquad \textbf{Eq. 2-1.}$$

In order to provide a high protective level and to ensure a quick and large response of resistivity change to even small increases in temperature this coefficient should be as large as possible. The larger the resistivity jump and the narrower the temperature interval the larger will be the non-linearity coefficient α.

(iii) At temperatures above the resistivity maximum T_{max} the electric resistivity drops with increasing temperature (regime of negative temperature coefficient, NTC regime) because at higher temperatures more and more trapped electrons at acceptor state are released to the conduction band, resulting in lowering the Schottky barrier height.

The origin of the PTC effect in semiconducting donor-doped $BaTiO_3$ has been extensively discussed and it is well-accepted that the non-linear behavior is a consequence of a conductivity inhomogeniety. More specifically, the phenomenon occurs only in polycrystalline ceramics and arises from insulating grain boundaries. While the interior regions of the $BaTiO_3$ grains remain highly conductive due to mobile electrons in the conduction band (n-type semiconductor), a repelling electrostatic space charge region on the grain boundaries impedes the electronic transport across the boundaries. Goodman from General Electric Co. compared a Sm-doped $BaTiO_3$ single crystal and polycrystalline ceramics of comparable chemical compositions and confirmed that the PTCR jump is only observed in the presence of

grain boundaries.[15] It is agreed that at grain boundaries internal electrically insulating back-to-back Schottky-type barrier layers generated during cooling after sintering in an oxidizing atmosphere are responsible for the distinct non-linear conductivity behavior of the overall ceramic.[16-19] These electrostatic potential barriers have been made visible for the first time by means of electrophoretic decoration and cathodeluminescence of grain boundaries in $BaTiO_3$ PTC thermistor ceramics with fine particles deposited from TiO_2 emulsion.[20] The physical background of the PTC effect in terms of these insulating grain boundary layers is largely comprehended, but several details of the phenomenon are still open, forming the subject of continued research efforts and activities. In particular the influence of stoichiometry and of the processing conditions on the exact nature and constitution of the barrier layers still require a better exploration. Both these parameter delicately regulate the defect chemistry and hence the insulating properties of the grain boundary regions.

2.2 Chalenges of material development: past and state of the art

After the discovery of the PTCR effect in $BaTiO_3$ by Haayman in 1952[5] many particularily scientific and technological efforts have been undertaken for many decades with the purpose (i) to control the transition temperature T_C, (ii) to realize an as large and as steep as possible change of resistivity with increasing temperature and finally (iii) to lower the cold resistivity in order to reduce power consumption under normal operating conditions, where the thermistor should consume as little electrical power as possible.

The transition temperature T_C at which the resistivity jump occurs can be controlled in a wide range between –90°C and 400°C through the addition of so-called shifter elements, such as Pb or Sr.[7-9,21] Replacing Ba by Pb up to 60 mol% increases T_C, whereas substitution by Sr up to 70 mol% lowers T_C. Saburi[21] also investigated the influence of other substitutions, such as Sn, Ca, Mg, Zr and Si on the shift of T_c and the PTCR characteristics. Actually Si does not affect T_C, since it is not soluble in $BaTiO_3$.

The most performing PTC thermistors available show a change in resistivity at T_C of six to eight orders of magnitude (see figure 2-1). This is possible by modifying donor-doped $BaTiO_3$ through the addition of small amounts typically up to several hunderds ppm of certain transition elements,[22-24] that affect the insulating potential barrier at

the grain boundaries. In particular Mn, Fe and Cu are found to act as very effective co-dopants and Mn^{2+} ions appear to offer the deepest acceptor-level to the conduction band of $BaTiO_3$.[24] This may explain why Mn has become the mostly used co-additive in manufacturing $BaTiO_3$-based PTCR. Regarding cold resistivity, often additions of Al_2O_3 or SiO_2 facilitating ceramic densification and permitting to reduce of the level of electrically insulating porosity are used.[25] The minimum values of cold resistivity reported are around 2 Ω·cm.

Technologically, the first PTC thermistors were simple disc-type shaped components consisting of a flat cylindrical ceramic part, terminated by electrodes on both face sides. Later in the 1990´s chip type PTC thermistors allowing for high density surface mounting were developed. In 2003 Murata presented the first Multilayer PTCRs with internal Ni-based electrodes, that could be processed under reducing atmosphere. These components offer, due to their internal structure of alternating metallic and ceramic layers, electrically connected in parallel, the advantage of substantially lowered values of resistance compared to disc-type devices of the same volume. The minimum resistance of a multilayered PTCR is 0.2 Ω, a value that is a factor 1000 smaller compared to a chip-type PTCR of equivalent volume. The lower limit for the minimum resistance of ML-PTCR is given by the minimum resistivity that can be acchieved for $BaTiO_3$ and which is around 2 Ω·cm.

Regarding the technological realization of ML-PTCR two major difficulties related to the inner metallic electrodes had to be solved in the past.[26] The main purpose of designing a PTCR component with a multilayered structure is the reduction of the total resistance. Therefore electrode materials with a work function as shallow as possible are needed in order to minimize the contact resistance to the ceramic layers. In the ideal case this contact should be ohmic. On the other side, however, metals or alloys with low work function are easily oxidized during cofiring with the ceramic phase $BaTiO_3$. For this reason sintering of the entire ML-PTCR structure must be carried out under reducing atmosphere. In order to achieve the desired strong non-linearity in resistivity with temperature a post-sintering annealing treatment in an oxidizing atmosphere has to follow. The problem of these two opposing requirements, (i) the necessity of sintering at low partial pressures of oxygen $p(O_2)$ and (ii) the indispensable need of a following reoxidation treatment were overcome by the development of donor doped BaO-rich PTCR compositions by Niimi et al.[11-14] The proposed ceramic formulations can be sintered at $p(O_2)$ values as low as

10^{-7} MPa and show a distinct PTCR effect after gentle reoxidation, typically at 700°C in air for two hours. The mechanism based on defect chemistry explaining this behaviour is not understood yet and is the main subject of the present study.

Chapter 3

Theoretical background

The present chapter introduces a couple of theoretical aspects describing the crystal structure, defect chemistry and electrical conductivity mechanisms of barium titanate. It will be demonstrated how defect chemical equilibria and thus their graphical representation in the form of Kröger-Vink diagrams can be simulated and predicted. This serves partially as a basis for own calculations, described in chapter 6. Also the already existing well-accepted models by Heywang[16-17], Jonker[18] and Daniels[19] that explain the PTCR effect in conventional $BaTiO_3$-based thermistors are presented. Since impedance spectroscopy plays an important role in the present study, a generalized description about the analytical assessment and modeling of impedance spectra is given in the final part of this chapter.

3.1 Crystal structure of the ferroelectric compound $BaTiO_3$

The crystallographic structure of the ferroelectric phase barium titanate $BaTiO_3$ can be described by the perovskite lattice[27], as illustrated in figure 3-1.

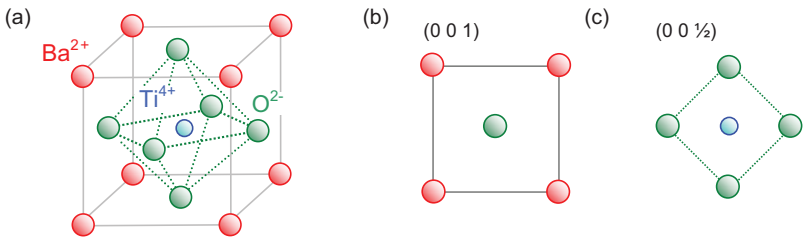

Fig. 3-1: Crystal lattice of the cubic polymorph of the compound $BaTiO_3$. (a) Crystal structure of $BaTiO_3$, belonging to the perovskite-family. Projections on the (0 0 1) and on the (0 0 ½) plane are shown in (b) and (c).

In principle the unit cell of this structure is built up by the two cationic metal sublattices of Ba^{2+} (A-site) and Ti^{4+} (B-site) and a sublattice, that is occupied by O^{2-} anions. At temperatures above $T_C = 125°C$, the so called Curie temperature, $BaTiO_3$ has a cubic structure (figure 3-1) and behaves as a paraelectric phase.[27-29] Here the

Ti^{4+} cation is located exactly in the room centre of the cubic elementary cell at the position ½ ½ ½ and is octahedrally coordinated by six surrounding O^{2-} anions. The Ba^{2+} cations are accommodated on the vertices of the unit cell. When cooling down to temperatures below 125°C pure barium titanate becomes ferroelectric and undergoes, as shown in figure 3-2, a series of phase transitions through three different polymorphs, depending on temperature and pressure.[29,30] At ambient pressure and room temperature the crystal structure of $BaTiO_3$ is tetragonally distorted. Below 5°C the structure changes to an orthorhombic polymorph and below -90°C to a rhombohedral one. The phase transition behavior of pure $BaTiO_3$ is illustrated in figure 3-2. Table 3-1 summarizes the corresponding transition temperatures, the respective structures, space groups and the electrical properties.

Temperature	Crystal structure	Space group	Electric properties
> 125°C	Cubic	*P*4*mm*	paraelectric
5°C ~ 125°C	Tetragonal	*Pm*3*m*	ferroelectric
90°C ~ 5°C	Orthorhombic	*Bmm*2	ferroelectric
< - 90°C	Rhombohedral	*R*3*m*	ferroelectric

Tab. 3-1: Phase transition temperatures, crystallographic polymorphs with corresponding space group symbols and electric properties of $BaTiO_3$ at ambient pressure.

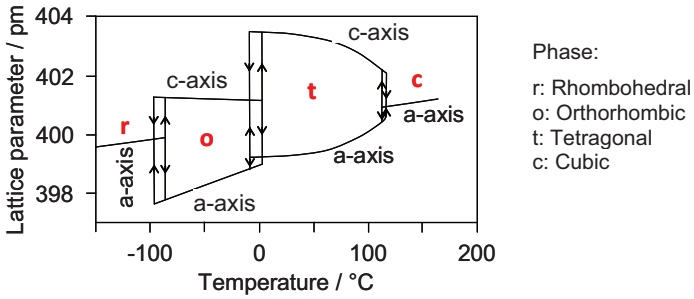

Fig. 3-2: Phase transition behavior of $BaTiO_3$ in dependence of temperature at ambient pressure.[30]

All distorted polymorphs are, as already mentioned, ferroelectric due to a spontaneous ionic polarization along the axis of distortion. This spontaneous polarization arises from a charge separation within the lattice, because the centers of gravity of the positively charged metallic cations and of the negatively charged oxygen anions do not coincide but are slightly displaced away from each other. An

explanation why this space displacement can take place in the lattice is provided by the situation that all three sublattices do not form an ideally dense packed structure. Generally the cubic lattice of the perovskite structure, represented in the general form by the expression ABO_3, tolerates, depending on the ionic radii r_A, r_B and r_O a certain range of deviation from the close packed ionic arrangement in which its isometric structure is still stable. This range is defined by the Goldschmidt tolerance factor t:[31,32]

$$t = \frac{r_A + r_O}{\sqrt{2} \cdot (r_B + r_O)} \qquad \textbf{Eq. 3-1.}$$

According to Goldschmidt an isometric perovskite lattice exists only when t is smaller than 1.05 but not smaller than 0.8. Taking the effective ionic radii listed by Shannon this is almost perfectly the case for the $SrTiO_3$ (t = 1.01),[33] a crystallographic isomorph of the high temperature modification of $BaTiO_3$. For $BaTiO_3$ the ionic radii after Shannon are $r_{Ba^{2+}}$ = 161 pm (for twelve-fold coordination), $r_{Ti^{4+}}$ = 60.5 pm (for six-fold coordination) and $r_{O^{2-}}$ = 142 pm (for eight-fold coordination) and consequently the tolerance factor amounts to 1.07. Since the size of the titanium ion is much smaller than the octahedral room formed by the surrounding oxygen anions, the ion Ti^{4+} is able to „rattle“ inside this octahedral cage. For this reason two stable crystallographic sites on the elongated axis within the tetragonally distorted lattice of $BaTiO_3$ can be occupied by Ti^{4+}. This is illustrated in figure 3-3, which represents schematically the dependence of the Gibbs free energy G from the ionic polarization P. Two distinct thermodynamically stable positions of the titanium ion corresponding to two polarization states + P_s and – P_s exist in ferroelectric $BaTiO_3$. If an external electric field is applied in the direction of the tetragonal distortion of the unit cell the titanium ion can switch between these two states, resulting in a relative displacement of the centers of gravity of the positive and negative electric charges. Taking into account the large valency of Ti^{4+} this shift is responsible for the high dielectric constant observed in $BaTiO_3$, which is typically around a few thousands or more in dielectric ceramics based on this phase.[3,34]

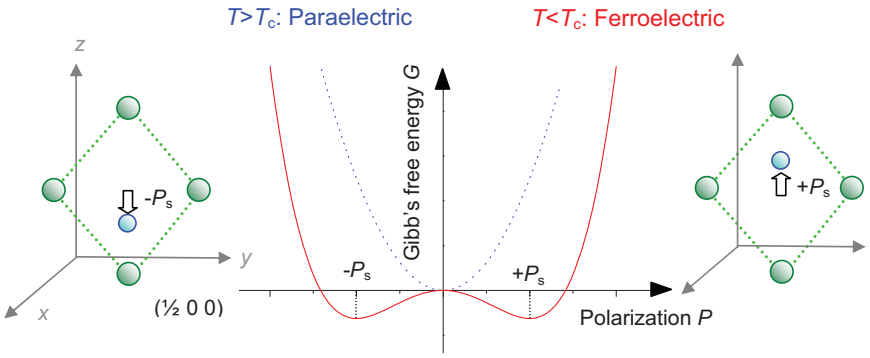

Fig. 3-3: Schematic representation of Gibbs free energy *G* in dependence of the polarization *P* and the corresponding two thermodynamically stable positions of Ti^{4+} in tetragonal $BaTiO_3$. The atomic projections on the left and right side show the crystallographic (½ 0 0) plane (refer to figure 3-1).

This relative dielectric constant ε_r is strongly dependent on temperature T and the relation between ε_r and T follows the so-called Curie-Weiss law:

$$\varepsilon_r(T) = \frac{C_0}{T - \theta_c} \qquad \textbf{Eq. 3-2.}$$

In equation 3-2 C_0 represents the Curie constant, which is a material parameter and amounts to 1.5×10^5 K for pure $BaTiO_3$. θ_c is the critical temperature, which is close but not identical to the Curie temperature T_C. The Curie-Weiss law describes the dielectric constant above Curie temperature.

Generally the perovskite lattice of $BaTiO_3$ can accommodate a large variety of foreign substitutional ions with different ionic radii and valencies,[31] as long as they fulfill the tolerance criterion of Goldschmidt, which was mentioned before. Large cations that are isovalent to Ba^{2+} preferentially occupy the A-site, such as Sr^{2+} ($r_{Sr^{2+}}$ = 144 pm) or Pb^{2+} ($r_{Pb^{2+}}$ = 149 pm).[33] Smaller cations that are isovalent to Ti^{4+} on the other hand are incorporated on the B-site, as for example Zr^{4+} ($r_{Zr^{4+}}$ = 72 pm).[33] Such substitutions lead to a wide range of possible solid solutions[35] based on $BaTiO_3$ with the possibility to tune dielectric or other physical properties. On the other hand the introduction of aliovalent substitutional doping ions is usually more limited because the additional or deficient electric charges have to be counterbalanced by the formation of lattice defects in order to ensure electroneutrality. In the case of the incorporation of isovalent ions only an elastic distortion of the lattice due to the

difference in ionic radius has to be overcome energetically. Depending on whether the substituting cation has a higher or lower valency compared to the host cationic site this compositional modification is referred to either as donor- or acceptor-doping, respectivily. In any case doping with aliovalent cations has a strong influence on the defect chemistry and electric conductivity of $BaTiO_3$, as presented and discussed in more detail in the next section 3.2 of this chapter. Table 3-2 only lists a few representatively selected examples of possible doping elements and their site preference in $BaTiO_3$.

	A-site ($r_{Ba^{2+}}$ = 161 pm)	**B-site** ($r_{Ti^{4+}}$ = 60.5 pm)	**A- or B-site**
Donor ions	La^{3+} (136 pm)	Nb^{5+} (74 pm) Sb^{5+} (60 pm)	Sm^{3+} (124 pm) Nd^{3+} (127 pm) Dy^{3+} (108 pm)
Acceptor ions	Na^{+} (139 pm)	Al^{3+} (53.5 pm) Mn^{2+} (67 pm)	

Tab. 3-2: Examples of possible acceptor and donor impurities in $BaTiO_3$ with their respective ionic radii according to Shannon.[33]

It should be noted, as shown in table 3-2 that some ions having an ionic radius which is between the one of Ba^{2+} and Ti^{4+} can be accommodated on both sites and act as donor and acceptor simultaneously. This behavior is referred to as amphoteric doping. This is discussed in section 3.2.2.4.

3.2 Defect chemistry and electric conductivity of $BaTiO_3$

The crystal lattice of perovskite-type materials such as $BaTiO_3$ is generally not perfectly symmetric. Usually irregularities from the previously described ideal structure occur. They include extrinsic point defects that arise from doping with aliovalent ions but also comprise intrinsic defects due to an incomplete or disordered occupancy of the sites of the anionic and cationic sublattice. Together with other two-dimensional crystal defects such as grain boundaries and twins in polycrystalline materials or crystal surfaces, in general, point defects have a decisive influence on the electric conduction behavior of $BaTiO_3$.

3.2.1 The Kröger-Vink notation

The most widely used method of describing different elements of point-type lattice disorder in solid crystalline materials is the notation proposed by Kröger and Vink.[36] Here point-type lattice irregularities are specified by a formalism that is illustrated in

figure 3-4.

Fig. 3-4: Principle of the formalism by Kröger and Vink.

M denotes the chemical symbol of the atom under consideration, or more specifically in the present case Ba, Ti or O atoms. Vacancies, i.e. unoccupied lattice positions are represented by the symbol V. Electrons are referred to by e and electron holes by h. The superscript C is the electronic charge of the defect relative to the regular site occupancy and is indicated by $\times$ for a neutral defect, $\bullet$ for a singly positive charge and $'$ for a singly negative charge. Higher ordered charges are represented by an according repetition of the respective symbol. The index S, finally, specifies through the corresponding chemical symbol the lattice site which is occupied by the species M, i.e. whether the Ba, Ti or O site is meant. Interstitially incorporated species are represented by a subscript i, but in the case of the relatively densely packed structure of $BaTiO_3$ such interstitials can be neglected.[37,38]

Kröger-Vink symbol	Description of the lattice defect
$Ba_{Ba}^{\times}$	Regularly occupied lattice positions without electrical charge
$Ti_{Ti}^{\times}$	
$O_{O}^{\times}$	
$La_{Ba}^{\bullet}$	Singly charged La-donor ion on a Ba-site
Al_{Ti}'	Singly charged Al-acceptor ion on a Ti-site
Mn_{Ti}''	Doubly charged Mn-acceptor ion on a Ti-site
V_{Ti}''''	Four-fold charged Ti vacancy
$V_{O}^{\bullet\bullet}$	Doubly charged O vacancy

Tab. 3-3: Examples of some common lattice defects occurring in $BaTiO_3$.

Table 3-3 lists for the sake of illustration a few very common lattice defects present in $BaTiO_3$ together with their respective nomenclatures by the notation of Kröger and Vink. Whenever concentrations of lattice point defects have to be addressed or quantified the corresponding symbol is put into squared brackets: $[M_S^C]$. In the examples of table 3-3 a La^{3+} cation that replaces Ba^{2+} carries an extra single positive

charge, because lanthanum ion is generally trivalent. A Mn^{2+} cation on the Ti^{4+} position on the other hand has two additional negative charges, since the manganese ion Mn^{2+} is only divalent. When a Ti^{4+} ion is missing completely the resulting vacancy involves four negative charges. Contrarily a vacant O^{2-} position holds two positive charges.

Using the described notation by Kröger-Vink the formation of point-type lattice imperfections and the corresponding quasi-chemical reaction equations, in which the defects are considered as a chemical species, can be readily established. This is shown exemplarily in equation 3-3 for the incorporation of lanthanum oxide into the perovskite lattice:

$$1/2La_2O_3 + TiO_2 \rightleftharpoons \underbrace{\boxed{La_{Ba}^{\bullet} + 3/4Ti_{Ti}^{\times} + 1/4V_{Ti}^{''''} + 3O_O^{\times}}}_{\text{perovskite crystal}} + \underbrace{1/4TiO_2}_{\text{Segregation}} \qquad \textbf{Eq. 3-3.}$$

Setting up such reaction equations correctly always requires that the laws of mass conservation, of electric neutrality and structural preservation be respected. This is because in chemical reactions no mass or electric charge can be created or annihilated. In the example of equation 3-3 the additional positive charge caused by the replacement of the divalent Ba^{2+} cations by La donor ions is compensated through the creation of negatively charged Ti vacancies. The rule of structural preservation means that all lattice positions of the unit cell must be preserved. In the case of La_2O_3 dissolved in $BaTiO_3$ as expressed in the present example the Ba position in the perovskite unit cell is occupied by La, the Ti sublattice partially by Ti cations and Ti vacancies and the oxygen site completely by O^{2-} anions. TiO_2 repelled out of the Pervoskite crystal due to the formation of Ti vacancies segregates or forms a secondary Ti-rich phase.

3.2.2 Lattice disorder and conductivity mechanisms

The defect chemistry of undoped and doped $SrTiO_3$ and $BaTiO_3$ is well described in the literature.[2,39-55] From the defect chemical point of view $SrTiO_3$ has been often considered as a model system [47-49,54] for the whole category of perovskite-type titanates such as the ferroelectric compound $BaTiO_3$. The alkaline-earth elements Ba as well as Sr both have the same electron configuration of the outer electron shell and therefore behave chemically in a similar way. In contrast to $BaTiO_3$, however, $SrTiO_3$ is paraelectric at room temperature and thereby any interaction of ferroelectric

spontaneous polarization with electronic or ionic conduction can be neglected. In the following the defect chemistry of acceptor- and donor-doped $BaTiO_3$ and $SrTiO_3$ are presented respectively. Finally the case of amphoteric doping is discussed. At first, intrinsic reactions related to the lattice disorder in $BaTiO_3$ are described.

3.2.2.1 Intrinsic reactions

Generally the defect chemical reactions involved have been revealed by measurements on the electrical conductivity, thermopower or Fermi level in dependence of oxygen partial pressure $p(O_2)$ and temperature T.[46,51] The reduction of $BaTiO_3$ at extremely low concentrations of oxygen of the surrounding atmosphere can be expressed by:

$$BaTiO_3 \rightleftharpoons BaTiO_{3-\delta} + 1/2\delta O_2^{(g)} \qquad \textbf{Eq. 3-4.}$$

The deficiency in oxygen δ is thus correlated with the release of gaseous pure oxygen O_2. This reaction is reversible. Electrically the deficiency in oxygen has a large impact on conductivity of $BaTiO_3$: due to charge neutrality every oxygen vacancy created through the release of oxygen is compensated by negative charged defects, mostly electrons in the case of $BaTiO_3$. This results in a semiconducting phase:

$$O_O^{\times} \rightleftharpoons 1/2O_2^{(g)} + V_O^{\bullet\bullet} + 2e \qquad \textbf{Eq. 3-5.}$$

The law of mass action for this reduction in equation 3-5 can be written as:

$$K_{red.} = \frac{[V_O^{\bullet\bullet}] \cdot n^2 \cdot \sqrt{p(O_2)}}{[O_O^{\times}]} \approx [V_O^{\bullet\bullet}] \cdot n^2 \cdot \sqrt{p(O_2)} = K_{red.}^0 \exp\left(\frac{-E_{red.}}{k_B T}\right) \qquad \textbf{Eq. 3-6.}$$

$K_{red.}$ is the equilibrium constant and $E_{red.}$ the activation energy of reduction. The number of regular oxygen anions $O_O^{\times}$ in the lattice is comparatively large (typically in the order of 5×10^{22} cm^{-3}) relative to a small variation upon oxygen release (typically in the order of 2×10^{17} cm^{-3} for non-doped $BaTiO_3$ at 800°C and $p(O_2) \approx 10^{-15}$ MPa). In consequence $[O_O^{\times}]$ can be approximated as being constant and can be included in the pre-exponential factor of equation 3-6.

Besides the formation of oxygen vacancies also metal vacancies of Ba and Ti are involved in the defect chemistry of $BaTiO_3$. Frenkel-type disorder involving interstitial ions of Ba, Ti or O can be neglected due to the closed packed perovskite-type crystal

lattice.[37,38] In consequence only Schottky-type disorder has to be taken into account as second defect chemical equilibrium in $BaTiO_3$ besides the redox reaction as specified in equation 3-7:

$$\text{nil} \rightleftharpoons V''_{Ba} + V''''_{Ti} + 3V^{\bullet\bullet}_{O} \qquad \textbf{Eq. 3-7.}$$

This Schottky equilibrium is only active at temperatures above around 1200°C,[41] which is a value close to the sintering conditions during materials preparation. Here the formation, diffusion and annihilation of all three kinds of vacancies are possible.

Due to the strong temperature dependence of the Schottky and redox equilibria three temperature regimes with a specific respective defect chemical characteristic are obtained: the (i) high, (ii) intermediate and (iii) low temperature regimes. In the high temperature regime (above 1200°C) both, the redox and the Schottky equilibria are active. For kinetic reasons the Schottky reaction is considered to be frozen-in at intermediate temperatures (500 – 1000°C) where the diffusivity of metal vacancies is too low to reach equilibration in reasonable time. In this temperature window which corresponds to the range of post-sintering cooling or annealing the concentration and distribution of these metal vacancies remain virtually unaltered, oxygen exchange through the gas phase, however, still occurs according to the redox equilibrium. This situation changes at temperatures below approximately 500°C, where even the gas-solid exchange kinetics of oxygen is retarded.[47,49] All three temperature regimes are summarized in the overview of table 3-4.

Regime	Schottky equilibrium	Exchange kinetics
High temperatures (1200°C < *T*)	active	active
Intermediate temperatures (500°C < *T* < 1000°C)	frozen	active
Low temperatures (*T* < 500°C)	frozen	frozen

Tab. 3-4: Three temperature regimes determining the defect chemistry of titanates and the respective active or inactive equilibria.

At relatively high partial pressures of oxygen $p(O_2)$ above approximately $10^{-6} – 10^{-1}$ MPa oxygen vacancies are filled again to form regular oxygen-sites and electron holes h are generated according to:

$$1/2O_2^{(g)} + V^{\bullet\bullet}_{O} \rightleftharpoons O^{\times}_{O} + 2h \qquad \textbf{Eq. 3-8.}$$

Therefore hole conduction only occurs if the oxygen exchange can take place, i.e. at temperatures above around 500°C. In this region the $p(O_2)$-dependence of conductivity then reveals a positive slope which typically indicates p-type conduction, as will be presented in more detail below, where the case of extrinsic lattice disorder is discussed. The transition oxygen partial pressure $p(O_2)$ from n-type conduction (equation 3-5) to p-type conduction (equation 3-8) is referred to electric intrinsic minimum. Assuming the mobilities of electron and electron hole are equivalent this electric intrinsic minimum corresponds to compositional stoichiometry.

3.2.2.2 Acceptor-doping

Nominally undoped titanates are always still practically acceptor-doped, because even very small impurity concentrations of transition metal ions such as Fe^{2+} or Mn^{2+} which stem from the raw materials cannot completely be avoided.[44] Therefore the defect chemistry of supposedly undoped titanates always corresponds to the case of acceptor-doping. As mentioned above charge neutrality must be fulfilled at any times and therefore the concentrations of all lattice defects are determined by this condition. Equation 3-9 shows the electroneutrality condition for the example of acceptor-doped $BaTiO_3$, where the acceptor is Al:

$$2[V_O^{\bullet\bullet}] + h = [Al'_{Ti}] + 2[V''_{Ba}] + 4[V''''_{Ti}] + n \qquad \textbf{Eq. 3-9.}$$

The left side of equation 3-9 takes into account all positively charged point defects, whereas the right side relates to all negatively charged ones. In acceptor-doped titanates the concentration of metal vacancies is negligibly small compared to the acceptor concentration (typically in the range of a few hundreds ppm) and thus $[V''_{Ba}]$ and $[V''''_{Ti}]$ can be ignored.

The defect chemistry of acceptor-doped titanates can be represented in a so-called Kröger-Vink diagram, showing the dependence of electric conductivity or of the concentrations of major electronic or ionic charge carriers from oxygen partial pressure $p(O_2)$. An example is shown for the intermediate temperature range in figure 3-5. This characteristics is divided into three regions. For highly reducing conditions, i.e. at $p(O_2)$ values below 10^{-13} MPa, the defect chemistry is dominated by a high concentration of oxygen vacancies, exceeding the acceptor concentration. These oxygen vacancies act as donors according to equation 3-5 and in consequence electrons are generated to compensate the extra positive charges of the oxygen

vacancies. Negatively charged metal vacancies cannot be generated, since the Schottky equilibrium is frozen in the intermediate temperature regime.

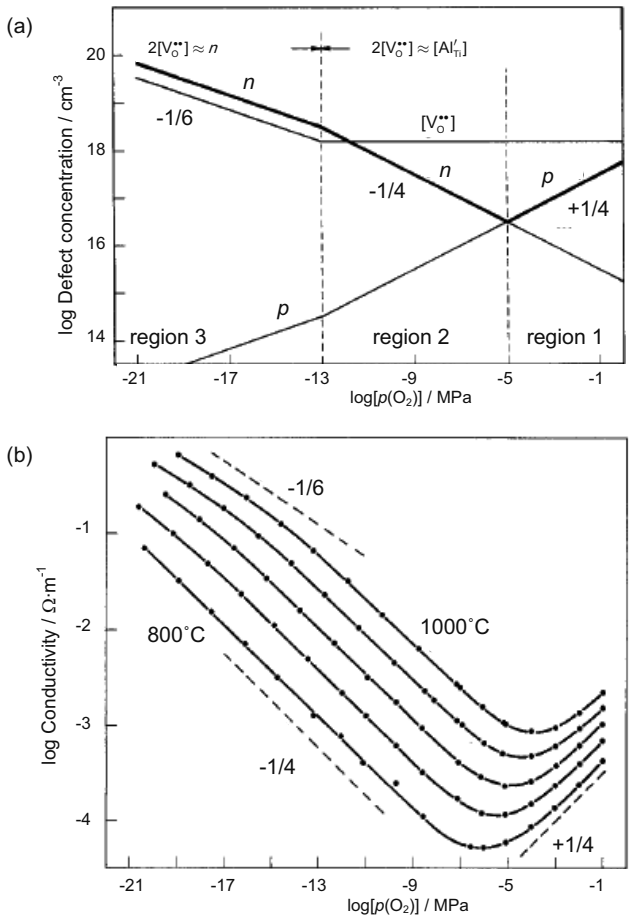

Fig. 3-5: Kröger-Vink diagram for acceptor-doped polycrystalline $SrTiO_3$ in the intermediate temperature range as a function of oxygen partial pressure:[43]
(a) Simulated concentration of lattice point defects and
(b) Experimentally measured conductivity at temperatures between 800 – 1000˚C.

Under these circumstances the generalized equation 3-9 can be approximated as:

$$2[V_O^{\bullet\bullet}] \approx n \qquad \textbf{Eq. 3-10.}$$

Substitution of $[V_O^{\bullet\bullet}]$ in the corresponding law of mass action expressed in equation 3-6 with equation 3-10 results in a modified equation for the equilibrium constant of the redox reaction being active here:

$$K_{redox} = 2n^3\sqrt{p(O_2)} \qquad \textbf{Eq. 3-11.}$$

With this relation the dependence of the electron concentration from the oxygen partial pressure $p(O_2)$ can be calculated.

The total conductivity generally consists not only of an electronic contribution but also includes an ionic part as expressed by equation 3-12. Each conductivity component is the product of the elementary electric charge, the mobility and its concentration. With this equation 3-12 is obtained.

$$\sigma_{\text{total}} = \sigma_{\text{electronic}} + \sigma_{\text{ionic}} = \mathrm{e}\left(\mu_{\mathrm{e}} n + \mu_{\mathrm{h}} h + 2\mu_{V_O^{\bullet\bullet}}[V_O^{\bullet\bullet}]\right) \qquad \textbf{Eq. 3-12.}$$

Here, μ_i denotes the mobility of each kind of charge carrier. On the other hand, the concentrations of electrons and electron holes are correlated by the recombination reaction:

$$\text{nil} \rightleftharpoons \mathrm{e} + \mathrm{h} \qquad \textbf{Eq. 3-13.}$$

The law of mass action for this equilibrium is:

$$K_{\text{recomb.}} = K^0_{\text{recomb.}} \exp\left(\frac{-E_{\mathrm{g}}}{k_{\mathrm{B}} T}\right) = n \cdot h \qquad \textbf{Eq. 3-14.}$$

Equation 3-14 implies that the concentration of electron holes becomes vanishingly small when the electron concentration is dominant and vice versa. Under reducing circumstances and at intermediate temperatures for which eq. 3-10 holds, electrons are considered to be the dominant charge carrier species and therefore the contribution of hole conduction can be neglected in eq. 3-12. The concentration of oxygen vacancies is almost close to that of electron according to eq. 3-10, however the contribution to conductivity is ignored in this case because the mobility of oxygen vacancies is much smaller than that of electrons. Equation 3-12 can then be simplified:

$$\sigma_{\text{total}} \approx \sigma_{\text{electronic}} \approx \mathrm{e}\mu_{\mathrm{e}} n \qquad \textbf{Eq. 3-15.}$$

Assuming that the electron mobility is not strongly dependent on temperature,[39] equation 3-15 shows that total conductivity is mostly governed only by the electron concentration n. In accordance with equations 3-11 and 3-15, the dependence of conductivity from partial pressure of oxygen $p(O_2)$ can be expressed by the following relation:

$$\left(\frac{\partial \log \sigma_{\text{total}}}{\partial \log p(\mathrm{O}_2)}\right)_T \approx \left(\frac{\partial \log n}{\partial \log p(\mathrm{O}_2)}\right)_T \approx -\frac{1}{6} \qquad \textbf{Eq. 3-16.}$$

This gives the relationship between total conductivity and oxygen partial pressure, namely the slope in a Kröger-Vink diagram. Theoretically the value of the slope for strongly reducing conditions at an intermediate constant temperature should be therefore -1/6.

In the intermediate range of $p(O_2)$, the concentration of intentionally or unintentionally added acceptor-type impurities becomes more dominant, because the intrinsic formation of oxygen vacancies is strongly reduced. The concentration of oxygen vacancies becomes almost equivalent to that of the acceptor dopants added and independent of $p(O)_2$. They now compensate the negative charges of the acceptor. This is articulated in equation 3-17 which holds for the intermediate $p(O)_2$ range and trivalent aluminum ion is selected as an example for an acceptor dopant.

$$2[V_O^{\bullet\bullet}] \approx [Al'_{Ti}] \qquad \textbf{Eq. 3-17.}$$

In this region of oxygen partial pressure, the concentration of oxygen vacancies remains constant at the level of the content of acceptor impurities which is defined by the materials preparation process and which can be regarded to be invariable. Combining equation 3-6 with equation 3-17, the slope in the Kröger-Vink diagram for intermediate partial pressures of oxygen can be derived:

$$\left(\frac{\partial \log \sigma_{total}}{\partial \log p(O_2)}\right)_T \approx -\frac{1}{4} \qquad \textbf{Eq. 3-18.}$$

The ideal value of -1/4 found here is also often obtained experimentally as shown in figure 3-5 (b).

Finally, the region representing the highest range of $p(O_2)$ is considered. With the progressive transition into more oxidizing conditions the electron concentration is further reduced and electron holes become the dominant charge carriers determining the electrical conduction. P-type conduction through electron holes can be active, however, only in the intermediate or high temperature range above approximately 500°C. Electron holes are generated by occupying empty oxygen vacancies with oxygen anions that are incorporated from the surrounding atmosphere. This reaction is represented already by equation 3-8. The corresponding law of mass action is articulated by:

$$K_p = \frac{h^2}{[V_O^{\bullet\bullet}] \cdot \sqrt{p(O_2)}} \qquad \textbf{Eq. 3-19.}$$

Since the concentration of oxygen vacancy is governed by equation 3-17, it can be assumed to remain almost constant. The expected slope value in the Kröger-Vink diagram is deduced from eq. 3-19. The slope of +1/4 is expected in the high oxygen partial pressure regime as represented by equation 3-20:

$$\left(\frac{\partial \log \sigma_{\text{total}}}{\partial \log p(\mathrm{O}_2)}\right)_T \approx \left(\frac{\partial \log h}{\partial \log p(\mathrm{O}_2)}\right)_T \approx +\frac{1}{4} \qquad \textbf{Eq. 3-20.}$$

On the basis of the reaction equations described for the three regimes of oxygen partial pressure the conduction mechanism can be expressed quantitatively in alkaline earth titanates. Figures 3-5 (a) shows calculated concentrations for electrons, electron holes and oxygen vacancies, and (b) represents measured conductivity values σ as function of temperature T and oxygen partial pressure $p(O_2)$ for the case of acceptor-doped $SrTiO_3$, respectively.[43] The trend of the calculated values agrees very well with the one for the measured data in figure 3-5.

3.2.2.3 Donor-doping

Influence of the slow kinetics of cationic diffusivity on equilibration

In contrast to acceptor-doped titanates experimental difficulties related to the investigation of the equilibration of donor-doped titanates have to be faced. This is because the mechanism of metal vacancy compensation involved in donor-doped titanates is very retarded and sluggish since cationic diffusivity in the perovskite lattice is very slow compared to the migration of oxygen. Migration of cations and anions in ionic crystals usually occurs via the mechanism of ambipolar diffusion.[56] Here the condition of charge neutrality requires that the mass transport in ionic systems takes place in a coupled and balanced way, anions and cations each migrating simultaneously on their specific sublattice avoiding charge separation. As already mentioned previously interstitials can be neglected in perovskite-type compounds such as $BaTiO_3$. Also the diffusion of positively charged metallic ions via positively charged oxygen vacancies can be excluded. This also holds true for the adversative case regarding the migration of negatively charged oxygen ions via negatively charged vacancies on the A- or B-site of the lattice. Considering the cubic high temperature modification of the perovskite structure the distance between two neighbouring oxygen anions is only $a/\sqrt{2}$, a being the lattice constant. Ba or Ti cations are separated from their corresponding counterparts by a distance of one entire lattice spacing a. Figure 3-6 illustrates this situation. The crystallographic

difference of the cationic and anionic sites is one of the reasons why metal vacancies diffuse so slowly and why oxygen uptake and migration even takes place at intermediate temperatures. Another factor determining the relatively high diffusivity of oxygen in the lattice is the eight-fold coordination of its ion in the lattice, while the metallic cations only have six equivalent nearest neighbouring sites.

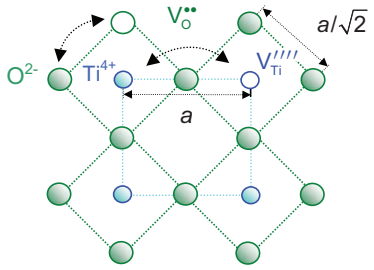

Fig. 3-6: Schematic image of the sublattices of oxygen and titanium in the (½ 0 0) plane.

Diffusion constants of oxygen and metal vacancies have been determined experimentally.[57,58] With the diffusion coefficients reported (refer to equations 3-21 and 3-22) the time needed for equilibration can be estimated as a function of the diffusion path, or more specifically in polycrystalline ceramics as a function of grain size. This calculation has been carried out for various temperatures and the results are shown in figure 3-7 by using the following equations:

$$D_{V_O^{\bullet\bullet}}(T) = 0.33 \exp\left(\frac{-0.98\text{eV}}{k_B T}\right) \quad \left[\text{cm}^2/\text{s}\right] \qquad \textbf{Eq. 3-21.}$$

$$D_{V_{Ba}''}(T) = 6.8 \times 10^{-2} \exp\left(\frac{-2.76\text{eV}}{k_B T}\right) \quad \left[\text{cm}^2/\text{s}\right] \qquad \textbf{Eq. 3-22.}$$

In the model calculation shown in figure 3-7 the diffusion process is assumed to start from the grain boundaries and not from the surface of the polycrystalline material. In order to demonstrate the large difference in the diffusivity of oxygen and metal vacancies an illustrative example is considered here: if the grain size of $BaTiO_3$ ceramics is assumed to be 40 μm, an oxygen vacancy would only need 0.2 s to migrate into the centre of the grain at 900°C (diffusion path: 20 μm). In the case of a metal vacancy $3 \cdot 10^7$ s would be required, for migrating the same distance. This corresponds to the duration of almost one year.

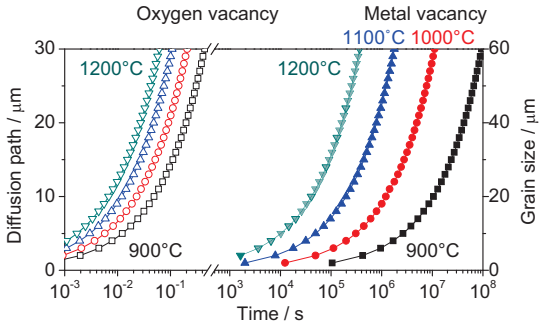

Fig. 3-7: Diffusion path length or grain size versus the time needed for equilibration at various temperatures. Time is calculated using the relation $d = \sqrt{D(T) \cdot t}$, where d is the diffusion path length and t the equilibration time. Open symbols represent the case of oxygen vacancies, closed symbol the one of metal vacancies. The calculation was done in steps of 100K in the temperature range from 900°C to 1200°C.

In order reduce the time needed for equilibrium, two theoretical possibilities arise: (i) increasing the temperature or (ii) reducing the grain size.

Defect chemical equilibria

Because of the reasons mentioned above the number of experimental reports on the defect chemistry of donor-doped alkaline earth titanates is relatively small compared to the acceptor-doped case. Table 3-3 lists some papers published in the literature. Some of the very first reports on the physicochemical aspects of point defect chemistry related to donor-doped $BaTiO_3$ have been presented by Daniels, Härdtl and Hennings from the Philips research laboratory. These authors measured DC conductivity at various oxygen partial pressures[41] and compared the results to the electron concentration estimated by thermogravimetric measurements (TGA).[42]

Author	Year	Ref.	System	Temperature	Major results
Daniels	1976	[41]	La-doped $BaTiO_3$	1200°C	Band diagram of donor-doped $BaTiO_3$ and equilibrium constants
Wernicke	1978	[58]	La-doped $BaTiO_3$	1000 – 1100°C	Diffusion coefficients of metal vacancies
Chan	1976	[40]	Nb-doped $BaTiO_3$	700 – 1000°C	Effective concentration of donors
Nowotny	1994	[53]	Nb-doped $BaTiO_3$	995 – 1135°C	Diffusion coefficient for Ti vacancy
Poignant	1999	[59]	Nb-doped $(Sr,Ca)TiO_3$	1000 – 1200°C	Diffusion constant of Sr vacancy
Yoo	2002	[60]	undoped $BaTiO_3$	800 – 1100°C	Reestablishment of defect chemistry for $BaTiO_3$
Katsu	2011		La-doped, BaO-rich $BaTiO_3$	700 – 1050°C	Oxidation behavior of BaO rich compositions.

Tab. 3-5: Experimental reports on electrical conductivity of donor-doped alkaline earth titanates

In the donor-doped case also a Kröger-Vink diagram has been successfully proposed to illustrate the point defect chemical reactions involved. The corresponding results are shown in figure 3-8.

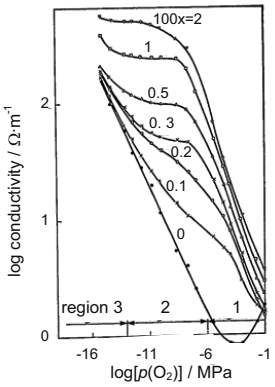

Fig. 3-8:
Oxygen partial pressure dependence of DC conductivity measurement which shows a conductivity decrease at higher oxygen partial pressures: 10^{-6}~10^{-1} MPa, indicating metal vacancy compensation.[41] The compositions of the sample follows the formula $(Ba_{1-x}La_x)Ti_{1.005}O_3$ (x = 0 ─ 0.025). The measurement was done at 1200˚C. The values x in the figure are multiplied by 100 for simplicity.

Figure 3-8 clearly demonstrates the transition of defect chemistry from the acceptor-doped to the donor-doped case with increasing lanthanum concentration from 0 to 2 mol%. According to these results, conductivity can be classified into three regions covering the whole range from oxidizing to reducing atmosphere: (i) regime of metal vacancy compensation, (ii) regime of electron compensation and (iii) majority regime of intrinsic oxygen vacancy. In the same manner as in the acceptor-doped case, electrical neutrality of all related charged point defects must be satisfied as follows:

$$2[V_O^{\bullet\bullet}] + h + [La_{Ba}^{\bullet}] = n + 2[V_{Ba}''] + 4[V_{Ti}''''] \qquad \textbf{Eq. 3-23.}$$

Instead of negatively charged acceptors in equation 3-9, the concentration of positively charged donors $[La_{Ba}^{\bullet}]$ must be taken into account here. For the intrinsic oxygen vacancy regime at the lowest $p(O_2)$ range the same scenario as for the acceptor-doped case is obtained. Equation 3-10 can be adopted again as approximation and the concentration of conducting electrons is mainly determined by the concentration of oxygen vacancies. Accordingly the slope of the Kröger-Vink diagram is -1/6 for strongly reducing conditions (region 3 in figure 3-8). At higher partial pressures of oxygen (region 2 in figure 3-8) a plateau-like regime around 10^{-13} – 10^{-6} MPa appears, where conductivity remains constant and is independent of $p(O_2)$ and temperature T. Here the electron concentration is governed by the amount of donor addition, in this case $[La_{Ba}^{\bullet}]$:

$$La_2O_3 + 2TiO_2 \rightleftharpoons 2La_{Ba}^{\bullet} + 2Ti_{Ti}^{\times} + 6O_O^{\times} + 2e + 1/2O_2^{(g)} \quad \textbf{Eq. 3-24.}$$

$$\Rightarrow n \approx [La_{Ba}^{\bullet}] \quad \textbf{Eq. 3-25.}$$

At even higher partial pressures of oxygen $p(O_2)$ above 10^{-6} MPa the donors are compensated by metal vacancies in order to ensure electroneutrality. However, as pointed out in the previous subsection, this process is only possible at very elevated temperatures above typically 1200°C, due to kinetic reasons. Only at such extremely high temperatures the defect chemical reactions related to metal vacancy compensation reach the thermodynamical equilibrium on a reasonable time scale. Daniels et al. [41] investigated the point defect chemistry of La-doped $BaTiO_3$ and established the corresponding Kröger-Vink diagram at 1200°C. He and his coauthors assumed barium vacancies as the main species compensating the donors in the corresponding oxidizing regime of relatively high $p(O_2)$, however, no direct evidence for the existence of V_{Ba}'' could be presented at that time. The respective defect chemical equilibrium in the oxidizing regime (region 1) was formulated as follows:

$$La_2O_3 + 3TiO_2 \rightleftharpoons 2La_{Ba}^{\bullet} + 3Ti_{Ti}^{\times} + 9O_O^{\times} + V_{Ba}'' \quad \textbf{Eq. 3-26.}$$

Equivalently the formation of titanium vacancies upon donor-doping could be assumed:

$$2La_2O_3 + 3TiO_2 \rightleftharpoons 4La_{Ba}^{\bullet} + 3Ti_{Ti}^{\times} + 12O_O^{\times} + V_{Ti}'''' \quad \textbf{Eq. 3-27.}$$

Actually a controversial debate, whether vacancies of barium, titanium or both prevail, has been carried out for a long time. An argument that often has been used in favor of barium vacancies is the very large four-fold charge that vacancies of titanium carry [61]. On the other hand, more recent calculations based on the potential model for the formation enthalpy of these defects [38] and studies on the phase relations in the system La_2O_3-BaO-TiO_2 by Jonker et al. [63] and by Makovek et al. [64] both express strong evidence for the preferred formation of Ti vacancies in the case of La-doped $BaTiO_3$.

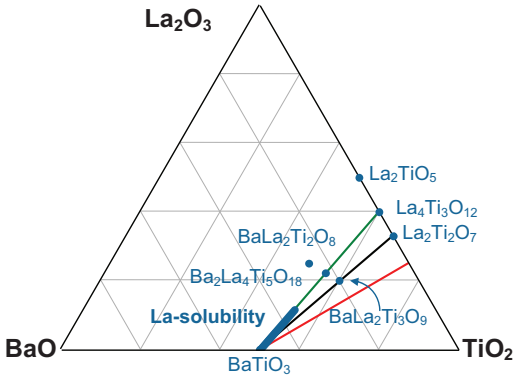

Fig. 3-9:
Schematic isothermal section (1350 – 1400°C) of the system La_2O_3-BaO-TiO_2 according to results from Jonker [60] and Makovec [61], suggesting the formation of Ti-vacancies in $BaTiO_3$ upon doping with La.

According to the two later studies $BaTiO_3$ dissolves up to approximately 12 mol% of La_2O_3 at 1350°C. This solubility limit is determined, as illustrated in figure 3-9, through the tie lines of the univariant phase equilibria (three phase regions) formed by the perovskite phase (Ba,La)TiO_3 with the La-rich compounds La_2O_3, $BaLa_2Ti_2O_8$, $Ba_2La_4Ti_5O_{18}$ and $BaLa_2Ti_3O_{10}$ [62, 63]. The homogeneity range of the doped perovskite phase exactly points into the direction of the compositions $Ba_2La_4Ti_5O_{18}$ and $La_4Ti_3O_{12}$ which can theoretically be thought of to correspond to the extension of the solubility under the assumption of Ti vacancy compensation according to

$$(Ba_{Ba}^{\times})_{1-x}(La_{Ba}^{\bullet})_x(Ti_{Ti}^{\times})_{1-\frac{1}{4}x}(V_{Ti}^{''''})_{\frac{1}{4}x}O_3 \qquad \textbf{Eq. 3-28,}$$

with x = 2/3 for the compound $Ba_2La_4Ti_5O_{18}$ and x = 1 for the compound $La_4Ti_3O_{12}$. Both authors concluded that Ti vacancy compensation is favorable over the counterpart of Ba in donor-doped $BaTiO_3$.

Combining equations 3-24 (electron compensation) with the equilibria expressed by equations 3-26 and 3-27 results respectively in:

$$4e + O_2^{(g)} \overset{\text{redox}}{\rightleftharpoons} 2O_O^{\times} + 2V_{Ba}'' \qquad \textbf{Eq. 3-29,}$$

$$4e + O_2^{(g)} \overset{\text{redox}}{\rightleftharpoons} 2O_O^{\times} + V_{Ti}'''' \qquad \textbf{Eq. 3-30.}$$

The electron compensation occurs under the reducing conditions and the metal compensation mechanism is the counterpart under the oxidation. In both cases the law of mass action gives the slope:

$$\left(\frac{\partial \log \sigma_{\text{total}}}{\partial \log p(O_2)}\right)_T \approx \left(\frac{\partial \log n}{\partial \log p(O_2)}\right)_T \approx -\frac{1}{4} \qquad \textbf{Eq. 3-31.}$$

Irrespective of the discussion, which kind of metallic vacancy compensates La-donors, the slope in the oxidizing regime of the Kröger-Vink diagram according to equations 3-26 and 3-27 is -1/4. This theoretically expected slope is experimentally confirmed (refer to figure 3-8).

There are a couple of experimental and theoretical reports about the energy levels and formation energies of lattice point defects in $BaTiO_3$ [37, 38, 41]. According to these references an electronic band diagram, as shown schematically in figure 3-10 can be set up.

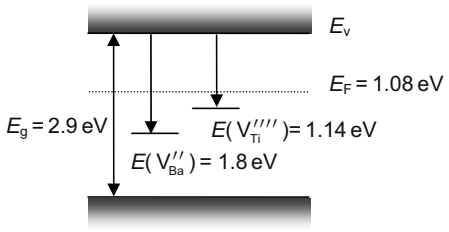

Fig. 3-10: Electronic band diagram showing the energy levels of the vacancies of Ti and Ba. Fermi level corresponds to the temperature of 1300˚C, $p(O)_2$ of 0.1 MPa and lanthanum concentration is 0.2 at.%

The energy level of Ba vacancies is located much deeper compared to that of Ti vacancies. They are considered to be fully ionized unless the Fermi energy overlaps these defect states at elevated temperatures. This means that Ti vacancies are regarded as four-fold charged negative point defects at lower temperatures.

The formation energies of the different possibilities of Schottky type defects, as they have been determined from calculations on the basis of potential models [64] are listed in table 3-6. These theoretical predictions show basically the same energy levels for every intrinsic Schottky reactions. This result suggests that metal vacancy compensation could be governed by the stoichiometry of barium titanate.

Schottky-disorder	Formation energy per defect [eV]
$V_{Ba}'' + V_{Ti}'''' + 3V_O^{\bullet\bullet}$	2.29
$V_{Ti}'''' + 2V_O^{\bullet\bullet}$	2.91
$V_{Ba}'' + V_O^{\bullet\bullet}$	2.58

Tab. 3-6: Formation energies of different Schottky-type lattice disorder in $BaTiO_3$ [37, 38].

3.2.2.4 Amphoteric doping

Finally the case of amphoteric doping of barium titanate is briefly presented. As shown in the previous two sections on acceptor- and donor-doping the incorporation of aliovalent ions into the perovskite lattice takes preferentially place either on the A-site or on the B-site depending on the ionic radius. Mn^{3+} for instance favorably substitutes Ti^{4+} and acts as an acceptor, whereas La^{3+} rather occupies the Ba-positions and works as a donor. A number of so-called amphoteric ions, having an intermediate size between Ba^{2+} (161 pm) and Ti^{4+} (60.5 pm) [33], however, can be accommodated on both A-site and B-site simultaneously [62, 63]. Upon the addition of a certain excess of BaO or TiO_2 to $BaTiO_3$ these amphoteric ions, such as exemplarily Ca^{2+} ($r_{Ca^{2+}}$ = 134 pm) or the rare earth ions Y^{3+} ($r_{Y^{3+}}$ = 107.5 pm), Sm^{3+} ($r_{Sm^{3+}}$ = 124 pm) or Dy^{3+} ($r_{Dy^{3+}}$ = 108 pm) [33], can be shifted between the two distinct crystallographic sites, depending on whether the off-stoichiometry is in favor of the BaO- or TiO_2-rich side of the system [65-70]. Determined by their preferential site occupancy amphoteric ions may act as donor and/or acceptor. Taking the specific example of Dy^{3+}, this cation represents an acceptor when it occupies the B-site which is mainly the case for compositions that are rich in BaO. In the contrary case of TiO_2-excess Dy^{3+} rather occupies the A-site, where it acts as a donor. Amphoteric dopants are often employed for $BaTiO_3$-based materials used for multilayered ceramic capacitors (MLCC). Approximately thirty years ago, sintering these formulations under reducing conditions eventually resulted in the so-called “DC degradation” if not suitable measures were undertaken to prevent this deterioration in materials reliability. This relates to an insufficient insulation resistance, which is responsible for failure of devices due to a dielectric breakdown. The origin of such collapse in insulation relies on an unfavorable defect chemical situation [47-49] that arises during sintering of the material under reducing conditions: substantial amounts of oxygen vacancies are then formed in $BaTiO_3$. The low partial pressure of oxygen, however, is indispensable for cofiring the ceramic dielectric layers together with internal metallic electrodes that usually consist of metals such as Ni, which are easily oxidized at elevated temperatures. Such base metal electrodes are less costly but unfortunately vulnerable to corrosion by oxidation. Under a continuously applied electric DC-field during operation, demixing of the oxygen vacancies formed during sintering takes place. They migrate as positive ionic charge carrier through the lattice and gradually accumulate at grain boundaries facing the cathode side. These pile-ups of oxygen

vacancies come along with large local concentrations of electrons in order to maintain charge neutrality. This enrichment in electronic charge carriers at the grain boundaries is finally responsible for a catastrophic avalanche discharge causing large leakage currents. To prevent DC-degradation codoping (addition of acceptors as well as donors) or doping with amphoteric doping-ions, like Dy^{3+} or Y^{3+} has been applied in order to reduce the concentration of mobile oxygen vacancies.

In the case of modern reduction-resistant PTCR materials, as they are employed for multilayered chip-type devices, lanthanoids with larger ionic radius, such as La^{3+} or Nd^{3+} are generally added. Their main function is the realization of the desired n-type semiconduction in the grain interior during sintering in reducing conditions. Acceptor states on the grain boundaries appear after a reoxidation treatment and are responsible for the non-linearity of resistivity upon temperature increase. Amphoteric ions such as Sm^{3+} even enhance this strong resistivity increase [13]. Their exact defect chemical influence is not precisely understood yet.

In the present thesis intentionally the non-amphoteric ion La^{3+} which is believed to almost exclusively substitute Ba^{2+} on the A-site has been selected [71], because even in the case of reoxidized BaO-rich PTCR compositions originally fired under reducing conditions the defect chemical situation is largely unknown. In order to avoid an additional degree of complexity introduced by the possible shift of the impurity ion between A- and B-site – the certainly interesting case of amphoteric dopant ions – was not considered. It is the subject of future studies.

3.2.3 Defect chemical simulations: outline of the calculation algorithm

This section briefly introduces the methodology of defect chemical simulations applied in chapter 6 which was used to assess experimental results in terms of the equilibria presented previously in section 3.2.2. As shown before two opposite cases have to be distinguished regarding the charge compensation in donor-doped $BaTiO_3$, as they are relevant to PTCR thermistors: compensation (i) by electrons (equation 3-24) and (ii) by metal vacancies (equations 3-26 or 27). The theoretically possible situation of Frenkel-type lattice disorder can be excluded because the material category of titanates based on the perovskite structure generally reveals a closely packed and dense lattice that does not allow the formation of interstitially incorporated ions.

Under all circumstances the condition of electrical neutrality must be guaranteed, which is expressed by equation 3-23. Here all variables except the electron concentration have first to be eliminated for the simulation.

The valance state of Ti vacancies can fluctuate between V_{Ti}'''' and V_{Ti}''' depending on the position of the Fermi energy according to figure 3-10. This is expressed by equation 3-32:

$$V_{Ti}'''' \rightleftharpoons V_{Ti}''' + e \qquad \textbf{Eq. 3-32.}$$

The concentrations of fully ionized Ti vacancies $[V_{Ti}'''']$ and of trivalent Ti vacancies $[V_{Ti}''']$ are governed by the level of the Fermi energy. The Fermi-Dirac distribution is then derived:

$$[V_{Ti}''''] = \frac{[V_{Ti}^{Total}]}{1+\exp\left\{\left(E_F(T)-E_{V_{Ti}''''}\right)/k_B T\right\}} = \frac{[V_{Ti}''''] + [V_{Ti}''']}{1+\exp\left\{\left(E_F(T)-E_{V_{Ti}''''}\right)/k_B T\right\}} \qquad \textbf{Eq. 3-33.}$$

It is believed that the conduction mechanism for n-type $BaTiO_3$ has small polaron hopping nature [72]. Accordingly the Fermi energy $E_F(T)$ is then expressed as function of the density of state in the conduction band N_C and electron concentration:

$$E_F(T) = k_B T \cdot \ln\left(\frac{N_C}{n}\right) \qquad \textbf{Eq. 3-34.}$$

The concentration value in the conduction band N_C corresponds to the concentration of Ti ions in $BaTiO_3$, since electrons are strongly coupled with Ti ions in small polaron conduction:

$$N_C = 1.6 \times 10^{22}\ cm^{-3} \qquad \textbf{Eq. 3-35.}$$

All other relevant defect chemical equilibria that are necessary in order to calculate the electron concentration as function of oxygen partial pressure $p(O_2)$ and temperature T are summarized for illustration in table 3-7. Also all thermodynamic parameters needed for the simulation are listed here.

The Schottky equilibrium is practically only active during sintering. During cooling after firing the metal vacancies are considered to be frozen in and their concentration remains constant. This has to be taken into account, when low temperature equilibria have to be calculated.

	Equation	Law of mass action	K^0	E_a [eV]
Hole-electron recombination	$\mathrm{nil} \rightleftharpoons e + h$	$K_{\mathrm{recomb.}} = N_C \cdot N_V \cdot \exp\left(\frac{-E_g}{k_B T}\right)$	1×10^{45}	2.9
Intrinsic reduction	$O_O^{\times} \rightleftharpoons 1/2O_2^{(g)} + 2e + V_O^{\bullet\bullet}$	$K_{\mathrm{red.}} = [V_O^{\bullet\bullet}] \cdot n^2 \cdot \sqrt{p(O_2)}$	2.56×10^{71}	6.1
Schottky equilibrium	$\mathrm{nil} \rightleftharpoons V_{Ba}'' + V_{Ti}'''' + 3V_O^{\bullet\bullet}$	$K_{\mathrm{Schottky}} = [V_{Ba}''] \cdot [V_{Ti}''''] \cdot [V_O^{\bullet\bullet}]^3$	1×10^{116}	10.9

Tab. 3-7: Defect chemical reaction in $BaTiO_3$.

The ratio of vacancies on the Ba-site to those on the Ti-site is expressed by the coefficient κ in the calculations [73]:

$$\kappa = [V_{Ba}''] / [V_{Ti}^{\mathrm{Total}}] \qquad \textbf{Eq. 3-36.}$$

Together with the constant κ, the relations listed in table 3-7 and the equations 3-33 to 3-35, a system of five equations can be set up for a total of five variables: h, $[V_O^{\bullet\bullet}]$, $[V_{Ti}'''']$, $[V_{Ti}''']$ and $[V_{Ba}'']$. These variables can then be substituted in the formula of electroneutrality and finally one expression for the electron concentration n in dependence of the donor concentration $[La_{Ba}^{\bullet}]$, oxygen partial pressure $p(O_2)$, temperature T and the coefficient κ is obtained. The value of κ must be assumed, because it is unknown [73]. This is particularly true for off-stoichiometric compositions. In the present work κ = 0.1 is employed for simulations, a value that is reasonable on account of the Ba-rich compositions and the readiness of Ti vacancy formation in donor-doped $BaTiO_3$ [62, 63]. One more thing to be added is that the value κ affects metal vacancy concentrations, whilst it does not affect the electron concentration that can only be directly detected by DC conductivity measurement. The equation for electroneutrality (eqation 3-23) should be modified considering the influence of dissociation of electrons from V_{Ti}'''' at higher temperatures (equation 3-32):

$$2[V_O^{\bullet\bullet}] + h + [La_{Ba}^{\bullet}] = n + 2[V_{Ba}''] + 4[V_{Ti}''''] + 3[V_{Ti}'''] \qquad \textbf{Eq. 3-37.}$$

The final equation used for the calculation of n is an equation of fifth degree that has to be solved numerically:

$$\frac{K_{\mathrm{red.}}}{n^2\sqrt{p(O_2)}} + \frac{K_{\mathrm{recomb.}}}{n} + [La_{Ba}^{\bullet}] = n + 2\sqrt{\frac{\kappa \cdot K_{\mathrm{Schottky}} p(O_2)^{3/2} n^6}{(K_{\mathrm{red.}})^3}} + 4\sqrt{\frac{K_{\mathrm{Schottky}} p(O_2)^{3/2} n^6}{\kappa \cdot (K_{\mathrm{red.}})^3}} + 3\sqrt{\frac{K_{\mathrm{Schottky}} p(O_2)^{3/2} n^6}{\kappa \cdot (K_{\mathrm{red.}})^3}} \Bigg/ \left(1 + \frac{\exp\left(E_F - E_{V_{Ti}''''}\right)}{k_B T}\right) \qquad \textbf{Eq. 3-38.}$$

With the calculated electron concentration obtained from this relation the defect concentrations of all other defect chemical species can be determined at various oxygen partial pressures and temperatures. Also the simulation of electronic conduction can be done and compared to experimental values (chapter 6).

3.3 Basic models of barium titanate based PTCR ceramics

The origin of the PTCR effect in $BaTiO_3$ can be quantitatively explained by three fundamental models: according to a theory proposed by Heywang [16, 17] the appearance and variation of the insulating double Schottky barriers at the grain boundaries upon heating is expressed in terms of semiconductor physics. Later Jonker [18] took the effect of interactions of these interface barrier layers with ferroelectric domains into account in order to describe the regime of cold resistance below the Curie temperature. Finally Daniels [19] introduced a defect chemical model that characterizes the nature and behavior of the electrically charged point defects that are responsible for the development of the PTCR effect in $BaTiO_3$. At present a large multitude of different experimental and theoretical reports confirm all these three fundamental theoretical concepts which are presented in the following sections.

3.3.1 Heywang model: Schottky-type grain boundary junctions

Heywang from the Siemens research laboratory in Germany originally proposed in 1961 a model explaining why grain boundaries are needed to realize the PTCR effect in $BaTiO_3$.[16,17] He postulated that the unique non-linearity of electrical resistance with temperature is associated with negatively charged acceptor states that are localized at the grain boundaries. Without further specifying the exact nature of these acceptor states Heywang assumed that they are mainly responsible for the occurrence of an electrically insulating back-to-back Schottky-barrier above the Curie temperature T_C. The formation and enrichment of grain boundary acceptor states was related with the absorption of oxygen, because the PTCR effect often only appears after a suitable heat treatment in oxidizing atmosphere after sintering. According to Heywang´s model the height $\Phi(T)$ of the insulating grain boundary barrier layer is determined by temperature and can be directly derived from the Poisson equation by introducing the temperature dependence of the surface density $N_s(T)$ of the acceptors at the solid-solid interface:

$$\Phi(T) = \frac{e N_S^2(T)}{8\varepsilon_0 \varepsilon_r(T) N_D} \qquad \textbf{Eq. 3-39.}$$

Here e represents the elementary charge of the electron, ε_0 the dielectric permittivity of vacuum, ε_r the relative dielectric permittivity of the phase $BaTiO_3$ (depending on temperature T) and N_D the charge carrier density determined from the effective donor concentration in the lattice. The temperature dependence for the density of active acceptor state density $N_S(T)$ trapping electrons is described by the Fermi-Dirac distribution:

$$N_S(T) = N_S^0 \Big/ \left\{ 1 + \exp\left(\frac{E_F + e\Phi(T) - E_S}{k_B T} \right) \right\} \qquad \textbf{Eq. 3-40.}$$

N_S^0 refers to the total number of available acceptor states, E_S is the energy gap between the energy level of the acceptors and the conduction band, k_B the Boltzmann constant, and E_F the Fermi energy. The Fermi energy is given by:

$$E_F = k_B T \cdot \ln\left(\frac{N_C}{N_D} \right) \qquad \textbf{Eq. 3-41,}$$

where N_C represents the effective density of states in the conduction band. Since the conduction mechanism in $BaTiO_3$ is related to small polarons [72] N_C is determined by the concentration of Ti-ions. At room temperature this value corresponds to 1.59×10^{22} cm^{-3}. The relationship between electron concentration N_D, arising from the donors, the concentration of trapped electrons $N_S(T)$ and finally the width of the depletion layer b is given through the condition of charge neutrality by:

$$2 \cdot b \cdot N_D = N_S(T) \qquad \textbf{Eq. 3-42.}$$

Above the Curie temperature T_C – the regime for which Heywang physically predicted the Schottky barrier – the dielectric permittivity of the paraelectric phase $BaTiO_3$ follows the Curie-Weiss law:

$$\varepsilon_r(T) = \frac{C_o}{T - \theta_c} \qquad \textbf{Eq. 3-43.}$$

In equation 3-43 C_0 represents the Curie-Weiss constant (approximately 1.5×10^5 K) and θ_c a transition temperature, which is close but not necessarily identical to the Curie temperature of 125°C for pure $BaTiO_3$ [74]. Figure 3-11 summarizes

schematically the back-to-back Schottky barrier at the grain boundaries and all major physical parameter that are involved in Heywang´s model.

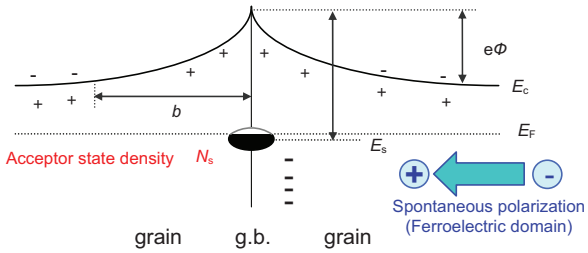

Fig. 3-11: Schematic image of the refined Heywang's model. A back-to-back Schottky barrier exists at the grain boundary because of a local accumulation of negative charges at this interface. They are represented by the acceptor state N_S and result in a depletion layer with the width b. The other relevant physical parameter in Heywang´s model are: (i) the height of the insulating grain boundary barrier Φ, (ii) the density of states in the conduction level N_c, (iii) the Fermi level E_F, (iv) the acceptor level E_s and (v) the density of states at the acceptor level.

Jonker derived the relation for the barrier height in equation 3-39 [18] and Kulwicki et al. deduced an expression for the resistance of one single grain boundary by applying the equations 3-39 to 3-43 [75]:

$$R_{g.b.}(T) = \frac{b}{N_D \cdot e^2 \cdot \mu_e} \cdot \frac{k_B T}{\Phi(T)} \cdot \exp\left(\frac{e\Phi(T)}{k_B T}\right) \qquad \textbf{Eq. 3-44.}$$

This relationship, however, only holds for small external voltages applied, i.e. for the case that a bias voltage does not or almost not affect the height of the Schottky barrier. The total resistivity being mainly determined by the insulating grain boundaries and not by the semiconducting cores of the grains, Heywang formulated from this the temperature dependence of the total resistivity of a $BaTiO_3$-based thermistor ceramics formulated as follows:

$$\rho(T) = \rho_{grain}\left(1 + \frac{b}{D} \cdot \frac{k_B T}{e\Phi(T)} \cdot \exp\left(\frac{e\Phi(T)}{k_B T}\right)\right) \qquad \textbf{Eq. 3-45.}$$

In equation 3-45 ρ_{grain} represents the resistivity of grain interior itself and D is the average grain size.

From the practical point of view, the relation represented in equation 3-45 is very valuable because it allows extracting the width and height of the Schottky barrier layer by fitting experimental resistivity values recorded in dependence of temperature. This permits to gain additional insight in the nature of the insulating

grain boundaries and possibly enables the design of new more performing thermistor materials.

The actual detailed procedure for such kind of simulations is described here, since own calculations based on the Heywang model are presented later in the present work (annex):

(i) Determination of the bulk resistivity ρ_{grain} at room temperature by impedance spectroscopy and evaluation of the average grain *D* size from SEM investigations on the microstructure.

(ii) As value for the mobility of conduction electrons in $BaTiO_3$ the temperature independent value of 0.5 $cm^2 \cdot V^{-1} \cdot s^{-1}$ reported previously [39] is applied. With this the electron concentration for the case of fully incorporated and ionized monovalent donors (e.g. La^{3+} on Ba^{2+}-site) N_D can be estimated using equation 3-46:

$$1/\rho_{grain} = e \cdot \mu_e \cdot N_D \qquad \textbf{Eq. 3-46.}$$

(iii) The value of the bulk resistivity is approximated to be virtually temperature independent [39]. This is certainly justifiable taking into account that the grain boundary resistivity depends much stronger on temperature.

(iv) Grain boundaries are estimated to be the major origin for the measured capacitance contributions, e.g. as they can be assessed by impedance spectroscopy in semiconducting $BaTiO_3$ since the thickness of the space charge layer *b* is very small compared to the average grain size *D*. The temperature dependence of the experimentally determined capacitance for the grain boundaries results together with the geometric dimensions of the sample in the corresponding values of $\varepsilon_{g.b.}(T)$ – the dielectric constant of the grain boundaries as a function of temperature.

(v) An estimated relation between *d*, the width *b* of the space charge zone and the dielectric constant ε_r, as it is represented by the Curie-Weiss law (equation 3-43) is given in equation 3-47:

$$\varepsilon_{g.b.}(T) = \frac{b}{D} \cdot \varepsilon_r(T) \qquad \textbf{Eq. 3-47.}$$

Using equation 3-47 the width of the depletion layer can be calculated. All other parameters involved in equations 3-39 to 3-45 are either determined by the steps (i)

to (iv) or have to be found by iteration. This especially holds for the parameter N_s and E_s [76-81].

3.3.2 Jonker model: the role of ferroelectric domains

Whereas Heywang model relatively well describes the non-linearity of resistivity of $BaTiO_3$-based thermistors upon heating into the paraelectric range above the Curie temperature T_C, this is not the case for the lower temperature regime of ferroelectricity. For this reason Jonker extended and refined the original model from Heywang.[18] Below T_C the former model does not explain, why cold resistivity nearly remains temperature independent and at a level of relatively low values. Obviously the insulating effect of the double Schottky barriers at the grain boundaries is largely depressed or should even partially vanish at low temperatures, but the theory presented by Heywang does not take this into account.

Jonker therefore suggested in 1964 that at temperatures below T_C the height of the insulating potential wall at the internal solid-solid interfaces is reduced in average roughly by a factor of 50% through the space charges arising from the spontaneous ferroelectric polarization of the tetragonal phase. This scenario is schematically shown in figure 3-12. Depending on the orientation relation of the polarization vectors for domains adjoining at a common grain boundary certain parts of the interface experience an additional negative interface charge. Other parts of the grain boundary network, however, are subject to an extra positive charge that reduces the net height of the insulating potential barrier. This local charge compensation and the reduction of the barrier height open current paths that explain the relatively low resistivity values in the temperature range where the ferroelectric phase is stable. Jonker estimated the state density of acceptor states at the grain boundaries by:

$$\Delta P_n = e \cdot N_S \qquad \textbf{Eq. 3-48.}$$

In this relationsship ΔP_n is a portion of the spontaneous ferroelectric polarization that results as a difference between the normal components of the polarization vectors of two adjacent domains at one and the same grain boundary. The local variation of ΔP_n depends on the domain structure and therefore either the negative interface charge is increased or decreased. At the Curie point, the maximum value of ΔP_n corresponds to 18 µC/cm^2. According to equation 3-48 N_s is then expected to be 1.1 × 10^{14} cm^{-2}.

This expected density of surface acceptor states describes well the insulating Schottky barrier above Currie temperature in Heywang's model.

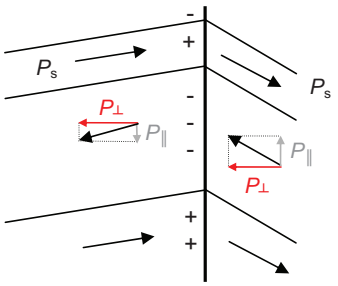

Fig. 3-12:
Schematic view of Jonker's model. The refinement with respect to the theory presented by Heywang relates to the partial compensation of charge carriers at the grain boundaries through ferroelectric domains below T_C.

This extension and refinement is often referred to as the Heywang-Jonker model. It successfully explains why the resistance drastically changes at the Curie temperature and which role the spontaneous polarization of the ferroelectric phase plays in this scenario.

3.3.3 Daniels model: the role of point defects

Daniels model was proposed in 1976 by Daniels and Wernicke from the Philips research laboratory. [19] The essential contribution of their perception is the answer to the question why donor doping is necessary for the PTCR effect, which is not clarified by Heywang model. There are two ways to make $BaTiO_3$ semiconducting: (i) oxygen deficiency by intrinsic reduction (equation 3-5), and (ii) donor-doping (equation 3-24). PTCR properties appear however only in the case of donor-doping. The proposed model by Daniels et al. is related with metal vacancy formation when donor dopants are added. First, DC conductivity measurements have been conducted and were confirmed by thermogravimetry on La-doped $BaTiO_3$ at very high temperature around 1300°C. A conductivity decrease was observed in oxidizing conditions around 10^{-6} – 10^{-1} MPa.[41,42] The result from DC conductivity measurement is already shown in figure 3-8. Figure 3-13 displays the electron concentration in dependence of oxygen partial pressure. Likewise the DC conductivity measurement, the decrease of electron concentration can be seen in figure 3-13.

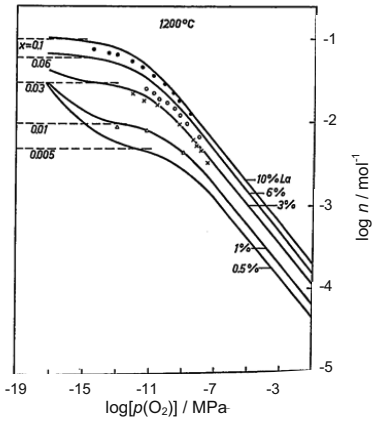

Fig. 3-13:
Electron concentration for different La-contents in dependence of $p(O_2)$ determined by TGA at 1200°C.[42] The results agree with conductivity measurements shown in figure 3-8.
The composition of the samples is $(Ba_{1-x}La_x)Ti_{1.005}O_3$ ($x = 0.005 - 0.1$).

Daniels et al. have attributed this conductivity decrease to barium vacancy compensation instead of electron compensation. This reaction is expressed by the following equation,

$$La_2O_3 + 3TiO_2 \overset{BaTiO_3}{\rightleftharpoons} 2La_{Ba}^{\bullet} + 3Ti_{Ti}^{\times} + 9O_O^{\times} + V_{Ba}'' \qquad \textbf{Eq. 3-49.}$$

In conjunction with the case of electron compensation, which is represented by equation 3-24, these equations result in:

$$1/2\,O_2^{(g)} + 2e \rightleftharpoons O_O^{\times} + V_{Ba}'' \qquad \textbf{Eq. 3-50.}$$

Metal vacancy compensation is therefore considered to be the oxidation formulation of electron compensation. Daniels et al. have considered that metal vacancies consist mainly of barium vacancies, although it is believed recently that titanium vacancy compensation is dominant as proved by the several experiments.[62,63] In contrast to free electrons, metal vacancies can be regarded as being totally immobile. The diffusion process of metal vacancies is too sluggish, so that there is almost no contribution to electrical conduction. Daniels and Wernicke have explained that a metal vacancy layer is formed only at grain boundaries through the very slow kinetics during cooling form sintering temperature. The interior of the grain remains semiconducting, because it takes time for metal compensation to reach the core. This metal vacancy rich layer is responsible for the insulating effect at the grain boundary and it is concluded that this is the origin of the PTCR effect. Metal vacancy compensation takes place only when donor dopant is added to $BaTiO_3$ and it is kept in highly oxidizing conditions at high temperature. This model explains why donor

dopant and oxidizing at high temperature are needed to realize the PTCR effect. The proposed model by Daniels et al. is schematically illustrated in figure 3-14.

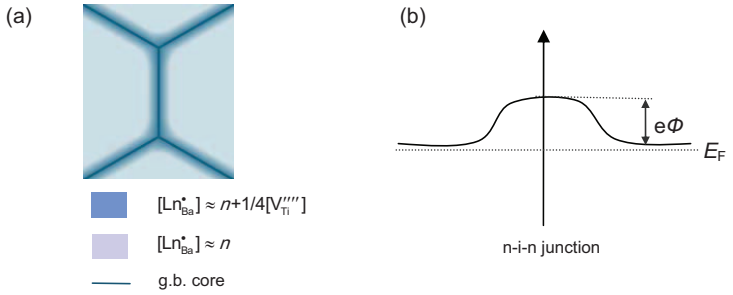

Fig. 3-14: Daniel's model: (a) Schematic image of electron compensated grain inside and metal vacancy compensated outer area and (b) electrical barrier at grain boundary which originates from n-i-n junction. Insulating layer corresponds to metal vacancy compensation layer.

Chapter 4
Experimental

La-doped ceramics on $BaTiO_3$-basis with different nominal chemical compositions have been consolidated, either by pressureless sintering under controlled atmospheres from powders prepared by solid state reaction or via spark plasma sintering (SPS) from nanocrystalline powders obtained by microemulsion mediated synthesis. The phase purity was confirmed by X-ray diffraction (XRD). Microstructural analysis included observation by scanning and transmission electron microscopy (FE-SEM, TEM, HR-TEM), partially in combination with electron backscattered diffraction (EBSD) and electron spectroscopic methods such as EDX. The investigation of the electrical properties comprised the analysis of impedance spectroscopic measurements and the determination of DC conductivity depending on temperature and oxygen partial pressure. Oxygen diffusion profiles were examined using ^{18}O isotope exchange annealing experiments and secondary neutral particle mass spectroscopy (SNMS). Optical properties of some translucent ceramics were studied by UV/VIS spectroscopy and ellipsometry.

4.1 Powder synthesis and ceramic processing

All ceramics compositions studied in the present work are summarized in table 4-1. Only with exception of the powders used for preparing ultrafine grained PTCR ceramics all other compositions have been synthesized via the solid state route. Table 4-2 shows the specification of the raw materials used for this purpose.

As a reference composition, for which the PTCR properties are presented in figure 2-1, a conventional codoped material with 1 mol.% of TiO_2-excess containing an addition of 0.3 at.% La as donor and of 0.07 at.% Mn as acceptor (Composition A in table 4-1) has been prepared in order to verify and ensure the reproducibility of the powder synthesis route, sintering procedure and finally the reliability of the electrical measurements.[82] In order to investigate the effect of BaO-excess *m* on the development of the PTCR characteristics in ceramics fired under reducing conditions

a series of compositions doped with 0.2 at.% of La, nominally specified by the formula $(Ba_{m\text{-}0.002}La_{0.002})TiO_{3+\delta}$ (compositions B-1 to B-6 in table 4-1) has been prepared. The parameter *m* represents the (Ba+La)/Ti ratio and was systematically varied in the range from 0 to 5 mol%. δ symbolizes the off-stoichiometry on the oxygen site. Although not showing any PTCR characteristics another compositional series was realized and studied, because of very unusual optical properties. These ceramic formulations contained 1 at.% of La-dopant and were over-stoichiometric with a slight TiO_2-excess of 0.5 at.% (compositions C-1 to C-3 in table 4.1). All these formulations prepared by the solid state route contained 0.7 wt.% of colloidal silica as sintering aid, in order to facilitate subsequent sintering.

Finally a stoichiometric batch containing 0.2 at.% of La-dopant and one off-stoichiometric batch with the same donor concentration, but with $m = 1.02$ has been prepared by microemulsion mediated synthesis[83] in order to consolidate ceramics with ultrafine microstructure and an average grain size well below 0.5 µm. These ceramics (compositions D-1 and D-2) were used to study scaling effects on the PTCR characteristics.

Denotation	Nominal composition	Comment
A	$(Ba_{0.997}La_{0.003})(Ti_{0.9993}Mn_{0.0007})_{1.01}O_{3+\delta}$	Reference: codoped TiO_2-rich
B-1	$(Ba_{0.998}La_{0.002})TiO_{3+\delta}$ ($m = 1.00$)	Ceramics with BaO-excess (0.7 wt.% SiO_2 included)
B-2	$(Ba_{1.008}La_{0.002})TiO_{3+\delta}$ ($m = 1.01$)	
B-3	$(Ba_{1.018}La_{0.002})TiO_{3+\delta}$ ($m = 1.02$)	
B-4	$(Ba_{1.028}La_{0.002})TiO_{3+\delta}$ ($m = 1.03$)	
B-5	$(Ba_{1.038}La_{0.002})TiO_{3+\delta}$ ($m = 1.04$)	
B-6	$(Ba_{1.048}La_{0.002})TiO_{3+\delta}$ ($m = 1.05$)	
C-1	$(Ba_{0.99}La_{0.01})Ti_{1.005}O_{3+\delta}$	Translucent ceramics
C-2	$(Ba_{0.985}La_{0.015})Ti_{1.005}O_{3+\delta}$	
C-3	$(Ba_{0.92}La_{0.02})Ti_{1.005}O_{3+\delta}$	
[§] D-1	$(Ba_{0.998}La_{0.002})_{1.00}TiO_{3+\delta}$	Ultrafine grained ceramics
[§] D-2	$(Ba_{0.998}La_{0.002})_{1.02}TiO_{3+\delta}$	

Tab. 4-1: Ceramic compositions studied in the present work ([§] via microemulsion mediated method)

Raw powder	Supplier / Purity	Average particle size D_{50} [μm]	Major impurities [ppm]						Minor impurities [ppm]
			Fe	Si	Ca	K	Na	Al	
$BaCO_3$	Sigma-Aldrich / > 99 %	2.23	4	N.A.	5	1	0.6	N.A.	Sr: 570, Cl: 20, S: 5
TiO_2 (rutile)	Sigma-Aldrich / > 99.9 %	1.05	15	N.A.	N.A.	N.A.	N.A.	10	
La_2O_3	Alfa Aesar / 99.999 %	10.53	20	28	18	N.A.	N.A.	N.A.	Ce, Cu, Ni, Pr, Cr: < 2
MnO	Alfa Aesar / 99.99 %								
Colloidal SiO_2	Aldrich chemistry	N.A. [§]					4000		

Tab. 4-2: Specification of the raw materials used for powders prepared via the solid state reaction ([§] specific surface area: 229 m^2/g; N.A.: not available).

4.1.1 Solid state reaction and sintering

In order to minimize the eventual uptake of moisture, all raw powders were constantly kept at 115°C in a drying chamber. Nominal compositions as specified in table 4-1 were carefully weighed using a digital balance and blended together in a 500 ml polyethylene bottle partially filled with balls of partially stabilized zirconia (PSZ, Toso, Japan). The typical batch size for powder synthesis was 30 g and the bottles were filled to approximately 40% of their volume with the zirconia balls of 2 and 3 mm in diameter. The powder mixtures were mixed and milled for six hours in isopropanol on a roller bench, dried using a rotary evaporator (Rotavapor® R-134 with waterbath B-480, Büchi, Switzerland) and calcined at 1150°C for two hours in a muffle furnace (HT08/17, Nabertherm, Germany) in air. The calcined powders were then milled again with PSZ balls for six hours in isopropanol on the roller bench, dried and mixed with 3 wt.% of polyvinyl acetate (PVAc) as binder. These powders were then pelletized by cold uniaxial pressing applying a pressure of 100 MPa in a cylindrical steel die that contained the powder. After compaction the green bodies were decarbonized at 600°C for ten hours in air using the above mentioned muffle furnace and then consolidated for two hours typically at temperatures between 1300°C and 1375°C in a gas-tight Al_2O_3 tube furnace using air or water-saturated Ar gas with 0.3 vol.% of H_2 as sintering atmosphere. This reducing moist gas mixture of Ar and H_2 results at 1300°C in a typical value for the oxygen partial pressure $p(O_2)$ of approximately 10^{-9} MPa. After consolidation samples with a diameter of 12 mm were

cut out of the sintered pellets with a diamond saw and grinded with SiC sandpaper. Whenever needed reoxidation of these ceramic discs was carried out in air for two hours respectively at various temperatures in the range from 700°C up to 1300°C. For the application of metallic electrodes, alternatively (i) sputtered Ni, (ii) sputtered Ti, (iii) evaporated Ag or (iv) a painted In-Ga alloy (weight ratio In:Ga = 25:75) have been employed. In the case of Ni and Ti electrodes a protective layer of sputtered Pt was applied in-situ to prevent excessive oxidation of the contacting electrodes.

4.1.2 Microemulsion mediated synthesis and spark plasma sintering

Nanocrystalline La-doped $BaTiO_3$ powders have been synthesized through the hydrolytic decomposition of suitable metal-organic precursors in microemulsions and have subsequently been processed to dense ultrafine grained ceramics through consolidation by spark plasma sintering (SPS). Nano-sized La-doped $BaTiO_3$ particles with and without BaO-excess were prepared from pure metallic barium dissolved in dried methanol mixed with the corresponding amounts of titanium-isopropoxide and lanthanum-propionate. Special care was taken in order to limit the oxidation of the Ba metal and the hydrolysis of the metalorganic chemicals before any further use for the synthesis. For this purpose all the reagents were kept and handled in an Ar-glovebox with an controlled atmosphere avoiding oxygen and moisture as much as possible (O_2-content < 2 ppm and H_2O-content < 1 ppm). Finally the La-doped $BaTiO_3$ nanopowders were then co-precipitated in mono-sized aqueous pools dispersed within the microemulsion that was added to this precursor. The reactions taking place here can be expressed in a simplified manner (without the doping) by the following equations:

$$Ba + 2HO-R_1 + Ti-(O-R_2)_4 \xrightarrow{CH_3OH} [BaTi-(O-R_{1,2})_n]_m + H_2^{(g)}\uparrow \qquad \textbf{Eq. 4-1,}$$

$$[BaTi-(O-R_{1,2})_n]_m + H_2O \rightarrow BaTiO_3 + nmR_{1,2}-OH \qquad \textbf{Eq. 4-2.}$$

(with R_1 representing a methyl- and R_2 an isopropyl-group).

The mixed probably oligomeric metalorganic alcoholate prepared through the reaction described by equation 4-1 reacts hydrolytically in the confined ultrasmall space of the aqueous nanodroplets of the microemulsion (equation 4-2). Therefore the average diameter of the resulting solid $BaTiO_3$ particles is also very close to the droplet size of the microemulsion. This is illustrated schematically in figure 4-1. The original stabilization of the corresponding nanosized water droplets occurs through

the addition of suitable surfactants. Table 4-3 lists the constituents of the microemulsion typically used in the present study.

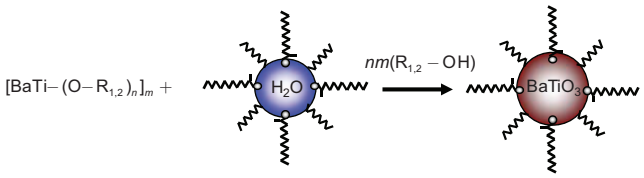

Fig. 4-1: Schematic representation of the template synthesis of nanocrystalline $BaTiO_3$ powders via a microemulsion.

Function	Chemical	Concentration [wt.%]
Surfactant	CTAB: Chetrimetylammoniumbromide	3.74
Co-surfactant	Pentanol	12.21
Oil	Cyclohexane	72.80
Water	Degassed H_2O	11.23

Tab. 4-3: Chemical composition of the microemulsion.

In order to enhance the densification and reduce the extent of grain growth during sintering the nanocrystalline powders were processed by spark plasma sintering (SPS). Through the combined application of temperature, external mechanical pressure and an electric discharge during consolidation a considerable reduction of the necessary sintering temperature and soaking time is achieved. This allows obtaining ultrafine grained ceramic materials with high density.[84] Ultrafine grained ceramics with an average grain size of a few hundred nm are prepared for the investigation of scaling effects on the PTCR characteristics.

4.2 Phase purity and crystallographic characterization

In order to assess the phase purity or crystallographic lattice structure of synthesized or calcined powders X-ray diffraction was applied using an X-ray goniometer in Bretano-configuration with copper X-ray source (X'pert system, Philips, The Netherlands). The measuring parameters were typically: (i) angular range of Bragg-reflections: 20 – 100° and (ii) scanning speed: 0.25°/min. In the case of BaO-rich compositions the secondary phase Ba_2TiO_4, which is known as barium orthotitanate is sometimes detected, with a typical Bragg diffraction peak located at 29.0 – 30.5°. Peaks of other Ba-rich secondary phases were attributed to the compound fresnoite $Ba_2TiSi_2O_8$, if its presence could be confirmed by transmission electron microscopy

(TEM). The determination of lattice parameters was carried out by Rietveld refinement of the respective XRD patterns using the FullProf software package (CEA-CNRS, France). Whenever necessary also XRD measurements and their refinements were carried out on consolidated bulk ceramic pellets.

4.3 Analytical powder characterization

After synthesis all powders were characterized with respect to phase purity using XRD. Additionally the average particle size, the powder morphology and weight losses of the synthesized products were determined when needed. In the case of powders prepared by solid state reaction the particle size distribution was measured by laser light scattering (Mastersizer, Malvern, UK). Powders prepared via microemulsion mediated synthesis were characterized by N_2 gas adsorbtion through the technique proposed by Brunauer, Emmett and Teller (BET, Gemini 2360, Micrometrics GmbH, Germany), electron microscopy/spectroscopy (refer to section 4.4.2) and thermogravimetric measurements (TGA, thermo microbalance TG 439, Netsch, Germany) in order to monitor weight losses due to removal of organic residues originating from the microemulsion.

4.4 Microstructural characterization

4.4.1 Sample preparation

All microstructural investigations were carried out using electron microscopy. This applies to both, the morphological characterization of synthesized powders as well as the visualization and analytical description of the microstructure of consolidated polycrystalline ceramic samples. In the case of powdery samples a small amount of the powder was dispersed in ethanol and coated on a retiform sample holder suitable for the observation by TEM. The observation of powder samples by SEM was more straightforward. Here some particles were directly deposited on a sticky carbon tape that could be mounted on the sample holder for the SEM. Bulk samples for SEM were carefully ground using consecutively SiC grinding paper with decreasing granularity and then polished using diamond slurries down to an average grain size of 0.25 µm. Particularly the preparation of microsections for EBSD observation required a special, very gentle and conservative polishing treatment in order to avoid distortions at the surface due to plastic deformation. For the investigation of ceramic samples by TEM, specimens are sliced into thin lamellae using a microtome and

further processed by Ar ion milling.

4.4.2 Electron microscopy

4.4.2.1 Scanning electron microscopy (FE-SEM and SEM)

For the microstructural analysis such as grain size distribution, field-emission SEM is employed (HITACH, Japan). Samples were kept in a high vacuum chamber and an electron acceleration voltage of 10kV was applied.

4.4.2.2 Transmission electron microscopy (TEM)

For the nanocale crystallographic investigation of the ceramic sample especially at grain boundaries, high resolution TEM was employed (JEM-3200, JEOL, Japan). This TEM was equipped with an EDX allowing spacially resolved chemical analysis.

4.4.2.3 Electron backscattered diffraction (EBSD)

In order to obtain a better contrast in particular for the grain boundaries of PTCR ceramics electron backscattered diffraction (EBSD) has been employed. This method allows to determine and to visualize the surface texture of a polycrystalline material and is commonly used in metallurgy and mineralogy.[85]

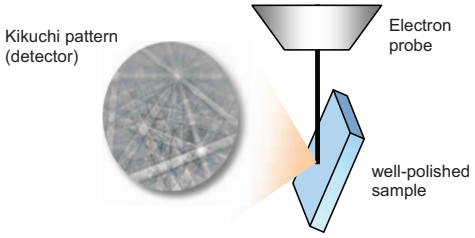

Fig. 4-2:
Principle of electron backscattered diffraction: the crystallographic orientation of the illuminated grains on the very surface of the polished ceramic sample is detected as Kikuchi pattern. Through the analysis of these diffraction patterns the texture of the sample can be determined.

The principle of EBSD is illustrated in figure 4-2 and relies on the analysis of Kikuchi patterns detected from electrons that have been backscattered during observation in SEM by the surface of the sample under consideration. Since this Kikuchi pattern is determined by the orientation of the grain, mapping of the texture and of the grain boundary misalignments can be readily measured. An example for an EBSD analysis is represented in figure 4-3. High quality measurements with a precise signal require particular care during sample preparation. Because internal strain or deformation induced during surface grinding and polishing affects the quality of the measurement

a very gentle and preserving surface treatment with little applied mechanical pressure is mandatory.

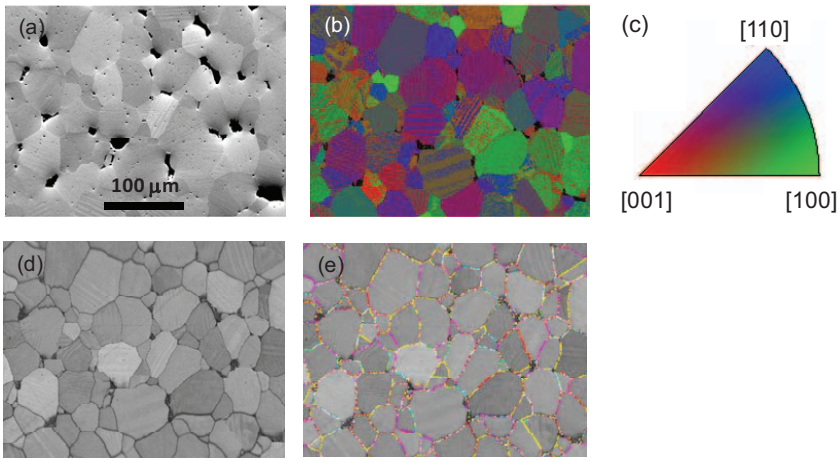

Fig. 4-3: Example of an EBSD analysis for a codoped PTCR ceramics with the nominal composition $(Ba_{0.997}La_{0.003})(Ti_{0.9993}Mn_{0.0007})_{1.01}O_{3+\delta}$ (Sample A) sintered for two hours at 1400°C in air:
(a) electron backscattering image of the microstructure, (b) mapping of the crystallographic orientation of individual grains, (c) orientation triangle, (d) pattern quality map (e) mapping of grain boundary misorientation: green → 0-15°, cyan → 15-30°, red → 30-45°, pink → 45-60°, yellow → 60-75°, white 75-90°.

4.5 Impedance spectroscopy

The resistive and capacitive response of polycrystalline electronic ceramics such as PTCR thermistors are composed of a variety of contributions arising from external interfaces such as those between electrodes and the ceramics surface, from internal interfaces such as grain or phase boundaries and finally from the individual crystallites or grains themselves. With electric DC conductivity measurement techniques it is generally impossible to separate these different parts of electrical response in a simple way and therefore a superposition of them is obtained. By measuring the complex electric AC impedance as a function of frequency, however, distinct resistive or capacitive components arising from various microstructural features of the ceramic may be assessed.

4.5.1 Measurements

In the present study an impedance analyzer (Alpha analyzer, Novocontrol System GmbH, Germany) equipped with a temperature control chamber has been used. As

geometrical dimensions for the flat cylindrical specimens employed in these measurements an electrode diameter of ϕ = 12 mm and a sample thickness d = 1 — 2 mm were typically selected. The impedance system is based on an auto-balanced bridge; an AC voltage amplitude of 0.1 V was applied to the sample and the impedances at different frequencies were recorded automatically. The frequency f was modulated in a wide range from 10^{-2} up to 10^{6} Hz. Impedance values can be measured within the limits from 10 to $10^{10}\,\Omega$ with 0.1% of accuracy. The temperature range accessible for impedance measurements in this set-up extends from -150°C up to 400°C. The atmosphere surrounding the ceramic sample during data acquisition consists of dry N_2, which is supplied by a Dewar flask with liquid N_2.

4.5.2 Data analysis according to the brick-wall model

In order to deconvolute and separate individual resistive or capacitive contributions from impedance spectra, often the brick-wall model is employed.[86-89] Figure 4-4 schematically shows an idealized representation of a polycrystalline electronic ceramics. The grains are assumed to be cubic in shape and of identical dimensions denoted by an average grain size D that corresponds to the length of edge of the cubes. All grains are separated by a grain boundary layer of thickness $\delta_{g.b.}$. The total population of all grains can then be assumed to have a resistance R_{grain} and a capacitance C_{grain}. The respective contributions of the grain boundaries can be respresented by $R_{g.b.\parallel}$, $C_{g.b.\parallel}$, $R_{g.b.\perp}$ and $C_{g.b.\perp}$, where the symbol $\parallel$ denotes grain boundaries running parallel to the path of electric conduction. The symbol $\perp$ stands for those grain boundaries that extend in the direction perpendicular to this path. Additionally external influences such as the resistance of the ceramic-electrode interface $R_{interface}$ and its capacitance $C_{interface}$ and inductive effects, represented by

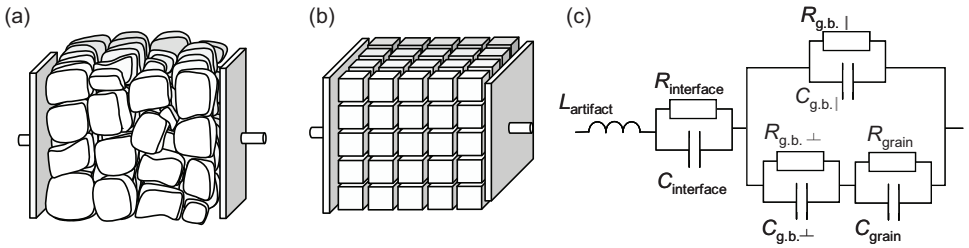

Fig. 4-4: (a) Schematic image of the microstructure of a polycrystalline electronic ceramics, (b) the corresponding brick-wall model representing the idealized microstructure. (c) the equivalent circuit for the brick-wall model.

$L_{artifacts}$ stemming from the measuring equipment and the connections to the sample have to be taken into account. On the basis of the brick-wall model and the assumptions made so far a simplified equivalent circuit for a polycrystalline electronic ceramic can be made as shown in figure 4-5.

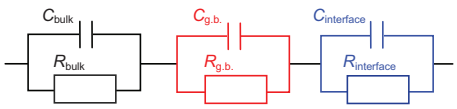

Fig. 4-5: Simplified equivalent circuit of a polycrystalline electronic ceramic corresponding to the schematic microstructure represented in figure 4-4.

Impedance analysis turns out to be a very effective tool for investigating PTCR thermistor ceramics on $BaTiO_3$-basis, due to the microstructural heterogeneity of conductivity: electrical responses from the semiconducting grains and from insulating grain boundary layers can be separated very efficiently. For this purpose *RC* elements for the bulk and for internal as well as for external interfaces have be modeled using a commercial software package (Zview, Scribner Associations Inc., USA). In the case of the PTCR ceramics under consideration here the contribution $R_{g.b.\parallel}$ for grain boundaries running perpendicular to the electrodes can be neglected in this analysis, because this resistive value is much higher compared to $R_{g.b.\perp}$ and R_{grain}. It is assumed that most of the current preferentially flows through the semiconducting grains and the grain boundaries parallel to the electrode planes.

4.5.3 Evaluation of impedance spectra as Cole-Cole diagrams

Although computational fitting and modeling of impedance data is quite

straightforward it must be stressed that the correlation of a given experimental spectrum to a reasonable equivalent circuit representing the individual microscopic contributions is not unambiguous. Generally the task of finding a physically meaningful equivalent circuit for a given impedance spectrum represents an inverse problem. For this reason, careful and critical assessment of the data through comparison with simulated spectra starting from assumed plausible material parameter is necessary for a meaningful physical interpretation.

The generalized equivalent circuit given in figure 4-5 can be further simplified under the assumption that the contact between the electrodes and the ceramic surface is ohmic. In this case the contact resistance and capacitance can be neglected. For a first qualitative estimation the work function of the electrode metal can be taken as a figure of merit. The lower the work function the easier is the transfer of electrons out of the metal into the ceramic. Mostly an In-Ga alloy, which has a quite low work function of around 4.0 eV, has been used in the present study. Here in a first approximation no resistive contribution of the external interface can be assumed.[90] Consequently the corresponding equivalent circuit reduces to only two *RC* elements: one for the grains and one for the grain boundaries parallel to the outer electrodes. Since $R_{\text{g.b.}\perp}$ and $C_{\text{g.b.}\perp}$ are connected in parallel the total impedance $Z_{\text{g.b.}\perp}$ of the grain boundaries can be written as:

$$Z_{\text{g.b.}\perp} = \frac{1}{\frac{1}{R_{\text{g.b.}\perp}} + \mathrm{j}\omega C_{\text{g.b.}\perp}} = \frac{R_{\text{g.b.}\perp}}{1+\mathrm{j}\omega R_{\text{g.b.}\perp} C_{\text{g.b.}\perp}} \qquad \textbf{Eq. 4-3.}$$

Here j is the imaginary unit and ω the angular frequency, i. e. $2\pi f$. Separating the expression in equation 4-3 for the grain boundary impedance into a real part $Z'_{\text{g.b.}\perp}$ and an imaginary part $Z''_{\text{g.b.}\perp}$ results in:

$$Z'_{\text{g.b.}\perp} = \frac{R_{\text{g.b.}\perp}}{1+\left(\omega R_{\text{g.b.}\perp} C_{\text{g.b.}\perp}\right)^2} \qquad \textbf{Eq. 4-4}$$

$$Z''_{\text{g.b.}\perp} = \frac{-\omega R^2_{\text{g.b.}\perp} C_{\text{g.b.}\perp}}{1+\left(\omega R_{\text{g.b.}\perp} C_{\text{g.b.}\perp}\right)^2} \qquad \textbf{Eq. 4-5.}$$

Similar relations hold for the real and imaginary parts of the bulk impedance, Z'_{grain} and Z''_{grain} :

$$Z'_{\text{grain}} = \frac{R_{\text{grain}}}{1+\left(\omega R_{\text{grain}} C_{\text{grain}}\right)^2} \qquad \textbf{Eq. 4-6,}$$

$$Z''_{\text{grain}} = \frac{-\omega R^2_{\text{grain}} C_{\text{grain}}}{1+\left(\omega R_{\text{grain}} C_{\text{grain}}\right)^2} \qquad \textbf{Eq. 4-7.}$$

The total impedance Z_{total}, its real part Z'_{total} and its imaginary part Z''_{total} of the polycrystalline ceramics can then be deduced from equations 4-4 to 4-7 as:

$$\begin{aligned} Z_{\text{total}} &= Z_{\text{g.b.}\perp} + Z_{\text{grain}} = \left(Z'_{\text{g.b.}\perp} + Z'_{\text{grain}}\right) + \text{j}\left(Z''_{\text{g.b.}\perp} + Z''_{\text{grain}}\right) \\ Z'_{\text{total}} &= Z'_{\text{g.b.}\perp} + Z'_{\text{grain}} \\ Z''_{\text{total}} &= Z''_{\text{g.b.}\perp} + Z''_{\text{grain}} \end{aligned} \qquad \textbf{Eq. 4-8.}$$

Using the corresponding fixed material parameters, like the dielectric constant ε_r of the grains $\varepsilon_{\text{grain}}$ and the grain boundaries $\varepsilon_{\text{g.b.}\perp}$ and the electrical resistivities ρ of the grains ρ_{grain} and the grain boundaries $\rho_{\text{g.b.}\perp}$ respectively, the real and imaginary part of the total impedance can be calculated in dependence of the angular frequency ω. The general equations giving the relation between these material parameter and the respective values of resistance *R* and capacitance *C* are given in equations 4-9 to 4-10, where *A* is standing for the cross area and *d* for the distance:

$$C = \varepsilon_0 \varepsilon_r \frac{A}{d} \qquad \textbf{Eq. 4-9}$$

$$R = \rho \frac{d}{A} \qquad \textbf{Eq. 4-10.}$$

The frequency response locus in which Z''_{total} is plotted versus Z'_{total} then yields in the Cole-Cole plot (or Nyquist plot) of the total impedance in the complex plane. The following simulated examples illustrate the approach of analyzing Cole-Cole diagrams in order to extract the relevant resistive and capacitive contributions for polycrystalline electronic ceramics.

4.5.3.1 One single parallel *RC* component

Figure 4-6 shows three impedance spectra calculated for a simple parallel *RC* circuit consisting of only one resistor *R* and one capacitance *C*. The respective values selected for *R* and *C* correspond to the approximate materials parameter for insulating $BaTiO_3$ ($\varepsilon_r \approx 10^3$ and $\rho \approx 10$ GΩ·cm) and have been derived for the specimen dimensions used in this work (ϕ = 12 mm and *d* = 1 mm). Electrode effects

are neglected and also the influence of grain boundaries is not considered for this consideration. The present case study therefore theoretically represents a capacitor consisting of insulating single crystalline $BaTiO_3$.

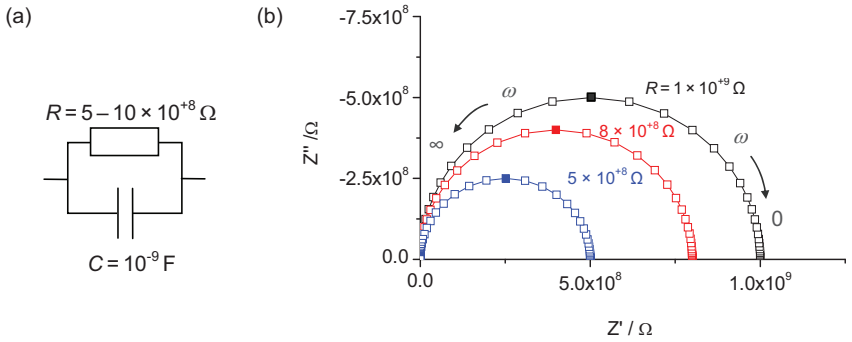

Fig. 4-6: (a) Example of a simple parallel *RC* circuit and (b) the corresponding impedance response for different values of resistance *R* (1 GΩ, 800 MΩ and 500 MΩ) and a fixed value of capacitance *C* (1 nF).

All semicircles representing different frequency loci in figure 4-6 end at the point of origin of the complex plane, being equivalent to the impedance at infinite frequencies $Z_{total}(\omega \rightarrow \infty)$. The intercept of these loci with the abscissa at the opposite, low frequency end $Z_{total}(\omega \rightarrow 0)$ is the DC resistance of the respective equivalent circuit. With decreasing values of ω the total impedance increases because lower frequency currents can only pass the capacitance with considerable delay. The maximum value of the imaginary part of the total impedance Z''_{total} is obtained for the case of relaxation, where the reciprocal angular frequency of the exciting electrical field just corresponds to the relaxation time τ of the circuit:

$$\tau = RC = (\rho \frac{d}{A})(\varepsilon_0 \varepsilon_r \frac{A}{d}) = \rho \varepsilon_0 \varepsilon_r \qquad \textbf{Eq. 4-11.}$$

The relaxation time, also referred to as time constant, only depends on the product of the materials resistivity ρ and dielectric constant ε_r. The respective values for the spectra shown in figure 4-6 are 0.5 s (f = 0.318 Hz) for R = 500 MΩ, 0.8 s (f = 0.199 Hz) for R = 800 MΩ and 1.0 s (f = 0.159 Hz) for R = 1 GΩ.

If instead of the case shown in figure 4-6 the resistance R is kept constant while the capacitance C is changed, the shape of the frequency response loci in the complex plane remain the unaltered, only the value of τ defining the maximum imaginary part

of the total impedance changes. Thus the capacitance can readily be calculated from equation 4-11 if the corresponding value of resistance is known. This possibility of determining capacitance and resistance at the same time is one of the main advantages of impedance spectroscopy compared to electrical DC measurements, where only the total DC resistance can be obtained.

4.5.3.2 Two parallel *RC* components in series

In the next case the influence of grain boundaries is also taken into account. A couple of impedance spectra for the case of two *RC* components in series are shown in figure 4-7. The first element represents the grain response the second one the behavior of the grain boundaries. For the sake of simplicity both resistances are assumed to have the same magnitude and correspond to the value of the first example above. The value of the capacitance for the grain element was again calculated from the approximate value of the dielectric constant of $BaTiO_3$ (sample geometry: ϕ = 12 mm and d = 1 mm), whereas the capacitance for the grain boundary element was varied in the range from 1 nF up to 1 µF.

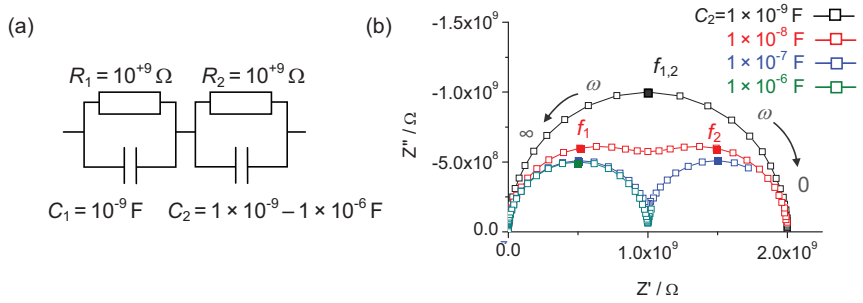

Fig. 4-7: (a) Example of two parallel *RC* components in series and (b) the corresponding impedance response with $R_1 = R_2 = 1\,G\Omega$, $C_1 = 1$ nF and various values of C_2 (1 nF, 10 nF, 100 nF and 1 µF). The frequencies range from 10 mHz up to 10 MHz. The relaxation frequencies f_2 are 0.159, 1.59×10^{-2}, 1.59×10^{-3}, and 1.59×10^{-4} Hz, respectively.

According to Frey et al. and Zhao et al. the dielectric constant of grain boundaries in polycrystalline $BaTiO_3$ ceramics is strongly reduced and amounts to only around 70 – 130 within a layer of 0.8 – 3 nm in thickness around the interface itself, whereas the bulk of $BaTiO_3$ has dielectric constant of over 1000.[91,92] Even if the dielectric constant in the grain boundary region is around one to two magnitudes smaller compared to the bulk phase the resulting capacitance value is a even few orders of

magnitude larger because the interface itself is extremely thin in contrast to the average grain size. In the present example the capacity value arising from the grain boundaries was increased from the original bulk value by a factor of up to 100.

Generally, as in the present example the two semicircles in the frequency response loci, resulting from grain and grain boundary respectively can practically only be distinguished and separated if the relaxation time for both components is different by a factor of at least 10.[93] The low frequency part of the green curve in figure 4-7 (corresponding to C_2 = 1 μF) is only shown incompletely, because a frequency of 1.6×10^{-4} Hz would be needed to realize the maximum of the second semicircle. Frequencies in this range, however, are very difficult to realize with the experimental equipment used in this study.

4.5.3.3 One parallel *RC* component in series with one resistor

In a very first approximation a simplified equivalent circuit that describes the impedance spectrum of $BaTiO_3$-based PTCR ceramics can be thought to consist of a single resistor, representing the semiconducting interior of the grains, connected in series with a parallel *RC* component that characterizes the insulating grain boundary layer regions. This configuration is shown in figure 4-8. In order to estimate the necessary relevant frequency range for impedance spectroscopic measurements on real PTCR ceramics, representative values for the capacitive and resistive responses of grains and grain boundaries had to be assumed. Through the effect of donor doping the resistivity of the grain interior is expected to be around 10 Ω·cm, which is a value that is considerably lower than the one used in the previous cases for insulating $BaTiO_3$. For the given sample geometry used in the present study (ϕ=12 mm and d = 1 mm) the resistance of the whole population of grains is approximately R_{grain} = 1 Ω. Since this value is so negligibly small a parallel capacitor of the magnitude used in the previous cases is not considered. The relaxation frequency

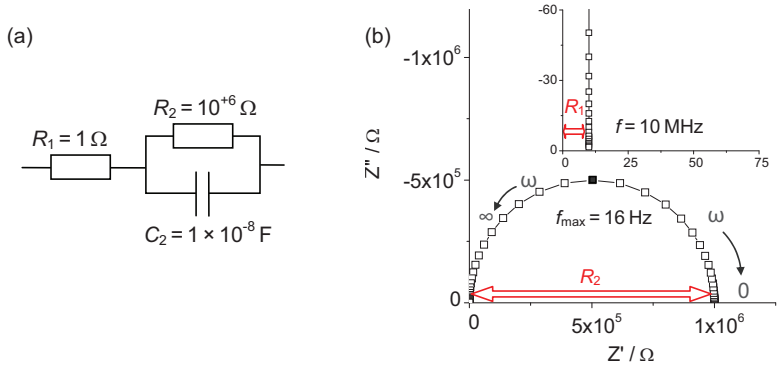

Fig. 4-8: (a) Typical equivalent circuit for a PTCR thermistor on $BaTiO_3$-basis and (b) the corresponding impedance spectrum. $R_1 = 1\,\Omega$ represents the semiconducting interior of the grains, whereas $R_2 = 1\,M\Omega$ and $C_2 = 100\,\mu F$ denote the contributions of the insulating grain boundary regions. The inset shows the high frequency part of the spectrum, where the intercept with the abscissa defines the grain resistance R_1. In the frequency range from 1 mHz to 10 MHz no semicircle for the response of the grains can be recorded experimentally due to the low values of capacitance and resistance.

from $R_{grain} = 1\,\Omega$ and such a capacitance $C_{grain} = 1$ nF is approximately 160 MHz, which cannot be measured with the experimental equipment foreseen for the present investigation. Experimental data and theoretical considerations suggest that the grain boundary resistance of microcrystalline PTCR ceramics with dimensions similar to those used in the present work is in the order of $R_{g.b.} = 1\,M\Omega$.[81] The capacitance contribution arising from the grain boundaries is assumed to be in the order of 100 nF. The relaxation frequency of the grain boundary is therefore around 16 Hz. Since the relaxation frequency of the grains is completely out of the range that is accessible by conventional impedance analyzers only one semicircle is mostly observed for the PTCR ceramics described by the equivalent circuit of figure 4-8. From the Cole-Cole diagram the bulk resistance can be obtained from the intercept of this single semicircle at the high frequency range close to the point of origin of the complex plane (inset of figure 4-8 (b)). It should be noted, however, that high frequency impedance data can be disturbed by noise arising from inductive effects from connection wires or similar artifacts.

4.5.3.4 Constant phase element analysis

The idealized microstructure represented by the brick-wall model in figure 4-4 does of course not reflect the real situation of a sintered ceramic. In general the grains reveal a variety of different crystallographic orientations and morphologies and their size is

usually not uniform but is rather described by a distribution function. Additionally eventual segregations at grain boundaries are also not distributed uniformly all over the polycrystalline ceramic. This results in inhomogeneous current densities. For this reason the relaxation time of every individual grain boundary is not exactly identical all over the volume of the material. Regarding impedance spectra this fact often results in distorted or depressed semicircles observed in the Cole-Cole diagram. The analysis of such distorted impedance spectra is practically carried out using a constant phase element CPE instead of a single capacitance value in order to fit the data.[89,94] Mathematically the impedance of a CPE is defined by two parameters Q^0 and n_{CPE}, describing the deviation from an ideal capacitor:

$$Z_{CPE} = \frac{1}{Q^0 (j\omega)^{n_{CPE}}} \qquad \textbf{Eq. 4-12.}$$

The parameter Q^0 corresponds to the capacitance C if no distortion has to be taken into account, whereas the exponent n_{CPE} quantifies the deviation from this idealized and perfect condition. If n_{CPE} = 1 (ideal capacitor) the impedance of the CPE just corresponds to that of a simple capacitor with capacitance C and with decreasing n the corresponding arc in the Cole-Cole diagram becomes more and more distorted. Both parameters in equation 4-12 Q^0 and n_{CPE} do not have any direct physical meaning but are only used to fit the experimental data. The representative real capacitance value C^* can be derived according to Hsu et al. [94], directly from the angular frequency ω^{max} corresponding to the apex of the depressed impedance arc with resistance R or from the parameter Q^0 and n_{CPE}:

$$C = \frac{1}{\omega^{max} R} \qquad \textbf{Eq. 4-13,}$$

$$C^* = \frac{Q^0}{(\omega^{max})^{n_{CPE}-1}} \qquad \textbf{Eq. 4-14.}$$

Figure 4-9 shows an example, how the parameter n_{CPE} affects the depression of a impedance arc in the Cole-Cole diagram.

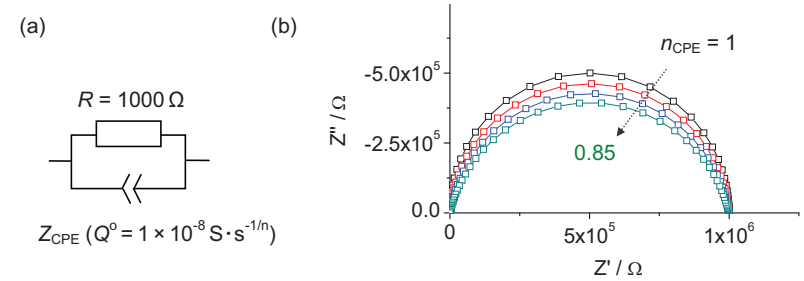

Fig. 4-9: (a) Equivalent circuit of an component containing a constant phase element CPE and (b) the corresponding Cole-Cole representation of the impedance spectra depending on the parameter n_{CPE} ranging from 1 down to 0.85 in steps of 0.05 (Q^0 =1 × 10^{-8} S·$s^{-1/n}$, R = 1 kΩ).

4.6 Measurement of DC conductivity

In order to assess the defect chemical equilibria and reactions involved in the formation of the insulating grain boundary layers of PTCR thermistor ceramics in more detail DC conductivity measurements in dependence of oxygen partial pressure $p(O_2)$ and temperature T have been carried out. Some of the technically relevant details related to these experiments are described in the following.

4.6.1 Experimental set-up

The system used for DC conductivity measurements is presented in figure 4-10. Square cut ceramic samples (dimensions: 1 × 2 × 10 mm^3) were connected to a current source (6220, Keithley, USA) and a voltmeter (PM2534, Philips, The Netherlands) according to the four-point probes method. Pt wires were used to firmly contact the specimens. A pair of two outer electrode wires was used to conduct a given current J through the sample along its largest length and two inner Pt-probes, separated by a distance of typically 5 to 6 mm were used for sensing the corresponding potential V. The resistivity of the sample then could be readily determined from the relative ratio of voltage drop V to current J and the geometrical dimensions of the sample (cross area A, distance d between the voltage sensing electrodes):

$$\rho = \frac{V}{J} \cdot \frac{A}{d} \qquad \textbf{Eq. 4-15.}$$

The measurements were carried out at various oxygen partial pressures $p(O_2)$ and temperatures T. For this purpose the samples were fixed in a gas-tight quartz tube

through which a gas mixture stream of defined $p(O_2)$ was guided. The quartz tube was connected to an oxygen pump (SEMG5, Zirox GmbH, Germany) used to control the $p(O_2)$ at the side of gas inlet and to a oxygen sensor (YSZ cell, Zirox GmbH, Germany) at the opposite side, where the gas was monitored with respect to the real $p(O_2)$ via the electromotive force. Both, the pump and sensor were made of an electrolyte based on yttrium stabilized zirconia. Since the oxygen pump and the sample containing quartz tube were separated high temperature measurements above 1000°C were possible without degrading the Pt wire leads of the ZrO_2 cell in the oxygen pump.

The whole arrangement of the quartz-tube with the containing ceramic sample was placed into a tubular furnace.

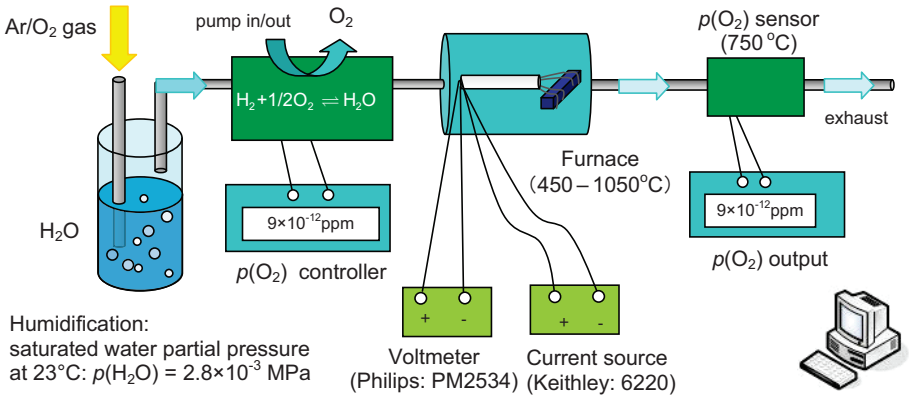

Fig. 4-10: Schematic representation of the experimental set-up.

4.6.2 Control of oxygen partial pressure

In the oxidizing regime down to approximately 10^{-1} MPa the partial pressure of oxygen $p(O_2)$ was controlled by pumping O_2 out of dry Ar (~10ppm O_2 included) using the oxygen electrolytic pump. The $p(O_2)$ within the reducing region on the other hand was established using moist pure Ar that was saturated with water at 23°C ($p(H_2O)$ = 2.8×10^{-3} MPa) by guiding the gas through a washing bottle filled with water before setting the $p(O_2)$ within the electrolytic Y:ZrO_2 cell. In this case the oxygen partial pressure at the sample in the furnace was calculated from the high temperature equilibrium between oxygen, hydrogen and water gas:

$$H_2^{(g)} + 1/2O_2^{(g)} \rightleftharpoons H_2O^{(g)} \qquad \textbf{Eq. 4-16.}$$

The law of mass action for the chemical equilibrium of equation 4-16 can then be written:

$$K_{H_2O} = \frac{p(H_2O)}{p(H_2)\cdot\sqrt{p(O_2)}} = K^0_{H_2O}\cdot\exp\left(\frac{-\Delta G_{H_2O}}{RT}\right) \qquad \textbf{Eq. 4-17.}$$

Equation 4-17 expresses the equilibrium constant for the equilibrium between gaseous water, hydrogen and oxygen in dependence of temperature T. ΔG_{H_2O} is the standard Gibb's free energy for the formation of water, R is the gas constant (8.413 J·K/mol). Hydrogen and oxygen gas is assumed to be generated through the decomposition of water gas as described by equation 4-17. Since ΔG_{H_2O} can be calculated from enthalpy and entropy values listed in handbooks of chemical constants for each compound at different temperatures,[95] the corresponding equilibrium constants at high temperatures can be readily obtained. In order to decrease the $p(O_2)$, oxygen gas is pumped out through the electrolytic cell and a corresponding higher relative proportion of hydrogen gas remains in the gas mixture that is led into the furnace tube. This generated hydrogen gas scavenges remnant oxygen gas, resulting in a low value of $p(O_2)$ inside the furnace. Setting the amount of thermally decomposed water in the gas mixture as Δx, the same amount of hydrogen should be generated at the temperature of the electrolytic cell (750°C). The partial pressure of hydrogen at this temperature can then be expressed as:

$$p(H_2)_{750°C} = \Delta x \qquad \textbf{Eq. 4-18.}$$

The water gas equilibrium in the oxygen pump at 750°C follows equation 4-20:

$$K_{H_2O}(750°C) = \frac{p(H_2O)_{750°C}}{p(H_2)_{750°C}\cdot\sqrt{p(O_2)}_{750°C}} = \frac{p(H_2O)_{23°C} - \Delta x}{\Delta x\cdot\sqrt{p(O_2)}_{750°C}} = 6.08\times10^{+9}\ \text{bar}^{-\frac{1}{2}} \qquad \textbf{Eq. 4-19.}$$

The partial pressure of oxygen at 750°C is recorded at the outlet of the electrolytic cell. With this and by applying equation 4-20 the concentrations or partial pressures of all other gaseous species at that temperature can be calculated: Δx, $p(O_2)_{750°C}$ $p(H_2)_{750°C}$ and $p(H_2O)_{750°C}$. Since the temperature in the furnace is, however, different from the temperature of the oxygen pump, a new equilibration has to be considered, taking into account the further decomposition of water, e.g. at 1000°C:

$$K_{H_2O}(1000°C) = \frac{p(H_2O)_{1000°C}}{p(H_2)_{1000°C} \cdot \sqrt{p(O_2)_{1000°C}}}$$
$$= \frac{p(H_2O)_{750°C} - \Delta y}{\left(p(H_2)_{750°C} + \Delta y\right) \cdot \left(p(O_2)_{750°C} + 1/2\Delta y\right)} = 2.00 \times 10^{+7}\ \text{bar}^{-\frac{1}{2}} \qquad \textbf{Eq. 4-20.}$$

The unknown parameters $p(H_2)_{750°C}$ and $p(H_2O)_{750°C}$ are derived from equation 4-19 and can be inserted in equation 4-20. In consequence solving the latter equation of third degree results in the shift of the water gas equilibrium at elevated temperatures and finally the oxygen partial pressure $p(O_2)_{1000°C}$ inside the furnace can be estimated. Figure 4-11 shows the relationship between the values of the oxygen partial pressure measured in the exhaust coming out of the furnace by the oxygen sensor in comparison to the expected and calculated $p(O_2)$ values in the furnace at several annealing temperatures.

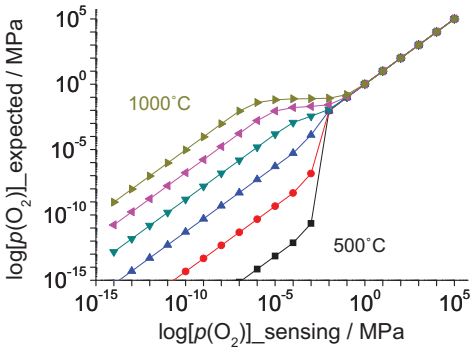

Fig. 4-11: Expected oxygen partial pressure in the furnace depending on temperature in the furnace. At lower $p(O_2)$, difference from the value of $p(O_2)$ sensor becomes prominent especially. Simulation was done between 500 – 1000˚C. Temperature step is 100K.

Because of Le Chatelier´s law gaseous phase is more stable at higher temperatures, leading to more decomposition of water. This results in lower equilibrium constant. Since the measured values of oxygen partial pressure are determined at 750°C by the sensor only at this furnace temperature the relation between the calculated and experimentally monitored data is linear. At higher temperatures the equilibrium in the furnace is shifted to the right side of equation 4-16 and according to this the measured $p(O_2)$ values are lower than the calculated ones. For lower temperatures the opposite holds true. This discrepancy occurs principally in the reducing regime. Above 10^{-7} MPa measured and calculated values are identical. In addition to this difficulty of determining experimentally the exact value of oxygen partial pressure in

the furnace a large gap at low temperatures between 10^{-12} and 10^{-2} MPa occurs at 500°C, as can be readily seen from figure 4-11.

A second obstacle in the precise determination of the oxygen partial pressure is the fact that especially in the intermediate range exact monitoring of the $p(O_2)$ by an external oxygen sensor on ZrO_2-basis is extremely problematic through the measured electromotive force (e.m.f.). Here the output voltage of the sensors results from the difference in the chemical potential of oxygen between the measured and reference gas. This potential difference is proportional to the gradient in concentration or partial pressure gradient of oxygen, and the electromotive force $E_{e.m.f.}$ can be expressed by the well-known Nernst equation:

$$E_{e.m.f.} = \frac{RT}{zF} \cdot \ln\left(\frac{p(O_2)_{reference}}{p(O_2)_{exhaust}}\right) \qquad \textbf{Eq. 4-21.}$$

In this relation R represents the gas constant, T the temperature of the sensor cell, z the ionic number involved in the charge transport and F the Faraday constant (9.65 $\times$ 10^4 A·s/mol). In the case of zirconia z corresponds to a value of 4 because per formula unit 2 oxygen ions O^{2-} convey the ionic transport. When $p(O_2)_{exhaust}$ changes continuously the e.m.f. should change linearly. It is often reported, however, that in the case of zirconia this linearity is not existing in the intermediate range of $p(O_2)$.[96] Both these problems make a reliable determination of $p(O_2)$ virtually impossible in the intermediate range and therefore conductivity data were simply omitted in this region.

4.7 Determination of ^{18}O diffusion profiles

Since the reoxidation process after sintering crucially determines the insulating characterisitics of grain boundaries in PTCR thermistors the oxygen penetration behavior has been studied in detail by investigating diffusion profiles of oxygen into the ceramics. An experimental technique commonly applied for such kind of measurements in perovskite-type oxides is the isotope exchange method combined with mass spectroscopy.[97-99] Generally $^{18}O_2$ isotope gas is used due to its chemical stability and high sensibility in mass spectroscopy compared to other isotopes, such as $^{17}O_2$. In situ exchange of oxygen ^{16}O from the perovskite lattice with ^{18}O from a surrounding gas atmosphere with a given volume concentration c_g of this isotope is carried out during annealing at elevated temperatures. Before this heat treatment samples were polished with 0.25 μm diamond paste until a shiny mirror surface was

obtained. This careful surface preparation is necessary in order to guarantee a precise analysis of the ^{18}O depth profile. All samples were tempered for two hours in a flowing gas mixture consisting of Ar and 20 vol.% of total O_2 ($^{16}O_2$:$^{18}O_2$ = 4:1). This oxygen concentration is equivalent to the oxygen content of air, the gas in which usually the ceramics are reoxidized during processing. Also the annealing time corresponds to the conditions of ceramic annealing. After the thermal treatment, typically carried out at temperatures between 700°C and 1000°C, the samples were analyzed with respect to the ^{18}O concentration depth profile from the surface into the interior by plasma secondary neutralized particle mass spectroscopy (Plasma-SNMS, INA-X, Specs GmbH, Germany). Oxygen diffusion profiles were determined using the concentration ratio of ^{18}O relative to ^{16}O. For this purpose the surface was sputtered with a plasma of Ar^+ ions. The released ionized secondary particles were neutralized and analyzed by mass spectroscopy. The sputtered area was approximately 3 mm in diameter and therefore significantly larger than the average grain size of the ceramics. The analyzed profiles therefore correspond to a superposition of grain-boundary and volume diffusion. A Dektak-profilometer was used to determine the depth of the sputtering crater. These measurements confirmed that the bottom of the crater was flat enough and that no selective sputtering occurred.

4.8 Optical characterization

In the course of the present study heavily donor-doped optically translucent La:$BaTiO_3$ ceramics have been successfully prepared for the first time. Although these ceramics do not show any PTCR-type behavior, but rather reveal semiconduction with a negative temperature coefficient (NTC) in the as sintered condition, it turned out that the exceptional optical properties, such as very high optical transmittance strongly depend on the defect chemistry. For this reason the optical characteristics have been studied in more detail. In particular the optical transmittance and the refractive index have been measured in dependence of the optical wavelength λ.

The transmittance is simply determined using a UV/VIS spectrometer (Lamda 950, Perkin Elmer, USA) as the ratio of light intensity I passing the sample relative to the original intensity I_0 that is detected without any sample in the light path. The transmittance is then defined as follows:

$$t = \frac{I}{I_0} \cdot 100\% \qquad \textbf{Eq. 4-22.}$$

The refractive index was measured using elipsometry (UVISEL system, Jobin Yvon, France). A schematic view of the experimental setup is shown in figure 4-12. Polarized light, with the oscillation plane of the electrical vector either perpendicular (s-polarized light) or parallel (p-polarized light) to the samples surface is irradiated onto the ceramic surface respectively. The reflected intensities I_s, and I_p are detected under a certain angle φ close to Brewer angle.

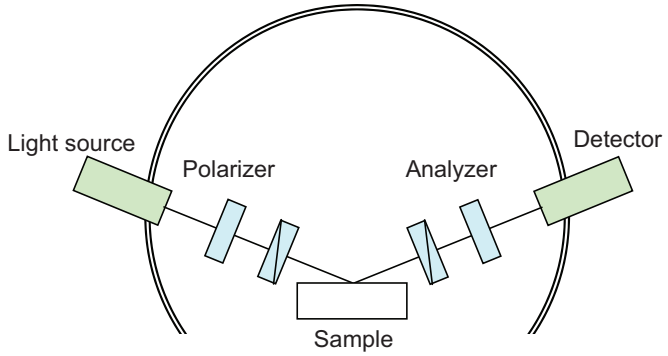

Fig. 4-12: Schematic image of ellipsometry.

The measurement variable is expressed by the following equation.

$$\rho = \frac{I_p}{I_s} \qquad \textbf{Eq. 4-23.}$$

Combining the results with an appropriate model (half sphere model) the real and imaginary parts of the refractive indices can be obtained.

Chapter 5

PTCR ceramics based on $BaTiO_3$ with BaO-excess

The following chapter describes and discusses experimental results obtained by impedance spectroscopy and the analysis of ^{18}O tracer diffusion profiles. The objective of these investigations is to reveal the microstructural and defect chemical mechanisms explaining the development of non-linear resistivity behavior in La-doped PTCR ceramics on $BaTiO_3$-basis sintered under reducing conditions. A particular focus of this study was placed on the role of the post-sintering reoxidation treatment. Impedance spectroscopy was employed to separate the different resistive contributions arising from the bulk phase, grain boundaries and external interfaces. As experimental parameters the amount of BaO-excess, the influence of the sample geometry and of the electrode metals used for the measurements have been systematically varied in order to obtain a detailed insight into the origin of the resistivity jump in these materials. Furthermore diffusion profiles of oxygen were examined in detail by Plasma-SNMS in order to understand which part the reoxidation treatment after sintering plays for the realization of the PTCR in $BaTiO_3$ ceramics with BaO-excess. Based on these findings a model based on defect chemistry is proposed. This model will be confirmed by the examination of the dependence of DC conductivity on $p(O_2)$ in chapter 6.

5.1 Microstructure, phase purity and crystallography

As presented in section 3.3 it is generally accepted that an electrically insulating layer at the grain boundaries is decisive for realizing the PTCR effect in $BaTiO_3$. The present part of this study focusses on the influence of BaO-excessive compositions on the materials behaviour. Since the solubility of BaO in $BaTiO_3$ is believed to be rather low (less than 100 ppm[100]), first the influence of the overstoichiometry on the microstructure, the phase purity and on the crystallography of the perovskite lattice have been investigated using SEM, HR-TEM and XRD in conjunction with Rietveld analysis. Figure 5-1 shows the fracture surfaces of La-doped (0.2 at.%) sintered

ceramics with a (Ba+La)/Ti ratio of up to $m = 1.05$ as they have been observed by SEM.

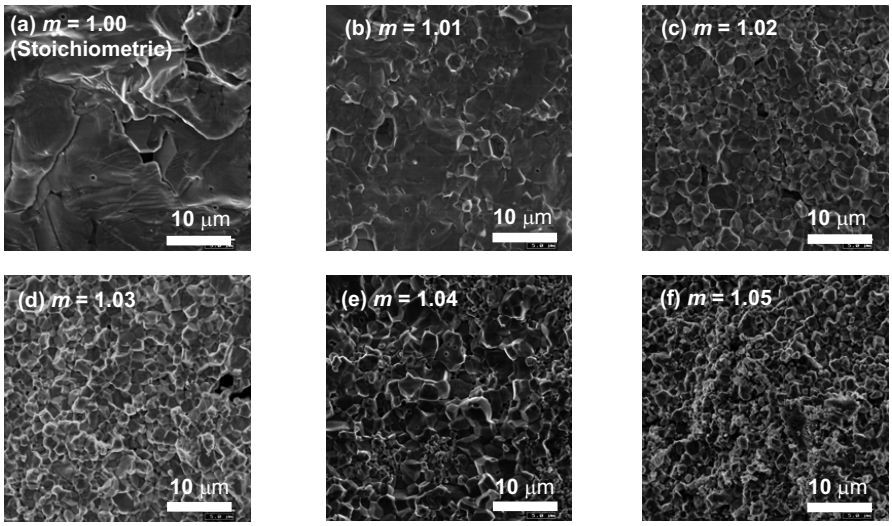

Fig. 5-1: Fracture surfaces of $(Ba_{m-0.002}La_{0.002})TiO_{3+\delta}$ ceramics with various BaO-excess ranging from $m = 1.00$ (stoichiometric composition) up to 1.05 (hyper-stoichiometric composition) sintered at 1300°C and $p(O_2) = 10^{-9}$ MPa.

The samples shown in figure 5-1 have all been electrically characterized by impedance spectroscopy and high temperature DC conductivity measurements (chapter 6). All these ceramics were sintered at 1300°C in reducing atmosphere using moist gas mixtures of Ar with 0.3 vol.% of H_2. The partial pressure of H_2O was kept constant at 2.8×10^{-3} MPa since the gas mixture was moisturized at a fixed temperature of 23°C. At sintering temperature the partial pressure of oxygen $p(O_2)$ amounts to 10^{-9} MPa, a value that is more than one order of magnitude below the Ni/NiO equilibrium ($p_{O_2}^{Ni/NiO}(1300°C) = 10^{-7.6}\,MPa$). These conditions correspond to the processing environment needed for preventing the oxidation of inner Ni electrodes during the consolidation of multilayer PTCR. The densities of all samples investigated were confirmed to be above 96.9% of the theoretical value using the Archimedes method and thus no open porosity is expected to be contained.

With increasing amount of BaO-excess the average grain size of the ceramics gradually decreases from several tens of micrometers down to the micrometer or even submicrometer level. It is well-known that barium oxide inhibits grain growth in $BaTiO_3$-based ceramics during sintering, through the formation of secondary phases such as barium orthotitanate (Ba_2TiO_4).[101] Besides this refinement in grain size,

figure 5-1 reveals that upon the addition of BaO the fracture mode changes from intragranular to intergranular crack growth. This observation possibly indicates that the bonding strength of the grain boundaries between adjacent crystallites is reduced when BaO is added. A statistical quantification of the average grain size has been performed on polished microsections, etched in an aqueous solution of HCl (30 vol.%) using a computer assisted method. The results are shown in figure 5-2 and confirm that excessive BaO drastically decreases the mean grain size of the ceramics considered here. The grain growth behavior of donor doped $BaTiO_3$ has been intensively studied by Drofenik. The author suggests that the exaggerated grain growth of donor-doped $BaTiO_3$ is related to the release of oxygen when the donor ions are incorporated into the perovskite lattice during sintering.[102] For this reason possibly the hampering of grain growth is responsible for incomplete dissolution of the added La_2O_3 in the perovskite lattice. In other words, eventually the donor ion concentration inside the grains could be lower than the expected theoretical value (0.2 at.%). From the analytical point of view the detection of such subtle compositional variations is problematic even using modern spectroscopic methods. Also the inspection of the exact lattice parameters combined Rietveld refinement of individual phases upon La-addition does not allow a reliable evaluation (see figure 5-3 (b)). Possibly the influence of the conductivity behavior of the perovskite matrix may give the answer to this question. This discussion is taken up again in section 5.2.2.

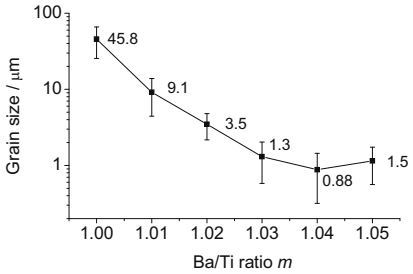

Fig. 5-2:
Average grain size in dependence of BaO-excess in $(Ba_{m\text{-}0.002}La_{0.002})TiO_{3+\delta}$ ceramics sintered at 1300°C and $p(O_2) = 10^{-9}$ MPa. The error bars show the standard deviation.

Phase purity, crystallinity and the lattice parameter of the as sintered $BaTiO_3$-based thermistor ceramics were investigated in dependence of their BaO-excess using XRD in conjunction with an assessment by Rietveld analysis. Figure 5-3 shows the corresponding experimentally recorded diffraction patterns and the results regarding the lattice parameters *a* and *c* of the $BaTiO_3$ matrix.

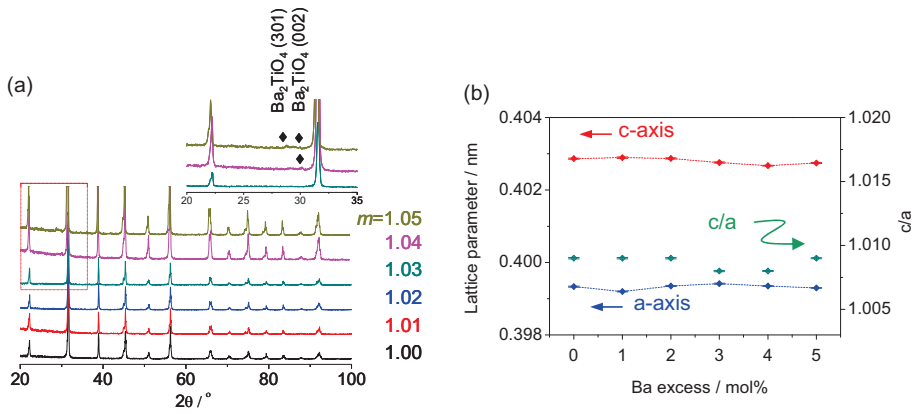

Fig. 5-3: (a) Experimental XRD patterns recorded for barium titanate $(Ba_{m-0.002}La_{0.002})TiO_{3+\delta}$ ceramics with various (Ba+La)/Ti ratios *m* up to 1.05 sintered at 1300°C and $p(O_2) = 10^{-9}$ MPa. The inset shows a magnified view on the range of double Bragg angles between 20° and 35° and reveals the presence of barium orthotitanate as a secondary phase (♦). (b) Dependence of the lattice parameter *a* and *c* and tetragonality *c*/*a* from BaO-excess obtained by Rietveld refinements.

All major diffraction peaks are related to the tetragonal polymorph of $BaTiO_3$. Some minor reflections arising from the secondary phase barium orthotitanate Ba_2TiO_4[103] can only be detected for compositions with a (Ba+La)/Ti ratio *m* above 1.04. The formation of this secondary phase is not surprising taking into account the large amount of excessive BaO added. Other impurities, such as the fresnoite type phases from the system $BaO\text{-}TiO_2\text{-}SiO_2$[104,105] formed through the addition of SiO_2 as sintering flux were expected to be present but could not be found by XRD, probably because their volume fraction is below the detection limit of the goniometer. From all these results it can be concluded that the solubility of BaO in $BaTiO_3$ must be well below a (Ba+La)/Ti ratio *m* of 1.04.

Figure 5-3 (b) confirms that the incorporation of BaO into the bulk of the $BaTiO_3$ crystallites is very limited; both lattice parameters *a* and *c* are virtually independent of the BaO-excess. Consequently also the tetragonality *a*/*c* remains nearly constant upon BaO-addition.

A more detailed examination of the phase composition of two selected thermistor ceramics with 3 and 5 mol% of BaO-excess respectively ($m = 1.03$ and $m = 1.05$) was carried out by TEM in combination with EDX. Figure 4-4 represents the corresponding bright field images taken. Even up to $m = 1.05$ no secondary phase enriched along the grain boundaries that might affect the PTCR-related behavior could be identified. The core of the grain boundaries seems to be crystallographically

sharp and clear. Its width is estimated to be around less than 2 nm, a value that is close to the one observed for similar material systems (acceptor-doped $Sr(Ti_{0.998}Mn_{0.002})_{1.01}O_{3+\delta}$).[106] Inside the grains ferroelectric domains can be recognized very clearly. The average grain sizes observed by TEM correspond to the results obtained by SEM (figure 5-2).

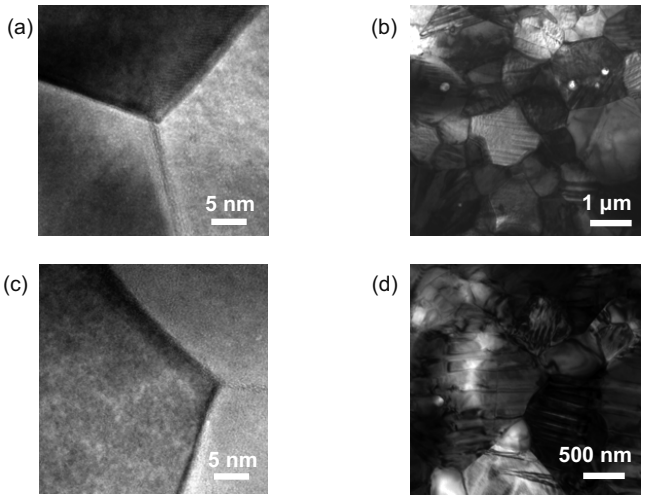

Fig. 5-4: Bright field TEM images showing the microstructures of $(Ba_{m\text{-}0.002}La_{0.002})TiO_{3+\delta}$ sintered at 1300°C and $p(O_2) = 10^{-9}$ MPa.
(a) and (b): $m = 1.03$.
(c) and (d): $m = 1.05$.

Secondary phases could be observed by TEM only as discrete inclusions or precipitates, as shown in figure 5-5 (a). They were found to be preferentially enriched in SiO_2 and mostly located at the triple points of grain boundaries of surrounding $BaTiO_3$ matrix grains. Local chemical analysis by EDX revealed that the main constituents of these inclusions were the elements Ba, Ti, Si and O. Therefore they are believed to act as BaO-sink during cooling after sintering. SiO_2 was added on purpose, because it acts as a sintering aid. This is because the eutectic point in the ternary system $BaO\text{-}TiO_2\text{-}SiO_2$ is as low as 1195 ± 5°C and therefore a liquid phase supports densification during sintering at 1300°C.

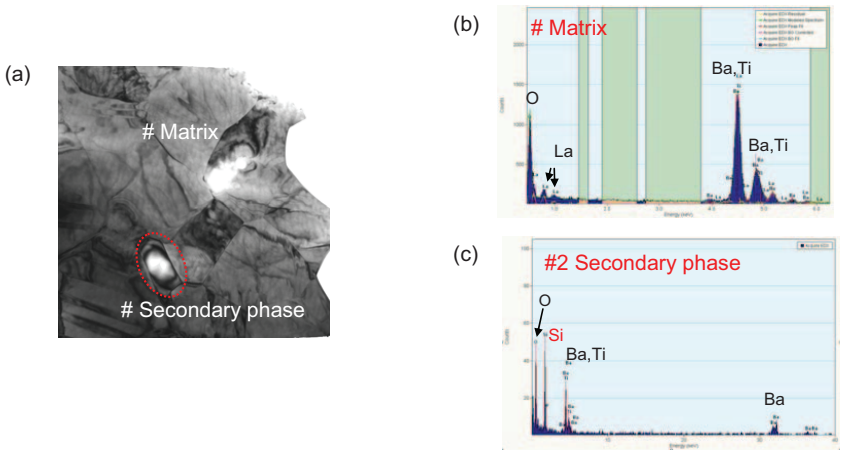

Fig. 5-5: (a) Bright field TEM images showing the microstructure of a $(Ba_{1.028}La_{0.002})TiO_{3+\delta}$ (m = 1.03) ceramic sintered at 1300°C and $p(O_2)$= 10^{-9} MPa.
(b) EDX spectrum of a $BaTiO_3$ matrix grain.
(c) EDX spectrum of a secondary phase inclusion.

When this liquid phase solidifies it apparently withdraws into the triple points of the grain boundaries in order to reduce surface energy and dissolves residual Ba- and Ti-oxide. The exact chemical composition of the secondary inclusions has not been verified. Most probably, however, these impurities consists of $Ba_2TiSi_2O_8$ (fresnoite) or $BaTiSiO_5$.[104]

Finally it can be concluded that all ceramics considered in this part of the work consist of tetragonal $BaTiO_3$ and secondary phases such as barium orthotitanate or silicates that partly dissolve also BaO and TiO_2. All these secondary phases preferentially crystallize as bulky inclusions in the triple points of the microstructure. No impurity phases wetting the grain boundaries and therefore possibly affecting the electric response of these interfaces could be identified. Still however the possibility of the formation of extended defects upon addition of excessive BaO has to be considered.

Extended defects were searched by EBSD and HR-TEM. Extendted defects are often observed in the same perovskite-type $SrTiO_3$,[107-109] where they have a structure classified as the rock-salt type. Little is however reported on $BaTiO_3$.[110] Figure 5-6 shows a SEM picture and the corresponding EBSD image for a hyper-stoichiometric sample, m = 1.05. The EBSD image shows that there is no distortion in the grain boundaries or the matrix. Further investigation was conducted by HR-TEM.

The pictures in the last column of figure 5-6 show high-resolution TEM images for the secondary phase, for the $BaTiO_3$ matrix and for the grain boundary (in the order from the top to the bottom).

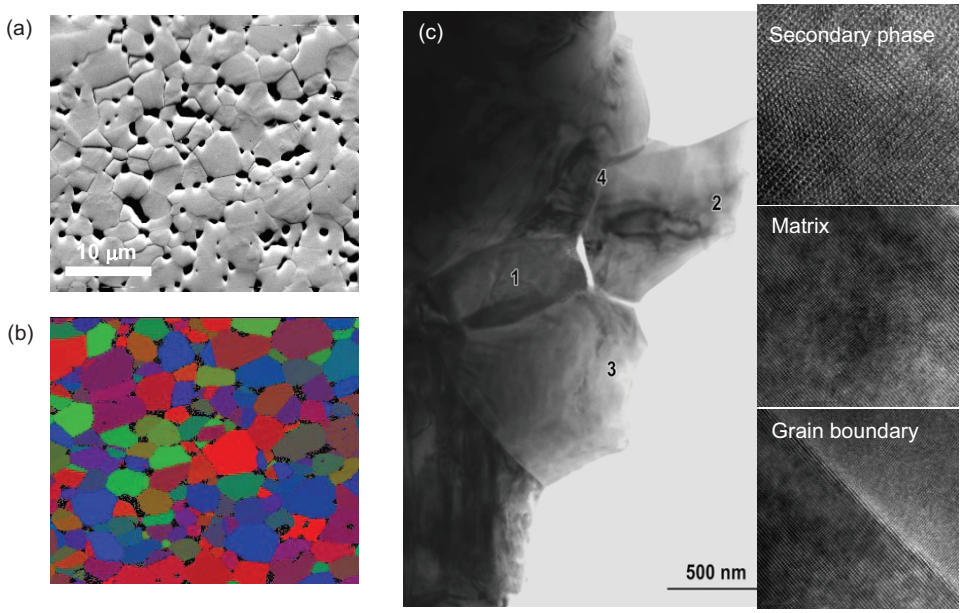

Fig. 5-6: (a) SEM and (b) corresponding EBSD images. (c) HR-TEM analysis of the composition $(Ba_{1.048}La_{0.002})TiO_{3+\delta}$ (m = 1.05) for the secondary phase (marked by 1, top picture on the right), $BaTiO_3$ matrix (marked by 2 and 3, middle picture on the right) and grain boundary (marked by 4, bottom picture on the right).

The HR-TEM picture for the secondary phase shows a periodric alignment of atoms, indicating that the phase is crystalline. The bottom picture shows a misalignment of the atoms at the grain boundary. However there was no extended defects detected in the form of layered structures as far as the greatest possible effort was made. The crystallographic structure at the grain boundary region is quite similar to that observed in the grains. Even if no extended defects could be found there still is the possibility that they are involved in the hyper-stoichiometric $BaTiO_3$ system. However this thesis proceeds the discussion based on the point defect chemistry hereafter. Further investigations are under way using STEM-EDX analysis in order to clarify the compositional distribution at the grain boundary. Since grain growth is inhibited by BaO-excess, it is very probable that enhanced concentration of BaO exist at the grain boundary region.

5.2 Origin of the PTCR effect in view of impedance spectroscopy

As pointed out in section 4.5 impedance spectroscopy represents a valuable non-destructive electric characterization technique that allows to determine different capacitive or resistive components in polycrystalline electronic materials, such as the thermistor ceramics on $BaTiO_3$-basis considered in this work. Compared to DC measurements, which only result in global information on the electric properties of the entire material, impedance spectroscopy provides the specific contributions from the bulk, the grain boundaries or external interfaces, if they behave electrically different. Although recording experimental data is quite straightforward, the interpretation of the obtained results is not always so easy. This is because generally one and the same given impedance spectrum can be modeled by a large multitude of equivalent circuits. In order to correctly identify different relaxation processes and to precisely correlate them to the microstructure or morphology of the material many aspects that delicately affect the experimental spectrum have to be critically taken into account during evaluation. These include effects arising from the electrode-ceramic interfaces or from the sample geometry and finally artifacts originating from the connection of the sample to the impedance analyzer.

In this part the influence of the BaO-content, of temperature, of the work function of the electrode metal, of sample thickness and of additional subsequent annealing after the impedance measurement have been examined systematically. All experimental data were analyzed by appropriate equivalent circuits, as described in sections 4.5.2 and 4.5.3.

5.2.1 Influence of BaO-excess on the total resistivity

For all material compositions studied in the present work no PTCR effect could be observed directly after reducing sintering without any post-sintering annealing. The desired non-linearity of resistivity developed when the ceramic pellets were reoxidized in air (typically two hours at 700°C). Figure 5.7 represents the PTCR curves showing the temperature dependence of resistivity for such $BaTiO_3$ ceramics (samples B-1 to B-6 in table 4.1) with a BaO-excess ranging from $m = 1.00$ to 1.05. The resistivity values were obtained from the total impedance and the respective sample geometries, like thickness and electrode area and correspond to the ones that would have been obtained by DC measurements. For every point shown here a

full impedance spectrum (not shown) has been measured for later analysis using an appropriate equivalent circuit. These results are presented in section 5.2.2.

As can be recognized from figure 5.7 the stoichiometric composition did not reveal any PTCR-type behavior. Here the resistivity was almost independent of temperature and amounts to approximately 2 Ω·cm, the lowest value reported for semiconducting $BaTiO_3$.[18] A jump in resistivity only occurred for compositions with *m* larger than 1.02. With increasing *m* the height of this jump and the values of cold resistivity of the ceramics became larger. The later effect can be understood in terms of smaller grain sizes when *m* increases. Since the grain boundaries are electrically insulating in these compositions, smaller grains imply a larger volume fraction of these resistive interfaces and in consequence the total resistivity of the ceramic pellet increases. A more detailed analysis of the grain boundary contribution to resistance is given in the following sections. A very distinct PTCR jump extending over at least two orders of magnitude in resistivity was obtained when *m* exceeded the value of 1.02. The largest resistive increase upon heating above the Curie temperature T_C develops for the case *m* = 1.03, reaching more than 3 orders of magnitude in total resistivity.

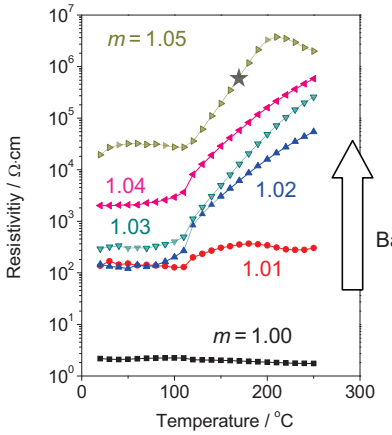

Fig. 5-7:
Temperature dependence of resistivity determined from the total impedance of $(Ba_{m-0.002}La_{0.002})TiO_{3+\delta}$ with *m* ranging between 1.00 and 1.05. The marked measurement at 160°C and *m* = 1.05 (★) is also represented as entire Cole-Cole diagram in figure 5-8.

5.2.2 Impedance spectra and modeled equivalent circuits

5.2.2.1 Resistive components

Figure 5-8 (a) exemplarily represents the Cole-Cole plot obtained for $(Ba_{1.048}La_{0.002})TiO_{3+\delta}$ (*m* = 1.05) measured at 160°C, a temperature situated almost exactly in the centre of the PTCR jump of this material. This measurement corresponds to the marked data point in figure 5-6 (★). It illustrates the frequency

response locus of the real part Z'_{total} and the imaginary part Z''_{total} of the electric impedance in the complex plane for this measurement. As can readily be recognized this specific spectrum is composed of three contributions that appear as separated semicircles in the complex plane. In other words this means that three parallel resistive and capacitive elements with different time constants τ are involved and contribute to the total impedance. In the course of optimizing the fitting of the respective experimental data with an appropriate equivalent circuit, it turned out, that instead of an ideal capacitance *C* a constant phase element Z_{CPE} (unit: F^n/Ω^{1-n}) had to be implemented in order to achieve a satisfactory model. The mathematical details of the constant phase element analysis are treated in section 4.5.3.4. The reason why an idealized capacitive element could not be used, is that often in polycrystalline systems local fluctuations in dielectric properties occur. In consequence the corresponding dielectric relaxation in the Cole-Cole diagram is not represented by an ideal semicircle anymore, but rather by a depressed one. The constant phase element Z_{CPE} takes mathematically into account these fluctuations and the depression of the corresponding semicircle. The equivalent circuit used to fit the experimental spectrum in figure 5-8 (a) is represented in figure 5-8 (b). It contains besides the three mentioned RZ_{CPE} elements one resistor R_1 and one inductor L_1. The inductor was included in order to account for the effect of connecting leads between the impedance analyzer and the ceramic sample.

Theoretically and practically the appearance of a total number of three relaxation processes in the impedance spectra of figure 5-8 is quite surprising. Measurements by Saburi[111] regarding the frequency dependence of the dielectric constant and of resistivity of La-doped stoichiometric semiconducting $BaTiO_3$ only reveal one single *RC* element. Work from Sinclair et al.[112] reports the presence of two resistive components above the Curie temperature T_C in classical $BaTiO_3$-based PTCR compositions, which are attributed to the responses of the grain boundary core and of the space charge layer respectively. It should be noted, however, that the distinction between these different relaxation processes could only be carried out successfully by analyzing the frequency dependence of the electric modulus *M*. In contrast to the present study Sinclair et al. could not distinguish more than one distinct and individual semicircle in the corresponding Cole-Cole diagrams.

The impedance spectra regarding BaO-rich PTCR ceramics on $BaTiO_3$-basis on the contrary show unambiguously three distinct and different relaxation phenomena,

through the presence of three separated semicircular arcs in the Cole-Cole diagram. In the following the different elements of the equivalent circuit are referred to as $RZ_{CPE,2}$, $RZ_{CPE,3}$ etc. in the order from higher frequencies to lower ones, for the case that the impedance spectra can be divided into several such components.

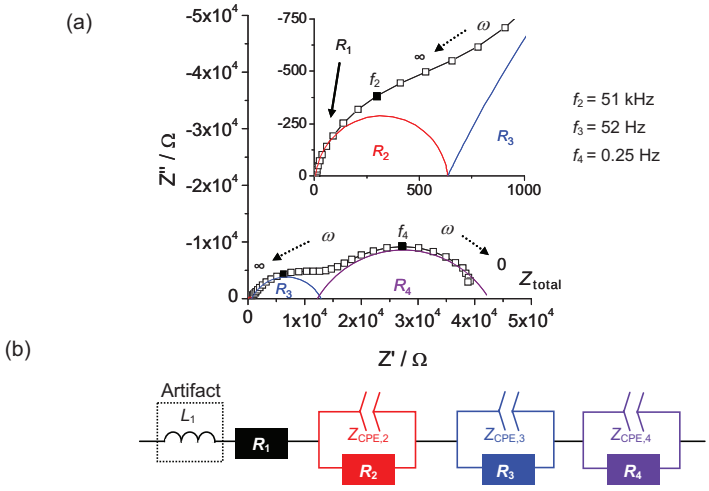

Fig. 5-8: (a) Cole-Cole diagram representing the impedance spectrum measured for $(Ba_{1.048}La_{0.002})TiO_{3+\delta}$ (m = 1.05) at 160°C. The inset shows the lower impedance part at high measuring frequencies which is not visible in the main part of the figure: this magnification reveals the contribution of a small resistive element R_2. The black open square dots represent the raw data and the black line is the total fitting results. Other colored lines are the fitting result for individual components. (b) Equivalent circuit used to fit the experimental data of figure 5-8 (a). Z_{CPE} represents a constant phase element.

Analogously pure resistances are referred to as R_1, R_2, R_3 and R_4 and capacitances as C_1, C_2, C_3 and C_4. As can be recognized from figure 5-8 the component $RZ_{CPE,4}$ provides the lowest angular relaxation frequency ω_{max} but the largest resistive contribution above T_C, which is decisive for the PTCR effect.

The analysis described in detail above has been applied to all impedance spectra measured in order to extract the temperature dependence of the resistive and capacitive components for every RZ_{CPE} element. Figure 5-9 shows the result obtained for the resistances of the components observed in

(a) $(Ba_{1.008}La_{0.002})TiO_{3+\delta}$ (m = 1.01),

(b) $(Ba_{1.028}La_{0.002})TiO_{3+\delta}$ (m = 1.03) and

(c) $(Ba_{1.048}La_{0.002})TiO_{3+\delta}$ (m = 1.05),

respectively.

In the case of $m = 1.01$ the PTCR effect is very small and seems to be dominated by the element R_2. Above the Curie temperature resistance only rises by a factor of 6. R_1 is thought to be the contribution of the semiconducting interior of La-doped $BaTiO_3$ grains and R_2 is attributed to the insulating grain boundaries.

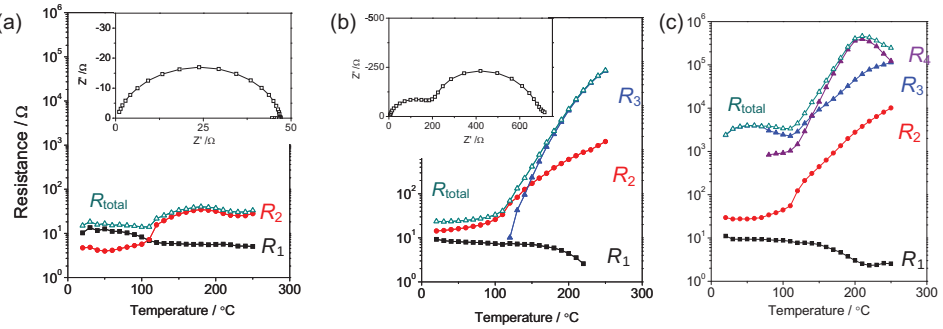

Fig. 5-9: Temperature dependence of the resistive components R_1, R_2, R_3 and R_4 for (a) $m = 1.01$, (b) $m = 1.03$ and (c) $m = 1.05$. The insets in (a) and (b) show two Cole-Cole diagrams taken at 160°C respectively.

This assumption is based on the rather weak temperature dependence of R_1, revealing a slight decrease of resistance upon heating, a characteristics that is expected for an n-type semiconductor. For the two cases of a higher BaO-excess m = 1.03 (figure 4-8 (b)) and m = 1.05 (figure 4-8 (c)) R_1 shows a similar behavior respectively. All R_1 elements are therefore concluded to originate from the bulk interior. This conclusion is reasonable taking into account that no corresponding capacitive element appears. The values for R_1 are taken from the intercept of the semicircular arc representing $RZ_{CPE,2}$ with the axis of the real part of impedance at frequencies tending to infinity. From these values the resistivity of the grains ρ_{grain} at room temperature (20°C) can be estimated provided that the thickness of the grain boundaries $\delta_{g.b.}$ is negglegible compared to the average grain diameter D ($\delta_{g.b}$ << D) to be approximately 100 Ω·cm. In this estimation the mobility of the electrons in $BaTiO_3$ was assumed to be 0.5 $cm^2/V{\cdot}s$.[39] This estimated resistivity is an order of magnitude larger than the value that would be expected for donor-doped $BaTiO_3$ with 0.2 mol% La addition. A possible explanation for this enhanced resistivity could be an incomplete incorporation of La into the perovskite lattice if m > 1.01 due to the grain growth inhibition.

Compared to the case of low BaO-excess (m = 1.01), where only the grain boundaries seem to contribute to the PTCR effect, higher values of m above 1.03

reveal at least one more resistive component. For 3 mol% of BaO-excess a third resistive components R_3 which almost dominates the temperature characterisitics of the overall resistance appears. According to equation 5.1 a generalized temperature coefficient of the high temperature regime above T_C can be defined for a given temperature interval between T_1 and T_2:

$$\alpha_{T_2\text{-}T_1} = \ln 10 \cdot \frac{\log\left(R_{T_2}/R_{T_1}\right)}{T_2 - T_1} \qquad \textbf{Eq. 5-1.}$$

Comparing the steepness of the resistance increase upon heating for R_2 and R_3 for this composition (m = 1.03) shows that the PTCR coefficient $\alpha_{250°C\text{-}150°C}$ for R_3 (5.6) is much larger than for R_2 (2.2). Since a PTCR coefficient as large as possible is desired for high performing thermistors the origin of this highly insulating resistive component is of high scientific and technological interest in order to explain PTCR mechanisms in reoxidized $BaTiO_3$ with BaO-excess. This is the subject of the following sections of this chapter. Figure 5-10 illustrates the case of 5 mol% BaO-excess.

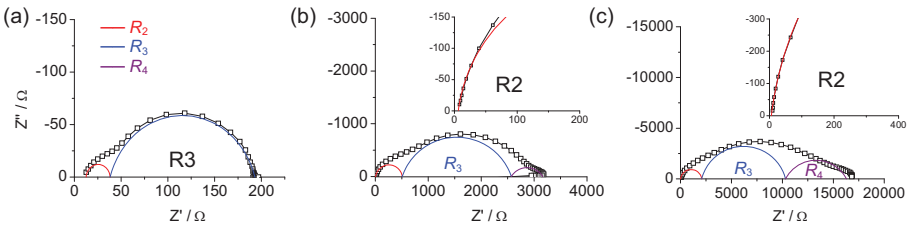

Fig. 5-10: Cole-Cole diagrams for the composition $(Ba_{1.048}La_{0.002})TiO_{3+\delta}$ at:
(a) 20°C, (b) 150°C and (c) 200°C.
The open symbols represent experimental data and the line the calculated spectrum based on the respective equivalent circuit. The insets in (b) and (c) show a magnified view on the high frequency region.

Here three Cole-Cole diagrams for three different temperatures of 20, 150 and 200°C are represented. Since the results shown here have been obtained from another specimen compared to the data shown in figure 5-9, the absolute values of resistance are different. However the tendency observed in both experiments was the same. At room temperature (20°C) the total impedance is determined by a bulk contribution R_1 and two other resistive components R_2 and R_3 that also appeared in the ceramics with m = 1.03. Above 150°C a fourth impedance element R_4 comes up.

At rather high temperatures, e.g. 200°C this fourth component is again dominating the PTCR effect, because R_4 becomes much larger than R_3.
Similar as in the case of R_3 the origin of R_4 is inspected in more detail in the following sections.

5.2.2.2 Capacitive components

As already mentioned above, only the three resistive elements R_2, R_3 and R_4 had a capacitive counterpart C_2, C_3 or C_4 within their respective equivalent circuits. These corresponding representative capacitance values C were calculated from the CPE-parameters and resistance using equation 5-2 (fundamentals on CPE are given in section 4.5.3.4):[94]

$$C = \frac{(R \cdot Q)^{\frac{1}{n}}}{R} \qquad \textbf{Eq. 5-2.}$$

Figure 5-11 shows the temperature dependence of the capacitance values and their reciprocal values. According to section 3.1 and equation 3-2 the reciprocal values of capacitance should follow a linear relationship with temperature if the temperature characteristics of the dielectric permittivity follows the Curie-Weiss law. C_2 revealed the smallest capacitance in comparison to all elements and was in the order of 0.1 nF. This component clearly follows the Curie-Weiss law and the corresponding critical temperature θ_C was determined to be 52°C. Since the critical temperature θ_C is usually smaller than the Curie temperature T_C, as it can be determined by thermal analysis,[74] it is reasonable to assume that C_2 is intrinsically related to the ferroelectricity of the perovskite phase $BaTiO_3$. This is a further confirmation that apparently the element RC_2 is related to the grain boundaries of the polycrystalline ceramics. The trace of the reciprocal values of C_3 (order of 100 nF) and C_4 (order of 10 μF) show some deviation from the Curie-Weiss behavior. Whereas $1/C_3$ still shows somehow a similar tendency as $1/C_2$ versus temperature the fourth component $1/C_4$ definitely does not follow the Curie-Weiss law. Therefore at least R_4 and C_4 may result from extrinsic effects such as interface effects between the ceramics and metal electrodes. This hypothesis is examined in more detail in the next section 5.2.3.

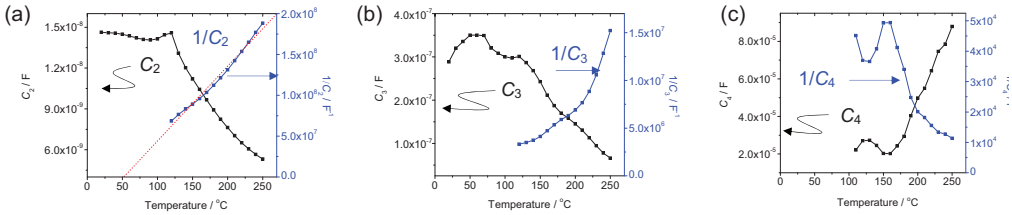

Fig. 5-11: Temperature dependence of the capacitance (black curves) and the reciprocal capacitance (blue curves) for the elements (a) C_2, (b) C_3 and (c) C_4 in $(Ba_{1.048}La_{0.002})TiO_{3+\delta}$.

5.2.3 Influences of the electrode-ceramic interface

In order to clarify how the interfaces formed by the metallic electrodes on the surface of the ceramic material influence the temperature characteristic of resistance, impedance spectra in the temperature range between 20°C and 250°C have been recorded and analyzed according to the equivalent circuit model of section 5.2.2 for metals with different work function. Since the ceramic composition $(Ba_{1.048}La_{0.002})TiO_{3+\delta}$ included all four resistive or capacitive contributions observed so far in this work a sample with a BaO-excess of 5 mol% was selected for this investigation. Table 5-1 gives an overview on the different metallic materials used for metallization together with the values of their work functions.

	W_M [eV]	Metallization technique
In-Ga alloy	4.09 – 4.32	Painting
Ti	4.33	Sputtering
Ag	4.52 – 4.74	Evaporating
Ni	5.04 – 5.34	Sputtering

Tab. 5-1: Different metallic materials used as electrodes with their work function[113] and the respective technique used for metallization. The eutectic In-Ga alloy used contained 16.5 at.% In.

As outlined above the contact resistance between the electrodes and the ceramic surface could be one possibility explaining the observed surface effects. This contact resistance of a semiconductor to a metal is strongly dependent on the work function W_M of the respective metal and the corresponding value for the semiconductor W_S. If W_M is larger than W_S, as shown schematically in figure 5-12 (a), the interface between metal and semiconductor is non-ohmic due to the insulating Schottky barrier

formed. In the opposite case, which is illustrated in figure 5-12 (b), the contact is ohmic and electrons can be directly transferred from the semiconductor into the metal. Referring to table 5-1 again, it is evident that the eutectic In-Ga alloy that melts at 15.5°C and reveals the lowest work function of all four metallic systems presented here results in an ohmic contact with the n-type semiconductor $BaTiO_3$.[114]

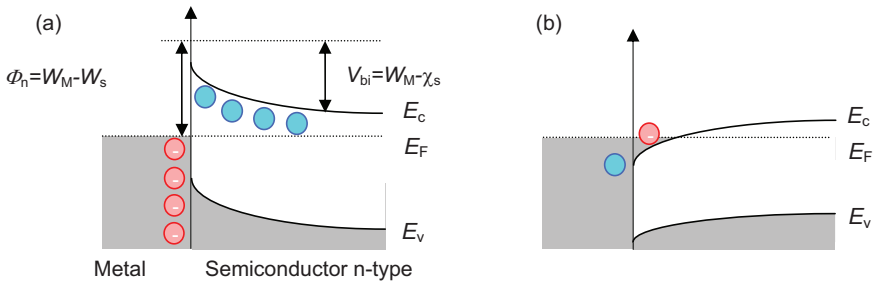

Fig. 5-12: Schematic illustration of the electronic band diagram of an interface between a metal electrode (left) and a n-type semiconductor (right).
(a) Schottky contact with $W_M > W_S$ and (b) Ohmic contact with $W_M < W_S$.
E_C represents the energy level of the conduction band, E_V that of the valence band, E_F is the Fermi level, χ_S the electron affinity, Φ_n the Schottky barrier height and V_{bi} the built-in potential.

The different metals listed in table 5-1 are ordered with increasing work function. Therefore it can be expected that the variation of the electrodes in the order presented in table 5-1 leads to an increasing tendency towards a non-ohmic Schottky type barrier. Ag electrodes are well known to form a Schottky-type contact on $BaTiO_3$. Ni, is somehow an exception in this list. Although Ni has a deeper work function than Ag it is often used as ohmic contact on barium titanate. This is because Ni is easily oxidized by gettering oxygen from $BaTiO_3$ resulting in the reduction to $BaTiO_{3-\delta}$ and the generation of abundant free electrons compensating the oxygen vacancies formed close to the metal-ceramic interface. These additional free electrons lower the height and reduce the thickness of the Schottky barrier. In consequence electron passing the barrier through tunneling is facilitated.

Figure 5-13 represents the results obtained for the temperature dependence of the resistive components R_2, R_3 and R_4 measured by impedance spectroscopy using the four different metallic electrodes presented in table 5-1: a eutectic In-Ga alloy, pure Ti, pure Ag and pure Ni. In order to prevent oxidation Ti and Ni electrodes were all covered by a thin Pt cap electrode. These measurements clearly prove that all three temperature characteristics of R_2, R_3 and R_4 are not systematically affected by the

type of metallic electrode and independent within the range of experimental errors from the work function W_M. Even with the use of Ag which is known to generate non-ohmic contacts on $BaTiO_3$ the temperature dependence of all three resistive components could be reproduced, as it was determined with the low melting eutectic In-Ga alloy. Therefore it must be concluded that all resistive elements involved in the PTCR effect of BaO-rich, La-doped thermistor ceramics on $BaTiO_3$-basis which do not follow the Curie-Weiss law (section 5.2.2.2) do not originate from a contact resistance at the interface but rather from the ceramic material itself.

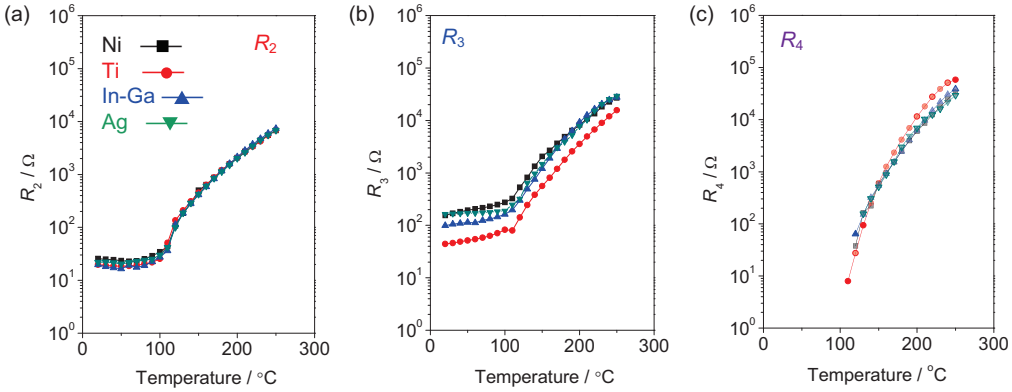

Fig. 5-13: Temperature dependence of different resistive components in $(Ba_{1.048}La_{0.002})TiO_{3+\delta}$ (m = 1.05) measured by impedance spectroscopy using different metallic electrodes: Ni, Ti, In-Ga alloy and Ag: (a) R_2, (b) R_3 and (c) R_4.

The experimental evidence from figure 5-13 confirms that the contribution R_2 must be attributed to the effect of insulating grain boundaries and implies that the elements R_3 and R_4 are also related to the ceramic. Nevertheless the temperature dependence of C_2 was investigated for the four different metallic electrodes applied (not shown here). It is not surprising to recognize that in all four cases studied the Curie-Weiss law applies.

5.2.4 Variation of sample geometry

As shown in the previous sections 5.2.2 and 5.2.3 the strong PTCR effect in reduction resistant La-doped $BaTiO_3$ with BaO-excess does not rely only on one single grain boundary contribution as in the case of conventional compositions that are usually sintered in oxidizing conditions. The situation in the present material system seems to be more complex. The investigations described in section 5.2.3

clearly proved that the effects observed here are inherent to the ceramic material and are not related to contact resistances at the ceramic-electrode interface. In order to clarify the origin of the two additional resistive elements which strongly affect the insulating behavior above the Curie temperature T_C the question whether these elements are homogeneously distributed over the entire sintered ceramic pellet or not must be addressed. The objective was to study whether possibly compositional gradients, for instance towards the surface play any significant role. In the case that the distribution is homogeneous over the whole volume the change of the geometry of the sample to be measured would also affect the magnitude of these resistive and capacitive contributions. For the occurrence of a volumetric effect a reduction of the thickness to half of its initial value would then, as outlined in table 5-2, result in a corresponding decrease of resistance to half of the original value. The capacitance is expected to be double as large as before. If however a surface effect is responsible for the yet not understood resistive and capacitive elements, then both values or resistance and capacitance should remain unchanged. The corresponding relaxation time τ should also remain unaffected, since it is geometry independent, as shown in equation 5-3.

	Bulk effect		**Interface effect**	
Thickness	Resistance	Capacitance	Resistance	Capacitance
d	R_{Bulk}	C_{Bulk}	$R_{Int.}$	$C_{Int.}$
***d*/2**	$R_{Bulk}/2$	$2 \cdot C_{Bulk}$		

Tab. 5-2: Influence of the sample geometry on the response in impedance.

$$\tau = R \cdot C = \frac{R}{2} \cdot (2C) = \rho \cdot \varepsilon_r \cdot \varepsilon_0 \qquad \textbf{Eq. 5-3.}$$

The expected change of the corresponding impedance spectra is illustrated in figure 5-14 which shows simulated Cole-Cole diagrams.

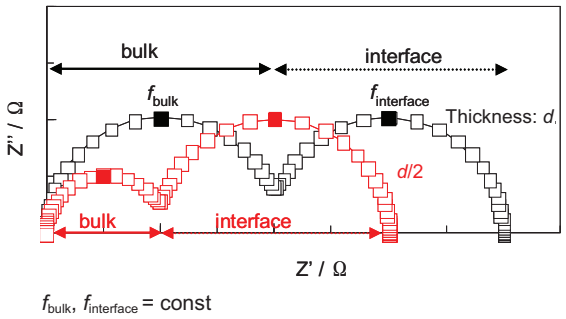

Fig. 5-14: Variation of volumetric and superficial impedance upon reduction of the sample thickness.

Figure 5-15 shows the temperature dependence of the total resistance and the resistive elements R_1, R_2 and R_3 for two measurements performed on one and the same ceramic pellet with the composition $(Ba_{1.018}La_{0.002})TiO_{3+\delta}$ (m = 1.02): (a) in the as annealed condition and (b) after grinding off the surfaces on both sides with SiC

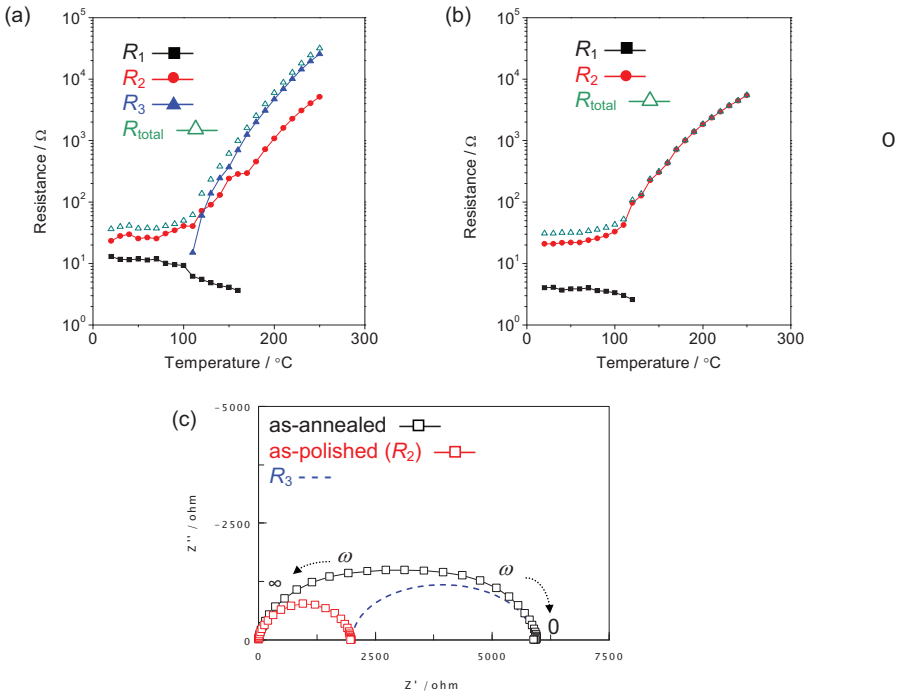

Fig. 5-15: Temperature dependence of the total resistance R_{total} and the resistive elements R_1, R_2 and R_3 for the composition $(Ba_{1.028}La_{0.002})TiO_{3+\delta}$ (m = 1.03):
(a) after post-sintering annealing, (b) after subsequent surface grinding. Part (c) shows a corresponding impedance spectrum recorded at 200°C.

sandpaper resulting in a reduction of the thickness by approximately 10% (Δd = 300 μm). Two impedance spectra recorded at 200°C for both these conditions are included in figure 5-15 (c). After the post-sintering annealing treatment the total resistance is mainly determined by the element R_3. This resistive contribution, however, completely vanishes after grinding off the surface layer on both sides of this sample and the total resistance is then predominantly controlled by R_2, which was assigned to the grain boundaries in the interior of the ceramic. Interestingly the magnitude of R_3 is almost one order of magnitude larger than this grain boundary resistance. From this experiment it can be directly concluded that the large resistive contribution must be related to a modification of the ceramic surface. Any potential secondary phases wetting some parts of the grain boundary network in the interior could be excluded since no such internal impurity layers could be found by TEM observation (section 5.1). The very steep increase in resistance upon heating, expressed by the large PTCR coefficient $\alpha_{250°C\text{-}150°C}$ of 5.6, originates from microstructural features that are not homogenously distributed over the whole volume but rather localized close to the surface area of the ceramic. Similar conclusions could be drawn for the resistive contribution R_4, which also disappeared after grinding.

5.2.5 Effect of the reoxidation treatment during annealing

As shown beforehand the main contribution to the PTCR effect in BaO-rich compositions of La-doped $BaTiO_3$ arises from the outer surface. Certainly also the internal grain boundary network also plays a part but the magnitude of the rise in resistivity is by far not so large. In section 5.2.4 it has been shown that the resistive surface layer can be removed and therefore the assumption that its regeneration by a second annealing treatment is possible appears to be quite straightforward. The oxidizing post-sintering annealing treatment is essential for the realization of the PTCR effect. During this process essentially grain boundary regions are reoxidized through diffusion and absorption. The density of the as sintered ceramics was in all cases above 96% of the theoretical value respectively and therefore open internal porosity can be excluded. For this reason the penetration of oxygen into the material starts at the ceramic outer surface. The influence of reoxidation on the impedance spectra has been investigated in order to better understand this phenomenon.

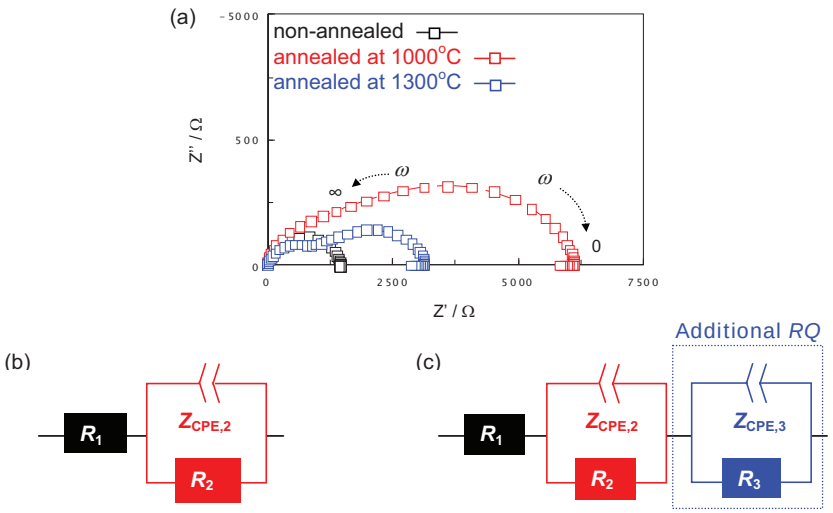

Fig. 5-16: (a) Cole-Cole diagram showing the impedance spectra of $(Ba_{1.028}La_{0.002})TiO_{3+\delta}$ (m = 1.03) at 200°C for different conditions: after removal of the resistive outer surface layer (black open symbols), after a subsequent annealing in air at 1000°C (red open symbols) and at 1300°C (blue open symbols).
(b) Equivalent circuit representing the impedance spectrum without external resistive surface (Starting condition: one RC element).
(c) Equivalent circuit representing the impedance spectrum with external resistive surface (annealed condition: two RC elements).

Figure 5-16 presents the impedance spectra obtained for $(Ba_{1.018}La_{0.002})TiO_{3+\delta}$ (m = 1.02) in the hot stage above T_C without resistive surface layer, which was removed by grinding, and for the cases of subsequent oxidizing treatments in air at 1000°C and 1300°C for two hours. In the original state before these annealing cures at high temperature the impedance spectrum only consists of one single relatively small semicircle, which represents the contribution of the grain interior (R_1) and of internal grain boundaries (R_2). After annealing at 1000°C an additional resistive component being approximately four times larger appears in the lower frequency region. If the ceramic is further annealed at 1300°C this extra component is still present but deteriorated compared to the 1000°C treatment. Removal of the resistive outer surface layers results again in the original condition where only one semicircle is obtained.

The entire PTCR curves showing the temperature dependence of the total resistance of $(Ba_{1.028}La_{0.002})TiO_{3+\delta}$ after various annealing treatments in the temperature range from 1000 °C up to 1300 °C is represented in figure 5-17.

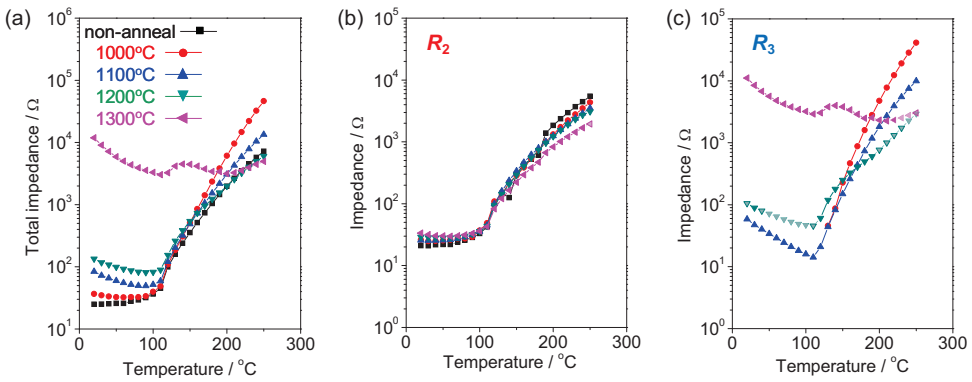

Fig. 5-17: Temperature dependence of the total resistance, the resistive elements R_2 and R_3 of $(Ba_{1.028}La_{0.002})TiO_{3+\delta}$ after annealing in air at various temperatures in the range from 1000°C up to 1300°C for two hours.
(a) Total resistance, (b) R_2 and (c) R_3.
The original condition before annealing and after removal or the outer resistive surface layer is represented by the solid black squares (■).

The resistance of the internal grain boundaries is comparatively little affected by the high temperature annealing procedure (figure 5-17 (b)). However the component R_3, representing the outer resistive surface layer of the ceramics, strongly depends on the maximum annealing temperature. Up to 1000°C the PTCR effect is enhanced. At higher temperatures, however, the magnitude of the resistivity jump at T_C is reduced since the cold resistance increases and the resistance in the hot condition decreases. This behavior is apparently closely related to the temperature characteristics of R_3 after annealing (figure 5-17 (c)). At temperatures higher than 1000°C, not only oxygen diffusion plays a role, but also the formation and migration of metal vacancies become active, because the Schottky reaction is in operation. This might alter the appropriate electrical configuration at grain boundaries, resulting in a deterioration of the PTCR effect.

5.3 Characteristics of oxygen diffusion during reoxidation

The previously described impedance spectroscopic investigations lead to the conclusion that several different phenomena are responsible for the development of the PTCR effect in reoxidized La-doped ceramics based on $BaTiO_3$ with BaO-excess that were sintered under reducing conditions. Upon reoxidation a relatively small contribution arises from the internal grain boundary network inside the volume of the ceramics. Additionally reoxidation also results in the generation of insulating layers at

the external surface of the material. In order to understand more precisely how these layers are formed during the post-sintering heat treatment the oxygen penetration has been studied by recording concentration profiles with the help of ^{18}O tracer diffusion. The isotope exchange method is commonly used for the investigation of diffusion profiles in oxides and relies on the incorporation of the stable isotope gas $^{18}O_2$ into the solid and subsequent analysis with mass spectroscopy.[97-99] In the present work plasma secondary neutralized particle mass spectroscopy (Plasma-SNMS) was employed for ^{18}O detection.

5.3.1 Experimental results

Plasma-SNMS signals were detected from the main constituents Ba, Ti, ^{16}O, ^{18}O, Si and La. In addition the impurities Na, Fe, Mn and C were analyzed. Their concentration was below 0.1 at.% except for C, which is believed to be a contamination due to processing (binder, gas atmosphere etc.). The other impurities originate almost certainly from the raw materials used for ceramic powder preparation.

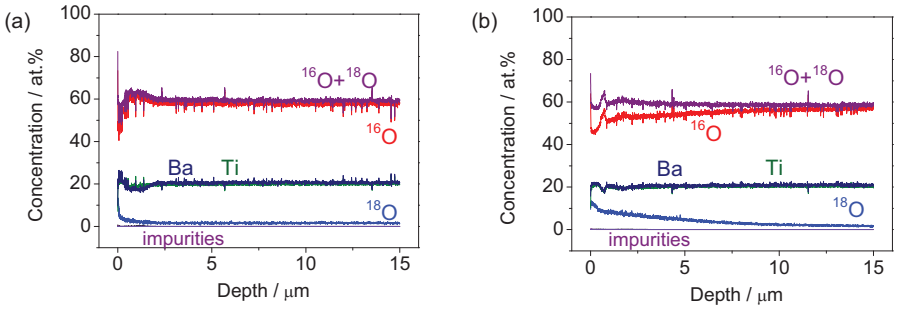

Fig. 5-18: Concentration depth profiles for Ti, Ba, ^{16}O and ^{18}O recorded for $(Ba_{1.048}La_{0.002})TiO_{3+\delta}$ (m = 1.05) annealed at:
(a) 700°C and (b) 1000°C for two hours.

Figure 5-18 represents depth profiles of the concentration of Ba, Ti, ^{16}O and ^{18}O in $(Ba_{1.048}La_{0.002})TiO_{3+\delta}$ (m = 1.05) the composition with the highest excess of BaO studied in the present work, which revealed two additional resistive components besides the insulating grain boundaries in the interior of the material. The ratio of the atomic concentrations of the main elements Ba, Ti and the sum of ^{16}O and ^{18}O almost ideally corresponds to 20:20:60, which represents the stoichiometry of $BaTiO_3$. As expected due to enhanced diffusivity at higher temperatures the total concentration of ^{18}O is larger in the case for annealing at 1000°C compared to 700°C. Also at 1000°C the isotope ^{18}O penetrated deeper into the volume of the material leading to a longer

diffusion tail. The relative atomic fraction of ^{18}O normalized to the total oxygen content $^{18}O + {}^{16}O$ expressed in dependence of diffusion time t and the distance x from the surface can be calculated from the raw data presented in figure 5-18 as:

$$c(x,t) = \frac{I(^{18}O)}{I(^{16}O) + I(^{18}O)} \qquad \textbf{Eq. 5-4.}$$

$I(^{16}O)$ and $I(^{18}O)$ correspond to the detected normalized intensities or atomic concentrations of ^{16}O and ^{18}O respectively. The highest ^{18}O concentration is observed directly at the surface because the exchange of ^{16}O by ^{18}O is initiated here. If the surface exchange kinetics is fast enough this concentration is always in equilibrium with the surrounding gas atmosphere. All isotope exchange experiments were carried out above the critical temperature where this equilibration freezes.[115]

5.3.2 Simulation of the diffusion profiles

5.3.2.1 The role of volume diffusion

The migration of incorporated ^{18}O into the volume of the solid occurs via the exchange of oxygen ions and vacancies. Under the assumption of an infinite source of ^{18}O at the gas-solid interface this volume diffusion process can be theoretically described based on both Fick´s laws by a Gaussian complementary error function:

$$\tilde{c}(x,t) = \frac{c(x,t) - c_0}{c_g - c_0} = \mathrm{erfc}\left(\frac{x}{2\sqrt{D_{vol.} \cdot t}}\right), \qquad \textbf{Eq. 5-5.}$$

$$\text{where } \mathrm{erfc}(X) = \frac{2}{\sqrt{\pi}} \int_x^{\infty} \exp(X^2)\,dX, \quad X = \frac{x}{2\sqrt{D_{vol.} \cdot t}}$$

In equation 5-5 $\tilde{c}(x,t)$ represents the theoretical normalized ^{18}O concentration. The variables c_g and c_0 are the respective ^{18}O concentrations in the gas atmosphere used for the isotope exchange and in ambient air in which the phase formation during calcination and sintering occurs. In the present study the following parameters apply: c_g = 0.2, c_0 = 0.002 and t = 7200 s. Figure 5-19 shows the experimental and the simulated diffusion profiles, based on the analysis expressed by equation 5-5, i.e. only considering volume diffusion in the model. In the case of m = 1.00, the experimental result is perfectly fitted by the theoretical curve, indicating that the predominant diffusion process is volume diffusion. On the contrary, for the hyper-stoichiometric materials, it turns out that this expression for volume diffusion only

satisfactorily fits the experimental results at the very outer surface region within a depth of typically 100 to 200 nm. In deeper regions the measured concentrations of ^{18}O are much larger than the ones predicted by volume diffusion. For instance 2 µm below the surface the normalized experimental values are around 0.2 (for 800°C) and as high as 0.4 for annealing at 1000°C (not shown here). In both these cases the theoretical curve however already reaches the baseline ($\tilde{c}(x,t) \approx 0$). This discrepancy implies that not only volume diffusion determines the reoxidation behavior in the interior of the ceramics. The calculated values for the volume diffusion coefficients at 700°C, 800°C, 900°C and 1000°C are listed in table 5-3.

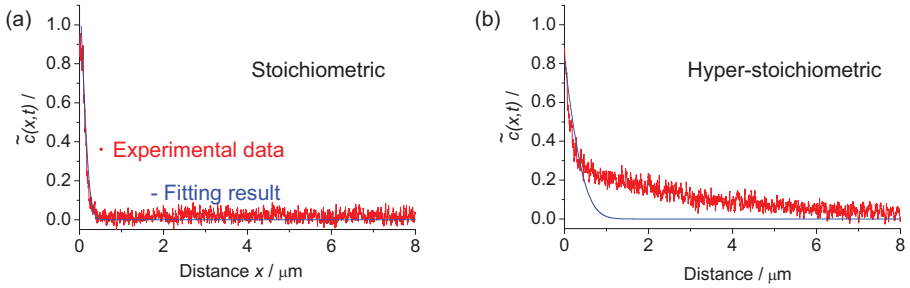

Fig. 5-19: Normalized experimental (red curve) and theoretical (blue curve) concentration depth profiles of ^{18}O for $(Ba_{m-0.002}La_{0.002})TiO_{3+\delta}$ (a) m = 1.00 and (b) m = 1.05 annealed at 800°C.

	Volume diffusion coefficient $D_{vol.}$ [cm²/s]	
	Stoichiometric	**Hyper-stoichiometric**
700°C	-	1.4×10^{-13}
800°C	1.5×10^{-14}	1.9×10^{-13}
900°C	-	3.7×10^{-13}
1000°C	-	7.9×10^{-13}

Tab. 5-3: Calculated diffusion coefficients describing ^{18}O penetration by volume diffusion at the surface of $(Ba_{1.048}La_{0.002})TiO_{3+\delta}$ for different annealing temperatures.

5.3.2.2 The role of grain boundary diffusion

According to the results presented before volume diffusion is not the only process involved during oxygen incorporation during reoxidation. Apparently grain boundary diffusion also plays an important role here, since the detected ^{18}O concentrations in the interior of the material are much larger than the expected ones. Very probably the grain boundaries act as additional pathes for oxygen to diffuse into the ceramics, as

reported for polycrystalline ZnO.[116] The diffusion coefficient for grain boundary diffusion $D_{g.b.}$ can be theoretically expressed by:[117]

$$D_{g.b.} \cdot \delta_{g.b.} = 0.66 \cdot \sqrt{\frac{4D_{vol.}}{t}} \cdot \left(\frac{\partial \log[c(x,t)]}{\partial x^{6/5}} \right)^{5/3} \qquad \textbf{Eq. 5-6.}$$

In equation 5-6 $\delta_{g.b.}$ represents the crystallographical width of the grain boundary. Following this expression it can be concluded that grain boundary diffusion takes place if the relation between $\log[c(x,t)]$ and $x^{6/5}$ is linear. Figure 5-20 shows the dependence of $\log[c(x,t)]$ from $x^{6/5}$ derived from the the tracer diffusion experiments carried out in this study. For all annealing temperatures considered here (700°C to 1000°C) a linear relation is obtained at least in the interior region under the surface, where volume diffusion does not satisfactorily describe the experimental measurements. At the very surface region volume diffusion dominates and accordingly a deviation from this linear relationship is observed.

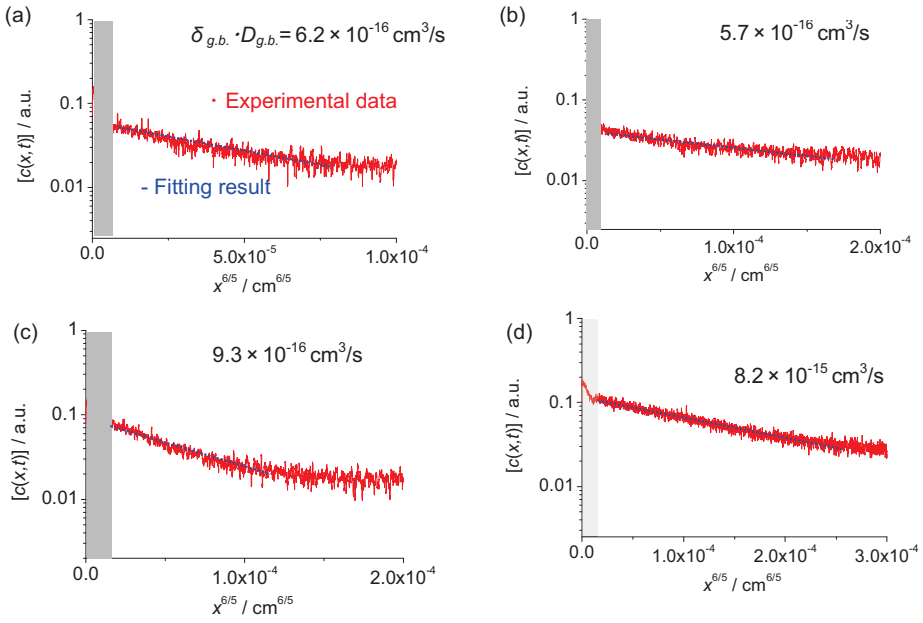

Fig. 5-20: Dependence of $\log[c(x,t)]$ from $x^{6/5}$ derived from the ^{18}O diffusion profiles recorded (red) for $(Ba_{1.048}La_{0.002})TiO_{3+\delta}$ at: (a) 700°C, (b) 800°C, (c) 900°C and (d) 1000°C. The blue lines show the simulated values obtained using equation 5-6.

The calculated values for fitting the experimental data shown in figure 5-20 of the product $D_{g.b.} \cdot \delta_{g.b.}$ are listed in table 5-4.

	$D_{g.b.} \cdot \delta_{g.b.}$ [cm^3/s]
700°C	6.2×10^{-16}
800°C	5.7×10^{-16}
900°C	9.3×10^{-16}
1000°C	8.2×10^{-15}

Tab. 5-4: Calculated values of $D_{g.b.} \cdot \delta_{g.b.}$ describing the ^{18}O penetration by grain boundary diffusion below the external surface of $(Ba_{1.048}La_{0.002})_{1.05}TiO_{3+\delta}$ for different annealing temperatures.

5.3.2.3 Impact of defect chemistry on the diffusion behavior

Figure 5-21 and table 5-5 show the temperature dependence of the volume diffusion coefficient $D_{vol.}$ and of the product $D_{g.b.} \cdot \delta_{g.b.}$ in the form of an Arrhenius representation in comparison to data from the literature.[118,119]

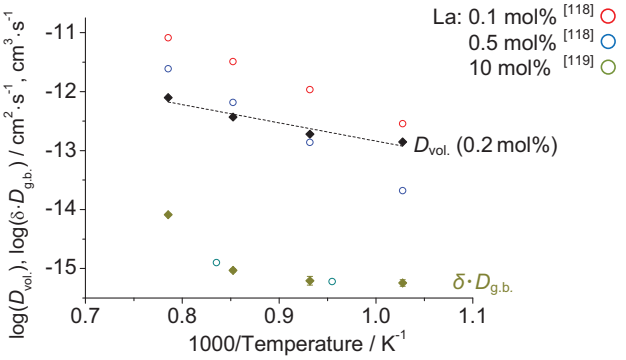

Fig. 5-21: Temperature dependence of the bulk diffusion coefficient $D_{vol.}$ and of the product $D_{g.b} \cdot \delta_{g.b.}$experimentally determined in this study in comparison with results from literature for different concentrations of La-donor doping. [118,119]

The diffusion coefficients and the activation energy determined in the present study are in good agreement to the results reported by Ito et al.[118] and Shirasaki et al.[119] From figure 5-21 it can be easily recognized that the introduction of La into the perovskite lattice weakens the diffusivity of oxygen in $BaTiO_3$. This is believed to be due to the reduction of the concentration of oxygen vacancies upon La addition, as expressed by equations 5-7 and 5-8 that represent the defect chemistry of barium titanate for La incorporation and for intrinsic reduction respectively. When La is introduced as a donor, conducting electrons are generated in order to compensate the extra positive charge of the La^{3+} ion on the Ba^{2+} site.

La-concentration [mol%]	BaO/TiO_2 ratio	Activation energy [eV]	Reference
0	stoichiometric	1.69 ± 0.07	[118]
0.1	stoichiometric	1.17 ± 0.05	
0.2	5 mol% BaO-excess	$^{(\S)}$0.62 ± 0.11	this study
		$^{(\S\S)}$0.76 ± 0.31	
0.5	stoichiometric	1.73 ± 0.33	[118]
10	stoichiometric	0.63	[119]

Tab. 5-5: Activation energies for oxygen diffusion in La-doped $BaTiO_3$: comparison of own results (§volume diffusion and §§grain boundary diffusion) with data from literature.

Consequently the concentration of oxygen vacancies according to the intrinsic reduction equilibrium is decreased. The diffusivity of oxygen takes place via the site exchange of O^{2-} ions with vacant lattice positions.

$$La_2O_3 \rightleftharpoons 2La_{Ba}^{\bullet} + 2O_O^{\times} + 2e + 1/2O_2^{(g)} \qquad \textbf{Eq. 5-7,}$$

$$O_O^{\times} \rightleftharpoons 1/2O_2^{(g)} + V_O^{\bullet\bullet} + 2e \qquad \textbf{Eq. 5-8.}$$

It therefore depends on both the availability and the mobility of oxygen vacancies. A reduction of the concentration of oxygen vacancies thus also implies a decrease of the diffusion coefficient. As the results presented in the previous sections 5.3.2.1 and 5.3.2.2 show, grain boundary diffusion is the dominating process for the incorporation of oxygen into the ceramic for the temperature range considered here. Enhanced grain boundary diffusion in donor-doped electroceramics is also observed in other materials systems, such as for example in the case of n-type semiconducting ZnO varistors.[116] Referring to the microstructural characterization of $(Ba_{1.048}La_{0.002})TiO_{3+\delta}$ ceramics by TEM (section 5.1) a grain boundary width of approximately $\delta_{g.b.} \approx 2$ nm can be assumed.

For an exemplarily chosen temperature of 800°C the calculated coefficient for grain boundary diffusion (1.5×10^{-8} cm^2/s) can be consequently compared to the one measured for volume diffusion (1.9×10^{-13} cm^2/s). This comparison reveals that grain boundary diffusivity of oxygen along grain boundaries is enhanced by many orders of magnitude. Even if the grain boundary width would be broader than the assumed value of 2 nm, this situation does not change dramatically and still a very large difference in diffusion coefficients is observed.

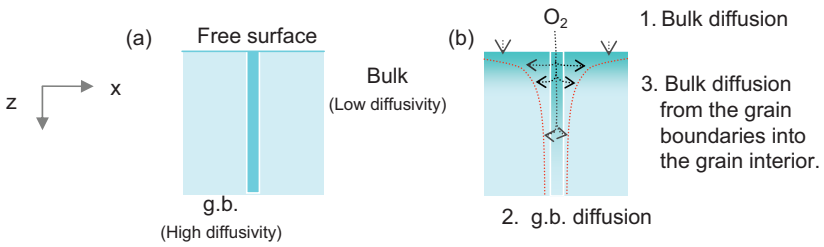

Fig. 5-22: Proposed model for the reoxidation behavior of $BaTiO_3$ thermistor ceramics with BaO-excess: (a) initial situation after sintering under reducing conditions, (b) penetration of oxygen by volume diffusion into the surface, grain boundary diffusion into the bulk and volume diffusion from the grain boundaries towards the interior of the grains.

One reason why the contribution of oxygen transport via grain boundaries prevails is the large volume fraction of these internal interfaces due to the relatively small grain size in BaO-excess $BaTiO_3$. They facilitate the incorporation of oxygen ions within a zone reaching from a few hundreds of nm up to several μm below the surface of the material. This enhanced oxygen uptake by grain boundary diffusion is illustrated schematically in figure 5-22.

As shown in section 3.3.1 the Heywang model describes the barrier height of the insulating double Schottky junction at the grain boundaries, which is responsible for the hot resistance of PTCR ceramics on $BaTiO_3$-basis as function of the density of acceptor states at the interface N_s and of the donor concentration N_D. High values of N_s and low values of N_D enhance the barrier height. It is well known that oxygen absorption at the grain boundaries creates surface acceptor states.[17] This is the reason, why reoxidation after sintering is necessary for the realization of the PTCR effect. When oxygen is incorporated into the perovskite lattice oxygen vacancies are occupied and free electrons are captured to maintain electrical neutrality. This means that the total donor concentration is lowered, since $V_O^{\bullet\bullet}$ acts as donor.

Another peculiarity of the present material system is the role of BaO-excess. If additional BaO (represented by the molar portion *m*') is dissolved in the perovskite phase the following defect chemical reaction can be assumed:

$$m'BaO + BaTiO_3 \rightleftharpoons Ba_{1+m'}TiO_{3+m'}$$
$$\equiv (1+m')Ba_{Ba}^{\times} + Ti_{Ti}^{\times} + m'V_{Ti}^{''''} + (3+m')O_O^{\times} + 2m'V_O^{\bullet\bullet} \qquad \textbf{Eq. 5-9.}$$

According to equation 5-9 the incorporation of additional BaO into $BaTiO_3$ causes the formation of both titanium vacancies $V_{Ti}^{''''}$ and oxygen vacancies $V_O^{\bullet\bullet}$ during sintering.

This process represents a partial Schottky reaction and only takes place at sufficiently high temperatures, typically above 1200°C, because of kinetic reasons (sufficient mobility of metal vacancies). It is believed that this partial Schottky reaction preferentially takes place at the grain boundaries for the following reasons: (i) BaO excess is dissolved in secondary phases at the triple points of the $BaTiO_3$ grains, (ii) the solubility of the perovskite lattice is expected to increase with temperature, (iii) the dissolution of extra BaO requires elastic distortion of the lattice, which is easier accommodated at the grain boundaries compared to the crystal interior. During post-sintering reoxidation the titanium vacancies created in the grain boundary regions essentially remain frozen-in and act as interface acceptor states. On the other hand additionally formed oxygen vacancies through the insertion of BaO are still mobile during the heat treatment at rather moderate temperatures and therefore the local enhanced concentration of $V_O^{\bullet\bullet}$ at grain boundaries results in an enhanced diffusivity of oxygen along these interfaces. Whether the here presented scenario is realistic is clarified by measurements of the DC conductivity in the intermediate temperature range where the PTCR effect evolves under different partial pressures of oxygen (see chapter 6).

5.3.3 Factors enhancing grain boundary diffusion

From oxygen isotope exchange experiments, an increased contribution of grain boundary diffusion was found in hyper-stoichiometric barium titanate. In this section, the reason for the increase is focused on. Accoring to Haneda et al.[116] the measured diffusion coefficient $D_{measured}$ is propotional to the diffusivity D^o and the defect concentration, in this case oxygen vacancy concentration $[V_O^{\bullet\bullet}]$. This is expressed by the following equation:

$$D_{measured} \propto D^0 \cdot [V_O^{\bullet\bullet}] \qquad \textbf{Eq. 5-10.}$$

D^o corresponds to the readiness of oxygen hopping from one site to another, and $[V_O^{\bullet\bullet}]$ increases the oxygen hopping probability. This relation is schematically illustrated in figure 5-23. It is quite difficult to evaluate the diffusivity D^o experimentally. Calculations based on density functional theory (DFT) have therefore been carried out in order to examine the influence of the existence of a Ti vacancy on the oxygen vacancy diffusivity.

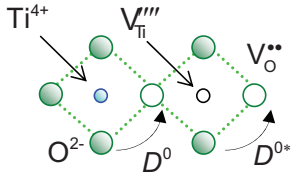

Fig. 5-23: Schematic representation of oxygen diffusion with and without the presence of a Ti vacancy in the vicinity.

5.3.3.1 DFT calculation of diffusivity

Density functional theory (DFT) calculations were conducted based on a 3 ×3 × 3 super cell as shown in figure 5-24 (a) by the theoretical simulation group of Murata Corporation.[120] It represents the cubic structure of the high temperature polymorph of $BaTiO_3$. Since the simulation of grain boundary diffusion requires an asymmetrical structure, which is quite difficult to model, a symmetrical structure of the perovskite lattice was employed here in a first approximation. In figure 5-24 (b) a simpified super cell image is shown to indicate the migration path of an oxygen ion. Three migration paths are under consideration: (i) from a first nearest site to another first nearest site (marked as 1^{st} to 1^{st}), (ii) from a first nearest site to a second nearest site (1^{st} to 2^{nd}) and (iii) from a second nearest site to a third nearest site around a Ti vacancy (2^{nd} to 3^{rd}).

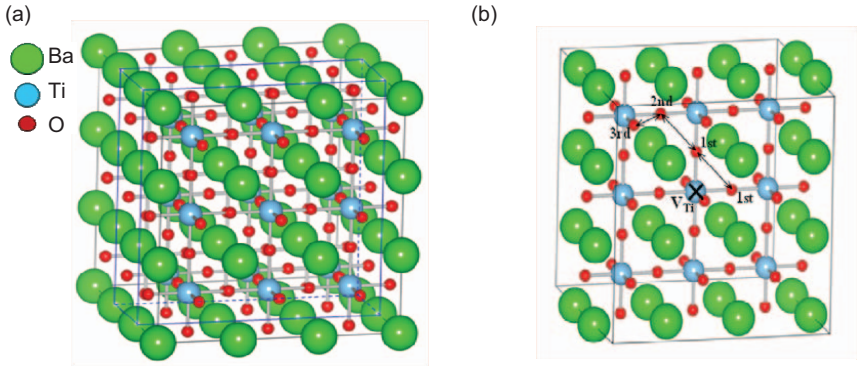

Fig. 5-24: (a) 3 × 3 × 3 super cell used for DFT calculations and (b) a simplified super cell showing the migration path of oxygen. The indications 1^{st}, 2^{nd} and 3^{rd} represent the first, second and third nearest site of an oxygen ion relative to a Ti vacancy site at the center of super cell.

The influence of the presence of a titanium vacancy is calculated and the results are shown in figure 5-25. The ordinate of the graph represents the migration energy and

the absicca the position of a migrating oxygen vacany relative to the one for the Ti vacancy. Withouth titanium vacancy it is clear that an oxygen ion on the oxygen site has the same energy level independent on the type of jump. This is quite reasonable, because every site calculated here is equivalent crystallographically. On the contrary, the situation changes completely when a Ti vacancy is present. The activation energy for migration, which is indicated by the height of the energy wall between two postions, becomes higher compared to the first case where no titanium vacancy was assumed. One more thing to be added is that energy levels at the 2nd and 3rd position are higher than that for the nearest site. In other words a migrating oxygen vacancy is more strongly bounded to the titanium vacancy. This conclusion is quite natural considering the electric charges of these point defects: the oxygen vacany is positively charged and the titanium vacancy negatively. These two defects tend to create a defect associate in the perovskite lattice. Shirasaki et al.[119] have found an increase of the diffusion coefficient above 950˚C for donor-doped $BaTiO_3$ and claimed that this is related to the dissociation of such defect associates. The present calculation results therefore correspond to Shirasaki et al. experimental findings.

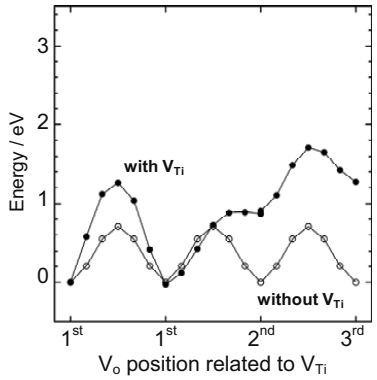

Fig. 5-25:
Energy of a migrating oxygen vacancy depending on the site in the perovskite lattice around a Ti^{4+} ion or a titanium vacancy. (Refer to figure 5-24)

The calcuation of this work was performed on the assumption that a Ti vacancy is located in the grain, not in the grain boundary. It is still believed that the result here can be at least qualitatively transposed to the grain boundary case in a very first approximation. Certainly the coordination of all cations and anions is not the same in this case as in the perfect perovskite lattice that was assumed in the present simulation. However, the fundamental attractive interactions between point defects of opposite charges illustrated by the present DFT calculation also take place. In conclusion an assumed enhancement of the mobility of oxygen vacancies is not

threoretically feasible for explaining the increased grain boundary diffusion of oxygen in BaO-excess $BaTiO_3$.

5.3.3.2 Quantitative estimation of oxygen absorption

Equation 5-10 suggests that the diffusion coefficient of oxygen vacancies and ions is increased by an increase of either the diffusivity D^0 or oxygen vacancy concentration. Since DFT calculations showed that enhanced diffusivity can be excluded, the concentration of oxygen vacancies was estimated by recording the maximum oxygen uptake using TGA. The experimental procedure was as follows: after isothermal soaking the specimens under reducing conditions (typically at a temperature of 700°C and a $p(O_2)$ of 10^{-21} MPa for four hours) the atmosphere was changed into an oxidizing one ($p(O_2)$ of 10^{-1} MPa). TGA was then employed to investigate the weight increase of the specimen due to oxygen uptake (typically kept at 700°C for 18 hours). $BaTiO_3$ with 4 – 5 mol% of BaO-excess did not show any saturation under reducing conditions, therefore this data is omitted here. Figure 5-26 shows the estimated oxygen uptake per one mol of $BaTiO_3$ by TGA.

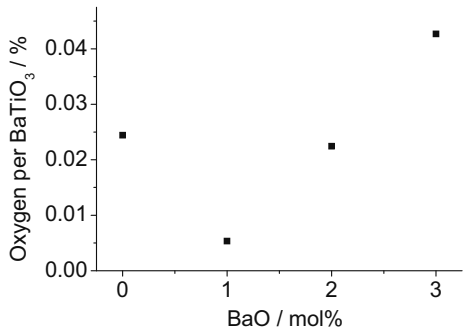

Fig. 5-26:
Oxygen uptake during reoxidation estimated by TGA at 700°C. The sample weight is around 100 mg respectively.

The TGA results show that the oxygen uptake tends to drastically increase with augmenting BaO-excess (except the 0 mol% sample). An increase of the BaO-overstoichiometry from 1 to 3 mol%, however, results in a growth of the relative absorbed oxygen amount by a factor of almost 10. This supports the idea that $BaTiO_3$ becomes easily oxidized when the Ba/Ti ratio is raised. Figures 5-1 and 5-2 show that the addition of BaO also results in a strongly refined microstructure. In other words: a higher volume fraction of grain boundaries exists in the hyper-stoicheometric compositions. Taking into account that grain boundary diffusion is enhanced as shown in figures 5-19 and 5-20, it is reasonable to conclude that $BaTiO_3$

with BaO excess is preferentially oxidized, especially at the grain boundaries. This is believed to activate the PTCR effect.

5.4 Summary

Impedance spectroscopic characterization of reduction resistant $BaTiO_3$-based thermistor ceramics doped with La and with BaO-excess used for the manufacturing of multilayer PTCR elements revealed that the microstructural origin for the non-linear increase in resistance observed upon heating is quite complex. It does not simply consist of bulk and grain boundary resistive or capacitive contributions. Additional surface contributions that dominate the PTCR effect for BaO-rich compositions could also be identified.

Because the formation of these external highly resistive layers is formed only upon reoxidation the oxygen penetration has been studied in detail by recording and analyzing diffusion profiles using the isotope exchange method in combination with Plasma-SNMS. The results suggest that not only volume diffusion should be considered for the explanation of the isolating surface layers. Also grain boundary diffusion plays an important role. Upon BaO addition the grain boundary diffusivity of oxygen is strongly enhanced, at least by a few orders of magnitude, compared to the stoichiometric case. In addition to this grain refinement resulting in a higher volume fraction of the grain boundary network due to the BaO-excess supports oxygen transport along these interfaces. On the basis of these findings a defect chemical model is proposed based on the creation of additional oxygen vacancies due to BaO incorporation in the grain boundary regions. These vacancies enhance the oxygen diffusion. In parallel the appearance of Ti vacancies acting as acceptor states and being responsible for building up the insulating Schottky barrier layers at the grain boundaries are suggested. Theoretical DFT calculations suggest that actually the mobility of oxygen vacancies is not enhanced but rather likely reduced when Ti vacancies are simultaneously present in the lattice or the regions close to the grain boundaries. It is therefore concluded that the local enrichment of oxygen vacancies at these interfaces is mainly responsible for the improved oxygen penetration into the ceramic during reoxidation.

Further investigations on the $p(O_2)$- and T-dependence of DC conductivity should confirm the model involving both oxygen as well as titanium vacancies and are presented in chapter 6.

Chapter 6
Kröger-Vink diagrams and defect chemistry

This chapter describes and discusses results obtained mainly through DC conductivity measurements in the intermediate temperature range between 700°C and 1000°C at various oxygen partial pressures from 10^{-21} MPa to 10^{-1} MPa. The experimental parameters chosen cover the relevant processing conditions applied during the reoxidation of reduction-resistant La-doped PTCR ceramics on $BaTiO_3$-basis with BaO-excess. For this reason it is anticipated that the defect chemical model proposed in the previous chapter can be verified by the present investigation even if thermodynamical equilibrium in the relatively low temperature range only partially occurs due to kinetic reasons. The objective of the corresponding experiments was to set up a series of Kröger-Vink diagrams that explain how the reoxidation treatment after sintering in reducing atmosphere is affected by the defect chemical equilibrium with different Ba/Ti ratios *m*. For TiO_2-rich PTCR compositions based on $BaTiO_3$ sintered under oxidizing conditions Daniels et al.[19,41] proposed a defect chemical model based on the $p(O_2)$ dependence of the electrical conductivity investigated by means of the DC measurement technique at high temperatures. Those experiments were performed at temperatures close to the actual sintering temperature of around 1300°C, where the Schottky equilibrium is active. Under the assumption of kinetically frozen-in Ba vacancies Daniels' PTCR model based on defect chemistry translated the situation at high temperatures to lower temperatures, at which the actual PTCR effect comes up. No experimental evidence for the existence of Ba vacancies was provided in the former reports. The results of the present work expose Kröger-Vink diagrams that do not correspond to the full thermodynamical equilibrium, but rather represent steady state conditions due to the slow diffusion of metal vacancies involved. These "modified" Kröger-Vink diagrams at intermediate temperatures reflect the point defect situation during post-sintering annealing under various partial pressures of oxygen. Besides this experimental part also theoretical calculations on the $p(O_2)$ dependence of the concentration of the point defects have been carried out in order to estimate and judge how far the measured data deviate from the theoretically expected ones. The following

compositions were exemplarily selected: (Ba+La)/Ti ratio m = 1.01, 1.03 and 1.05 (Sample B-2, B-4 and B-6). Among them only the latter two formulations show a good PTCR performance as shown in section 5.2.

6.1 Simulation of defect chemical equilibria

In order to verify whether the mathematical simulation of point defect equilibria reproduce the results reported earlier in the literature,[41,45] two cases, shown in figure 6-1, have been calculated for $BaTiO_3$ doped with 0.2 mol% of La: the high temperature equilibrium (at 1300°C) and the frozen-in steady state situation at an intermediate temperature (§at 1000°C after equilibration at 1300°C and $p(O_2) = 10^{-9}$ MPa). The details of the calculation procedure are described in section 3.2.3.

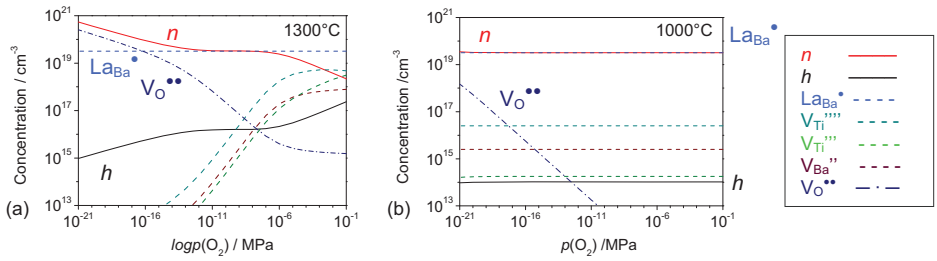

Fig. 6-1: Calculated $p(O_2)$ dependence of the point defect concentrations for $(Ba_{0.998}La_{0.002})TiO_{3+\delta}$: (a) equilibrium at 1300°C, and (b) quenched state at 1000°C after equilibration at 1300°C and $p(O_2) = 10^{-9}$ MPa (Schottky equilibrium is frozen).

At 1300°C the majority carrier are electrons over the whole range of $p(O_2)$ simulated. Therefore the material is n-type semiconductive at this temperature. In accordance to Daniels' experiments, three distinct regions of oxygen partial pressure can be recognized.[2] Below approximately 10^{-13} MPa, the slope of the curve representing electron concentration in dependence of $p(O_2)$ reveals a slope of -1/6, which corresponds to the regime of electron compensation by oxygen vacancies. In the range between around 10^{-12} MPa to 10^{-6} MPa a nearly partial pressure independent region of electron concentration is observed, which is often referred to as a plateau region. Here the electron concentration is not govererned by the dominant donor-type oxygen vacancies but by the concentration of the donor La. Because the donor concentration is independent of temperature and oxygen partial pressure, electron concentration, i.e. electrical conductivity should remain unchanged at this level for

§ Assuming the experimental conditions for preceding sintering

any temperature. Above $p(O_2) = 10^{-6}$ MPa the slope of the calculated Kröger-Vink diagram becomes -1/4, being consistant with the compensation mechanism by metal vacancies, mainly fourfold charges of V_{Ti}'''' .[62-64] This is because a α-ratio of Ti to Ba vacancies of 10 was selected in this calculation.[73] All parameters used for this calculation are presented in detail in section 3.2. Metal vacancy compensation is for kinetic reasons only possible in the high temperature regime, where the Schottky equilibrium is active. The simulated curves for the electron concentration in figure 6-1 (a) correspond perfectly to the results reported by Daniels et al.[41]

In the quenched case at 1000°C (figure 6-1(b)), where the Schottky equilibrium is assumed to be inactive in the calculation, the electron concentration seems to be almost independent of $p(O_2)$. The amount of electrons generated by intrinsic reduction is nearly negligible, because the concentration of $V_o^{\bullet\bullet}$ is more than one order of magnitude lower than that of the donor dopant at $p(O_2) = 10^{-21}$ MPa from theoretical calculation. The Schottky mechanism is inactive in this region, because the formation and migration enthalpies of metal vacancies are considered to be too high.[64] The major conclusions deduced here are: (i) no electron hole conduction is expected in entire $p(O_2)$ range calculated and (ii) no conductivity increase due to intrinsic reduction is expected below 1000°C. Both illustrative examples shown here demonstrate that the conductivity behavior and the concentration of all major point defects can be successfully predicted with the simulation procedure described in section 3.2.3.

6.2 Experimental results

The results of the DC conductivity measurements in dependence of oxygen partial pressure $p(O_2)$ and temperature T are represented in figure 6-2 in a "modified" Kröger-Vink diagram for three compositions: $(Ba_{m\text{-}0.002}La_{0.002})TiO_{3+\delta}$ (m = 1.01, 1.03 and 1.05). It must be mentioned that in the case of relatively low Ba-excess $m = 1.01$ the measured conductivity values (open symbols) are not saturated in the region of high $p(O_2)$, typically around 10^{-6} – 10^{-1} MPa because the kinetics of the reactions involving metal vacancy compensation of electrons are too sluggish to reach equilibration within any reasonable time. Reliable saturated conductivity data for stoichiometric $BaTiO_3$ is reported elsewhere in Ref. 41, 51, 60, 121, 122.

The main results, that can be deduced from the modified Kröger-Vink diagram in figure 6-2 can be summarized as follows:

(i) under strongly reducing conditions ($p(O_2) < 10^{-11}$ MPa) the conductivity of compositions with small BaO-excess (m = 1.01) reveals a nearly temperature and $p(O_2)$ independent plateau,

(ii) under strongly reducing conditions ($p(O_2) < 10^{-11}$ MPa) compositions with high BaO-excess (m = 1.03 and 1.05) the conductivity vs. $p(O_2)$ curves have branches with the slope nearly -1/6,

(iii) the oxidizing regime (10^{-6} MPa < $p(O_2)$ < 10^{-1} MPa) reveals in the case m = 1.05 a branch in the conductivity vs. $p(O_2)$ curve with a positive slope, which is smaller than +1/4,

(iv) the conductivity minimum for very high BaO-excess (m = 1.05) is located at oxygen partial pressure $p(O_2)$ of approximately 10^{-6} — 10^{-4} MPa.

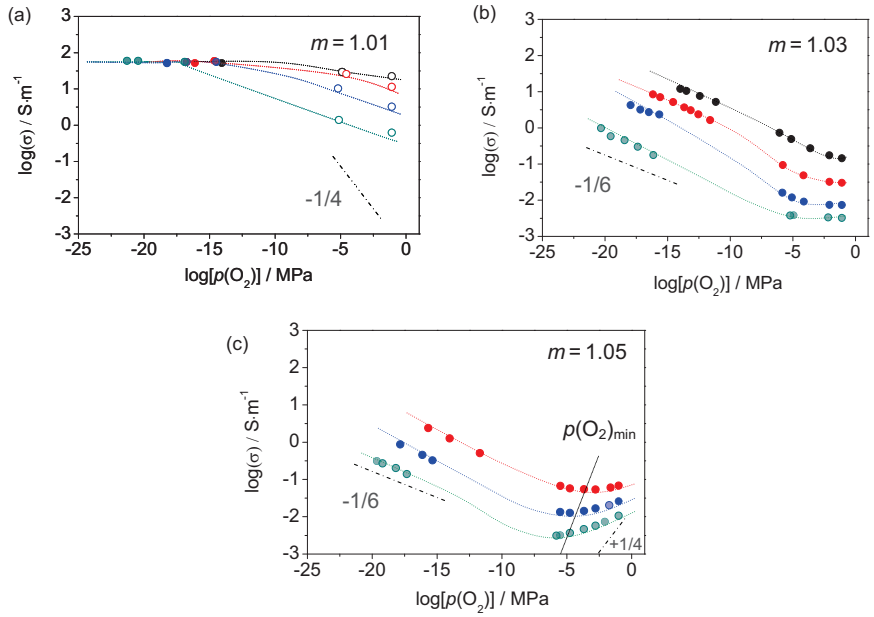

Fig. 6-2: Experimental modified Kröger-Vink diagrams showing the $p(O_2)$ dependence of conductivity at various temperatures for the compositions:
(a) $(Ba_{1.008}La_{0.002})TiO_{3+\delta}$,
(b) $(Ba_{1.028}La_{0.002})TiO_{3+\delta}$ and
(c) $(Ba_{1.048}La_{0.002})TiO_{3+\delta}$.
Open circles represent non-saturated conductivity values, closed ones saturated conductivity values.

In the following subsections the results summarized above discussed in the view of a defect chemical interpretation.

6.2.1 Low BaO-excess (*m* = 1.01)

In the case of little excessive BaO (*m* = 1.01) a rather modest PTCR effect was observed. Upon heating above the Curie temperature T_C resistivity increased only by a factor of 6 compared to the value at room temperature (see chapter 5). Figure 6-3 compares some experimental conductivity values obtained for this composition at various oxygen partial pressures with calculated ones. The plateau region in figure 6-2 was located at a conductivity level of $10^{+1.7}$ S·m^{-1}. From this conductivity value σ the concentration of free electrons *n* can be calculated using equation 6-1:

$$\sigma = \mathrm{e} \cdot n \cdot \mu_e \qquad \textbf{Eq. 6-1.}$$

Here μ_e represents electron mobility. With μ_e = 0.50 cm^2·V^{-1}·s^{-1}[39] the concentration of free electrons *n* can be estimated from the experimental conductivity value of the plateau at low partial pressures of oxygen to be around 6.9×10^{18} cm^{-3}. The concentration of La added was 0.2 mol%. This corresponds to 3.1×10^{19} La ions per cm^{-3}. The calculated electron concentration thus amounts only approximately a fifth of the value that would be expected if the added La-donor is fully incorporated into the perovskite lattice. For a similar case it is reported that only 74% of the donor is compensated by free electrons at a temperature range of 700 – 1000°C in Nb-doped $BaTiO_3$.[45] The con-centration of electrons created under highly reducing conditions through intrinsic reduction, i.e. in the $p(O_2)$ region where the slope of -1/6 is expected, can be calculated from the equilibrium constant K_{redox} ($1.8 \times 10^{+47}$). Assuming $p(O_2) = 10^{-21}$ MPa and *T* = 1000°C the concentration of oxygen vacancies amounts to $[V_o^{\bullet\bullet}] = 1.5 \times 10^{+18}$ cm^{-3}. Supposing furthermore that these vacancies are fully ionized and compensated by electron ($2[V_o^{\bullet\bullet}] \approx n$), approximately a value of 3×10^{-18} cm^{-3} can be expected as concentration of electrons generated by the intrinsic reduction equilibrium. This value is much smaller than the measured electron concentration, so that it is reasonable that the intrinsic reduction with the slope of -1/6 was not observed in the figure 6-2 (a).

In the oxidizing regime on the other hand, the reliable measurement of conductivity values is problematic due to the slow kinetics of equilibration of metal vacancies. The represented experimental results in figure 6-2 are plotted after adjusting temperature

and oxygen partial pressure for 24 hours. Additionally figure 6-3 shows two calculated curves for the case that the Schottky equilibrium is active (red line) or frozen-in (blue line). In the region of high $p(O_2)$ the measured data are located for the here considered intermediate temperature range in between these two extreme states. In this intermediate temperature range around 1000°C, metal vacancy formation might be taking place very slowly presumably from grain boundaries. A complete diffusion of these point defects into the interior of the ceramic grains, however, seems not to occur in reasonable periods of time at intermediate temperatures.[60]

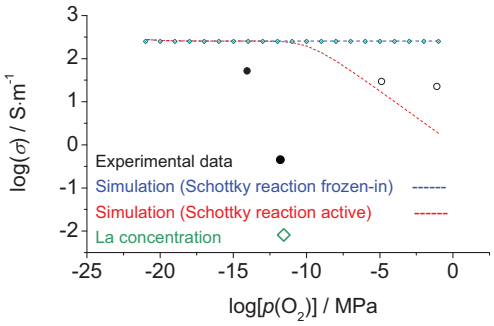

Fig. 6-3: Comparison between experimental data (open symbols: non-saturated values, closed symbols: saturated values) and simulation results (blue line: Schottky reaction frozen-in, red line: Schottky reaction active) at 1000°C. Green dots represent the conductivity expected from 0.2 mol% La donor addition.

The two main conclusions drawn here are: (i) the Schottky reaction is not completely inactive at intermediate temperatures around 1000°C and (ii) only a certain percentage of donor impurity is active as a "real" donor.

6.2.2 High BaO-excess ($m = 1.03$, or 1.05)

At high contents of BaO-excess the $p(O_2)$ dependence of DC conductivity differs quite strongly from the experimental results obtained for m = 1.01 and from the calculated curves shown in figure 6-1. In both cases of $m = 1.03$ and 1.05, basically a similar behavior is observed. At low partial pressures of oxygen the slope is negative and at large $p(O_2)$ values the slope is flat or even positive. The intermediate range of oxygen partial pressures where usually the conduction mechanism changes from n-type to p-type semiconduction could not be assessed in a reliable manner, because of the difficulty to control and maintain intermediate $p(O_2)$ properly.[96,123] These

problems arise from the fact that the Y:ZrO_2 oxygen sensor is quite imprecise in the region from 10^{-15} to 10^{-7} MPa, where the lambda ratio of O_2 concentration to H_2 concentration is close to unity and where the detected electromotive force does not follow the ideal Nernst equation, especially with the gas containing for instance CO or H_2O.[123]

Compared to the theoretically expected conductivity assuming that all donors are fully incorporated and ionized ($\sigma = 10^{+2.55}$ S·m) the observed values for the maximum conductivity in figures 6-2 (b) and (c) are significantly smaller ($\sigma = 10^{+1.05}$ S·m for $m =$ 1.03 at 1000°C and for $p(O_2) = 10^{-14}$ MPa; $\sigma = 10^{+0.38}$ S·m for $m = 1.05$ at 900°C and for $p(O_2) = 10^{-15.7}$ MPa). This difference amounts to one or two orders of magnitude. Apparently the BaO-rich compositions behave in total electrically more insulating compared to ceramics with low (Ba+La)/Ti ratio *m*. In order to clarify the origin of this discrepancy, in-situ AC impedance spectroscopy from 100 mHz up to 1 MHz has been performed at 700°C and $p(O_2) = 10^{-21}$ MPa, as shown in figure 6-4. At identical measurement conditions, the BaO-rich material with m=1.05 reveals a considerably higher DC impedance compared to the relatively BaO-poor composition.

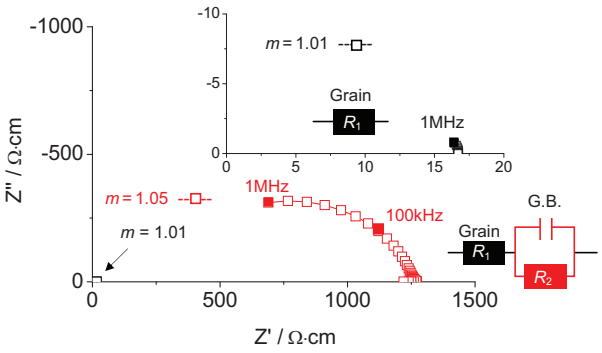

Fig. 6-4: In-situ impedance spectra of donor-doped $BaTiO_3$ with a (Ba+La)/Ti ratio of $m = 1.01$ and 1.05 at 700°C and $p(O_2) = 10^{-21}$ MPa. The inset shows the results for $m = 1.01$. The frequency range employed is $10^{-1} - 10^{6}$ Hz.

In the case of $m = 1.05$ a nearly semicircular shaped frequency arc was obtained, whereas for $m = 1.01$ no such locus could be observed. Since no semicircle is found in the latter case the existence of insulating barrier layers at the electrode-ceramic interface could be excluded. The semicircular arc measured for the BaO-rich composition with $m = 1.05$ is presumably arising from the resistive and capacitive contribution of insulating grain boundaries. It can therefore be concluded that the

difference of DC conductivity in BaO-rich compositions results from additional contributions of the grain boundaries, whereas in BaO-poor materials only the semiconducting bulk appears. The results from Moos et al.[124] support this idea. The authors presumed from high-temperature conductivity measurements on $Sr_{1-x}La_xTiO_3$ single crystals and ceramics an involvement of resistive grain boundaries related to the total conductivity in the case of polycrystalline specimens.

The slopes in the modified Kröger-Vink diagrams in figure 6-2 for m = 1.03 and m = 1.05 at the low $p(O_2)$ end are close to the value of -1/6. Figure 6-5 shows an Arrhenius plot of the electrical conductivity at $p(O_2) = 10^{-16}$ MPa for the case $m = 1.05$ in comparison to data for stoichiometric non-doped $BaTiO_3$ reported by Chan et al.[44] The activation energy for conduction in this area of oxygen partial pressure is determined to be approximately 1.8 eV. This value corresponds nearly to the reported one by Chan et al. (2.0 eV). Both these observations, the slope in the Kröger-Vink diagram as well as the activation energy allow the conclusion that intrinsic reduction of $BaTiO_3$ is taking place here.

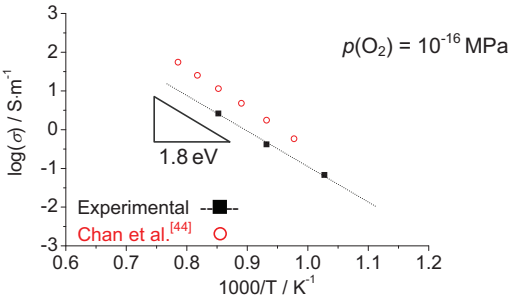

Fig. 6-5: Arrhenius plot of conductivity for $(Ba_{1.048}La_{0.002})TiO_3$ ($m = 1.05$) at $p(O_2) = 10^{-16}$ MPa, in comparison with the one for pure $BaTiO_3$ reported by Chan et al.[44]

At the high $p(O_2)$ region between 10^{-6} and 10^{-1} MPa the conductivity behavior of the BaO-rich PTCR compositions is quite striking. For $m = 1.03$ conductivity still falls with increasing $p(O_2)$ but this dependence becomes weaker at lower temperatures. In the case of $m = 1.05$, however, the conductivity is here enhanced with increasing $p(O_2)$. This positive slope in the respective region of the modified Kröger-Vink diagram indicates p-type semiconductivity, suggesting that electric transport is dominated by the motion of electron holes. It might be surprising that still in spite of a net donor doped material p-type conduction is observed, apparently the dominating effect of grain boundaries appears here. This behavior is also suggested by results gained

from measurements of the Seebeck coefficients as shown in figure 6-6. Whereas in the case of m = 1.01 (figure 6-6 (a)) perfect confirmation for n-type behavior was found (Seebeck coefficient S = -600.4 μV/K), BaO-rich compositions show a more complex behavior (figure 6-6 (b)), probably due to the electrical inhomogeneity or overlap of n-type and p-type conducting regions in the material. It is known that mixed conduction in the material reduces the absolute value of Seebeck cefficient.[125] The value of Seebeck coefficient obtained for m = 1.01 is within the same range reported by other groups,[126,127] confirming that measurement itself was conducted in a quite reliable manner.

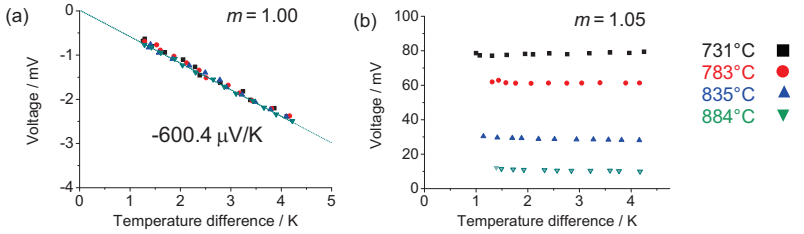

Fig. 6-6: Measurements of the Seebeck effect performed on (a) $(Ba_{1.008}La_{0.002})TiO_{3+\delta}$ and (b) $(Ba_{1.048}La_{0.002})TiO_{3+\delta}$ at various temperatures in air ($p(O_2)$ ~ 10^{-2} MPa).

Yoo et al. also report on partial p-type conduction in donor-doped $BaTiO_3$ ceramics by measuring thermoelectric power.[128] These authors found in particular for B-site deficient $Ba_{0.99}La_{0.01}Ti_{0.9975}O_3$ that the transference number of electron holes may reach 0.15 and that total electric conduction is therefore determined by 15% through a p-type mechanism. In this work this partial p-type conduction is related to the formation of Ti vacancies. This means, in other words, that p-type conduction is not completely inconsistent with donor-doped $BaTiO_3$ as presented in this study.

6.2.3 The intrinsic minimum of conductivity

At the intrinsic minimum of conductivity, which corresponds to the partial pressure of oxygen $p(O_2)_{min}$ with the lowest value of conductivity in the Kröger-Vink representation, the contributions of electrons and electron holes are equal, as expressed by equation 6-2:

$$\sigma_n = e \cdot n \cdot \mu_n = e \cdot h \cdot \mu_h = \sigma_h \qquad \textbf{Eq. 6-2.}$$

The intrinsic minimum represents “electronic” stoichiometry in the material.[129] When the mobility values of both electron and electron hole are identical, the intrinsic

minimum also corresponds to stoichiometry: namely oxygen deficiency or surplus is zero. The concentration of electrons *n* and electron holes *h* are derived from the law of mass action as outlined in section 3.2. The corresponding defect chemical equilibria are:

$$O_O^{\times} \rightleftharpoons V_O^{\bullet\bullet} + 2e + 1/2O_2^{(g)} \qquad \text{(Reduction)} \qquad \textbf{Eq. 6-3,}$$

$$V_O^{\bullet\bullet} + 1/2O_2^{(g)} \rightleftharpoons O_O^{\times} + 2h \qquad \text{(Oxidation)} \qquad \textbf{Eq. 6-4.}$$

According to these expressions and with the use of the corresponding equations that represent the respective law of mass action the value of $p(O_2)_{min}$ can be predicted by equation 6-5:

$$p(O_2)_{min} = \left(\frac{\mu_n}{\mu_h}\right) \cdot \frac{K_{red}^0}{K_{ox}^0} \cdot \exp\left(\frac{\Delta H_{ox} - \Delta H_{red}}{k_B T}\right) \cdot \frac{1}{[V_O^{\bullet\bullet}]^2} \qquad \textbf{Eq. 6-5.}$$

Assuming that the concentration of oxygen vacancies $[V_o^{\bullet\bullet}]$ is governed by acceptor impurities in the region of the conductivity minimum, the next approximation holds:

$$2[V_O^{\bullet\bullet}] \approx [A'] \qquad \textbf{Eq. 6-6.}$$

Similar expressions can be set up for higher charged acceptors. The relation in equation 6-6 implies together with equation 6-5 that the relationship between acceptor concentration [A'] and $p(O_2)_{min}$ can be expressed by:

$$\left(\frac{\partial \ln[p(O_2)_{min}]}{\partial \ln[A']}\right)_{T=\text{const}} = -2 \qquad \textbf{Eq. 6-7.}$$

This derivative expresses that an increase in the acceptor concentration [A'] always brings about a shift of $p(O_2)_{min}$ to lower values: quantitatively, a difference of one order of magnitude for [A'] results in shift of $p(O_2)_{min}$ by two orders of magnitude.[44]

Comparing the position of $p(O_2)_{min}$ for different BaO additions in figure 6-2(c) in fact a shift to lower values of oxygen partial pressure with increasing BaO content seems to occur. This suggests that BaO-excess in the materials investigated in this study acts as an effective acceptor.

This acceptor-type character was confirmed by examining the cases of stoichiometric and off-stoichiometric nominally undoped $BaTiO_3$. Lee et al.[130] reported that the incorporation of excessive BaO into the perovskite lattice of $BaTiO_3$ requires a relatively long heat treatment, because the migration of titanium vacancies requires a huge activation energy involved in this process.[37,38] Therefore three samples were

prepared to examine the acceptor-type effect by BaO addition: (i) undoped stoichiometric $BaTiO_3$ (m = 1.00), (ii) undoped over-stoichiometric $BaTiO_3$ (m = 1.05) and (iii) undoped over-stoichiometric $BaTiO_3$ (m = 1.05, soaked at 1300°C for 30 hours) Figure 6-7 shows the corresponding Kröger-Vink representations. The position of the intrinsic conduction minimum was estimated by extrapolation from the corresponding n-type and p-type branches of the conductivity curves. A comparison of the three samples at 700°C is shown in figure 6-7 (d). In the latter case the intrinsic minimum is shifted from $p(O_2) = 10^{-6.5}$ MPa down to $p(O_2) = 10^{-8.4}$ MPa. Further it could be shown that BaO-rich $BaTiO_3$ always has a smaller $p(O_2)_{min}$ for all temperatures studied here. These findings support the assumption of partial p-type conductivity behavior in BaO-excess donor-doped $BaTiO_3$.

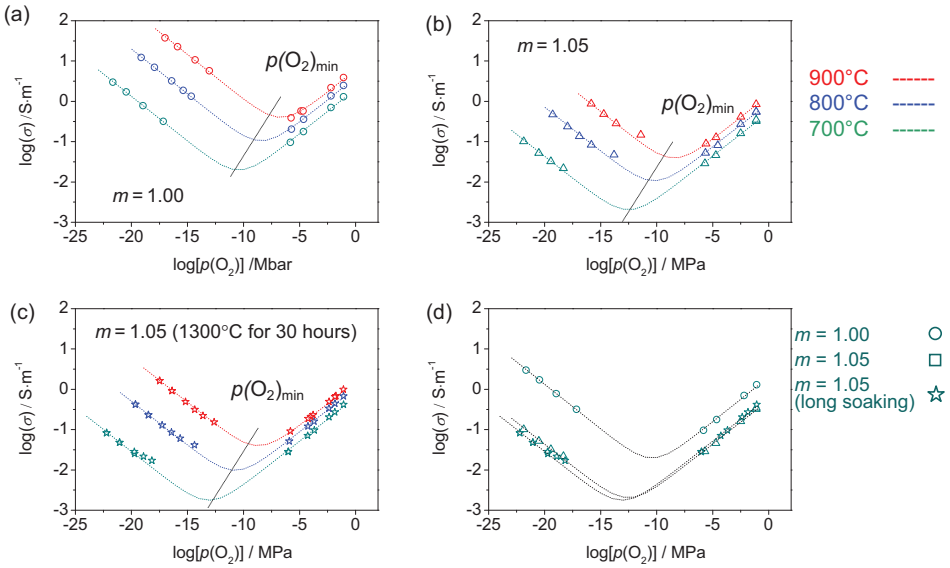

Fig. 6-7: Kröger-Vink diagrams for (a) stoichiometric (m = 1.00), and (b) hyper-stoichiometric (m = 1.05) nominally non-doped Ba_mTiO_{3+m} for normal sintering (1350°C for two hours) (c) m = 1.05 for long soaking (1300°C for 30 hours after normal sintering). (d) Comparison of the conductivities between m = 1.00 and 1.05 at 700°C.

6.3 P-type conductivity and its relation to the PTCR effect

The occurrence of p-type conduction in the present PTCR ceramics suggests that this mechanism is correlated with the electrical properties of the grain boundary regions, since normally donor-doped $BaTiO_3$ behaves as an n-type semiconductor as shown in the case of m = 1.01. For this reason the p-type regime was investigated in

more detail in order to obtain a clearer insight into the defect chemistry behind the PTCR effect of BaO-rich ceramics based on $BaTiO_3$.

Figure 6-8 shows an Arrhenius representation of the conductivity in the p-type regime for the composition $(Ba_{1.048}La_{0.002})TiO_{3+\delta}$ measured at a partial pressure of oxygen of $p(O_2) = 10^{-1}$ MPa. As a reference the data reported on nominally undoped $BaTiO_3$ from Chan et al.[44] is also included. According to the results the activation energy for electric conduction apparently shows two different temperature regimes. At elevated temperatures above 800°C the activation energy amounts to 1.58 ± 0.38 eV and below 800°C a smaller value of 0.66 ± 0.02 eV is found, which is very close to that reported by Chan et al. (0.56 eV). The low temperature activation energy was attributed by Chan et al. to the oxidation of $BaTiO_3$ according to equation 6-4. Therefore the activation energy determined here represents another evidence for p-type conduction, namely indicating the formation of electron holes. A different value of activation energy at high temperatures in donor-doped $BaTiO_3$ has also been described by Itoh et al.[118] and Shirasaki et al.[119] In their work the activation energy drastically changed from 0.62 – 0.67 eV to 2.32 – 2.88 eV above 950°C and they attributed this transition to the dissociation of defect complex $(V_o^{\bullet\bullet}\text{-}V_M'')^{\times}$ or the additional release of oxygen from the lattice. In both these cases p-type conduction is enhanced due to the increase of the concentration of free oxygen vacancies. Since one oxygen vacancy is correlated to two electron holes the activation energy per charge carrier would be half of the measured value. Possibly the increase of oxygen vacancy concentration is responsible for the higher conductivity above 850°C.

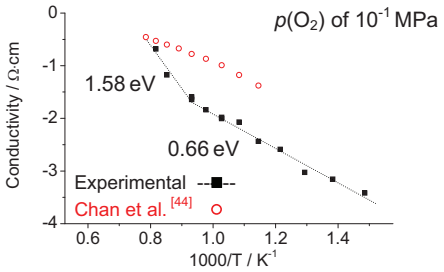

Fig. 6-8: Arrhenius plot of conductivity in $(Ba_{1.048}La_{0.002})TiO_{3+\delta}$ measured in pure oxygen, $p(O_2)=10^{-1}$ MPa at T = 450 – 950°C. The reference data reported by Chan et al. is for pure $BaTiO_3$.[44]

In order to clarify how the defect chemistry in the p-type regime affects the PTCR behavior the electrical conductivity, the impedance spectra of ceramics that were

annealed ex-situ at 700°C for two hours at different partial pressures of oxygen in the range from 10^{-20} up to $10^{-2.5}$ MPa after sintering were investigated. The magnitude of the resistivity increase above the Curie temperature T_C is quantified by the parameter η, which is defined by:

$$\eta = \log\left(\frac{\rho(250°C)}{\rho(20°C)}\right) \qquad \textbf{Eq. 6-8.}$$

ρ(250°C) and ρ(20°C) represent the resistivity values in the hot state at 250°C and in the cold state at 20°C respectively. The dependence of DC conductivity and η from the partial pressure of oxygen applied during post sintering annealing for the composition $(Ba_{1.048}La_{0.002})TiO_{3+\delta}$ is shown in figure 6-9 (a). The corresponding temperature characteristics revealing the influence of $p(O_2)$ on the PTCR effect are represented in figure 6-9 (b).

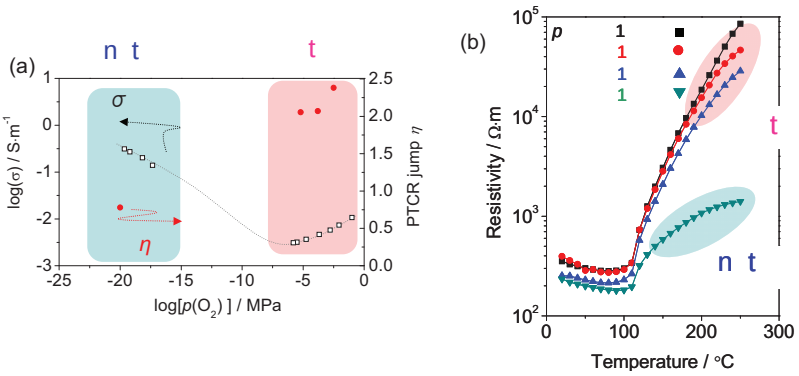

Fig. 6-9: (a) DC conductivity and the PTCR parameter η in dependence of $p(O_2)$ at 700°C.
(b) Temperature characteristics of resistivity depending on $p(O_2)$.The material composition considered here is $(Ba_{1.048}La_{0.002})TiO_{3+\delta}$ and the electrical properties were determined after ex-situ annealing at 700°C.

The results clearly prove that the PTCR jump is directly related to the conductivity type in the modified Kröger-Vink diagram of figure 6-8 (a), where a drastic increase of η appears when BaO-rich and La-doped $BaTiO_3$ is annealed above an oxygen partial pressure of $10^{-6.2}$ MPa. This significant enhancement is apparently related to the appearance of p-type conductivity at relatively high values of $p(O_2)$, which is connected with the oxidation of the grain boundaries.

6.4 The case of Nb-doped $BaTiO_3$ with BaO-excess

Before finally concluding the defect chemistry of BaO-excess PTCR compositions based on $BaTiO_3$, a possible scenario has to be excluded. The high amount of BaO added could result in expelling the La-donor ions from the A-site of the perovskite structure causing a reduction of the effective donor concentration in the grain interior. Since the donor content of the PTCR ceramics studied in this work is rather low, a direct analytical detection by electron spectroscopic methods, such as EDX, is problematic, unless local segregation or enrichment occurs.

To exclude this hypothetic assumption Nb-doped $BaTiO_3$ has been prepared and its electric characteristics have been investigated. The ionic radius of the Nb^{5+} (64 pm for six-fold coordination) is very similar to that of the Ti^{4+} ion (60.5 pm).[33] For this reason it is believed that the donor Nb^{5+} preferentially occupies the B-site in the perovskite lattice. Since the chemical composition studied in this context is rich in BaO, it is highly probable that Nb^{5+} is completely soluable in $BaTiO_3$, unless Nb_2O_5 and BaO form secondary phases. Figure 6-8 shows the PTCR characteristic and the Kröger-Vink diagram of Nb-doped (0.2 mol%) barium titanate with 5 mol% of BaO excess.

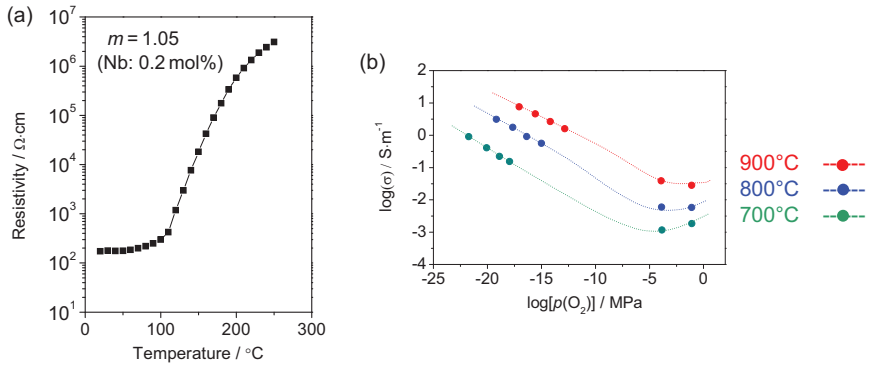

Fig. 6-10: (a) Temperature characteristics of resistivity and (b) DC conductivity depending on $p(O_2)$ at intermediate temperatures. The material composition considered here is $Ba_{1.05}(Ti_{0.998}Nb_{0.002})O_{3+\delta}$ and the electrical properties were determined after ex-situ annealing at 700°C.

The results clearly demonstrate that the PTCR effect in BaO-rich $BaTiO_3$ does not depend on the kind of donor used. Even if a donor that occupies the B-site is used a strong increase of resistivity is observed at T_C. Decisive is the crucial BaO-excess not the donor. The Kröger-Vink diagram for Nb-doped $BaTiO_3$ shows again p-type

conductivity in the regime of high $p(O_2)$ values. Chan and Smyth reported that a small portion of Nb even around 0.02 mol% is enough to achieve n-type conductivity over the whole $p(O_2)$ regime measured here.[45] The barium titanate composition described in figure 6-10 contains a concentration of Nb donor one order of magnitude higher than that from Chan and Smyth, suggesting the strong p-type (acceptor) contribution by the BaO addition.

6.5 The mechanism of the PTCR effect base on defect chemistry

This section focusses on the mechanism for the PTCR effect caused by BaO addion. Independent of the experimental evidence presented in chapters 5 and 6, two different possibilities regarding a defect chemical mechanism that explain the PTCR effect can be considered. The first one is the model proposed by Daniels and Wernicke taking into account the formation of metal vacancies in the grain boundary regions.[19] The second one considers the incorporation of BaO into the perovskite lattice of the phase $BaTiO_3$. Equations 6-9 and 6-10 represent the respective defect chemical equilibria:

$$2La_2O_3 \rightleftharpoons 4La_{Ba}^{\bullet} + 6O_O^{\times} + 4V_{Ti}'''' \qquad \textbf{Eq. 6-9,}$$

$$\begin{aligned} &m\text{BaO}+\text{BaTiO}_3 \rightleftharpoons \text{Ba}_{1+m}\text{TiO}_{3+m} \\ &\equiv (1+m)\text{Ba}_{\text{Ba}}^{\times} + \text{Ti}_{\text{Ti}}^{\times} + m\text{V}_{\text{Ti}}'''' + (3+m)\text{O}_{\text{O}}^{\times} + 2m\text{V}_{\text{O}}^{\bullet\bullet} \end{aligned} \qquad \textbf{Eq. 6-10.}$$

The first case can be immediately excluded in the present case for the following reasons. Daniels et al.[19] claimed that metal vacancies are formed only close to the grain boundaries in order to compensate the positive charges of the donor during the cooling process. In the grain interior these positive charges are balanced by electrons. With this defect chemical model, Daniels et al. explained the PTCR effect. The reaction responsible for the creation of metal vacancies, however, necessitates high temperatures (above 1000°C) and high oxygen partial pressures. Otherwise electron compensation is more favorable. High temperatures and partial pressures of oxygen are however contradictory to the processing conditions used for the realization of reduction resistant BaO-rich compositions of $BaTiO_3$-based PTCR ceramics. A distinct and large resistivity increase above T_C is obtained after sintering under reducing conditions and a subsequent annealing treatment at moderate temperatures (typically 700°C), far below the temperature at which the Schottky reaction activates. Thus simple metal vacancy compensation represented by

equation 6-9 does not seem feasible for the materials considered in the present study.

The second scenario presented in equation 6-10 has to be regarded as controversial. It has been accepted for a long time that the concentration of incorporated BaO into $BaTiO_3$ is quite small. Hu and Smyth[100] reported that the solubility limit of BaO in barium titanate is not more than 100 ppm. This solubility limit was deduced from defect chemical investigations based on high-temperature conductivity measurements. Only rather recently the idea that even more BaO is soluable is supported by several studies. Lee and Randall reported that up to 1 mol% of BaO can be incorporated into the lattice of $BaTiO_3$ at least at elevated temperatures above 1300°C, which correspond to a range in which sintering is typically carried out. This observation was based on differential thermal analysis.[131] Ihlefeld et al.[132] even found a total BaO-incoroporation into $BaTiO_3$ thin films up to 5 mol%. From the viewpoint of kinetic reasons related to metal vacancies,[60,130] it seems that rather conflicting experimental results have been presented.

Based on this background it is therefore realistic to assume that upon sintering sufficiently large amounts of BaO are soluable in $BaTiO_3$, at least or in particular in the grain boundary regions. As expressed in equation 6-10 extra BaO in the lattice is accompanied by the formation of titanium and oxygen vacancies. The oxygen vacancies, however, may be easily filled with atmospheric oxygen even at moderate temperatures. Titanium vacancies however are considered to be frozen-in in this temperature range due to their high migration enthalpy.[29] Oxygen vacancies act as a source of electron holes as described by equation 6-4. According to this reaction, p-type conductivity can be expected by the incorporation of BaO. Strong experimental evidence for the local existence of p-type conductivity has been presented in the present work (see figures 6-2, 6-7).

Figure 6-11 illustrates a schematic Kröger-Vink diagram together with a view on the defect chemical and electrical character of the grain boundaries in BaO-excess $BaTiO_3$ thermistors after annealing in the n-type and in the p-type regime of partial pressure of oxygen.

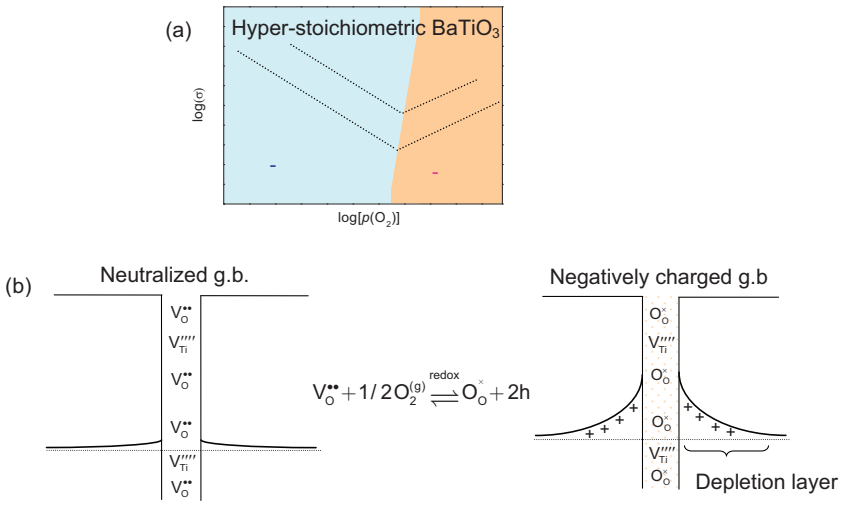

Fig. 6-11: Schematic representation of the defect chemistry in hyper-stoichiometric donor doped barium titanate and the consequences for the electric character of the grain boundaries in respective PTCR ceramics:
(a) Schematic Kröger-Vink devided into two conductivity regimes: n-type behavior for reducing and p-type behavior for oxidizing conditions. (b) Model of the defect chemistry in the grain boundaries after annealing in reducing (n-type conduction) and oxidizing (p-type conduction) conditions.

Due to the relatively short dwelling time during sintering, BaO uptake of the Peroskite lattice of barium titanate is considered to take place mostly at the grain boundaries. According to the respective oxygen partial pressure the redox reaction is believed to occur at the grain boundaries. During annealing under oxidizing conditions at higher values of $p(O_2)$ the oxygen vacancies formed during sintering are – at least partially – filled by ambient oxygen gas. In consequence titanium vacancies and electron holes dominate the defect chemistry of the grain boundaries. During operation of the resulting PTCR material at room temperature or low temperatures below T_C electron holes are mostly immobile or captured by the acceptor states created through V_{Ti}''''. This results in the formation of an electrically insulating layer at the grain boundaries. This model description is very similar to the concept proposed by Waser et al. regarding the improvement of electrical degradation of insulating dielectric ceramics based on $BaTiO_3$ sintered under reducing conditions.[47]

At very low partial pressures of oxygen donor-type oxygen vacancies represent the majority defect chemical species that create large amounts of free electrons. This results in the annihilation of the electrically insulating layer at the grain boundaries

and in consequence the PTCR effect is expected to vanish. This view is in accordance with the results shown for BaO-rich ceramics annealed at different $p(O_2)$ as shown in figure 6-9. Chiang and Takagi have refined Daniels model and claimed that acceptor-rich grain boundaries are formed due to intrinsic positive charges at the grain boundary core.[133] Negatively charged metal vacancy acceptor states are formulated due to intrinsic positive charges at grain boundaries. On the other hand, positive charges are neutralized by oxygen adsorption or oxidation during the cooling process after sintering or during subsequent annealing. The authors postulated that this acceptor state is the origin of the PTCR effect. In the present study titanium vacancies formed during sintering due to BaO-incorporation have been identified to represent these formerly unknown acceptor states. The metal vacancies remain frozen at intermediate temperatures or below. The present explanation is consistent with the view proposed by Chiang and Takagi.[133 (b)]

6.6 Summary

In the present chapter, results on the dependence of DC conductivity from temperature and partial pressure of oxygen have been presented and discussed. The Kröger-Vink diagram that illustrates this dependence is strongly influenced by the (Ba+La)/Ti ratio *m* because incorporation of BaO in the perovskite phase $BaTiO_3$ results in a shift of the intrinsic conductivity minimum to lower values of $p(O_2)$. This shift is also observed in ceramics without donor doping, confirming that the addition of excessive BaO has an acceptor character. Impedance spectroscopic measurements described in chapter 5 showed that the insulating grain boundary resistance is strongly affected by the BaO-content in hyper-stoichiometric compositions. These insulating grain boundaries show p-type conduction at high partial pressures of oxygen. The origin of this p-type behavior is believed to originate from the formation of oxygen and titanium vacancies upon incorporation of excessive BaO in the lattice especially around the grain boundaries. The key factor that is necessary to realize the PTCR effect in reduction-resistant BaO-rich donor-doped $BaTiO_3$ ceramics is the formation of these Ti vacancies as acceptor centers in the grain boundaries. Different activation energies for electric conduction in the oxidizing regime support the idea, already expressed in chapter 5 in connection with the diffusivity of oxygen vacancies, that dissociation of metal and oxygen defect associates plays an important role. The superposition of the n-type conducting grain interior and the p-type conducting grain

boundaries could further be evidenced by measurements of the Seebeck coefficient. A comparison with Nb-doped PTCR ceramics with BaO excess proved that not the kind of donor – occupying preferentially the A-site as in the case of La or the B-site , on the other hand, as in the case of Nb – is decissive for the defect chemistry related to the PTCR effect. Important is only the excess in BaO.

Chapter 7
PTCR effect in ultrafine grained $BaTiO_3$ ceramics

7.1 Introduction

Regarding the general technological trend of further miniaturization of many kinds of passive electronic components, also multilayer PTC thermistors on $BaTiO_3$-basis should be as small as possible. This development is driven by the ongoing reduction of dimensions in electronic circuitry for many applications that require high performing miniaturized components without forfeiting a loss in their functionality. Insulating dielectric devices based on $BaTiO_3$ are at present produced as multilayer ceramic capacitors with a layer thickness of 300 nm.[134] Each dielectric layer is built up by less than 10 ceramic grains on the top of each other and in consequence the grain size must be well below 100 nm. In this dimensional range many physical properties distinctly depend on the grain size, a phenomenon that is commonly referred to as "size effect".[34,91,92] In the specific case of nanostructured $BaTiO_3$ ceramics, the material parameter that determines ferroelectric ordering and thus the magnitude of the dielectric constant deteriorates with decreasing grain size. On the other hand industrial modern multilayer thermistors based on reduction-resistant $BaTiO_3$ compositions similar to those reported in chapters 5 and 6 presently have a layer thickness of approximately 20 μm that consist of grains with an average size of a few μm. Similar to the case of MLCC, the further reduction of grain size is believed to have a theoretically determined lower limit,[81,135] below which the PTCR characteristics must vanish. If the grain size comes into the range of the width of the insulating grain boundary layer the volume fraction for the semiconducting interior of the grains gradually becomes smaller with decreasing grain size, until finally the interface barrier would overlap.[137,138] In this speculative scenario the material is expected to become completely insulating or at least charge neutrality requires that the characteristics of the space charge layers essentially change. The fundamental scientific question that arises at this point is, whether it is generally possible to realize $BaTiO_3$-based PTCR ceramics with a grain size of only a few hundreds of nm and if such a theoretical lower limit exists or not. This is the subject of the present part of this thesis.

Basically processing of such ultrafine grained materials by conventional ceramic technology is problematic because powder agglomeration and grain growth at elevated sintering temperatures generally do not allow achieving such small grain sizes. Therefore microemulsion mediated synthesis of nanocrystalline $BaTiO_3$ powders[83] with a very sharp particle size distribution in combination with consolidation by spark plasma sintering (SPS)[138] was used to prepare ultrafine grained ceramics. This chapter is committed to the question whether such a reduction of grain size is feasible for the realization of miniaturized multilayer PTCR components.

Following up the last two chapters on BaO-rich $BaTiO_3$ compositions two cases are envisaged in this study: stoichiometric and hyper-stochiometric La-doped $BaTiO_3$. The latter composition relates to the ones used in chapters 5 and 6 of the present thesis and was prepared to verify if the material concept described there can be applied also for ultrafine grained ceramics.

7.2 Microstructural and analytical characterization

Figure 7-1 shows a TEM image of the as-synthesized stoichiometric $BaTiO_3$ nanopowder doped with 0.2 mol% La. The picture indicates that the primary particles after powder preparation are nearly monodisperse and that the average particle size is approximately 10 to 20 nm.

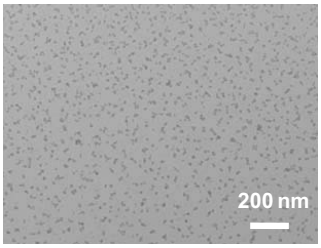

Fig. 7-1: TEM image of the as synthesized stoichiometric $(Ba_{0.998}La_{0.002})TiO_3$ nanopowder revealing a sharp and narrow particle size distribution.

It is apparent that the nanopowder has a rather sharp and narrow particle size distribution. The question whether La-doping is distributed homogeneously after synthesis is difficult to answer, because the nominal concentration of 2000 ppm is too small to be detected in a reliable way by electron spectroscopy such as EDX. Two

basic material compositions have been prepared: one is stoichiometric and the second one contains a BaO-excess of 2 mol%.

In order to determine a suitable calcination temperature for the removal of organic residues like surfactants from the raw powder thermogravimetric measurements were carried out. The result is shown in figure 7-2. Even 24 hours of rinsing the powders with cyclohexane under reflux was not sufficient to remove the surfactants thoroughly. The complete burnout of these organics is however necessary to prevent gas emission and contamination during SPS. A large weight loss during continuous heating occurs at approximately 650°C.

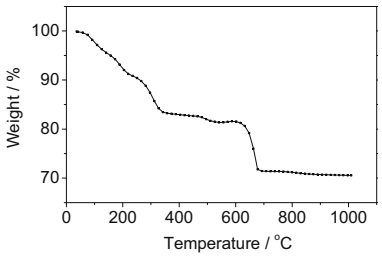

Fig. 7-2: TGA result showing a continuous weight loss of stoichiometric $(Ba_{0.998}La_{0.002})TiO_3$ nanopowders upon heating to a temperature of approximately 1000°C.

Above this critical temperature no further loss in weight is observed. The total weight loss upon heating up to 650°C could be attributed to the pyrolysis of the surfactant and the removal of physically or chemically adsorbed water. On the basis of these results all powders were calcined at 700°C for one hour before SPS consolidation. The resulting average particle size after this heat treatment was verified by measuring the free surface through N_2 gas adsorption (BET method). The average particle size according to BET d_{BET} is calculated from the density ρ and from the specific surface area S_{BET} using the following relationship:[83]

$$d_{BET} = \frac{6}{\rho \cdot S_{BET}} \qquad \textbf{Eq. 7-1.}$$

Table 7-1 summarizes the results from this analysis.

Powder	BaO-excess [mol%]	S_{BET} [m^2/g]	d_{BET} [nm]
D-1	0	4.49	223
D-2	2.0	7.10	141

Tab. 7-1: Average particle sizes after calcination estimated from BET specific surface area.

The crystallinity and phase purity of both, the as-synthesized as well as of calcined powders were investigated using XRD. The results are presented in figure 7-3.

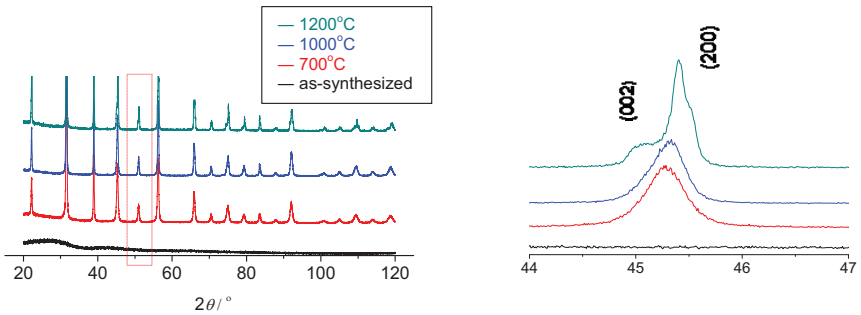

Fig. 7-3: XRD patterns (left part) of raw and calcined powders for the composition $(Ba_{0.998}La_{0.002})TiO_3$. In the right part the (200) and (002) Bragg reflection peaks are shown in a higher magnification.

The as-prepared powder is amorphous: no peak corresponding to the perovskite structure can be identified. After annealing at a temperature of 700°C or even higher the specific reflection peaks of $BaTiO_3$ appear. Below 1000°C the structure is pseudo-cubic, above 1200°C the lattice is tetragonally distorted resulting in a splitted (200)/(002) reflection line at a Bragg angle of approximately 45°.

Figure 7-4 (a) shows a dilatometer curve representing the consolidation profile during spark plasma sintering at 1000°C in Ar. The mechanical pressure applied during the process was 75 MPa and the current was 400 to 600 A. Shrinkage starts at about 800°C and consolidation is completed within a few minutes after the maximum temperature upon heating is reached. An example of the resulting densified ceramic is shown in figure 7-4 (b).

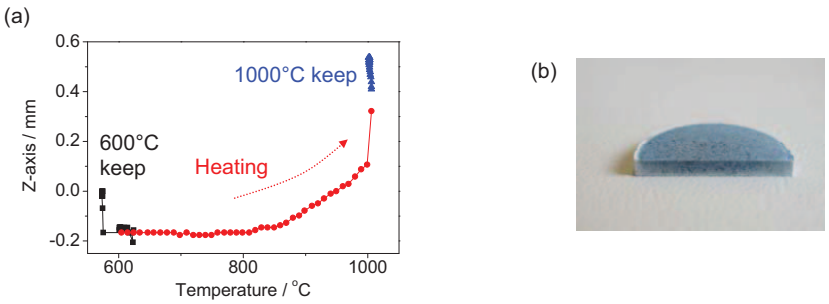

Fig. 7-4: (a) SPS profile for the consolidation of ultrafine grained $(Ba_{0.998}La_{0.002})TiO_3$ processed at 1000°C for 5 minutes at a pressure of 75 MPa. The heating rate is 90°C/min. (b) SPS processed ceramic pellet with the composition $(Ba_{0.998}La_{0.002})TiO_3$.

As can be recognized from figure 7-4 (b) the consolidated nanoceramics are basically bluish in color, but at the fringe a white border occurs. Possibly this is due to an inhomogeneous temperature distribution over the materials volume. The densities of both the stoichiometric and hyper-stoichiometric compositions were confirmed to be larger than 5.81 g/cm^3 through measurements based on the Archimedes method. The relative density values are well above 96% of the theoretical density of $BaTiO_3$.

Figure 7-5 presents XRD patterns of consolidated stoichiometric ceramics in comparison with the one obtained from the corresponding original calcined powder. It proves their phase purity. A closer view on the (200) Bragg reflection peak at approximately 45° reveals that the sintered ceramic shows considerable peak broadening. Basically two different factors responsible for this broadening can be thought of: (i) refinement of the grain size and (ii) internal stresses. Since a reduction of grain size can be excluded it is believed that the high pressures applied during SPS are the cause for peak broadening by internal mechanical distortions. Remarkable is that even after spark plasma sintering at 1000°C no tetragonal splitting of the (200) peak is observed.

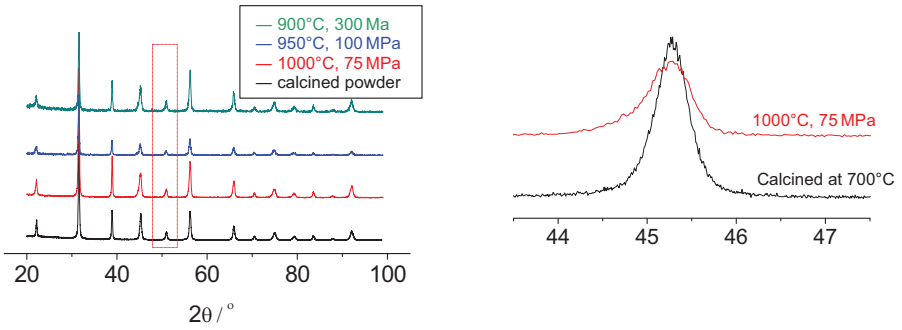

Fig. 7-5: XRD patterns of nanocrystalline $(Ba_{0.998}La_{0.002})TiO_3$ consolidated by SPS with different processing conditions (temperature and mechanical pressure). The right part shows a comparison with the initial powder, that was calcined before SPS at 700°C.

Observation of the microstructure by TEM (figure 7-6 (a)), however, clearly reveals the presence of ferroelectric domains, which are an important prerequisite for the reduction the electric resistivity of grain boundary regions below the Curie temperture in PTCR ceramics.[18] The image presented here also obviously demonstrates the high density and the small average grain size achieved (figure 7-6 (b)): a statistical evaluation resulted in a value of less than 200 nm for all sintering conditions applied. This implies that practically no grain growth occurred during densification and in summary it can be concluded that the grain size is very much below typical values

observed in classical PTCR ceramics on $BaTiO_3$-basis where anomalous grain growth usually may take place.

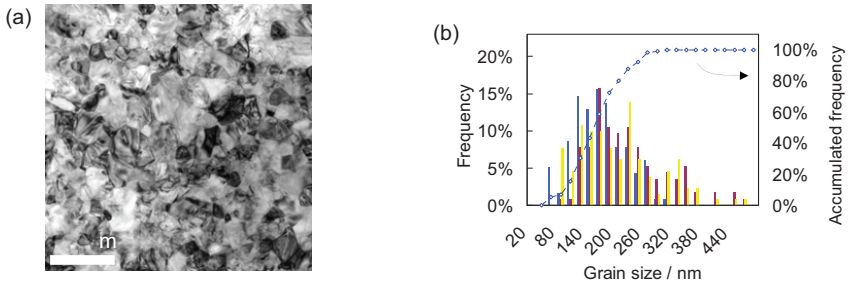

Fig. 7-6: (a) TEM image of SPS processed $(Ba_{0.998}La_{0.002})TiO_3$ ceramics sintered at 1000°C with an external pressure of 75 MPa after reoxidation at 500°C. (b) Grain size distribution for the same composition but for various sintering temperatures and pressures. (Blue: 900°C and 300 MPa, red: 950°C and 100 MPa and yellow: 1000°C and 75 MPa)

7.3 Electrical characterization

Since the partial pressure of oxygen during SPS could be relatively low ($p_{O_2}^{CO_2/C}(1000°C) = \sim 10^{-21}$ MPa), reoxidation of the grain boundaries is essential for realizing the PTCR effect. This indispensable heat treatment was typically carried out at 500°C in order to avoid substantial grain growth. It must be pointed out that the annealing temperature applied is significantly lower than the one used for Ti-rich barium titanate thermistors, which is typically 800 – 1200°C.[139-141] The second important requirement, however, is a low cold resistance below Curie temperature. Figure 7-7 shows the influence of the consolidation temperature and annealing treatment on the cold resistivity of stoichiometric and hyper-stoichiometric La-doped $BaTiO_3$ with ultrafine grain size.

As a general trend ceramics sintered at higher temperatures result in lower cold resistivity, no matter whether they were reoxidized or not. This indicates that the incorporation of La into the lattice of $BaTiO_3$ is not completely achieved at the respective sintering temperature. After reoxidation at 500°C for two hours in air the cold resistivity drastically decreases, especially for low sintering temperatures. Compared to conventional and relatively coarse grained PTCR ceramics on $BaTiO_3$-basis which are typically reoxidized in a temperature range between 800 and 1200°C, the reoxidation temperature is extremely low.

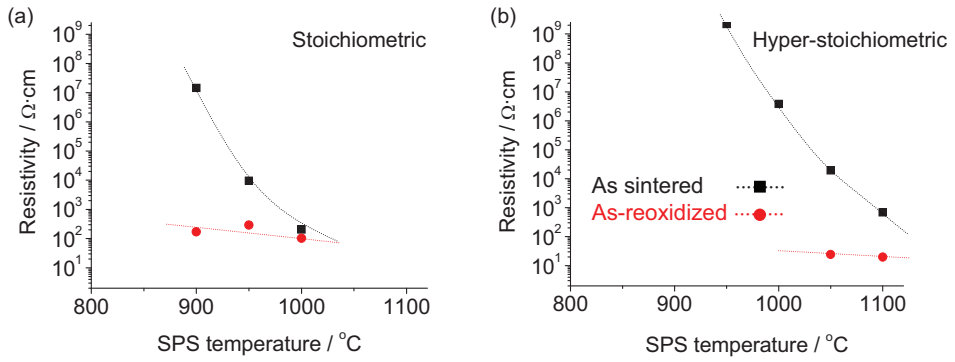

Fig. 7-7: Room temperature resistivity measured at 20°C for ultrafine grained (a) stoichiometric and (b) hyper-stoichiometric La-doped $BaTiO_3$. The black symbols and curves correspond to the as sintered condition and the red ones to the reoxidized state after annealing at 500°C in air.

It is believed that the small grain size also implies an improved diffusivity of oxygen during reoxidation. Since generally a cold resistivity above 10^5 Ω·cm is too high for realizing the PTCR effect, only ceramics sintered at high temperatures were considered in the further studies.

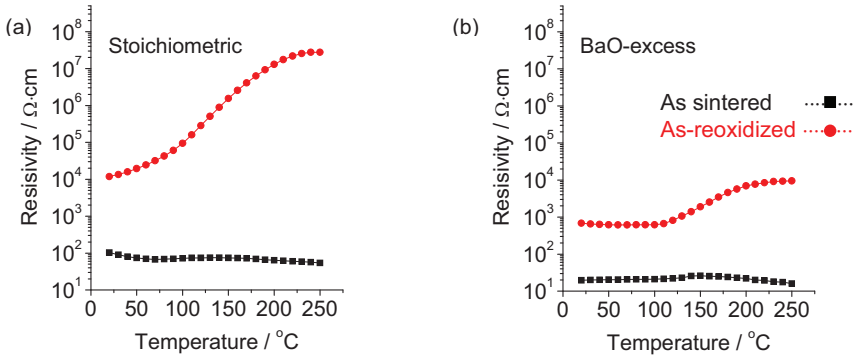

Fig. 7-8: Temperature dependence of resistivity for ultrafine grained (a) stoichiometric La-doped $BaTiO_3$ sintered at 1000°C and (b) hyper-stoichiometric La-doped $BaTiO_3$ sintered at 1100°C. The black symbols correspond to the as sintered condition and the red ones to the reoxidized state after annealing at 500°C in air.

Excellent PTCR characteristics are obtained for the stoichiometric case, which reveals an increase in resistivity of more than three orders of magnitude upon heating above the Curie temperature. The composition with BaO-excess, in contrary to earlier expectations, only results in a rather poor PTCR jump. Apparently the material concept which results in a favorable PTCR performance in relatively coarse grained ceramics (refer to chapters 5 and 6) cannot be simply transferred to ultrafine grained materials.

7.4 Discussion

7.4.1 Stoichiometric composition

To the best knowledge of the author from the present study the possibility of realizing ultrafine grained PTCR ceramics on $BaTiO_3$ has been demonstrated for the first time. In order to clarify the size effect on the PTCR characteristics of La-doped $BaTiO_3$ the oxygen absorption of fine grained and coarsened stoichiometric ceramics have been compared by thermogravimetric measurements, as shown in figure 7-9.

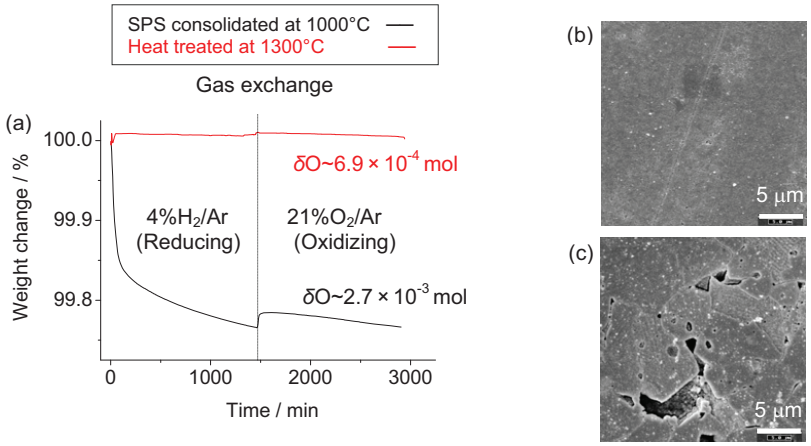

Fig. 7-9: (a) TGA profiles of ultrafine grained and microcrystalline La-doped $BaTiO_3$ ceramics in comparison at 500°C. $p(O_2)$ is altered from reducing to oxidizing atmosphere by switching the flowing gas from a 4%H_2/Ar to a 21%O_2/Ar gas mixture after 1500 min. Polished surface images taken by SEM of (b) SPS processed nano-sized ceramics (D ~ 200 nm from TEM image in figure 7-6) and of (c) the same ceramics subsequently heat treated at 1300°C for 2 hours for grain growth.

TGA is performed to investigate how much oxygen the ceramics absorb during reoxidation. For comparison two samples have been prepared: (i) SPS consolidated ceramics and (ii) subsequently annealed coarse grained ceramics (at 1300°C for two hours). With this heat treatment at elevated temperature, normal grain growth is

expected. In fact it could be confirmed by SEM as shown in Fig. 7-9 (c). This condition is referred to as microcrystalline $BaTiO_3$ hereafter. The average grain size apparently exceeds 5 μm after the heat treatment. The same piece of the specimen has been employed for TGA, the only difference is therefore whether the heat treatment at 1300°C is carried out or not. Figure 7-9 (a) shows weight change profiles at 500°C, a temperature that is equivalent to the reoxidation temperature in the previous section. The atmosphere in the TGA is altered from reducing to oxidizing condition in order to investigate how much oxygen uptake occurs in each material. The oxygen uptake δ was estimated from the weight increase at the point of gas exchange. It is estimated to be 2.7×10^{-3} mol and 6.9×10^{-4} mol per one mole $BaTiO_3$, respectively. The nano-crystalline ceramic thus absorbs four times more oxygen than the coarser one. The large decrease in reducing gas could be ascribed to the residual organic substances or liberation of crystal water, which remained even after the consolidation. Guo et al. also finds the similar experimental result, showing more oxygen uptake in nanocrystalline pure $BaTiO_3$ compared to microcrystallne one.[142] The authors have attributed this higher uptake in nanocrystalline $BaTiO_3$ to a decreased enthalpy for oxidation. In other words, nanocrystalline ceramics are easier to be oxidized. Reoxidation is vital for the realization of the PTCR effect. The readiness for oxygen uptake in nanocrystalline $BaTiO_3$ is believed to lead to the activation of the PTCR effect.

A comparison of the PTCR effect was carried out between the nanocrystalline and the microcrystalline stoichiometric $BaTiO_3$ ceramics, prepared by re-sintering SPS consolidated ceramics at 500 – 1200°C in moist H_2/Ar gas. All samples were reoxidized at 500°C in air before the electric measurements. Figure 7-10 (a) shows the temperature dependence of resistivity. Apparently only a weak PTCR effect is detected for the microcrystalline $BaTiO_3$ ceramic annealed at 1200°C. Figure 7-10 (b) shows resistivities and the PTCR jump defined by equation 6-8 in dependence of the annealing temperature. Above 1000°C apparently the PTCR parameter $\log(\rho_{max}/\rho_{min})$ decreases, because the PTCR properties deteriorate after a high temperature heat treatment. It is expected that grain growth above 1000°C takes place resulting in smaller PTCR jump. Cold- and hot-resistivity represented by ρ_{max} and ρ_{min} drastically decreases above 1000°C, suggesting enhanced further incorporation of La donor dopant into the matrix and the increase of the grain size. ρ_{max} and ρ_{min} increase in the temperature range between 700°C and 1000°C. The reason for this phenomenon is

not clear at present. In summary it has however been confirmed that the PTCR effect strongly depends on the grain size in $BaTiO_3$.

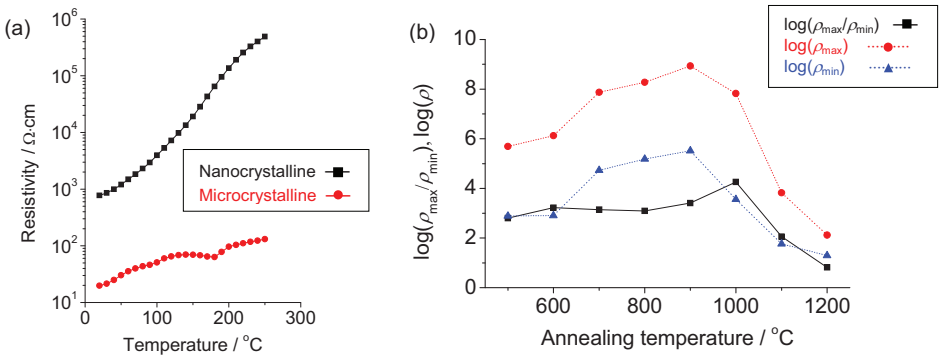

Fig. 7-10: (a) Temperature dependence of resistivity for stoichiometric La-doped $BaTiO_3$, SPS processed specimen and one after the heat treatment at 1200°C. (b) PTCR jump and maximum and minimum resistivities after the heat treatments at various temperatures.

To clarify the origin of PTCR effect in nanocrystalline La-doped $BaTiO_3$-based ceramics, a Kröger-Vink diagram has been measured at 500°C. Due to the low measuring temperature selected it is believed that a possible change in grain morphology during the experiment is avoided or at least minimized. Figure 7-11 (b) shows the saturation in conductivity after 120 hours, assuring that the measurement was done correctly.[53] Figure 7-11 (a) shows the Kröger-Vink diagram obtained for ultrafine grained $BaTiO_3$. Even upon the addition of the donor dopant, the diagram shows a positive slope at high oxygen partial pressures. This indicates p-type conduction. Considering the high cold resistivity of approximately $10^3\,\Omega$·cm, it can be speculated that the incorporation of the donor-dopant lanthanum is not completed or that at least the La ions do not work as an effective donor at the SPS processing temperatures applied. It should be mentioned in this context that the soaking time during SPS consolidation is very short (5 min).

An impedance measurement has been conducted at room temperature for assessing the conductivity. Figure 7-12 shows a complex impedance plot with two semicircular arcs. Assuming that one arc with the higher relaxation frequency is attributed to the grains of nanocrystalline $BaTiO_3$, resistivity and permittivity of the grains are estimated to be 141 Ω·cm and 6097, respectively. It should be noted that the high apparent dielectric constant deduced here is due to the high conductivity in ceramics. The resistivity value is higher than the expected value for donor-doped $BaTiO_3$ and

therefore two semicircular arcs are observed in the Cole-Cole plot. This experimental result could be other evidence indicating that lanthanum incorporation is not completed.

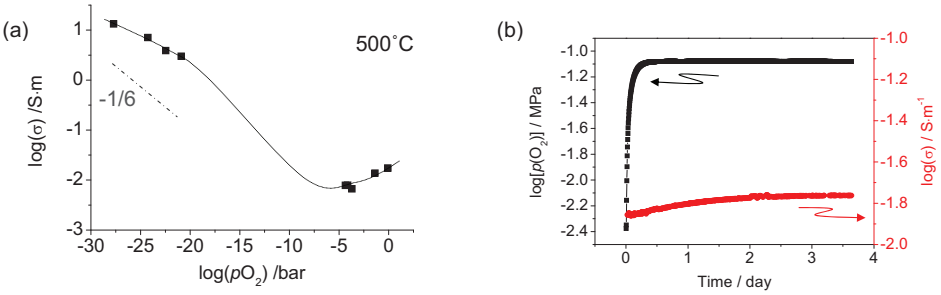

Fig. 7-11: (a) Kröger-Vink diagram measured at 500°C for ultrafine grained stoichiometric La-doped $BaTiO_3$. (b) Exemple of the time dependence of conductivity for saturation within three days after setting temperature and oxygen partial pressure.
The sample size is 1 × 1 × 6 mm^3.

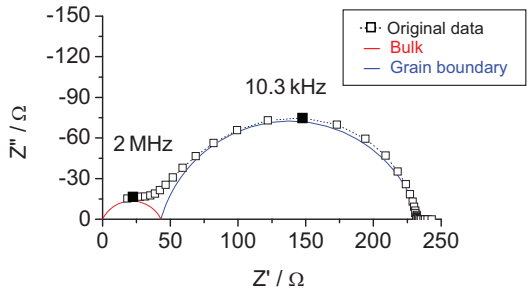

Fig. 7-12: Cole-Cole plot of a SPS processed specimen after reoxidation at 500°C. The measuring temperature is 20°C and the materials composition is stoichiometric (D-1). The sample thickness is 1.2 mm and the area is 0.39 cm^2.

7.4.2 Hyper-stoichiometric case with BaO-excess

As shown in Fig. 7-8 (b), only a poor PTCR effect is observed for hyper-stoichiometric ultrafine grained $BaTiO_3$. This could be caused by the high SPS processing temperature which causes grain growth. On the other hand, the sample processed by SPS at 1000°C has a resistivity of over 10^6 Ω·cm, as shown in Fig. 7-7 (b). This value is too high for PTCR applications. According to the results discussed in chapters 5 and 6, the hyper-stoichiometric $BaTiO_3$ was expected to yield in a satisfactory PTCR performance. The reason for this discrepancy might be related

to the missing SiO_2 additive. No SiO_2 was added in this experiment for simplicity because the powder synthesis method chosen did not allow this addition at present. Drofenik reports on the positive effect of SiO_2 to donor-doped $BaTiO_3$ ceramics with BaO-excess.[101] Samples containing SiO_2 as additive yield in much lower electrical resistance. Even if SiO_2 cannot be incorporated into the perovskite $BaTiO_3$ lattice as an impurity due to its small ionic radius (40 pm for six-fold coordination),[33] it can still modify the conductivity of the matrix by redistributing lanthanum donor ions in the microstructure during sintering. SiO_2 and $BaTiO_3$ may then also form secondary phases such as the compound Fresnoite $Ba_2TiSi_2O_8$. This phase was detected in the sample series B-1 to B-6. It is believed that the Fresnoite phase acts as a buffer for additional BaO. That is probably why the reaction represented by Eq. 7-1 could be optimised by SiO_2 addition:

$$m\,\mathrm{BaO} + \mathrm{BaTiO_3} \Leftrightarrow \mathrm{Ba_{1+m}TiO_{3+m}}$$
$$\Leftrightarrow (1+m)\,\mathrm{Ba_{Ba}^{\times}} + \mathrm{Ti_{Ti}^{\times}} + m\,\mathrm{V_{Ti}^{''''}} + (3+m)\,\mathrm{O_O^{\times}} + 2m\,\mathrm{V_O^{\bullet\bullet}} \qquad \textbf{Eq. 7-1.}$$

7.5 Summary

In the present chapter, novel PTCR properties of ultrafine grained $BaTiO_3$ are demonstrated for the first time. Nanocrystalline donor-doped $BaTiO_3$ yields in sufficiently good PTCR properties if the compositions are stoichiometric and if a mild reoxidation at rather low temperatures around 500°C is carried out. TGA measurements performed for both nanocrystalline and microcrystalline ceramics have revealed that the former absorbs significantly more oxygen under identical reoxidation conditions. Conductivity measurements at various oxygen partial pressures clarified that also here p-type conduction occurs at high partial pressures of oxygen. It has been concluded that high inclination toward reoxidation in nanocrystalline $BaTiO_3$ is responsible for the realization of PTCR properties. Coarsening the microstructure seems to result in a deterioration of the materials performance. In consequence a different mechanism determining the materials characteristics must prevail in ultrafine grained PTCR ceramics on $BaTiO_3$-basis.

Chapter 8
Optically translucent heavily La-doped $BaTiO_3$ ceramics

8.1 Introduction

$BaTiO_3$-based electroceramics are generally opaque, even though they have a rather large bandgap of ~3.0 eV. In the case of insulating dielectric materials as they are used in capacitor applications usually a light yellow color appears. Semiconducting ceramics containing a large number of free electrons have a dark blue color, because the high concentration of these charge carriers results in absorbtion of the low frequency range of visible light. On the other hand ceramics derived from the perovskite oxide $(Pb,La)(Zr,Ti)O_3$ are probably the historically most prominent and typical examples of translucent or even transparent electrooptical oxide materials.[143] In order to realize translucency in such compositions a tradeoff between high density and a small size of residual pores is unavoidable. Since pores represent the major origin of light scattering, low values of internal porosity,[144] as they generally can be achieved by elevated sintering temperatures and extended soaking times, are aimed to enhance densification. After such thermal treatment, however, a small number of very large pores often remain. Lowering the sintering temperature or limiting the duration of the thermal treatment on the other hand typically results in many rather small pores and in a too modest density. Therefore the use of nanocrystalline or ultrafine powders and the application of advanced consolidation techniques that lower the sintering temperature and shorten the consolidation time resulting in very fine grained ceramics have been proposed.[145-149] In this context for example hot pressing or plasma spark sintering (SPS) take advantage of external mechanical pressure and/or an electrical discharge that enhance densification. In consequence highly densified fine grained translucent ceramics, with only a few very small pores may be obtained.

In the present chapter the possibility of preparing translucent heavily donor-doped ceramics on $BaTiO_3$-basis exploiting the defect chemistry and the phenomenon of the so-called grain growth anomaly has been examined via conventional ceramic technology.

It is well known that donor-doped $BaTiO_3$ shows semiconduction only in a very limited concentration range. Above a critical donor concentration of approximately 0.4 – 0.5 mol%, donor-doped $BaTiO_3$ ceramics are typically insulating and reveal very small grain sizes, as shown in figure 8-1.[18,58,111,150,151] In the range of low donor concentrations where semiconductivity appears, ceramics are usually relatively coarse with an average grain size of several microns. This grain growth anomaly is a quite unique observable phenomenon for $BaTiO_3$ in the whole family of titanate-based perovskite ceramics.[13]

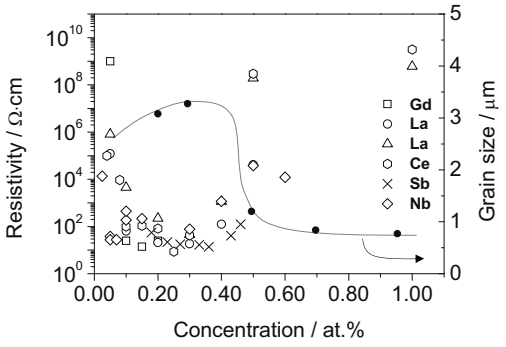

Fig. 8-1: Grain growth anomaly and the transition from electrical semiconduction to insulation in donor-doped polycrystalline $BaTiO_3$ ceramics in dependence of donor concentration for different types of doping elements. Data are taken from references [18], [58], [111], [150] and [151].

The aim of the present work is to investigate whether the application of the above-mentioned principles in addition to a defect chemical consideration allows the preparation of translucent $BaTiO_3$-based ceramics with donor levels well above the critical concentration. The possible use of nanocrystalline powders and the application of pressure assisted condolidation techniques were not taken into account. Rather the ceramics were derived from powders fabricated by conventional solid phase reaction (refer to section 4.1.1), which is a simple and economic route still particularly significant to industrial applications. In order to realize high densities compositions with TiO_2-excess were selected, since a Ti-rich liquid phase is expected to form and enhance densification during sintering. [104] The La-concentration was varied in the range from 1 – 2 mol%. Additions of the sintering flux SiO_2 were avoided in order to circumvent the possible deterioration of the optical properties through the additional formation of foreign inclusions. Such heterogeneities involving interfaces between two phases with different refractive indices are believed to act as further

scattering sites for the light. Besides high anticipated values of density, a small grain size a third major beneficial contribution to the optical properties was expected to arise from a low concentration of free electrons. A high concentration of free electrons is known to absorb red and infrared light from the spectrum of electromagnetic radiation.[153] For this reason all compositions were sintered or heat treated at high partial pressures of oxygen. Sintering was carried out in pure oxygen ($p(O_2)$=0.1 MPa). In order to enhance translucency some ceramics were subsequently annealed in pure oxygen at 1000°C, in order to further reduce the concentration of free electrons.

8.2 Analytical and microstructural characterization

Table 8-1 summarizes the composition, thickness and densities of the ceramics investigated in this chapter:

Denotation	La-content [mol%]	Thickness [mm]	Density [g/cm^3]
C-1	1.0	0.72	5.93
C-2	1.5	0.71	5.93
C-3	2.0	0.78	6.02

Tab. 8-1: Sample specification of the translucent ceramics studied in this work.

All ceramics revealed very high density values approaching almost the theoretical value of pure $BaTiO_3$ even after pressureless sintering. Besides only very minor traces of impurities in the case of high La-content all compositions were essentially phase pure. Figure 8-2 represents the corresponding XRD patterns and the dependence of the lattice parameters of the perovskite unit cell estimated using Rietveld refinement depending on the amount of La-added. All major Bragg reflections detected could be attributed to the tetragonal phase $BaTiO_3$. Additional peaks for 1.5 and 2.0 mol% of La addition were ascribed to small amounts of the Ti-rich secondary phases $BaTi_2O_5$ and $Ba_6Ti_{17}O_{40}$, which are believed to arise from the TiO_2-excess in the ceramics.

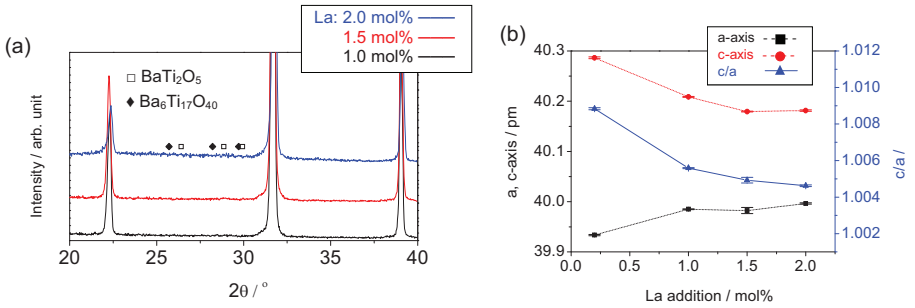

Fig. 8-2: (a) XRD patterns obtained for heavily La-doped $BaTiO_3$ sintered and annealed in pure oxygen and (b) lattice parameter in dependence of La-concentration obtained by Rietveld analysis. Minor impurity phases are indicated. The composition of the ceramics were $(Ba_{1-x}La_x)Ti_{1.005}O_3$, with *x* in the range between 0.01 and 0.02. A low La-content composition with 0.2 mol% in (b) was added as a reference.

As the results from Rietveld refinement suggest, the donor La is substantially dissolved in the perovskite lattice, since tetragonality drastically decreases upon La-addition.

Figure 8-3 (a) shows the microstructure of the composition $(Ba_{0.99}La_{0.01})Ti_{1.005}O_3$ examined by transmission electron microscopy and confirms the high density of this material. No pores could be found and additionally an extremely small average grain size appears. The grain size distribution, obtained by a statistical evaluation of about 100 grains observed by TEM, is given in figure 8-3 (b) in comparison to the particle size distribution of the calcined powder used for sintering this ceramic. The distribution is remarkably uniform and the average grain size after sintering is only about 500 nm. It can be concluded that substantial grain growth did not occur during densification even at temperatures as high as 1350°C. Comparing this with the average crystallite size of 100 nm before sintering it can be estimated that the volume fraction of grains that survived as nuclei from the calcined state in the powder until the finally densified ceramics is about 1%. The rest of the microstructure was formed through the dissolution and transport of the remaining 99% of the materials volume. This is not surprising taking into account that the material was densified at very high temperatures through a liquid phase sintering process. In the case of exaggerated grain growth where the grain size usually exceeds a few tens of microns, and which typically is observed for undoped materials or low La-concentrations, secondary recrystalli-zation and the appearance of a few giant grains embedded in a fine grained matrix can be detected.[154] This scenario apparently did not occur in the present case of heavily doped $BaTiO_3$ that was sintered in pure O_2. Sintering in

oxygen could also strongly impede the formation of giant grains. Very clearly the domain structure can be observed inside the ferroelectric grains of the phase $BaTiO_3$ in figure 8-3 (a). The ferroelectric and dielectric characteristics of this sample will be referred to in section 8.5.

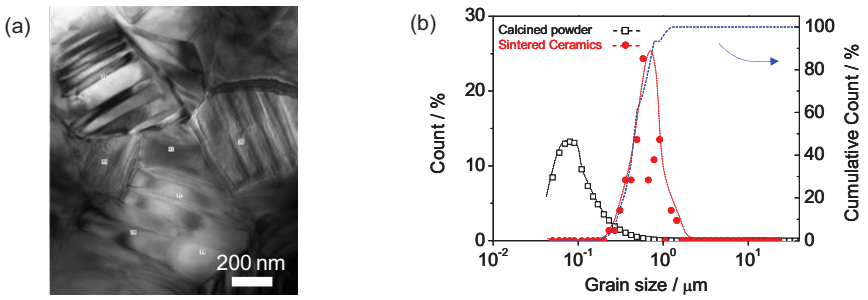

Fig. 8-3: (a) Representative TEM image of $(Ba_{0.99}La_{0.01})Ti_{1.005}O_3$ sintered in pure oxygen and (b) the corresponding grain size distribution obtained by a statistical evaluation of approximately 100 grains, observed by TEM. As a reference the particle size distribution determined on the initial calcined powder used for sintering this ceramic is included (black curve).

Further studies on the chemical composition were performed using EDX in combination with SEM. A corresponding image of the microstructure obtained after mechanochemical polishing is shown in figure 8-4 (a).

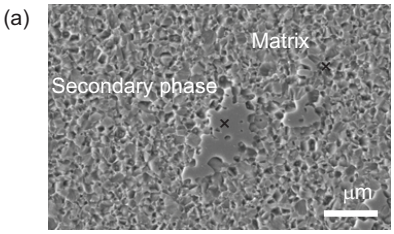

(b)

Position	O	Ti	Ba	La
Secondary phase	65.1	25.3	9.6	0.1
Matrix	58.7	21.3	20.0	0

Fig. 8-4: (a) SEM image of the polished surface of $(Ba_{0.99}La_{0.01})Ti_{1.005}O_3$ sintered in pure oxygen and (b) the corresponding results obtained from EDX analysis for all main constituent elements in molar percent.

A large inclusion formed by a secondary phase is clearly recognized due to the difference in the chemical etching rate. The optical contrast in the electron microscopic image is much darker than the one of the surrounding matrix of the phase $BaTiO_3$ suggesting substantial differences in the chemical composition. Results obtained by EDX show that the ratio of Ba/Ti is close to unity for the matrix, whereas this value is as low as 0.38 for the secondary inclusion. The present observation therefore supports the results obtained by XRD and it can be concluded

that this phase corresponds indeed to the TiO_2-rich compound $Ba_6Ti_{17}O_{40}$ (ideal Ba/Ti = 0.35).

The ceramics shown in figure 8-4 was prepared with a nominal overshoot of 0.5 mol% of TiO_2 and therefore the appearance of this secondary phase is not surprising. From the defect chemical point of view the incorporation of lanthanum into barium titanate at high oxygen partial pressures results in the formation of titanium vacancies, as it has been empirically proved.[62,63] The corresponding reaction equation for this equilibrium can be written as:

$$2La_2O_3 + 4TiO_2 \overset{BaTiO_3}{\rightleftharpoons} 4La_{Ba}^{\bullet} + 3Ti_{Ti}^{\times} + V_{Ti}^{''''} + 12O_O^{\times} + TiO_2 \qquad \textbf{Eq. 8-1.}$$

According to this the formation of titanium vacancies also results in the precipitation of titanium dioxide from the $BaTiO_3$ matrix. Very probably this is another reason why Ti-rich secondary phases arise when La is added. Such compositional inhomogeneities with different optical refraction index should, however, be avoided in order not to deteriorate the translucency. Therefore too high values of the La-content were not considered in the following anymore. Relating to equation 8-1 one mole of titania is equivalent to four moles of lanthanum incorporated onto the A-site of the perovskite lattice.

8.3 Optical transmittance

Figure 8-5 shows the appearance of a $BaTiO_3$ ceramics with a La content of 2 mol% after sintering for two hours at 1350°C and annealing at 1000°C for 30 hours in pure oxygen respectively. The thickness of this pellet is 0.78 mm and it still clearly translucent to visible light.

Fig. 8-5: Translucent $BaTiO_3$ ceramic pellet containing 2 mol% of La addition after sintering and subsequent annealing in pure oxygen (2 hours at 1350°C and 30 h at 1000°C). The nominal composition is $(Ba_{0.98}La_{0.02})Ti_{1.005}O_3$. The bar indicates 10 mm in length.

The optical transmittance t of a translucent material of arbitrary thickness d is only defined by the intensity ratio of the transmitted to the incident light beam, denoted as I and I_0 respectively:

$$t = \frac{I}{I_0} \qquad \textbf{Eq. 8-2.}$$

When the properties of optical materials of different thicknesses are compared it is often useful to introduce a normalized value t_n. If the transmittance of a material with a thickness of d (specified in mm) has a value of t than the corresponding value for a sample with a thickness of 1 mm can be calculated according equation 8-3:

$$t_n = t^{1/d} = \left(\frac{I}{I_0}\right)^{1/d} \qquad \textbf{Eq. 8-3.}$$

The optical transmittance t of the material shown in figure 8-5 has been measured by UV/VIS spectroscopy and compared to data in the literature. The own experimental results and those reported from other authors are represented in figure 8-5. Table 8-2 summarizes the most important material parameter regarding these measurements and reports and compares the values of the normalized transmittance t_n using the relation stated in equation 8-3. Even though only conventional solid state reaction and simple sintering in O_2 were used in this study, comparably high values of normalized optical transmittance could be realized compared to the works of other authors. The maximum value of t_n obtained was 28.6% at a wavelength of 800 nm. This value is not the highest one achieved so far for $BaTiO_3$ but it is far superior to the ones reported for sol-gel based thick films.[144,145]

Also in comparison the hot pressed ceramics prepared from oxalate-derived powders,[3] the present result signifies a clear improvement. Only ceramics prepared by SPS[6] reveal a slightly higher normalized optical transmission coefficient.

It should be stressed out again here, that the ceramics prepared in the present study did not involve any complicated or costly preparative procedure. Figure 8-6 (a) shows that the transmittance improves in the region of visible light with increasing La content. On the other hand the transmittance decreases with the wavelength above 800 nm. Above a lanthanum concentration of 1.5 mol% a considerable drop of transmittance is observed in the infrared region.

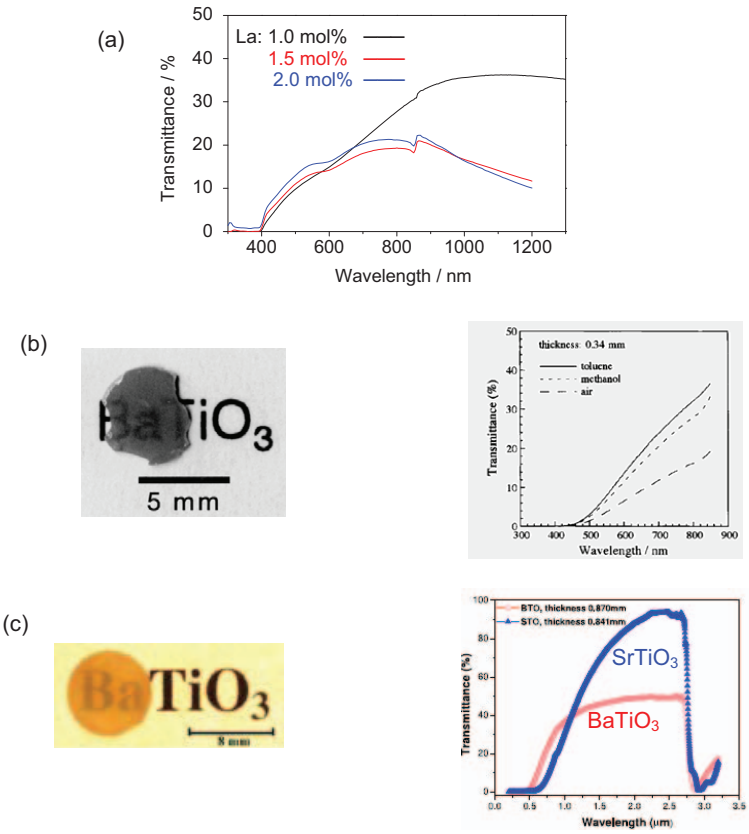

Fig. 8-6: (a) Transmittance *t* of La-doped $BaTiO_3$ after sintering in pure oxygen. The compositions are $(Ba_{1-x}La_x)Ti_{1.005}O_3$ with x = 0.01 – 0.02. Comparable materials reported in the literature are shown:
(b) $BaTiO_3$ – thick film prepared via a sol-gel process.[146]
(c) $BaTiO_3$ – nanoceramics prepared via plasma spark sintering.[148]

	Powder Synthesis	Process	*d* [mm]	*t* [%]	t_n [%]	Ref.
Thick films	Sol-gel synthesis	Sintering	0.32	16	0.33	[146]
		Sintering	0.2	32	0.34	[147]
Ceramics	Oxalate route	Hot pressing	1.07	22	23.8	[145]
	Commercial powder	SPS	0.87	38	32.9	[148]
	Solid phase reaction	Sintering in O_2	0.76	39	28.6	This work

Tab. 8-2: Summary of the most important material parameter regarding the measurement of the optical transmittance and processing from the present work in comparison to results reported in the literature. Optical transmission values correspond to the ones determined at λ = 800 nm.

8.4 Defect chemistry: charge compensation mechanism

After sintering the present ceramics all show a bluish colour. This observation suggests the existence of relatively large concentrations of free conducting electrons that absorb the high frequency spectrum of visible light in the red and infrared wavelength range above 600 nm.[153] Measurements of electrical conductivity confirm this conclusion. Figure 8-6 represents the temperature dependence of resistivity and of the dielectric permittivity of $BaTiO_3$ ceramics doped with 1.0 or 2.0 mol% of La after sintering in pure oxygen and after subsequent annealing in O_2.

For 1.0 and 2.0 mol% of La-addition a strong increase in resistivity is observed upon annealing in pure oxygen, especially for the higher dopant concentration. The latter composition showed a lower optical transmittance in the infrared light region, which is attributed to the higher concentration of free conducting electrons. The temperature characteristics of the dielectric permittivity reveal maximums at around 90°C and 70°C for each composition respectively. The decrease in Curie temperature is nearly consistent with former reports stating that T_C decreases with the addition of La by 20 K/mol%.[155] The increase in resistivity upon annealing in pure oxygen is, as already mentioned, believed to be related to the decrease of the concentration of conducting electrons. Defect chemically this is expressed by:

$$4e + 4O_2^{(g)} \rightleftharpoons 4O_O^{\times} + V_{Ti}^{''''} \qquad \textbf{Eq. 8-4.}$$

According to equation 8-4 it is expected that upon oxidation translucency is increased, since free electrons are captured by Ti vacancies acting as acceptor. The influence of the post-sintering reoxidation treatment on optical transmittance and absorbance is shown in figure 8-8.

Whereas transmittance is strongly enhanced with increasing wavelength, especially in the infrared region, the absorbance shows a hump at around λ = 600 nm. This optical behaviour is thus in consistence with the electrical behaviour and the reduction of the concentration of free electrons. The hump in figure 8-7 (b), referred to as the adsorption A2 is attributed to the existence of oxygen vacancies,[150] which upon annealing in oxidizing conditions disappears. This can be clearly recognized in the absorbance spectrum and therefore it is concluded that t number of oxygen vacancies are reduced.

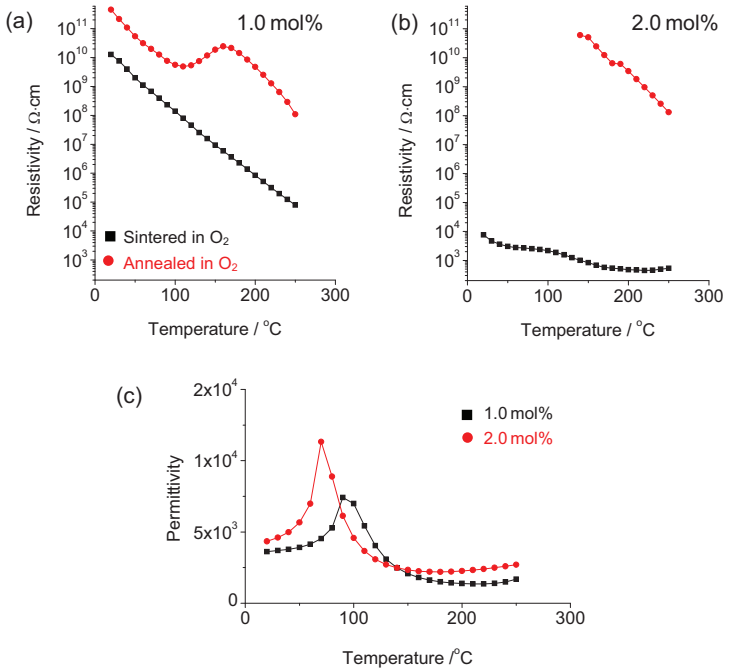

Fig. 8-7: Temperature dependence of resistivity before and after annealing in pure oxygen of (a) $(Ba_{0.99}La_{0.01})Ti_{1.005}O_3$ and (b) $(Ba_{0.98}La_{0.02})Ti_{1.005}O_3$. (c) Temperature dependence of dielectric permittivity measured at 1 kHz for both these compositions.

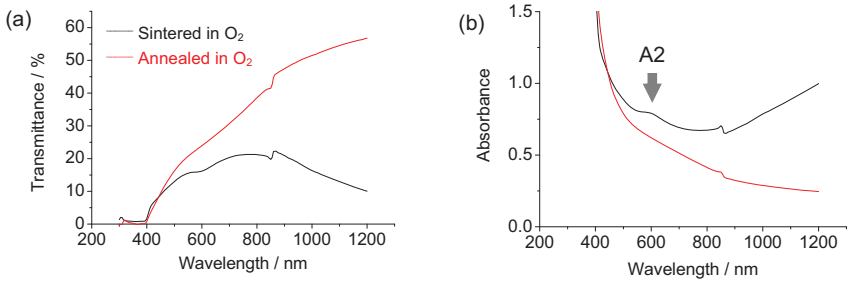

Fig. 8-8: (a) Transmittance and (b) absorbance of $(Ba_{0.98}La_{0.02})Ti_{1.005}O_3$ before and after annealing at 1000°C in pure oxygen for 30 hours.

8.5 Ferroelectric properties

In order to investigate whether the poling state of highly translucent and heavily La-doped $BaTiO_3$ ceramics affects the optical refractive index, the ferroelectric characteristics of this material had to be quantified first. Figure 8-8 shows ferroelectric hysteresis loops $P(E)$ depending on the maximum electric field strength applied. In the initial stage before the measurement the sample was thermally depolarized. The as sintered condition was not investigated since the resistivity was too low to record ferroelectric hysteresis loops. For reoxidized translucent $(Ba_{0.98}La_{0.02})Ti_{1.005}O_3$ ceramics the coercive field amounts to 210 V/mm and the remanent polarization to 4.18 $\mu C/cm^2$ after applying a maximum electric field of 1260 V/mm.

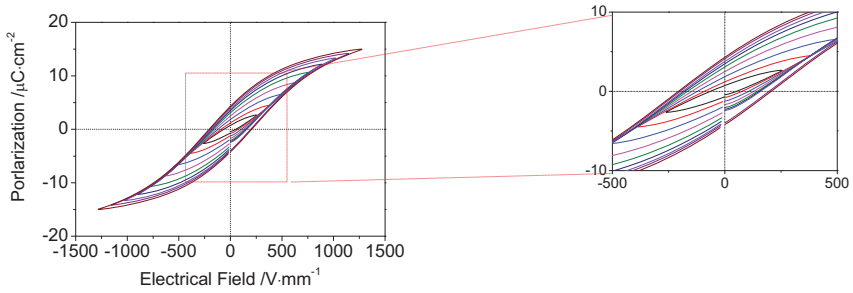

Fig. 8-9: Ferroelectric $P(E)$-hysterisis loop or oxidized translucent $(Ba_{0.98}La_{0.02})Ti_{1.005}O_3$ measured at room temperature and 1 Hz. The maximum electric field was gradually increased from 256 V/mm up to 1260 V/mm in steps of 128 V/mm. The thickness of the ceramic pellet was 0.78 mm.

Compared to pure single crystalline $BaTiO_3$[29,156] the value of the coercive field is enhanced and the remanent polarization is inferior. But unambiguously the material is, as also previously shown by the temperature dependence of dielectric permittivity, ferroelectric at room temperature and therefore the poling state is expected to influence also optical refraction.

The strongly reduced value of remanent polarization is probably due to the reduced tetragonal distortion of the lattice related to the incorporation of La as shown in section 8-2. Also the size effect describing the reduction of the dielectric constant with decreasing grain size below approximately 700 nm,[34,157] is a possible source for the inferior remanence. Anyhow, the present measurements clearly show the presence of a stable spontaneous polarization and therefore the refractive index should be anisotropic in a poled ceramics.

8.6 Optical refraction

The optical refractive index of translucent $(Ba_{0.98}La_{0.02})Ti_{1.005}O_3$ was measured by ellipsometry after polarization at room temperature with a maximum electric field of 1260 V/mm and also after subsequent thermal depolarization far above the Curie temperature at 115°C for 72 hours. Dielectric measurements confirmed the position of the Curie point at 70°C (refer to section 8.4).

The refractive indices were remeasured several times at different incident angles around the Brewster angle to confirm that the measured values are independent of the angle of incidence and that the measurement was carried out correctly. Pure $BaTiO_3$ has a Brewster angle of 67.61°.[158] From the intensity data recorded the refractive indices were analyzed and calculated using a half-space model,[159] under the assumption that no other material beside $BaTiO_3$ exists at the ceramic surface. In the case of the poled ceramic the metallic electrodes (100 nm thick Pt) that had been applied for in-situ poling during the measurement of the ferroelectric hysteresis were removed by polishing. Then the ellipsometric measurement was performed. The identical sample was thermally depolarized as described before measuring the refractive indices for the depolarized state. In this way the effect of a different surface roughness caused by polishing on the refractive index could be excluded. A rough surface is considered to be equivalent to the refracting layer consisting of the mixture of the matrix and air. This might have a significant impact on ellipsometric measurements. The results are shown in figure 8-10 for the measurement directly after polarization and after depolarization respectively.

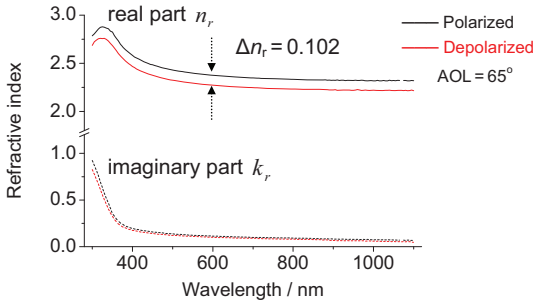

Fig. 8-9: Real part and imaginary part of the refractive index of oxidized translucent $(Ba_{0.98}La_{0.02})Ti_{1.005}O_3$ after polarization (black line) and depolarization (red line). The real part is described by the solid line and the imaginary part by the dotted line respectively. The incident angle of light (AOL) is 65°.

It can be readily seen that the real part of the refractive index n_r is decreased over the whole range of wavelengths measured after depolarization. The imaginary part, on the other hand, is almost identical for both cases. In comparison to earlier reports on single crystalline $BaTiO_3$,[160] the measured difference in refractive index is larger than the expected value. At a wavelength of 600 nm the difference of the refractive indices of $BaTiO_3$ single crystals for a- and c- axis amounts to only 0.058. In the case of the poled translucent ceramic the difference is, however, as high as 0.102. This discrepancy could be thought to result from the influence of La-doping on the reduced tetragonality of the lattice compared to a pure $BaTiO_3$. Nevertheless in this case a smaller difference rather than a larger one would be expected. It should be pointed out that at present it is not clear how La affects the optical refractive indices of $BaTiO_3$. Another issue that should be noted is that the temperature yielding the maximum permittivity for La-doped barium titanate is strongly shifted to lower temperatures in comparison to pure $BaTiO_3$. A direct analogy between the dielectric constants and thus between the refractive indices is not given.

For many oxide-, chalcogenide- and halide-based materials it is known for long that the refractive index follows the so-called single oscillator model that was originally proposed by DiDomenico and Wempel.[160] This model predicts the interaction of light with the chemical bonding strength between cations and anions. According to this theory the dependence of the refractive index n_r from the angular frequency ω ($\omega=2\pi c/\lambda$) is expressed by the following relation:

$$n_r^2(\omega) - 1 = \frac{E_d \cdot E_0}{E_0^2 - (\hbar \cdot \omega)^2} \qquad \textbf{Eq. 8-5.}$$

In equation 8-5 E_0 represents the average oscillator strength, E_d the dispersion energy and $\hbar$ the reduced Planck constant. The parameter E_d is a measure for the strength of interband optical transitions and can be represented by an empirical relationship:

$$E_d = \beta \cdot N_c \cdot Z_a \cdot N_e \qquad \textbf{Eq. 8-6.}$$

Here N_c is the number of nearest neighboring cations, Z_a the formal anion valency and N_e the effective number of valence electrons per anion. In the case of pure $BaTiO_3$ these parameter are: $N_c = 6$, $Z_a = 2$ and $N_e = 2$. The empirical parameter β formally represents an energy and takes only two values for a large variety of inorganic compounds depending on the character of chemical bonding. For ionic bonding this parameter is 0.26 ± 0.04 eV and for covalent bonding 0.37 ± 0.05 eV.

In order to determine the parameter E_0, E_g and β and compare them with reference data from prior reports[160] the relationship between $n_r^2(\lambda) - 1$ and $1/\lambda^2$ has to considered as shown in figure 8-10.

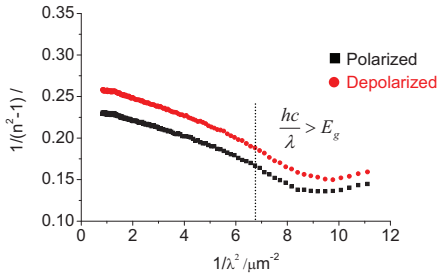

Fig. 8-10: Representation of $n_r^2(\lambda) - 1$ versus $1/\lambda^2$ based on the single oscillator model analysis for $(Ba_{0.98}La_{0.02})Ti_{1.005}O_3$ after polarization (black symbols) and depolarization (red symbols).

If the single oscillator model applies this relationship should be linear. In the region below $1/\lambda^2 = 6.25\ \mu m^{-2}$, corresponding to the regime of visible light above 400 nm, this is the case and the parameter obtained by fitting using equations 8-5 and 8-6 are listed in table 8-3. The result for the empirical parameter β clearly indicates that ionic bonding predominates, which is consistent with the expectation for the ionic compound $BaTiO_3$. Also the other two energy parameters E_d and E_0 correspond well with data reported on crystalline $BaTiO_3$.

Sample		E_0 [eV]	E_d [eV]	β [eV]	Ref.
Crystal		5.63	24.0	0.25	[160]
Thin film		9.21	31.0	0.32	[161]
Polycrystal	**Polarized**	6.27	26.1	0.27	this work
	Depolarized	6.38	23.8	0.25	this work

Tab. 8-3: Parameters resulting from the single oscillator analysis of the present work in comparison to values reported in the literature.

Below a wavelength of 400 nm, corresponding to $1/\lambda^2$ = 6.25 μm^{-2}, no linear relationship between $n_r^2(\lambda)-1$ and $1/\lambda^2$ is observed anymore. The reason for this deviation is that the energy of the light in this range of wavelengths exceeds the intrinsic band gap energy of $BaTiO_3$ and in consequence photons are absorbed by the material. This analysis based on single oscillator model assures the optical measurement was done correctly.

8.7 Summary

The possibility of preparing translucent ferroelectric heavily donor-doped $BaTiO_3$ rich in TiO_2 has been demonstrated by conventional ceramics processing based on the synthesis via the solid state method reaction and on subsequent sintering in pure oxygen. The resulting ceramics possess very high densities and fine microstructures with a very narrow grain size distribution. Under oxidizing conditions large amounts of the donor – in this case La – can be incorporated into the perovskite lattice during sintering, as the variation of the lattice parameters determined by combined XRD and Rietveld refinement suggests. The electrons released from these donors are most probably captured by vacancies of titanium, which act as acceptors. The optical properties are largely determined by the defect chemistry and in particular by the concentration of free conducting electrons. Especially the reduction of the free electron concentration is believed to be mainly responsible for the high degree of optical translucency. The normalized values of transmittance almost reach the best values reported so far for nanocrystalline barium titanate consolidated by SPS. Measurements of the refractive index indicated that it can be modified by the state of polarization. This newly developed material opens a door to novel electro-optical application.

Chapter 9 (Annex)
PTCR curve fitting based on Heywangs model

The present chapter presents the physical parameters obtained by fitting the experimental resistance vs. temperature curves using Heywangs model based on simulations. The detailed procedure followed for the simulation is described in section 3.3.1. By fitting the experimental curves, essential physical parameters such as the depth and the density of the acceptor states, which feature the PTCR properties can be obtained. In consequence the PTCR performance can be discussed based on these physically important parameters.

The experimental and calculated resistance vs. temperature curves for co-doped (Ba,La)(Ti,Mn)$O_{3+\delta}$ (sample: A in table 3-1), reduction-resistant $(Ba,La)_{1.05}TiO_{3+\delta}$ (B-6) and ultrafine grained (Ba,La)$TiO_{3+\delta}$ (D-1) are shown in figure 9-1. Co-doped (Ba,La)(Ti,Mn)$O_{3+\delta}$ reveals the steepest jump in resistivity among these three materials, however $(Ba,La)_{1.05}TiO_{3+\delta}$ shows the highest temperature T_{max}, for which resistivity reaches its maximum value ρ_{max}.

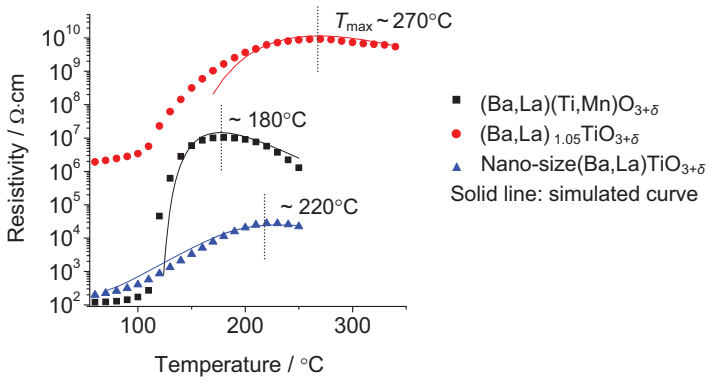

Fig. 9-1: Resistance vs. temperature curve (dots) for co-doped (Ba,La)(Ti,Mn)$O_{3+\delta}$, reduction-resistant BaO-excess (Ba,La)$TiO_{3+\delta}$ and ultrafine grained (Ba,La)$TiO_{3+\delta}$ together with the corresponding simulated curves (solid lines). The temperatures shown in the figure are the points at which the highest resistivity ρ_{max} is observed.

Nano-sized (Ba,La)$TiO_{3+\delta}$ only shows a relatively weak PTCR effect compared with the other two ceramics. All experimental data are satisfactorily fitted by the simulated curves except for the onset of the PTCR jump just above the Curie point.

The density $N_{s,0}$ and depth E_s of the acceptor states influence T_{max} most. These parameters are determined by mapping T_{max} and ρ_{max} as shown in figure 9-2. Figure 9-2 shows that deeper levels of acceptor states E_s result in significantly higher values of ρ_{max}. T_{max} is only slightly affected by E_s. The density of the acceptor state $N_{s,0}$, on the other hand, has more impact on T_{max} rather than on ρ_{max}. Figure 9-2 is an example for co-doped (Ba,La)(Ti,Mn)$O_{3+\delta}$. With this mapping the optimum values for $N_{s,0}$ and E_s can be determined. [§]

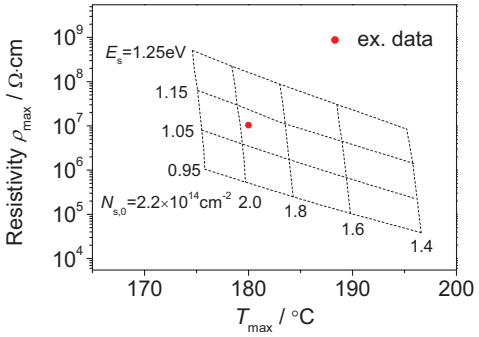

Fig. 9-2: T_{max} and ρ_{max} depending on the depth E_s and density $N_{s,0}$ of the acceptor states. The figure shows an example of co-doped (Ba,La)(Ti,Mn)$O_{3+\delta}$.

Table 9-1 represents the physical parameters obtained by simulation calculations based on Heywangs model together with other reference data published in literature.[76,80,81] In a first stage the quality of the fittings should be examined by comparing with other data. The depth of the acceptor states of conventional co-doped compositions is reported to be around 1.1eV and the density of acceptor states around 1×10^{14} cm^{-2}. The results from own simulations of the present study correspond to these expected values. Comparing with the conventional compositions, reduction-resistant $(Ba,La)_{1.005}TiO_{3+\delta}$ has apparently a much deeper acceptor level at 1.75eV. This most likely results from the experimental fact that T_{max} for this material is much higher than that of other compostions listed in table 9-1. Based on high-temperature DC conductivity measurements reported in chapter 6 it has been

[§] In mapping the relationship between T_{max} and ρ_{max}, the width of the acceptor state also should be decided. Suitable parameters are selected in a way that they result in an optimum fit to the experimental curves based on the logarithmic least-squares method.

concluded that acceptor-type Ti vacancies are responsible for the PTCR effect in BaO-excess compositions. Ti vacancies have been reported to posses rather deep acceptor levels.[41,73,162] Therefore the present simulations support the defect chemical conclusions of this thesis and confirm, that actually Ti-vacancies enriched at the grain boundary are responsible for the excellent PTCR performance of BaO-rich reduction resistant $BaTiO_3$.

On the contrary the ultrafine grained sample considered here reveals acceptor states at almost the same energy level as conventional co-doped materials, i.e. E_s~1.1eV. A distinct difference observed between the conventional and ultrafine grained composition is however the density of the acceptor states $N_{s,0}$. Fine grained $BaTiO_3$ only shows a rather poor PTCR effect and it is considered that this is due to the low density of the acceptor states. Since this material has the same depth of the acceptor states compared to the conventional composition, it is anticipated that an increase of the density of the acceptor states enhances the PTCR jump. This could be acchieved by adding acceptor impurities like for example Mn.

Composition	ρ_{max}/ρ_{min}	E_a [eV]	$N_{a,o}$ [cm^{-2}]	Acceptor band width [eV]	Ref.
$(Ba,Sb)(Ti,Mn)O_3$	5.2	1.14	3.6×10^{14}	1.0	[76]
$BaTiO_3$ with Y, Mn	5.8	1.18	8.38×10^{13}	-	[80]
Unknown (commercial PTCR)	5.8	1.11	1.37×10^{14}	-	[81]
$(Ba,La)(Ti,Mn)O_3$ (sample: A)	4.9	1.12	2.1×10^{14}	0.94	This work
$(Ba,La)_{1.05}TiO_3$ (sample: B-6)	3.8	1.75	1.5×10^{13}	1.91	This work
$(Ba,La)TiO_3$ (sample:D-1)	2.2	1.15	1.3×10^{13}	0.71	This work

Tab. 9-1: The physically relevant parameters for Heywang model obtained by the fitting.

Finally the Curie-Weiss law is considered in view of the presented simulations. According to this law, the reciprocal values of permittivity ε should give a linear relationship with temperature. In the case of PTCR ceramics the measured permittivity ε_m is mostly related to a depression layer formed in the vicinity of the grain boundaries, resulting in a deviation from the Curie-Weiss law because the width of this depression layer changes in dependence of temperature. In order to apply the

law precisely, the width of the depression layer must be taken into consideration. For this purpose the following equation is deduced:

$$\varepsilon_r = \varepsilon_m(2b/d) = \varepsilon_m(N_a / dn) \qquad \textbf{Eq. 9-1}$$

Figure 9-3 shows both the measured and corrected permittivity ε_m and ε_r respectively according to equation 9-1. In every sample the corrected permittivities result in a linear relationship with temperature, confirming that the Curie-Weiss law is maintained in these ferroelectric materials. This confirms that the deviation from the Curie-Weiss law is due to the temperature dependent depletion layer width.

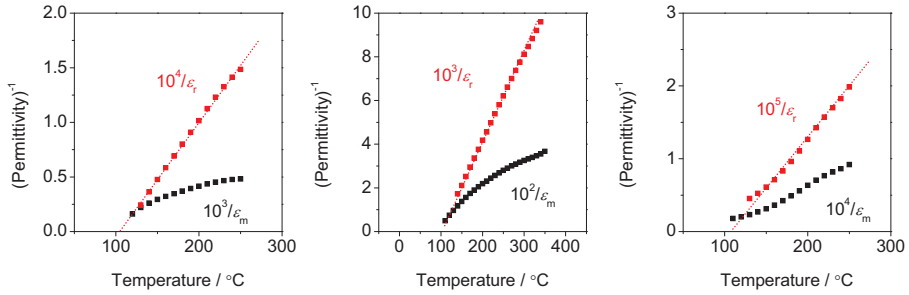

Fig. 9-3: The reciprocal plot of the measured and corrected permittivities in dependence of temperatures. (left) (Ba,La)(Ti,Mn)$O_{3+\delta}$, (center) BaO-excess (Ba,La)$TiO_{3+\delta}$ and (right) ultrafine grained (Ba,La)$TiO_{3+\delta}$.

In summary the physical parameters obtained by fitting the experimental resistance versus temperature curve using Heywangs model have been presented. In the case of reduction-resistant BaO-excess $BaTiO_3$, the most eminent feature is that this composition reveals deeper acceptor levels than conventional co-doped $BaTiO_3$. In the defect chemical model intensively discussed in chapter 6, the formation of the acceptor states by Ti vacancies was concluded to be the main reason for the realization of the PTCR effect. The present simulation results also suggest that a deeper acceptor state is formed in reduction-resistant BaO-excess $BaTiO_3$ compared to conventional co-doped $BaTiO_3$. The acceptor level in fine grained PTCR ceramics is comparable to that in conventional PTCR compositions, however the density of the acceptor states is one order of magnitude lower compared to the co-doped reference composition. This results in a relatively poor PTCR effect.

Chapter 10
General conclusions

The present thesis describes a consistent microstructural and defect chemical model that explains why reduction-resistant $BaTiO_3$-based PTCR ceramics with BaO-excess for multilayer applications obtain their outstanding temperature characteristic of resistivity upon heating in operation after being processed under reducing conditions for consolidation with a subsequent gentle reoxidation annealing treatment at partial pressures of oxygen typically around 10^{-7} MPa. On pupose the present study focussed on La donor-doped ceramics, since here any additional complexity arising from amphoteric behavior can be excluded – La preferentially occupying the Ba site in the perovskite lattice. Impedance spectroscopic investigations showed that essentially the reoxidation of the external surface region results in a pronounced and even dominating PTCR effect whereas contributions of grain boundaries as they are known from classical disc-type TiO_2-rich compositions fired and cooled in oxidizing atmosphere only play a secondary role in the present case. This is an extremely important observation regarding the further development of future multilayer thermistors on $BaTiO_3$-basis. Through a systematic study it could be excluded that heterojunctions due to metal-semiconductor interfaces at the contact between electrode and ceramic do not play any significant role. Also the modification of grain boundaries by secondary phases that surround the surface of the semiconducting grains could be excluded. The presence of any extendend defects as they are frequently reported, could not be confirmed by HR-TEM. A second reoxidation treatment after grinding off the surface of previously reoxidized samples clearly revealed that the major effect is due to the reoxidation of the exterior faces. The process is therefore reproducible and reversible. These surface effects come into operation favourably at an (Ba+La)/Ti ratio *m* above 1.02. Upon this observation the question how the reoxidation treatment after sintering under reducing conditions affects the resistive contributions of external surfaces and internal grain boundary interfaces had to be answered. For this purpose experiments using the isotope ^{18}O

for in-situ reoxidation or oxygen exchange were performed in conditions that correspond to the actual processing parameters used for the preparation of the PTCR ceramcs. The results confirmed that the reoxidation of the surface by volume diffusion only affects a very thin skin of a few hunderds nm in thickness. Preferentially oxygen diffuses into the material via grain boundary diffusion. The diffusion profiles were modeled using existing and well established models. The enhanced penetration of oxygen in BaO-rich compositions was confirmed by a comparison with a purely stoichiometric composition, where no grain boundary diffusion contribution could be evidenced. Enhanced oxidation of the grain boundary regions inside the ceramics motivated to the assumption of a preliminary defect chemical explanation: during sintering excessive BaO is incorporated at least partially in the grain boundary regions of the $BaTiO_3$ grains due to a higher solubility at elevated temperatures. This causes a local enrichment of titanium and oxygen vacancies in these regions (partial Schottky reaction). During post-intering annealing in oxidizing conditionss the titanium vacancies remain spacially frozen-in due to its high enthalpy for migration. In the intermediate temperature region where reoxidation occurs, however, the enhanced concentration of mobile oxygen vacancies in the grain boundary region results in an enhanced exchange of oxygen in these regions with the surrounding atmosphere. This conclusion could be fortified by DFT calculations that showed that the presence of titanium vacancies actually reduces the mobility of oxygen vacancies, probably due to the formation of defect associates between titanium and oxygen vacancies. The enhanced diffusivity of oxygen along grain boundaries must therefore result from a higher concentration of vacant oxygen sites.

This assumption was further elucidated by measurements of DC conductivity in dependance of temperature and oxygen partial pressure. The resulting Kröger-Vink diagrams confirm that apparantly BaO is incorporated into the perovskite lattice in regions close to the grain boundaries. In consequence the conductivity behavior at high partial pressures of oxygen is strongly influenced by p-type resistive grain boundaries even if the material is donor-doped and the grain interior is determined by n-type semiconduction. It appears that the enrichment of BaO at the grain boundaries has the same influence as local acceptor-doping in these regions. Comparisons with nominally undoped ceramics with BaO-excess or Nb-doped compositions – Nb preferentially occupying the B-site of the perovskite lattice in contrast to La which favors the A-site – show that in fact only the excess of BaO controls p-type

conduction. From the defect chemical point of view it is believed that the model proposed on the basis of the impedance spectroscopic investigations and of the study of oxygen diffusivity is consolidated. Immobilie vacancies of titanium and mobile oxygen vacancies determine the insulating properties of the grain boundaries. The nature of this electrical inhomogeniety in the microstructure could be confirmed by an investigation of the Seebeck effect and by the comparison of activation energies in the oxidizing regime with data from literature. The latter comparative study approves the formely stated hypothesis of the presence of metal – oxygen vacancy associates, their decomposition and their impact on the electric characteristics.

In view of the further technological development of miniaturized multilayer PTCR components the question, whether also extremely fine grained materials can be realized was adressed. From the theoretical point of view the existance of a lower limit in grain size is anticipated, where the material becomes completely insulating. It suprisingly appeared however that novel PTCR materials with an ultrafine grained microstructure – the average grain size being only being several hundereds of nm large – can be developed yielding in sufficiently good properties. Apparently only a very mild reoxidation treatment at temperatures as low as 500°C was necessary to reoxidize the grain boundaries in this ultrafine material. This behaviour together with a larger oxygen absorbtion compared to a coarse reference ceramic of identical composition led to the conclusion that oxygen penetration along grain boundaries in the nanocrystalline state is favored intrinsically. In contrast to the rather coarse grained examples treated before, however, it turned out that in the submicron-region stoichiometric compositions are more favorable. A BaO-excess did not bring along any expected benefical effect. Coarsening the ultrafine microstructure also seemed to result in a detereoration of the PTCR effect. Therefor it was assumed that a different mechanism operates and determines the PTCR effect in the submicron range.

Finally optically ferroelectric translucent heavily donor-doped $BaTiO_3$ ceramics with TiO_2-excess were prepared through a rather simple conventional ceramic process, that involved powder synthesis via the solid state reaction and sintering in pure oxygen. Due to preparation proceedure high amounts of the donor – in this case La – could be incorporated into the perovskite lattice. The released free electrons from these donors were captured most probably by titanium vacancies and in

consequence the low concentration of mobile electrons that absorb a part of the visible electromagnetic spectrum results in very high values of optical translucency. Also a highly dense and ultrafine microstructure, with little pores, as it was obtained supports the excellent normalized optical transmittance, which was superior compared to thick films of comparable compositions that were reported to be processed by sol-gel related techniques. The values acquired in the present work almost reached the best data reported so far in literature for nanocrystalline $BaTiO_3$ ceramics consolidated via spark plasma sintering. Measurements of the refractive index showed that it is affected by the polarization state. It should be emphasized in this context that all translucent ceramics, with such switchable refractive index, prepared in the present work were simply processed with standadard and economic ceramic techniques. The interesting properties found are worthy of noting and are possibly attractive to the practical use in novel electro-optical functions, although they are not directly related to the PTCR effect. This final part of the present work evolved from the detailed insight into the defect chemistry of donor-doped $BaTiO_3$.

Literature

[1] A. J. Moulson and J. M. Herbert: in *Electroceramics, Materials, Properties and Applications*, Chapman and Hall, New York, USA (1990).

[2] (a) S. A. Long and R. N. Blumenthal: „Ti-rich non-stoichiometric $BaTiO_3$: I, high-temperature electrical conductivity measurements“, *J. Am. Ceram. Soc.* 54 (1971) 515.
(b) S. A. Long and R. N. Blumenthal: „Ti-rich non-stoichiometric $BaTiO_3$: II, analysis of defect structure“, *J. Am. Ceram. Soc.* 54 (1971) 577.

[3] R. Waser, D. Hennings and T. Baiatu: „Dielektrische Keramiken“ in *Keramik – Werkstoffe und Bauelemente der Elektrotechnik*, ed. H. Schaumburg, B. G. Teubner, Stuttgart, Germany (1994) 277

[4] Y. Sakabe: „Multilayer ceramic capacitors“, *Curr. Opin. Solid State Mat. Sci.* 2 (1997) 584.

[5] P. W. Haayman, R. W. Dam and H. A. Klasens: „Verfahren zur Herstellung halbleitenden Materials“, *German Patent 929350* (1955).

[6] B. Huybrechts, K. Ishizaki and M. Takata: „The positive temperature coefficient of resistivity in barium titanate“, *J. Mat. Sci.* 30 (1995) 2463.

[7] E. Andrich and K. H. Härtl: „Investigations on $BaTiO_3$ semiconductors“, *Philips Techn. Rev.* 26 (1965) 170.

[8] E. Andrich: „Properties and applications of PTC thermistors“, *Electr. Appl.* 26 (1965/1966) 123.

[9] E. Andrich: „PTC thermistors as self-regulating heating elements“, *Philips Techn. Rev.* 30 (1969) 119.

[10] M. Q. Zhang and H. M. Zeng: in *Handbook of Thermoplastics*, Marcel Dekker Inc., New York, USA (1997)

[11] H. Niimi, A. Ando, M. Kawamoto and M. Kodama: „Semiconducing ceramic material and electronic part employing the same“, *US-Patent 2001/0003361 A1* (2001).

[12] K. Mihara and H. Niimi: „Laminate-type posistive temperature coefficient thermistor“, *US-Patent 7,075,408 B2* (2006).

[13] H. Niimi, T. Ishikawa, K. Mihara, Y. Sakabe and M. Kuwabara: „Effects of Ba/Ti ratio on positive temperature coefficient of resistivity characteristics of donor-doped $BaTiO_3$ fired in reducing atmosphere“, *Jap. J. Appl. Phys.* 46 (2007) 675.

[14] H. Niimi, K. Mihara, Y. Sakabe and M. Kuwabara: „Preparation of multilayer semiconducting $BaTiO_3$ ceramics co-fired with Ni-inner electrodes“, *Jap. J. Appl. Phys.* 46 (2007) 6715.

[15] G. Goodman: „Electrical conduction anomaly in Samarium-doped barium titanate“, *J. Am. Ceram. Soc.* 43 (1963) 48.

[16] W. Heywang: „Bariumtitanat als Sperrschichthalbleiter“, *Solid-State Electron.* 3 (1961) 51.

[17] W. Heywang: „Resistivity anomaly in doped barium titanate“, *J. Am. Ceram. Soc.* 47 (1964) 484.

[18] G. H. Jonker: „Some aspects of semiconducting barium titanate“, *Solid-State Electron.* 7 (1964) 895.

[19] J. Daniels and R. Wernicke: „Part V. New aspects of an improved PTC model“, *Philips Res. Rep.* 31 (1976) 544.

[20] (a) P. Gerthsen and K. H. Härdtl: „Eine Methode zum direkten Nachweis von Leitfähigkeitsinhomogenitäten an Korngrenzen“, *Z. Naturfors. Sect. A – J. Phys. Sci.* A18 (1963) 423.
(b) H. Ihrig and M. Klerk: „Visualization of the grain-boundary potential barriers of PTC-type $BaTiO_3$ ceramics by cathode luminescence in an electron-probe microanalyzer“, *Appl. Phys. Lett.* 35 (1979) 307.

[21] O. Saburi: „Semiconducting bodies in the family of barium titanate“, *J. Am. Ceram. Soc.* 44 (1961) 54.

[22] T. Matsuoka, Y. Matsuo, H. Sasaki and S. Hayakawa: „PTCR behaviour of $BaTiO_3$ with Nb_2O_5 and MnO_2 additives“, *J. Am. Ceram. Soc.* 55 (1972) 108.

[23] H. Ueoka: „The doping effects of transition elements on the PTC anomaly of semiconductive ferroelectric ceramics“, *Ferroelectrics* 7 (1974) 351.

[24] H. Ihrig: „PTC effect in $BaTiO_3$ as a function of doping with 3d elements“, *J. Am. Ceram. Soc.* 64 (1981) 617.

[25] T. Matsuoka, Y. Matsuo, H. Sasaki, and S. Hayakawa: *Japanese Patent 487 455* (1966).

[26] A. Kanda, S. Tashiro, H. Igarashi: „Effect of firing atmosphere on electrical properties of multilayer semiconducting ceramics having positive temperature coefficient of resistivity and Ni-Pd internal electrode”, *Jpn. J. Appl. Phys.* 33 (1994) 5431.

[27] H. D. Megaw: „Crystal structure of double oxides of the perovskite type“, *Proc. Phys. Soc.* 58 (1946) 133.

[28] H. F. Kay: „Preparation and properties of crystals of barium titanate, $BaTiO_3$“, *Acta Cryst.* 1 (1948) 229.

[29] W. J. Merz: „The electric and optical behavior of $BaTiO_3$ single-domain crystals“, *Phys. Rev.* 76 (1949) 76.

[30] R. Clarke: „Phase transition studies of pure and flux-grown barium titanate crystals“, *J. Appl. Cryst.* 9 (1976) 335.

[31] V. M. Goldschmidt: „Geochemisce Verterlungsgesetze der Elemente“, *Norske Videnskap,* Oslo (1927).

[32] A. S. Bhalla, R. Guo and R. Roy: „The Perovskite structure – a review of its role in ceramic science and technology“, *Mat. Res. Innovat.* 4 (2000) 3.

[33] R. D. Shannon: „Revised effective ionic radii and systematic studies of the interatomic distances in halides and chalcogenides“, *Acta Cryst. A* 32 (1976) 751.

[34] G. Arlt and D. Hennings: „Dielectric properties of fine-grained $BaTiO_3$ ceramics“, *J. Appl. Phys.* 58 (1985) 1619.

[35] R. Roy: „Multiple ion substitution in the Perovskite lattice“, *J. Am. Ceram. Soc.* 37 (1954) 581.

[36] F. A. Kröger and H. J. Vink: „Relations between the concentration of imperfections in crystalline solids“, in *Solid State Physics* 3, ed. By F. Seitz and D. Turnbull, Academic Press, New York, USA (1956) 307.

[37] G. V. Lewis and C. R. A. Catlow: „PTCR effect in $BaTiO_3$”, *J. Am. Ceram. Soc.* 68 (1985) 555.

[38] G. V. Lewis and C. R. A. Catlow: „Defect studies of doped and undoped barium titanate using computer simulation techniques”, *J. Phys. Chem. Solids* 47 (1986) 89.

[39] A. Seuter: „Defect chemistry and electrical properties of $BaTiO_3$“, *Ph.D. thesis, University of Twente,* The Netherlands (1974).

[40] N. H. Chan and D. M. Smyth: „Defect chemistry of $BaTiO_3$“, *J. Electrochem. Soc.* 123 (1976) 1584.

[41] J. Daniels and R. Wernicke: „Part I. Electrical conductivity at high temperature of donor-doped barium titanate ceramics“, *Philips Res. Rep.* 31 (1976) 489.

[42] D. Hennings: „Part III. Thermogravimetric investigations“, *Philips Res. Rep.* 31 (1976) 516.

[43] N. H. Chan and D. M. Smyth: „Nonstoichiometry in $SrTiO_3$“, *J. Electrochem. Soc.* 128 (1981) 1762.

[44] N. H. Chan, R. K. Sharma and D. M. Smyth: „Nonstoichiometry in acceptor-doped $BaTiO_3$“, *J. Am. Ceram. Soc.* 65 (1982) 167.

[45] N. H. Chan and D. M. Smyth: „Nonstoichiometry in donor-doped $BaTiO_3$“, *J. Am. Ceram. Soc.* 67 (1984) 286.

[46] G. M. Choi, H. Tuller and D. Goldschmidt: „Electronic transport behavior of single crystalline $Ba_{0.03}Sr_{0.97}TiO_3$“, *Phys. Rev. B* 34 (1986) 6972.

[47] R. Waser, T. Baiatu and K. H. Härdtl: „DC electrical degradation of Perovskite-type titanates: I, ceramics“, *J. Am. Ceram. Soc.* 73 (1990) 1645.

[48] R. Waser, T. Baiatu and K. H. Härdtl: „DC electrical degradation of Perovskite-type titanates: II, single crystals“, *J. Am. Ceram. Soc.* 73 (1990) 1654.

[49] R. Waser, T. Baiatu and K.-H. Härdtl: „DC electrical degradation of Perovskite-type titanates: III, a model of the mechanism“, *J. Am. Ceram. Soc.* 73 (1990) 1663.

[50] J. Nowotny and M. Rekas: „Defect chemistry of $BaTiO_3$“, *Solid State Ionics* 49 (1991) 135.

[51] J. Nowotny and M. Rekas: „Defect structure, electrical properties and transport in barium titanate. II. Consistency requirements between defect models and crystal properties“, *Ceram. Int.* 20 (1994) 217.

[52] J. Nowotny and M. Rekas: „Defect structure, electrical properties and transport in barium titanate. III. Electrical conductivity, thermopower and transport in single crystalline $BaTiO_3$“, *Ceram. Int.* 20 (1994) 225.

[53] J. Nowotny and M. Rekas: „Defect structure, electrical properties and transport in barium titanate. VII. Chemical diffusion in Nb-doped $BaTiO_3$“, *Ceram. Int.* 20 (1994) 265.

[54] R. Waser: „Electronic properties of grain boundaries in $SrTiO_3$ and $BaTiO_3$ ceramics“, *Solid State Ionics* 95 (1995) 89.

[55] M. J. Akhtar, Z.-U.-N. Akhtar, R. A. Jackson and C. R. A. Catlow: „Computer simulation studies of strontium titanate“, *J. Am. Ceram. Soc.* 78 (1995) 421.

[56] Y.-M. Chiang, D. Birnie and W. D. Kingery: in *Physical Ceramics - Principles*, *Ceramic Science and Engineering*, John Wiley, New York, USA (1997) 236.

[57] A. E. Paladino: „Oxidation kinetics of single-crystal $SrTiO_3$“, *J. Am. Ceram. Soc.* 48 (1965) 476.

[58] R. Wernicke: „The influence of kinetic processes on the electrical conductivity of donor-doped $BaTiO_3$ ceramics“, *phys. stat. sol. (a)* 47 (1978) 139.

[59] F. Poignant and P. Abelard: „The mechanism of oxidation in semiconducting A(= Sr, Ca)TiO_3 ceramic materials“, *Radiation Effects and Defects in Solids* 151 (1999) 103.

[60] H.-I. Yoo, C.-R. Song and D.-K. Lee: „$BaTiO_{3-\delta}$: „Defect structure, electrical conductivity, chemical diffusivity, thermoelectric power, and oxygen nonstoichiometry*", J. Electroceram.* 8 (2002) 5.

[61] A. M. Seuter: „Defect chemistry and electrical transport properties of barium-titanate", *Philips Res. Rep. Suppl.* 3 (1974) 1.

[62] G. H. Jonker and E. E. Havinga: „The influence of foreign ions on the crystal lattice of barium titanate", *Mater. Sci. Bull.* 17 (1982) 345.

[63] D. Makovec, D. Samardžija, U. Delalut, and D. Kolar: „Defect structure and phase relations of highly lanthanum-doped barium titanate", *J. Am. Ceram. Soc.* 78 (1995) 2193.

[64] G. V. Lewis and C. R. A. Catlow: „Potential models for ionic oxides", *J. Phys. C: Solid State Phys.* 18 (1985) 1149.

[65] Y. H. Han, J. B. Appleby and D. M. Smyth: „Calcium as an acceptor impurity in $BaTiO_3$", *J. Am. Ceram. Soc.* 70 (1987) 96.

[66] J. Zhi, A. Chen, Y. Zhu, P. M. Vilarinho and J. L. Baptista: „Incorporation of yttrium in barium titanate ceramics", *J. Am. Ceram. Soc.* 82 (1999) 1345.

[67] D. Hennings and H. Schreinemacher: „Ca-acceptors in dielectric ceramics sintered in reducive atmospheres ", *J. Eur. Ceram. Soc.* 15 (1995) 795.

[68] A. Hitomi, X. Liu, T. R. Shrout and C. A. Randall: „Hypotheses on rare earth doping of $BaTiO_3$ ceramic capacitors", *The Eighth US-Japan Seminar on Dielectrics and Piezoelectrics*, Plymouth, USA (1997).

[69] W. H. Lee, W. A. Groen, H. Schreinemacher and D. Hennings: „Dysprosium doped dielectric materials for sintering in reducing atmospheres ", *J. Electroceram.* 5 (2000) 31.

[70] A. Sakabe and H. Takagi: „Nonreducible mechanism of $\{(Ba_{1-x}Ca_x)O\}_mTiO_2$ (m > 1) ceramics", *Jpn. J. Appl. Phys.* 41 (2002) 6461.

[71] Y. Tsur, T. D. Dunber and C. A. Randall: „Crystal and defect chemistry of rare earth cations in $BaTiO_3$ ", *J. Electroceram.* 7 (2001)25.

[72] H. Ihrig and D. Hennings: „Electrical transport properties of n-type $BaTiO_3$", *Phys. Rev. B* 17 (1978) 4593.

[73] S.-H. Yoon and H. Kim: „Effect of donor (Nb) concentration on the bulk electrical resistivity of Nb-doped barium titanate", *J. Appl. Phys.* 92 (2002) 1039.

[74] N. Hirose and A. R. West: Impedance spectroscopy of undoped $BaTiO_3$ ceramics", *J. Am. Ceram. Soc.* 79 (1996) 1633.

[75] B. M. Kulwicki, A. J. Purdes: „Diffusion potentials in $BaTiO_3$ and the theory of PTC materials", *Ferroelectrics* 1 (1970) 253.

[76] H. Ihrig and W. Puschert: „A systematic experiment and theoretical investigation of the grain-boundary resistivities of n-doped $BaTiO_3$ ceramics", *J. Appl. Phys*. 48 (1977) 3081.

[77] C.-H. Lai, Y.-Y. Lu, and T.-Y. Tseng: „Calculations and modelling of grain-boundary acceptor states for $(Ba,Pb)TiO_3$ positive temperature coefficient ceramics*", J. Appl. Phys*. 74 (1993) 3383.

[78] C.-H. Lai and T.-Y. Tseng: „Investigation of resistivity and permittivity for $(Ba,Pb)TiO_3$, PTCR ceramics", *J. Am. Ceram. Soc.* 77 (1994) 2419.

[79] C.-H. Lai, C.-T. Weng, T.-Y. Tseng: „The effects of Nd_2O_3 additives and Al_2O_3-SiO_2-TiO_2 sintering aids on the electrical resistivity of $(Ba,Sr)TiO_3$ PTCR ceramics", *Mater. Chem. Phys.* 40 (1995) 168.

[80] E. Brzozowski and M. S. Castro: „Conduction mechanism of barium titanate ceramics", *Ceram. Int.* 26 (2000) 265.

[81] W. Preis, A. Bürgermeister, W. Sitte, P. Supancic: „Bulk and grain boundary resistivities of donor-doped barium titanate ceramics", *Solid State Ionics* 173 (2004) 69.

[82] L. U. Schneider-Störmann: „Transiente Vorgänge in donatordotierten Bariumtitanat-Keramiken" *Ph.D. Thesis*, *Faculty of electrical engineering and information technology*, *Rheinisch-Westfälische Technische Hochschule Aachen* (1997).

[83] C. Pithan, Y. Shiratori, J. Dornseiffer, F. H. Haegel and R. Waser: „Preparation, processing and characterization of nano-crystalline $BaTiO_3$ powders and ceramics derived from microemulsion-mediated synthesis", *J. Am. Ceram. Soc.* 89 (2006) 2908.

[84] Z. A. Munir, U. Anselmi-Tamburini and M. Ohyanagi: „The effect of electric field and pressure on the synthesis and consolidation of materials: a review of the spark plasma sintering method", *J. Mater. Sci.* 41 (2006) 763.

[85] J. Seaton and C. Leach: „Formation and retention of low Σ interfaces in PTC thermistors", *Acta. Mater.* 53 (2005) 2751.

[86] N. M. Beekmans and L. Heyne: „Correlation between impedance, microstructure and composition of calcia-stabilized zirconia", *Electrochim. Acta* 2 (1976) 303.

[87] T. van Dijk and A. J. Burggraaf: „Grain boundary effects on ionic conductivity in ceramics $Gd_xZr_{1-x}O_{2-(x/2)}$ solid solutions", *phys. stat. sol. (a)* 63 (1981) 229.

[88] M. J. Verkerk, B. J. Middelhuis and A. J. Burggraaf: „Effect of grain boundaries on the conductivity of high-purity ZrO_2-Y_2O_3 ceramics", *Solid State Ionics* 6 (1982) 159.

[89] N. Bonanos, B. C. H. Steele and E. P. Butler: „Applications of impedance spectroscopy" in *Impedance spectroscopy – Theory, Experiment, and Applications*, ed. by E. Barsoukov, J. R. Macdonald, Wiley-Interscience, Hoboken, USA (2005) 494.

[90] D. Cann and C. Randall: „Electrode effects in positive temperature coefficient and negative temperature coefficient devices measured by complex-plane impedance analysis", *J. Appl. Phys.* 80 (1996) 1628.

[91] M. H. Frey, Z. Xu, P. Han and D. A. Payne: „The role of interfaces on an apparent grain size effect on the dielectric properties for ferroelectric barium titanate ceramics", *Ferroelectrics* 206-207 (1998) 337.

[92] Z. Zhao, V. Buscaglia, M. Viviani, M. T. Buscaglia, L. Mitoseriu, A. Testino, M. Nygren, M. Johnson and P. Nanni: „Grain-size effects on the ferroelectric behavior of dense nanocrystalline $BaTiO_3$ ceramics", *Phys. Rev. B* 70 (2004) 24107.

[93] G. Spinolo, G. Chiodelli, A. Magistris and U. A. Tamburini: „Data processing for electrochemical measurements with frequency response analyzer", *J. Electrochem. Soc.* 135 (1988) 1420.

[94] C. H. Hsu and F. Mansfeld: „Concerning the conversion of the constant phase element parameter into a capacitance", *Corrosion* 57 (2001) 747.

[95] I. Barin in *Thermochemical data of pure substances*, 3rd edition, Wiley-VCH Verlagsgesellschaft GmbH, Germany (2004).

[96] A. D. Brailsford, M. Yussouff, E. M. Logothetis, T. Wang and R. E. Soltis Braisford: „Experimental and theoretical study of the response of ZrO_2 oxygen sensors to simple one-reducing-gas mixtures", *Sensors and Actuators B* 42 (1997) 15.

[97] Y. Oishi and W. D. Kingery: „Self-diffusion of oxygen in single crystal and polycrystalline aluminum oxide", *J. Chem. Phys.* 33 (1960) 480.

[98] R. A. de Souza, J. Zehnpfenning, M. Martin and J. Maier: "Determining oxygen isotope profiles in oxides with time-of-flight SIMS", *Solid State Ionics* 176 (2005) 1465.

[99] R. A. de Souza and M. Martin: "Using $^{18}O/^{16}O$ exchange to probe an equilibrium space-charge layer at the surface of a crystalline oxide: method and application" *Phys. Chem. Chem. Phys.* 10 (2008) 2356.

[100] Y. H. Hu, M. P. Harmer and D. M. Smyth: „Solubility of BaO in $BaTiO_3$", *J. Am. Ceram. Soc.* 68 (1985) 372.

[101] M. Drofenik, D .Makovec, I. Zajc and H. T. Langhammer: „Anomalous Grain Growth in Donor-Doped Barium Titanate with Excess Barium Oxide", *J. Am. Ceram. Soc.* 85 (2002) 653.

[102] M. Drofenik: „Oxygen partial pressure and grain growth in donor-doped $BaTiO_3$", *J. Am. Ceram. Soc.* 70 (1987) 311.

[103] (a) J. A. Bland: „The crystal structure of barium orthotitanate, Ba_2TiO_4" *Acta. Cryst.* 14 (1961) 875.
(b) JCPDS card No. 35 813.

[104] D. E. Rase and R. Roy: „Phase equilibria in the system $BaTiO_3$-SiO_2", *J. Am. Ceram. Soc.* 38 (1955) 389.

[105] K. H. Felgner, T. Müller, H. T. Langhammer and H.-P. Abicht: „Investigation on the liquid phase in barium titanate ceramics with silica additives", *J. Eur. Ceram. Soc.* 21 (2001) 1657.

[106] M. Vollmann: „Elektronische Korngrenzeneigenschaften akzeptordotierter $SrTiO_3$-Dielektrika", *Ph.D. thesis*, *Faculty of electrical engineering and information technology*, *Rheinisch-Westfälische Technische Hochschule Aachen* (1997).

[107] S. Ruddlesden and P. Popper: „The compound $Sr_3Ti_2O_7$ and its structure", *Acta. Crystallogr.* 11 (1958) 54.

[108] M. A. McCoy, R. W. Grimes and W. E. Lee: „Phase stability and interfacial structures in the SrO-$SrTiO_3$ system", *Philos. Mag. A* 75 (1997) 833.

[109] R. Meyer and R. Waser: „Cationic surface segregation in donor-doped $SrTiO_3$ under oxidizing conditions", *J. Electroceram.* 9 (2002) 101.

[110] K. Szot, C. Freiburg and M. Pawelczyk: „Layer structures BaO-$BaTiO_3$ in the region of p-type conductivity on the surface of $BaTiO_3$", *Appl. Phys. A* 53 (1991) 563.

[111] O. Saburi: „Properties of semiconductive barium titanate", *J. Phys. Soc. Jap.* 14 (1959) 1159.

[112] (a) D. C. Sinclair and A. R. West: „Impedance and modulus spectroscopy of semiconducting $BaTiO_3$ showing positive temperature coefficient of resistance", *J. Appl. Phys.* 66 (1989) 3850.
(b) D. C. Sinclair and A. R. West: „Effect of atmosphere on the PTCR properties of $BaTiO_3$ ceramics", *J. Mater. Sci.* 29 (1994) 6061.

[113] CRC Handbook of Chemistry and Physics, ed. by R. D. Lide, 88 (2008) 12.

[114] D. P. Cann, J.-P. Maria and C. A. Randall: „Relationship between wetting and electrical contact properties of pure metals and alloys on semiconducting barium titanate ceramics", *J. Mater. Sci.* 36 (2001) 4969.

[115] H.-I. Yoo, C.-R. Song, Y.-S. Lee, D.-K. Lee: „Surface reaction kinetics in oxygen non-stoichiometry re-equilibration of $BaTiO_{3-\delta}$", *Solid State Ionics* 160 (2003) 381.

[116] H. Haneda, I. Sakaguchi, A. Watanabe, T. Ishigaki and J. Tanaka: „Oxygen diffusion in single- and polycrystalline zinc oxides", *J. Electroceram.* 4 (1999) 41.

[117] A. D. Le Clair: „The analysis of grain boundary diffusion measurements", *Brit. J. Appl. Phys.* 14 (1963) 351.

[118] J. Ito, D.-C. Park, N. Ohashi, I. Sakaguchi, I. Yamashima, H. Haneda and J. Tanaka: „Oxygen defects related to electrical properties of La-doped $BaTiO_3$", *Jap. J. Appl. Phys.* 41 (2002) 3798.

[119] (a) S. Shirasaki, M. Tsukioka, H. Yamamura, H. Oshima and K. Kakegawa: „Origin of semi-conducting behavior in rare-earth doped barium titanate", *Solid State Communications* 19 (1976) 721.
(b) S. Shirasaki, H. Yamamura, H. Hanade, K. Kakegawa and J. Moori: „Defect structure and oxygen diffusion in undoped and La-doped polycrystalline barium titanate", *J. Chem. Phys.* 73 (1980) 4640.
(c) S. Shirasaki, H. Haneda, K. Arai and M. Fujimoto: „Electrical property and defect structure of lanthanum-doped polycrystalline barium titanate", *J. Mater. Sci.* 22 (1987) 4439.

[120] (a) S. Higai, A. Honda, Y. Motoyoshi, N. Wada, H. Takagi and Y. Sakabe: „Industry meets theory: computational R & D for innovative products", *J. Phys.*: *Condens. Matter.* 22 (2010) 384209.
(b) to be published by A. Honda and S.Higai

[121] D. M. Smyth: „The Defect Chemistry of Donor-Doped $BaTiO_3$: A Rebuttal", *J. Electroceram.* 9 (2002) 179.

[122] C.-E. Lee and H.-I. Yoo: „Ba/Ti ratio effect on oxygen re-equilibration kinetics of donor-doped $BaTiO_3$", *Solid State Ionics* 179 (2008) 338.

[123] A. Bürgermeister, A. Benisek and W. Sitte: „Electrochemical device for the precise adjustment of oxygen partial pressures in a gas stream", *Solid State Ionics* 170 (2004) 99.

[124] R. Moos and K. H. Härdtl: „Electric transport properties of $Sr_{1-x}La_xTiO_3$ ceramics", *J. Appl. Phys*. 80 (1996) 393.

[125] J. P. Straley: „Thermoelectric properties of inhomogeneous materials", *J. Phys. D: Appl. Phys.* 14 (1981) 2101.

[126] S. Lee, G. Yang, R. H. T. Wilke, S. Trolier-McKinstry and C. A. Randall: „Thermopower in highly reduced n-type ferroelectric and related perovskite oxides and the role of heterogeneous nonstoichiometry", *Phys. Rev. B* 79 (2009) 134110.

[127] T. Kolodiazhnyi, A. Petric, M. Niewczas, C. Bridges, A. Safa-Sefat and J. E. „Greedan: „Thermo-electric power, Hall effect, and mobility of n-type $BaTiO_3$", *Phys. Rev. B* 68 (2003) 085205.

[128] H.-I. Yoo, S. W. Lee and C. E. Lee: „P-type partial conductivity of donor (La)-doped $BaTiO_3$", *J. Electroceram.* 10 (2003) 215.

[129] D. M. Smyth: „The Defect Chemistry of Metal Oxides", Oxford University Press, Oxford, UK (2000).

[130] S. Lee, C. Randall and Z.-K. Liu: „Factors limiting equilibrium in fabricating a simple ferroelectric oxide: $BaTiO_3$", *J. Am. Ceram. Soc*. 92 (2009) 222.

[131] (a) S. Lee, C. Randall and Z.-K. Liu: „Modified phase diagram for the barium oxide-titanium dioxide", *J. Am. Ceram. Soc.* 90 (2007) 2589.
(b) S. Lee, C. Randall and Z.-K. Liu: „Comprehensive linkage of defect and phase equilibria through ferroelectric transition behavior in $BaTiO_3$-based dielectrics: Part 2. defect modeling under low oxygen partial pressure conditions", *J. Am. Ceram. Soc.* 91 (2008) 1753.

[132] J. F. Ihlefeld, P. R. Daniels, S. M. Aygün, W. J. Borland and J.-P. Maria: „Property engineering in $BaTiO_3$ films by stoichiometry control", *J. Mater. Res.* 25 (2010) 1064.

[133] (a) Y. M. Chiang and T. Takagi: „Grain-boundary chemistry of barium titanate and strontium titanate: I, High-temperature equilibrium space charge", *J. Am. Ceram. Soc.* 73 (1990) 3278.
(b) Y. M. Chiang and T. Takagi: „Grain-boundary chemistry of barium titanate and strontium titanate: II, Origin of electrical barriers in positive-temperature-coefficient thermistors", *J. Am. Ceram. Soc*. 73 (1990) 3286.

[134] M. J. Pan and C. A. Randall: „A brief introduction to ceramic capacitors", *IEEE Electrical Insulation Magazine* 26 (2010) 44.

[135] C.-J. Kim, K. No: „Impedance analysis of cooling-rate effects on the depletion layer of PTCR materials", *J. Mater. Sci*. 28 (1993) 5765.

[136] J. Daniels, K. H. Härdtl and R. Wernicke: „The PTC effect of barium titanate", *Philips. Tech. Review.* 38 (1978) 73.

[137] P. Lupetin, G. Gregori and J. Maier: „Mesoscopic charge carriers chemistry in nanocrystalline $SrTiO_3$", *Angewandte Chemie* 49 (2010) 1.

[138] J. Liu and Z. Shen: „Spark plasma sintering behavior of nano-sized $(Ba,Sr)TiO_3$ powders: Determination of sintering parameters yielding nanostructured ceramics", *J. Am. Ceram. Soc.* 89 (2006) 2689.

[139] D. Makovec, N. Ule and M. Drofenik: „Positive temperature coefficient of resistivity effect in highly donor-doped barium titanate", *J. Am. Ceram. Soc.* 84 (2001) 1273.

[140] M.-P. Chun, J.-H. Nam, J.-H. Cho and B.-I. Kim: „Effect of re-oxidation firing on PTCR properties of Sm-doped barium titanate ceramics", *J. Ceram. Proces. Res*. 11 (2010) 112.

[141] H. T. Langhammer, D. Makovec, Y. Pu, H. P. Abicht and M. Drofenik: „Grain boundary reoxidation of donor-doped barium titanate ceramics", *J. Eur. Ceram. Soc*. 26 (2006) 2899.

[142] X. Guo, C. Pithan, C. Ohly, C.-L. Jia. J. Dornseiffer, F.-H. Haegel and R. Waser: „Enhancement of p-type conductivity in nanocrystalline $BaTiO_3$ ceramics", *Appl. Phys. Lett.* 86 (2005) 082110.

[143] G. H. Haertling and C. E. Land: „Hot-pressed $(Pb,La)(Zr,Ti)O_3$ ferroelectric ceramics for electro optic applications", *J. Am. Ceram. Soc.* 54 (1971) 1.

[144] J. G. J. Peelen and R. Matselaar: „Light scattering by pores in polycrystalline materials: Transmission properties of alumina", *J. Appl. Phys*. 45 (1974) 216.

[145] H. Yamamura, H. Haneda, A. Watanabe and S. Shirasaki, „Hot-pressing of barium titanate prepared by oxalate method in ethanol", *Jap. J. Appl. Phys.* 24 (1985) 433.

[146] H. Shimaoka, S. Kohiki, T. Kobayashi and M. Kuwabara: „Preparation of translucent barium titanate ceramics from sol–gel-derived transparent monolithic gels", *J. Mater. Chem.* 10 (2000) 1511.

[147] J.-H. Cho, W.-Y. Choi, S.-H. Kim and M. Kuwabara: „Ferroelectric and optic properties of the translucent $BaTiO_3$ ceramics derived from nanocrystalline monolith", *Integrated Ferroelectrics* 69 (2005) 287.

[148] J. Liu, Z. Shen, W. Yao, Y. Zhao and A. K Mukherjee: „Visible and infrared transparency in lead-free bulk $BaTiO_3$ and $SrTiO_3$ nanoceramics", *Nanotechnology* 21 (2010) 075706.

[149] U. Anselmi-Tamburini, J. N. Woolman and Z. A. Muniret: „Transparent nanometric cubic and tetragonal zirconia obtained by high-pressure pulsed electric current sintering", *Adv. Funct. Mater.* 17 (2007) 3267.

[150] T. Murakami, M. Nakahara, T. Miyashita and S. Ueda: „Electrical conduction of rare-earth-doped $BaTiO_3$ single crystals", *J. Am. Ceram. Soc.* 56 (1973) 291.

[151] K. Kakegawa and J. Mohri: „Synthesis of Nb-doped barium titanate semiconductor by a wet-dry combination technique", *J. Mater. Science. Lett*. 4 (1985) 1266.

[152] M. Drofenik: „Origin of the grain growth anomaly in donor-doped barium titanate", *J. Am. Ceram. Soc.* 76 (1993) 123.

[153] X. Chen and C. Burda: „The electronic origin of the visible-light absorption properties of C-, N- and S-Doped TiO_2 nanomaterials", *J. Am. Chem. Soc.* 130 (2008) 5018.

[154] J. G. Fisher, B.-K. Lee, S.-Y. Choi, S.-M. Wang, S.-J. L. Kang: „Inhibition of abnormal grain growth in $BaTiO_3$ by addition of Al_2O_3", *J. Eur. Ceram. Soc.* 26 (2006) 1619.

[155] F. D. Morrison, D. C. Sinclair and A. R. West: „Electrical and structural characteristics of lanthanum-doped barium titanate ceramics", *J. Electroceram*. 86 (1999) 6355.

[156] W. J. Merz: „Double hysteresis loop of $BaTiO_3$ at the Curie point", *Phys. Rev.* 91 (1953) 513.

[157] K. Uchino, E. Sadanaga and T. Hirose „Dependence of the crystal structure on particle size in barium titanate", *J. Am. Chem. Soc.* 72 (1989) 1555.

[158] Handbook of Optics, ed. M. Bass, 3rd edition, Volume IV, McGraw-Hill, New York, USA (2009).

[159] H. Fujiwara in *Spectroscopic Ellipsometry - Principles and Applications*, John Wiley, New York, USA (2007).

[160] (a) S. H. Wempel and M. DiDomenico Jr: „Behavior of the electronic dielectric constant in covalent and ionic materials", *Phys. Rev. B*. 3 (1971) 1138.
(b) M. DiDomenico Jr. and S. H. Wempel: „Oxygen-octahedra ferroelectrics. I. Theory of electro-optical and nonlinear optical effects", *J. Appl. Phys*. 40 (1969) 720.

[161] H. Basantakumuar Sharma: „Structural and optical properties of sol-gel derived barium titanate thin film", *Int. J. Mod. Phys. B* 21 (2007) 1837.

[162] H.-S. Kwon, H.-I. Yoo, C.-H. Kim and K.-H. Hur: „Semiconductor-to-insulator transition of undoped-$BaTiO_3$ in quenched state", J. Appl. Phys. 107 (2010) 083702.

1. **Ferrocenes as Potential Building Blocks for Molecular Electronics**
   Self-Assembly and Tunneling Spectroscopy
   by L. Müller-Meskamp (2008), 153 pages
   ISBN: 978-3-89336-509-8

2. **Magnetic Proximity Effects in Highly-ordered Transition Metal Oxide Heterosystems studied by Soft x-Ray Photoemission Electron Microscopy**
   by I. P. Krug (2008), XX, 180 pages
   ISBN: 978-3-89336-521-0

3. **Seltenerd-basierte ternäre Oxide als alternative Gatedielektrika**
   von J. M. Roeckerath (2008), 148 Seiten
   ISBN: 978-3-89336-543-2

4. **Strominduzierte Magnetisierungsdynamik in einkristallinen Nanosäulen**
   von R. Lehndorff (2009), I, 86 Seiten
   ISBN: 978-3-89336-564-7

5. **Magnetization Dynamics in Magnetically Coupled Heterostructures**
   von A. Kaiser (2009), X, 121 pages
   ISBN: 978-3-89336-577-7

6. **Resistive switching in Pt/TiO_2/PT**
   by D. S. Jeong (2009), vii, 133 pages
   ISBN: 978-3-89336-579-1

7. **Electromechanical Force Microscopy and Tip-Enhanced Raman Spectroscopy for Polar Oxide Nanoparticles**
   by S. Röhrig (2009), vi, 114 pages
   ISBN: 978-3-89336-600-2

8. **Investigation of resistive switching in barium strontium titanate thin films for memory applications**
   by W. Shen (2010), 114 pages
   ISBN: 978-3-89336-608-8

9. **Nanostrukturierte Metallelektroden zur funktionalen Kopplung an neuronale Zellen**
   von D. Brüggemann (2010), vii, 160 Seiten
   ISBN: 978-3-89336-627-9

10. **Integration of resistive switching devices in crossbar structures**
    by Chr. Nauenheim (2010), XII, 142 pages
    ISBN: 978-3-89336-636-1

11. **Correlation between Raman spectroscopy and electron microscopy on individual carbon nanotubes and peapods**
by C. Spudat (2010). xiv, 125 pages
ISBN: 978-3-89336-648-4

12. **DC and RF Characterization of NiSi Schottky Barrier MOSFETs with Dopant Segregation**
by C. J. Urban (2010), iv, 151 pages
ISBN: 978-3-89336-644-6

13. **Alternative Systems for Molecular Electronics: Functionalized Carboxylic Acids on Structured Surfaces**
by M. C. Lennartz (2010), 183 pages
ISBN: 978-3-89336-667-5

14. **Highly conductive electrodes as diffusion barrier for high temperature applications**
by B. Meši (2010), VII, 138 pages
ISBN: 978-3-89336-670-5

15. **Modeling, Fabrication and Characterization of Silicon Tunnel Field-Effect Transistors**
by C. P. Sandow (2010), XIII, 112 pages
ISBN: 978-3-89336-675-0

16. **Substituted Coronenes for Molecular Electronics: From Supramolecular Structures to Single Molecules**
by P. Kowalzik (2010), ix, 149 pages
ISBN: 978-3-89336-679-8

17. **Resistive switching in TiO2 thin films**
by L. Yang (2011), VII, 117 pages
ISBN: 978-3-89336-707-8

18. **Crystal- and Defect-Chemistry of Fine Grained Thermistor Ceramics on $BaTiO_3$ Basis with BaO-Excess**
by H. Katsu (2011), xxvii, 163 pages
ISBN: 978-3-89336-741-2

Information / Information
Band / Volume 18
ISBN 978-3-89336-741-2

JÜLICH
FORSCHUNGSZENTRUM